Multiscale characterisation of subchondral trabecular bone changes in the osteoarthritic ankle

Lekha L. H. Koria

Submitted in accordance with the requirements for the degree of
Doctor of Philosophy

School of Mechanical Engineering
The University of Leeds

July 2021

DECLARATION

The candidate confirms that the work submitted is their own, except where work which has formed part of jointly authored publications has been included. The contribution of the candidate and the other authors to this work has been explicitly indicated below. The candidate confirms that the appropriate credit has been given within the thesis where reference has been made to the work of others.

Chapter 6 of this thesis contains materials published in a jointly authored paper:

Koria, L., Mengoni, M., & Brockett, C. (2020). Estimating tissue-level properties of porcine talar subchondral bone. Journal of the Mechanical Behavior of Biomedical Materials, 110, 103931.

The candidate developed the computational methods and analysed the results in this paper. Co-authors contributed their technical expertise, including the optimisation methodology, and valuable discussion of the results.

ACKNOWLEDGEMENTS

I would like to wholeheartedly thank everyone who helped me with my PhD.

A huge thank you to Dr Claire Brockett and Dr Marlène Mengoni for their expertise, endless guidance and unwavering support. Thank you to Dr Elena Jones for bringing her knowledge and ideas to my improve and expand my research. I have learnt so much from all of you and I am so very grateful to have had such a fantastic and inspiring team of supervisors for the last four years.

I would like to thank our clinical collaborators at Leeds, Mr Ippokratis Pountos & Mr Nazzar Tellisi, and at Harrogate, Mr Mark Farndon & Mr David Lavalette, for your expertise and invaluable contributions to this research. Thank you also to our academic collaborators at Heriot-Watt University, Dr Uwe Wolfram and Mr Sam McPhee, for their knowledge and support with the nanoindentation study. Thanks also to Ms Teodora Dinescu at Columbia University, who provided guidance and support for the ITS software.

I am also thankful to the lovely members of the iMBE, all of whom have been approachable, knowledgeable and supportive since the beginning. In particular, a huge thank you to: Dr Nagitha Wijayathunga, Dr Anthony Herbert, Dr Michelle Casper-Taylor, Dr Gavin Day, Dr David Rochelle, Mr Phil Wood & all of the iMBE technicians for their help and patience in the lab.

Thank you to the iMBE ankle research group, the FASTER group and the iMBE computational group for creating a friendly environment that allowed for discussion and improvement of this research.

I am also grateful to have worked alongside some amazing researchers as part of the CDT. Thank you so much for your support, the laughs and making this journey much easier.

This work was funded by the EPSRC. Thank you to the patients, tissue donors and their families.

ABSTRACT

An increasingly younger population are seeking treatment for osteoarthritis of the ankle. Current late-stage surgical interventions sacrifice the upper levels of the distal tibia and talus to allow for joint replacement implantation. This can lead to multiple failure modes with regards to the success of the device, as well as low bone stock at revision. Changes to subchondral bone with osteoarthritis is well studied in the hip and knee, but the ankle remains highly under-reported. Medical imaging and validated computational modelling can provide predictive capabilities of bone properties in the ankle and help to inform surgical interventions.

Hence, the aim of the studies compiled in this thesis was to characterise the structural and mechanical changes to subchondral bone in the late-stage osteoarthritic ankle. Using mechanical characterisation and medical imaging, a specimen-specific finite element methodology was developed using porcine tissue and translated for use on non-diseased human trabecular bone to estimate tissue-level properties through the optimisation of grayscale-based material properties. Nanoindentation was used to directly measure tissue mechanical properties, which aided in assessing changes to the apparent-level stiffness of osteoarthritic bone. High-resolution medical imaging provided a means of detailed, three-dimensional morphological evaluation of the trabecular architecture, thus providing an insight to the remodelling of the bone with osteoarthritis and its influence on bone stiffness.

The porcine and non-diseased human FE models showed good agreement between computational and experimental stiffness values. Evaluation of osteoarthritic bone showed significant remodelling of trabecular microarchitecture, higher apparent stiffness, and altered tissue properties. Further investigation is needed to fully understand the impact of multiscale bone changes with osteoarthritis in the ankle, but this work has provided the foundations for understanding these changes. Such information will be crucial to aid future implant design and the development of joint strength prediction models using medical images, to inform surgical decisions.

CONTENTS

Declaration

Acknowledgements

Abstract

List of Figures

List of Tables

List of Abbreviations

Introduction

LIST OF FIGURES

LIST OF TABLES

LIST OF ABBREVIATIONS

AVG	Average (Mean)
aBV/TV	Axial Bone Volume Fraction
BMI	Body Mass Index
BV/TV	Bone Volume Fraction
BW	Body Weight
CCC	Concordance Correlation Coefficient
CoV	Coefficient of Variance
Conn.D	Connectivity Density
CT	Computed Tomography
DA	Degree of Anisotropy
E	Elastic (Young's) Modulus
E_{tiss}	Tissue e=Elastic Modulus
EF	Ellipsoid Factor
FE	Finite Element
GS	Grayscale
hFE	Continuum-Level (Homogenised) Finite Element
HR-pQCT	High Resolution Peripheral Quantitative CT
HU	Hounsfield Units
ITS	Individual Trabecular Segmentation
k	Stiffness
ND	Non-Diseased
OA	Osteoarthritic
pBV/BV	Plate Tissue Fraction
pBV/TV	Plate Volume Fraction
pBV/rBV	Plate-Rod Ratio
PMMA	Polymethylmethacrylate
PR/PP Junc.D	Plate-Rod/Plate-Plate Junction Density
pTb.Th/pTb.N/pTb.S	Mean Plate Trabecular Thickness/Number/Surface Area
PTOA	Post-Traumatic Osteoarthritis
RMSE	Root Mean Square Error
rBV/BV	Rod Tissue Fraction
rBV/TV	Rod Volume Fraction
RR Junc.D	Rod-Rod Junction Density
rTb.Th/rTb.N/rTb.l	Mean Rod Trabecular Thickness/Number/Length

ROI	Region of Interest
SBP	Subchondral Bone Plate
SD	Standard Deviation
SMI	Structure Model Index
TAA	Total Ankle Arthroplasty
TAR	Total Ankle Replacement
Tb.Th	Trabecular Thickness
UK	United Kingdom
$\varnothing$	Diameter (mm)
ν	Poisson's Ratio
ρ	Density
μCT	Micro-CT
μFE	Micro-Finite Element
3D	Three-Dimensional

INTRODUCTION

Ankle osteoarthritis (OA) is a debilitating, degenerative disease of the talocrural joint. It is thought that 1% of the global population suffer from OA of the foot and ankle, and in the UK alone, around 30,000 symptomatic ankle OA patients seek treatment from specialists annually [Goldberg et al., 2012]. Ankle OA is predominantly post-traumatic; as many as 80% of cases are thought to be a direct consequence of ankle sprain or trauma [Horisberger et al., 2009, Valderrabano et al., 2009, Brown et al., 2006]. Naturally, ankle trauma is commonplace in sports, resulting in an increasingly younger patient population requiring treatment earlier than those with osteoarthritis of other joints [Delco et al., 2017, Saltzman et al., 2005].

In late-stage OA, surgical interventions such as total ankle arthroplasty (TAA) offer increased joint mobility, but at the cost of resecting several millimetres of bone from the distal tibia and talar dome [Hintermann and Ruiz, 2014]. Total ankle replacement (TAR) devices are therefore at risk of loosening, subsidence and increased fracture risk potentially caused by low bone stock of poor quality [Currier et al., 2019, Glazebrook et al., 2009]. Consequently, TARs have higher revision rates compared to other lower-limb joint replacements [Egloff et al., 2012]. Yet despite the risks, demand for TAA is rising annually in the UK [Goldberg et al., 2012, Commitee, 2019].

The use of patient-specific medical imaging for surgical planning is already common in many hospitals for orthopaedic applications, where computed tomography (CT) or magnetic resonance (MR) images can be used to generate simulated geometries computationally. However, this has yet to be extended to include reliable prediction of bone quality. The generation of such models would allow surgeons to better understand the biomechanical capabilities of a patients' joint, which may help inform surgical decisions or aid in determining appropriate early-stage conservative treatments that are less destructive.

An understanding of the influences of tissue properties and microarchitecture can help to predict variations to apparent bone stiffness in diseased and healthy states, but this requires multiscale characterisation to understand and calibrate material properties reliably. Chapter 1 explores and evaluates the current literature in detail, to determine the aims and objectives of this research. Chapter 2 then outlines the contents of the remaining chapters within this thesis.

CHAPTER 1

LITERATURE REVIEW

1.1 Ankle Anatomy

The ankle joint or talocrural joint is a synovial hinge joint in the lower limb that connects the leg to the foot. The talocrural joint complex is the combination of the talus, distal tibia and distal fibula (Fig. 1.1). The articulating surfaces of the distal tibia (the tibial plafond) and talus (trochlear surface or the talar dome), form a synovial hinge joint allowing dorsiflexion and plantarflexion of the foot [Brockett and Chapman, 2016].

The investigation of forces through the foot is significant to understanding the pathophysiology of disease in the ankle. Though similar in joint conformity to the knee, the ankle is a more congruent joint and its smaller contact area results in higher pressures through the joint [Huch et al., 1997]. Da Vinci described how forces in the ankle joint can exceed the force of body weight alone [Jastifer and Toledo-Pereyra, 2012]. This is now a well known concept; it is thought that peak vertical loads through the talar dome are around five times body weight (BW) during normal locomotion and thirteen times BW during exercise [Stauffer et al., 1977, Burdett, 1982, Kakkar and Siddique, 2011]. The talar dome (approximately 11-13 cm^2 area) predominately bears the transfer of forces from the leg to the foot, with the majority of contact focused at the anterio-lateral area of the joint in neutral position [Kimizuka et al., 1980]. With degenerative joint diseases however, joint load can decrease to approximately three times BW [Stauffer et al., 1977].

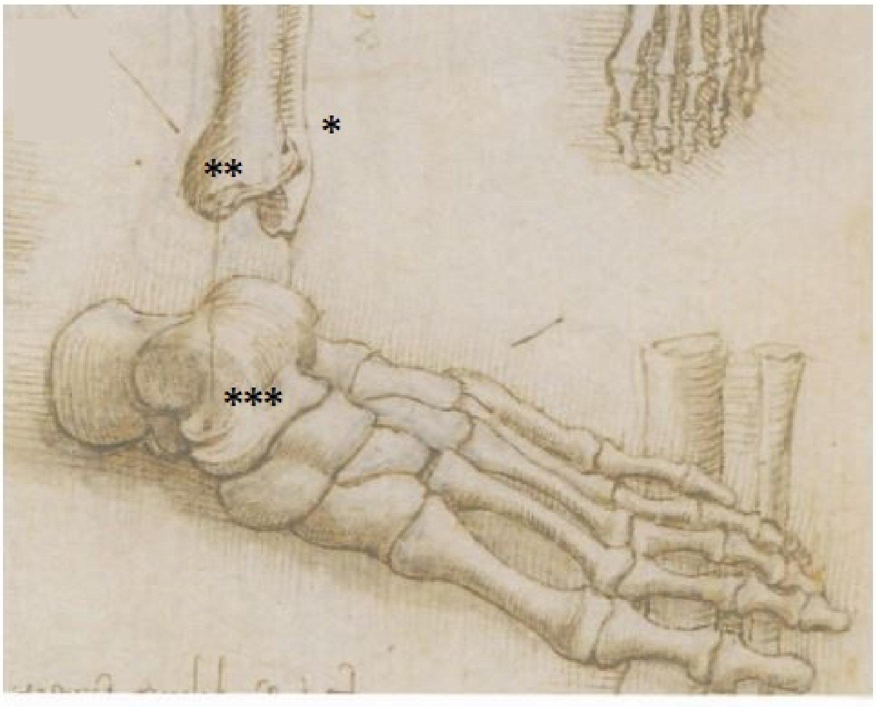

Figure 1.1: Medial view of the foot and ankle complex. Ankle bones labelled as follows: * distal fibula, ** distal tibia and *** talus. *Adapted from [Jastifer and Toledo-Pereyra, 2012] with permission from Taylor & Francis, www.tandfonline.com, © Journal of Investigative Surgery.*

1.2 Hierarchical Structure of Bone

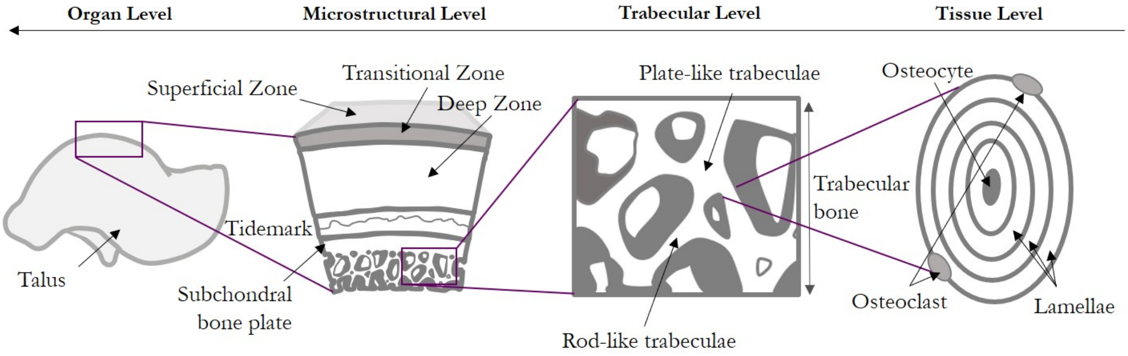

Figure 1.2: Hierarchical levels of articular cartilage and subchondral bone.

The osteochondral unit generally comprises of articular cartilage and subchondral bone. Articular cartilage provides a low-friction surface for joint articulation and wear prevention. It is comprised of different zones: from the superficial zone down to the deep zone (Fig. 1.2) through which collagen thickness, orientation and proteoglycan content alter. In the ankle, the thickness of articular cartilage varies, but is typically around 1.1 mm thickness [Millington et al., 2007]. The tidemark is a trilaminate band of dense, mineralised cartilage [Madry et al., 2010].

This osteochondral junction marks the end of the deep zone and the beginning of the calcified cartilage, thus joining cartilage to the underlying subchondral bone [Sophia Fox et al., 2009]. The term, *subchondral bone*, encompasses both the subchondral bone plate (SBP, a thin cortical layer) and subchondral cancellous, or trabecular bone [Johnston et al., 2016]. The continuum, or apparent level of subchondral trabecular bone is defined as a continuous volume which spans multiple trabeculae and the marrow. The tissue level of bone is defined as the bone material level on the scale of a bone structural unit (60 μm) which is derived from matrix-level, or intra-lamallar level properties (2-7 μm) [Zysset, 2009].

1.2.1 Composition

The composition, architecture and morphology of bone provides the properties suited for its structural and supportive function in the human skeleton. Bone is a mineralised connective tissue, composed of approximately, 65% mineral, 25% organic material and 10% water by mass [Hernandez, 2016]. The organic phase of bone is formed of type I collagen (90%) and non-collagenous proteins arranged in parallel with each other, providing elasticity to the tissue [Keaveny et al., 2004]. The inorganic phase comprises of hydroxyapatite, a ceramic crystalline material that provides rigidity to the bone and nests between the collagen fibrils.

1.2.2 Microarchitecture

As stated previously, the subchondral bone plate (SBP) is a thin cortical layer immediately beneath calcified cartilage. Here, collagen fibrils stack unidirectionally into sheets to form lamellae, alternating angles between the layers [Keaveny et al., 2004]. Lamallae are organised into tightly packed concentric layers. Such functional units of lamallae form Haversian systems [Rho et al., 1998] and are connected together by Volkmann's canals and contain small cavities, home to osteocytes. The SBP provides a link between the articulating cartilage and subchondral trabecular bone [Li et al., 2013]. In the talus for example, this is thought to be in the order of 0.8 mm thick [Nakasa et al., 2014], compared to the tibial plateau which can exceed 1.5 mm [Milz and Putz, 1994].

Trabecular bone microstructure was first described in the late 1600s by Crisóstomo Martinez (1638-1694) using a simple microscope [Gomez, 2002]. His studies of the structure and function of bone led to his depiction of the intricate lattice network of trabeculae that provide the strength to the epiphyses and metaphyses. In trabecular bone, collagen fibres infused with a semi-crystalline mineral component form an anisotropic, porous matrix structure, referred to as the trabecular architecture [Rho et al., 1998]. Its porous structure is saturated with bone marrow, blood and body fluid [Pal, 2014], which altogether provide its shock-absorbing and supportive abilities to the joint [Halgrin et al., 2012].

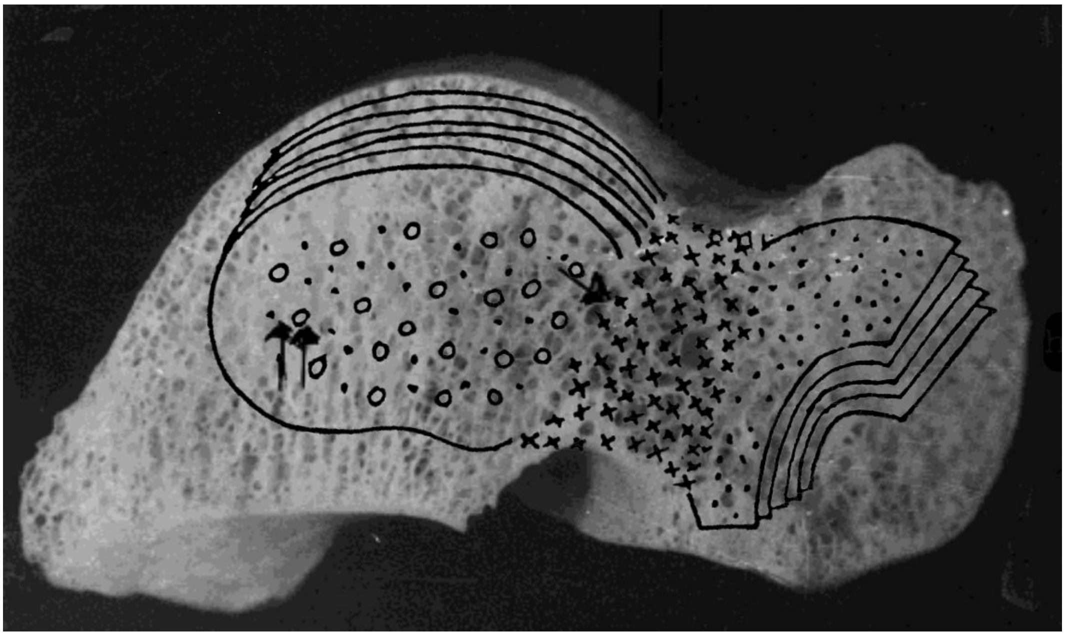

Figure 1.3: Trabecular patterns of trabeculae in the talus: **lines** over the talar body indicate vertical plates; **crosses** in the talar neck indicate irregularly arranged plates and **dots** in the talar head indicate semiarched plates. *Adapted from [Pal and Routal, 1998] with permission from John Wiley and Sons, © 2005 The Anatomical Record: Advances in Integrative Anatomy and Evolutionary Biology.*

The ultra-structure of trabecular bone is honeycomb-like and the network of trabeculae is multi-directional to suit numerous load directions (Fig. 1.3). In the ankle, the flatter plates are suited to the high loads of the body of the talus, whereas irregularly and semi-arched plates dominate the neck and head of the talus to transfer loads to and from the foot [Pal and Routal, 1998, Athavale et al., 2008]. Trabecular organisation is termed *fabric* and the fabric tensor describes both anisotropy and orientation[1]. The popular plugin, BoneJ, for image analysis software, NIH ImageJ, features a measure of the degree of anisotropy, DA, of trabeculae on a scale of 0 (isotropic) to 1 (anisotropic) [Doube et al., 2010]. This measures how aligned trabeculae are within a volume, but does not provide information regarding directionality.

1.2.2.a Bone Density

The mechanical strength of trabecular bone is also highly dependent on bone density. The measure of bone density for research applications is determined

---

[1] A fabric tensor is a symmetric, traceless second order tensor, whose eigenvectors correspond to trabecular orientation and whose eigenvalues correspond to magnitude in the trabecular direction. It is typically derived using the mean intercept length (MIL) [Whitehouse, 1974, Harrigan and Mann, 1984, Cowin, 1985]

by numerous parameters, such as apparent density, ash density and tissue density [Hernandez, 2016]. The apparent density describes the total volume of bone (including pore spaces but not bone marrow) by dividing the wet weight by total sample volume. Typical values of trabecular bone apparent density vary between 0.05 and 1.1 g/cm^3 [Hernandez, 2016]. Both ash density (ash weight divided by the true volume of material) and the true tissue density (wet weight divided by the bone tissue volume) correlate to bone mineralisation [Johanson et al., 1993]. However, these measures of density are at risk of experimental errors. In lieu of these, image-based measures of bone density, such as bone volume fraction (BV/TV, total bone volume divided by total volume including marrow) are increasingly popular. This also allows for the measurement of bone density in a clinical setting. Typical BV/TV values range between 5% and 60% for trabecular bone [Hernandez, 2016]. BV/TV is proportional to apparent density and can be a useful comparator between samples if it is assumed variations in tissue density are small [Hernandez et al., 2001]. However, this measure is dependent on the consistency of image thresholding techniques and image scanner settings.

1.2.2.b Trabecular Morphology

The architectural properties of trabecular bone can be further decomposed into its combination of basic rod-like and plate-like trabeculae (Fig. 1.2) [Rho et al., 1998]. Rod-plate ratios vary with anatomical location [Keaveny et al., 2004] and have been found to influence trabecular mechanical properties, such as elastic modulus and yield strength [Stauber et al., 2006, Wang et al., 2015, Chen et al., 2018]. Historically, this was quantified using the structure model index (SMI) [Hildebrand and Rüegsegger, 1997]. SMI values range from 0 to 4, where a value of 0 indicates majority plate-like trabeculae, 3 for rod-like trabeculae and 4 for solid spheres. However, it has been argued that this does not account for concave surfaces and therefore deemed unsuitable for use on characterising trabecular bone as it does not fully represent the geometry of the tissue [Doube, 2015, Salmon et al., 2015].

Alternative measures by which to evaluate trabecular morphology include the ellipsoid factor (EF), which fits ellipsoids to the geometry and measures the ratios of axis lengths to determine how prolate (rod-like) or oblate (plate-like) the trabeculae are [Doube, 2015]. EF can be calculated using BoneJ [Doube et al., 2010]. Highly prolate ellipsoids have a single long axis (c) and two short axes (a,b), whereas highly oblate ellipsoids have two longer axis (b,c) and one shorter axis (a). The mean EF value lies between -1 (oblate, plate-like; a « b < c) and +1 (prolate, rod-like; a < b « c) and determines the shift of the peak towards either plate- or rod-like trabeculae present in the volume [Doube, 2015]. Flinn peak plots are also generated and depict the volume-weighted axis ratios of the fitted ellipsoids (a/b and b/c).

Similarly, dedicated software that decomposes the trabecular geometry into individual plates and rods can be used to explore rod and plate properties in more detail [Liu et al., 2006, Liu et al., 2008, Liu et al., 2009]. This method employs digital topological analysis (DTA), performed using skeletonisation, topological classification and volumetric reconstructive steps [Liu et al., 2006, Liu et al., 2008, Liu et al., 2010]. 3D Individual trabecular segmentation (ITS) is an example of this. The image first undergoes skeletonisation to transform the volume into a minimised representation of the bone shape, comprising of surfaces (plates) and curves (rods), whilst preserving the trabecular topology (cavities, tunnels etc.) and rod-plate morphology. The classification algorithm then determines the topological features (surface, curve, edge or junction) at each voxel in the skeletonised image [Liu et al., 2008, Liu et al., 2006]. Finally, rod and plates can be individually reconstructed from the skeleton to which their relative biomechanical contribution can be evaluated by measure of ITS-based morphological parameters [Liu et al., 2008].

Liu et al. adopt the American Society of Bone and Mineral Research bone histomorphometric nomenclature to define their ITS-based parameters [Parfitt et al., 1987]:

- plate and rod bone volume fractions (pBV/TV and rBV/TV) is calculated as the total volume of plate or rod bone voxels divided by the bulk volume (which were then used to calculate the plate-rod ratio, pBV/rBV);
- plate and rod tissue fractions (pBV/BV and rBV/BV) is calculated as the total volume of plate or rod bone voxels divided by the total volume of bone voxels;
- trabecular plate and rod numerical density (pTb.N and rTb.N, 1/mm) is calculated as the cubic root of the total number of trabecular plates or rods divided by the bulk volume;
- P-R, R-R, and P-P junction density (Junc.D; 1/mm^3) is calculated based on the arc-skeleton of the original trabecular bone image as the total number of those junctions normalized by the bulk volume; and
- the axial bone volume fraction (aBV/TV) is evaluated as the volume of axially aligned trabecular plates and rods to the longitudinal axis.

A variety of image analysis packages exist to characterise trabecular microarchitecture. This includes software provided by imaging equipment, such as ScanCo's Image Processing Language (IPL). Most studies characterise standard morphological properties, such as bone density (BV/TV), DA, SMI/EF and trabecular thickness (Tb.Th). However, commercial software or in-house developed software, such as ITS-based morphological analytical software, are increasingly popular due to their ability to characterise microstructure in more detail.

Table 1.1 details the indices that can be determined from both standard and ITS-based analyses. A recent 2020 study compared and constrasted the results of numerous packages and noted critical variations in measured anisotropy of trabecular bone [Steiner et al., 2020]. This highlights the need for standardisation of protocols to allow a more meaningful comparison of studies. Further to this, explanations of the underlying algorithms by which these tools evaluate morphological properties would also help understand the limitations of results to other studies.

STANDARD INDICES	
BV/TV	Bone Volume Fraction
DA	Degree of Anisotropy
Tb.Th (mm)	Trabecular Thickness
Conn.D (mm^{-3})	Connectivity Density
EF	Ellipsoid Factor
SMI	Structure Model Index
ITS-BASED INDICES	
pBV/TV (%)	Plate Volume Fraction
rBV/TV (%)	Rod Volume Fraction
pBV/rBV	Plate-Rod Ratio
aBV/TV	Axial Bone Volume Fraction
pBV/BV	Plate Tissue Fraction
rBV/BV	Rod Tissue Fraction
pTb.N (1/mm)	Mean Plate Trabecular Density
rTb.N (1/mm)	Mean Rod Trabecular Density
pTb.Th (mm)	Mean Plate Trabecular Thickness
rTb.Th (mm)	Mean Rod Trabecular Thickness
pTb.S (mm^2)	Mean Trabecular Plate Surface Area
rTb.l (mm)	Mean Trabecular Rod Length
RR Junc.D (1/mm^3)	Rod-Rod Junction Density
PR Junc.D (1/mm^3)	Plate-Rod Junction Density
PP Junc.D (1/mm^3)	Plate-Plate Junction Density

Table 1.1: Histomorphic nomenclature for microstructural characterisation of trabecular bone [Liu et al., 2008, Liu et al., 2009].

1.3 Bone Biomechanics

The apparent biomechanical behaviour of bone, or *bone quality*, is governed by the individual mechanical properties of different length scale components, all of which influence bones' resistance to fracture [Currey, 1984, Fyhrie, 2005, Hernandez and Keaveny, 2006, Torres-del Pliego et al., 2013]. In this way, diseased bone is characterised by its decreased bone quality and its increased state of fracture risk. As bone is hierarchical in structure, one can assume that a biomechanical test performed at a particular hierarchical level (<1mm, 1mm, 1cm etc.) with no differences in bone quality means that there are no net effects originating at lower hierarchical levels. Therefore performing tests at multiple levels can isolate the level from which the most clinically relevant effects to bone quality originate [Hernandez and Keaveny, 2006]. This size effect raises the question of which hierarchical level properties resemble those observed macroscopically and hence an understanding of both materials and structural-level is required to understand whole-bone mechanical properties and interactions between levels [Rho et al., 1998].

Trabecular bone is a heterogeneous material, and its mechanical properties are known to be influenced by variations to anatomical site, age, weight and sex [Keaveny et al., 2001, Morgan et al., 2003, Nowakowski et al., 2013]. It provides shock-absorbing capabilities under load, with high resistance to strain (50% yield), but less resistance to stress compared to cortical bone [Hart et al., 2017]. It has been shown that bone exhibits slight non-linear elasticity even at small strains (0-0.1%) in both uniaxial tension or compression [Morgan et al., 2001]. However, trabecular bone is generally modelled as linearly elastic[2] until yielding during compression (Fig. 1.4). Trabecular bone is a viscoelastic material, such that its stress-strain behaviour is time or rate dependent. This can be defined through its creep, stress relaxation and hysteresis properties.

Bone is highly adaptive to loading conditions and will remodel its trabecular structure to withstand changes in its biomechanical environment. This behaviour is described by Wolff's Law [Wolff, 1986], which states that bone undergoing repetitive, increased loads will initiate adaptive responses (mechanotransduction) enabling the bone to better withstand these loads. This is crucial to the understanding of bone responses to disease. For example, the reorientation of trabeculae in response to altered joint biomechanical environment is known to correlate with cartilage degradation in the talus [Schiff et al., 2007]. Bone is anisotropic, meaning that its mechanical properties are directional, i.e. differ with direction,

---

[2] Linear elastic materials subjected to small deformations can be described by Hooke's Law, $F=kx$, where F is force, k is stiffness and x is displacement.

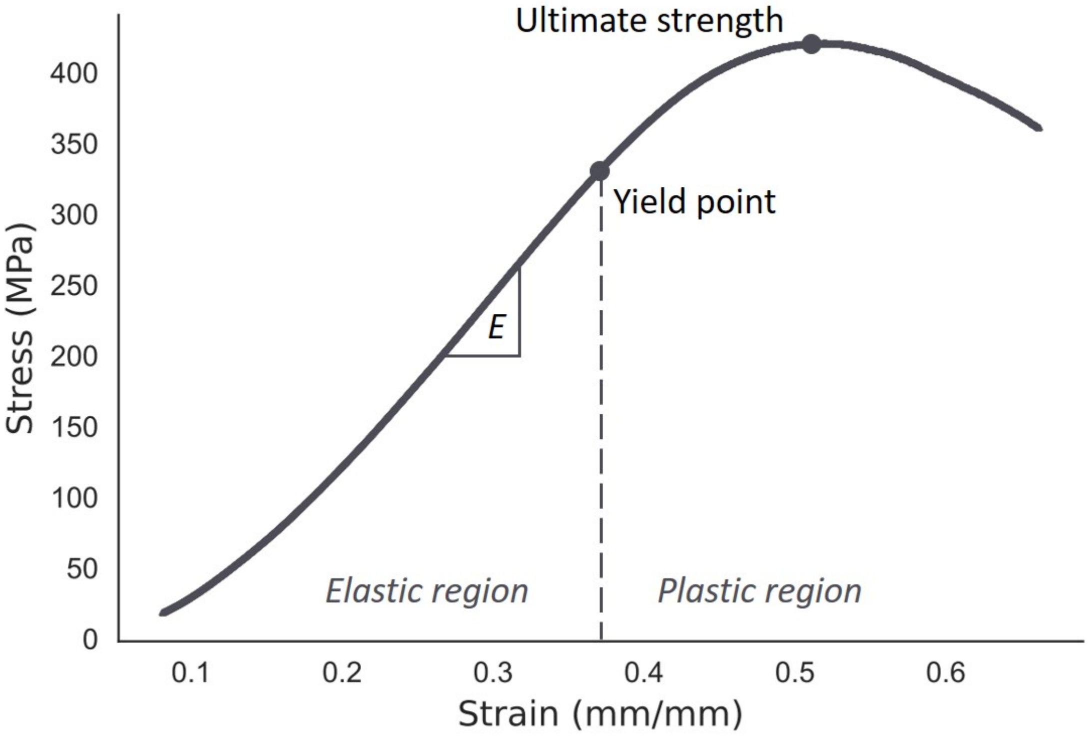

Figure 1.4: Exemplary plot of the behavioural response of trabecular bone under quasi-static uniaxial compression. The slope of the elastic region of the stress-strain curve is used to calculate Young's Modulus, *E*.

and hence requires multidirectional characterisation to fully understand its behaviour. Microarchitectural properties, namely bone density and anisotropy, are known to highly influence trabecular bone stiffness [Ulrich et al., 1999, Ding et al., 2002b, Maquer et al., 2015] and appear to have more influence on variations to mechanical properties than the actual material composition. Maquer et al. analysed bone specimens from multiple anatomical locations and found that variations in bone elastic properties originated mostly from BV/TV (around 87%) and fabric anisotropy (around 10%) [Maquer et al., 2015].

On a microstructural level, the stiffness of bone is determined predominantly by the properties of the organic and inorganic components. Tissue mechanical properties are governed by changes to the bone extracellular matrix, which can provide an insight into the relationship between matrix mechanical function and disease [Lewis and Nyman, 2008]. Tissue-level characterisation can be highly clinically relevant, for example when investigating the impact of medication on bone mineral density and fracture risk [Day et al., 2004a]. Collagen provides the elasticity and ductility to the trabeculae, and hence provides toughness to the bone [Viguet-Carrin et al., 2006]. The interaction of collagen to the mineral phase, and the orientation of the collagen fibrils provide the strength of bone under load, and therefore alterations to bone collagen can also impact on overall bone stiffness. The stiffness of lamellar or osteonal components of trabecular bone can be derived using depth-sensing indentation techniques (e.g. nanoindentation or microhardness testing). The unloading portion of the load-displacement curve can be used to directly measure Young's modulus [Oliver and Pharr, 1992], where the initial loading portion is assumed perfectly elastic (Fig. 1.5).

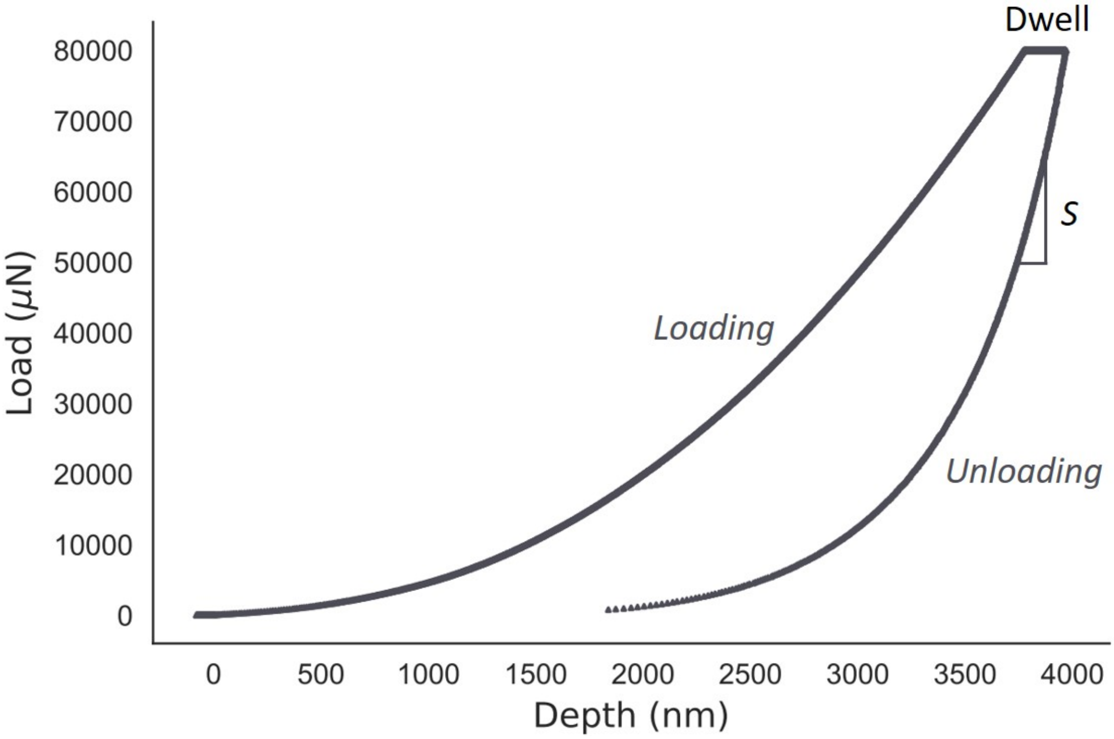

Figure 1.5: Exemplary plot of load vs. depth during nanoindentation of trabecular bone. The slope of the unloading curve, S, is used to calculate the stiffness of contact.

1.3.1 Predicting the Mechanical Behaviour of Trabecular Bone

It is clear that macroscopic mechanical tests do not reflect the mechanical behaviour of components on the microscopic level. Relationships between mechanical properties and morphology provide the link between each hierarchical level of bone and allows for the complete understanding of the influence of components at each level on overall mechanical performance.

Numerous empirical relationships between density (ρ) and mechanical properties (Young's modulus, E) have been derived for trabecular bone based around Equation 1.1, where a, b and c are constants to be determined [Cowin and Yang, 1997, Zysset and Curnier, 1995] (Table 1.2). The relationships have been further expanded to include microstructural properties, as well as yield and strength criterion [Cowin, 1986, Keaveny et al., 2004, Zysset and Rincón, 2006, Wolfram et al., 2012].

$$E = a\rho^b + c \tag{1.1}$$

Similarly, a power law relationship between image grayscale (GS) and bone mineral density (BMD) can be established by normalising CT Hounsfield Units (HU) against known density values, typically measured during phantom calibration [Poelert et al., 2013]. This allows a relationship between mechanical properties and Computed Tomography (CT) GS to be established. However, these relationships are highly specific to the model of imaging equipment used and require the use of regular phantom calibration to allow the relationships to be verified.

Numerous studies report of different anatomical locations report second-order polynomial laws between elasticity and density [Morgan et al., 2003, Helgason et al., 2008]. However, some studies have shown that Equation 1.1 could be further simplified to a linear relationship [Linde et al., 1991] whilst maintaining its accuracy [Wijayathunga et al., 2008, Nazemi et al., 2017, Kopperdahl et al., 2002]. Wijayathunga et al. compared linear, square and cubic material relationships for eight vertebral models and found only slight differences in simulated load-displacement curves providing the constant, a, is optimised [Wijayathunga et al., 2008]. However, all of these investigations are limited by potential experimental artefacts [Keaveny et al., 1997] and the power of the relationship will depend on the range of grayscale values in the images. Moreover, the conclusions drawn for vertebral specimens used in these studies should be verified when being applied to other joints, such as the ankle.

Care must also be taken when considering pooled data from multiple anatomical locations however, as it is well known that such relationships are site-specific [Morgan et al., 2003, Carter and Hayes, 1977]. For example, Morgan et al. (2003) found that in the vertebra the power-law regression between elastic modulus and apparent density was E = $4730\rho^{1.56}$, whereas in the femoral neck it was: E = $6850\rho^{1.49}$ [Morgan et al., 2003].

Table 1.2: Density-elasticity relationships for human trabecular bone in the proximal tibia. *Abbreviations:* N = number of specimens, *rho* = density.

E (MPa) = $A\rho^B$

STUDY	N	A	B	ρ	r^2
[Linde et al., 1992]	31	4778	1.99	ρ_{app}	0.89
[Anderson et al., 1992]	31	3890	2.00	ρ_{dry}	-
[Keyak et al., 1994]	36	33,200	2.20	ρ_{ash}	0.92
[Rho et al., 1995]	144	0.51	1.37	ρ_{app}	0.96
[Morgan et al., 2003]	31	15,520	1.93	ρ_{app}	0.84

Many approaches exist for the derivation of density-elasticity equations for trabecular bone. Classical models simplify the real geometry by modelling some of the major characteristics of bone, such as porosity, and simple mechanical behavioural characteristics, such as deformation. These can be informed by equations developed for similar composite or cellular materials. However, with the rise in computing and advancement of medical imaging techniques, computational models can provide highly detailed simulation of the geometry and material behaviour are increasingly derived using numerical methods, such as the finite element method.

The inclusion of microstructural contributions to variations in mechanical properties of bone is known to improve model predictions in some cases [Maquer et al., 2015, Matsuura et al., 2008]. Morphology-elasticity relationships of human trabecular bone are an accurate means of estimating elastic properties using image data [Zysset, 2003]. Relationships between bone density (BV/TV) and mechanical elastic properties have been well developed, but are known to improve with the inclusion of fabric information [Cowin, 1985, Zysset and Curnier, 1995, Zysset, 2003]. However, standardised measurements of mechanical and morphological properties are needed to allow for a better comparison of results.

1.4 Mechanical Characterisation of Trabecular Bone

Trabecular bone poses more difficulties in its characterisation compared to cortical bone, due to the practicalities of measuring the properties of individual trabeculae. To fully characterise the anisotropic mechanical properties of bone, multiple tests on the same specimen are required. Moreover, the porous nature of trabecular bone makes it difficult to test in tension, and hence, mechanical characterisation typically involves a form of compression testing.

Numerous experimental factors impact bone biomechanics, such as *in vitro* test conditions and the inclusion of bone marrow. The strain rate sensitivity of trabecular bone originates from its viscoelastic properties (Section 1.3). Though only slightly viscoelastic when tested *in vitro*, the characteristic stiffening of bone marrow is observed at high strain rates (10^{-1}+ s^{-1}) [Carter and Hayes, 1977, Linde et al., 1991]. Put into context, *in vivo* tibial maxmimum strain rates during downhill running or sprinting have been found to be in the order of 0.05 s^{-1} [Burr et al., 1996]. Generally, stiffness increases as a function of strain rate [Wright and Hayes, 1976] and so mechanical testing of bone is typically performed under quasi-static conditions, where the viscous response of the tissue is almost negated. Strain rates should aim to resemble those encountered *in vivo*, between 0.01 and 0.08 s^{-1} [Turner et al., 2001]. In turn, hydration and temperature affect bone mechanical properties and physiological conditions should be replicated during testing by immersing specimens in temperature-controlled baths (37°C) filled with (saline) solution [Zhao et al., 2018].

1.4.1 Macromechanical Testing

Multiple methods exist to characterise macromechanical properties of trabecular bone, including ultrasound wave propagation [Zysset, 2003] and digital volume correlation [Liu and Morgan, 2007]. However, often the platen-technique (uniaxial compression testing) is used to characterise apparent biomechanical behaviour of macroscopic pieces of trabecular bone [Keaveny et al., 1997, Rincón-Kohli and Zysset, 2009, Rincón Kohli, 2003]. A frictionless surface on the platens can be assumed, though it is likely a minor source of error that may result in an overestimation of elastic modulus [Keaveny et al., 1993]. To address this, a rigid boundary condition is achieved with the use of endcaps [Keaveny et al., 1997, Linde et al., 1985]. The use of endcaps also allows structural end effects originating from the bending and buckling of trabeculae to be minimised. However, care must be taken to ensure measurements are not off-axis during testing resulting from misalignment of the specimen and the testing direction, as this can result in underestimation of mechanical properties [Öhman et al., 2007].

Specimen size and geometry must also be considered, as they impact on the measured elastic modulus [Linde et al., 1992]. The bone specimens should contain at least five trabeculae to satisfy the continuum assumption, i.e. that continuum properties (stress, strain, density etc.) do not vary significantly over the microstructure [Harrigan et al., 1988]. Structural artefacts have been shown to be minimised with increasing aspect ratio and specimen size. This led to the 2:1 (length:width) optimal specimen geometry to better the precision of the mechanical measures [Linde et al., 1991, Keaveny et al., 1993, Keaveny et al., 1997]. However, key limitations of this form of mechanical testing include the difficulties accounting for the anisotropic nature of bone. Namely, mechanical tests should be performed along the principle direction of the trabecular architecture, which may not be reflected when testing specimens that are highly anisotropic. This error can be accounted for with the consideration of anisotropy in deriving relationships between morphology and mechanical properties [Zysset and Curnier, 1995, Zysset, 2003, Matsuura et al., 2008].

Apparent-level characterisation of trabecular bone in the ankle is under-reported [Jensen et al., 1988], but some comparisons can be drawn from studies characterising bone in the knee [Hvid et al., 1983, Hvid and Jensen, 1984, Linde and Hvid, 1987, Morgan et al., 2003] due to their similarity in joint geometry and similar biomechanics. Though, a direct comparison is not feasible, due to the inherent differences in cartilage composition and bone structure [Treppo et al., 2000]. Review of apparent-level studies were focused on those characterising cylindrical specimens of bone (Table 1.3). Most studies were conducted a significant time ago, meaning only one study mentioned the use of endcaps during testing [Morgan and Keaveny, 2001], as all other studies predate the introduction of these. Across all studies, samples were removed 1 mm below the SBP and tested quasi-statically under hydrated conditions. Few studies included pre-conditioning cycles, which is used to increase reproducibility by reaching a steady viscoelastic state before the ramp to failure begins. The specimens in these studies did also not satisfy the recommended 2:1 ratio geometry. Selected studies were excluded from the review as they averaged data from multiple anatomical locations [Rincón-Kohli and Zysset, 2009], or simply did not give enough details on the specimens and report individual E values [Ciarelli et al., 1991]. The wide tissue donor age range [Hvid et al., 1983, Jensen et al., 1988] and low donor size [Linde and Hvid, 1987, Turner et al., 1999, Jensen et al., 1988] makes cross-comparisons difficult. This is demonstrated by the large range of E values reported in Table 1.3.

STUDY	BONE	SPECIMENS (⌀, H*)	COHORT (F/M) MEAN AGE (RANGE)	PRE-CONDITIONING	STRAIN RATE	OBSERVATIONS
[Hvid et al., 1983]	**PROXIMAL TIBIA**	18 (8, 8)	8 (4,4) 47 (19-65)	-	0.03 mms^{-1}	$\bar{E}_{2\text{-}3mm}$ = 92 MPa & $E_{8\text{-}9mm}$ = 126.89 MPa
[Hvid and Jensen, 1984]	**PROXIMAL TIBIA**	36 (7.5,8.5)	10 (5,5) -(52-93)	-	0.01 mms^{-1}	$\bar{E}_{combined}$= 136.39 MPa
[Linde and Hvid, 1987]	**PROXIMAL TIBIA**	18 (7.5,7)	3 (0/3) -(52-69)	30x 50% PUS, 0.3 Hz	0.01 s^{-1}	$\bar{E}_{11th\ cycle}$ = 335.11 MPa
[Morgan and Keaveny, 2001]	**PROXIMAL TIBIA**	15 (8, 20)	16 (0/16) 69 (40-85)	3x 0.1% ϵ	0.5% ϵs^{-1}	$\bar{E}$ = 1091 ± 634 MPa
[Jensen et al., 1988]	**DISTAL TIBIA & TALUS**	Tib:18 (7.5,6) Tal:12 (7.5,6)	17 (5/12) 68 (46-80)	-	0.08 mms^{-1}	$\bar{E}_{tib}$=827 MPa $\bar{E}_{tal}$=1224 MPa

Table 1.3: Summary of key studies characterising apparent compressive healthy, human subchondral trabecular bone properties of cylindrical bone cores in the knee and ankle. * Specimen length in mm. Abbreviations: ϵ= strain, σ = stress, $\bar{E}$= average Young's modulus, PL = preload, PUS = predicted ultimate strength.

The literature reports that talar subchondral bone is as much as 65% stronger than tibial bone, as expected by its load bearing function in the ankle joint [Hvid et al., 1985, Jensen et al., 1988], with no significant differences in ultimate strength and elastic modulus for either bone [Jensen et al., 1988]. Posteriorly, both bones are weaker compared to anterior regions [Ulrich et al., 2017, Hvid et al., 1983], perhaps due to anteriorly-focused contact pressures [Kimizuka et al., 1980].

The subchondral bone plate provides firm support to a joint and if it is sacrificed during surgical interventions this can result in raised abnormal stresses on the underlying subchondral bone [Calderale et al., 1983]. Aitken et al. showed that removing the SBP can lower average elastic modulus by 30-50% in the distal tibia. Though, this study did not provide any donor information and used relatively large intervals of 10 mm from the SBP to perform indentation tests (4 mm diameter) [Aitken et al., 1985].

In the proximal tibia, two studies evaluated depth-dependent properties at the apparent level (0-9 mm) [Hvid et al., 1983, Hvid et al., 1985]. In one study, the distal average elastic modulus (126.89 MPa) was greater than that measured proximally (92 MPa), but significant differences between the levels (2-3 mm and 8-9 mm) was observed [Hvid et al., 1983]. Statistically significant differences in bone strength were observed between the first (1.5-3.5 mm) and second levels (3.5-5.5 mm) of the proximal tibia [Hvid et al., 1985].

It is debated whether this follows in the ankle [Aitken et al., 1985, Jensen et al., 1988, Hvid et al., 1985]. Using osteopenetration, one 1985 study [Hvid et al., 1985] showed initially larger values of stiffness in the upper levels of the talus followed by a significant drop in stiffness with depth. However, this study did not include bone close to the SBP and specimens were obtained in different directions to the joint load force direction. Jensen et al. (1988) used compression testing to characterise ankle subchondral bone and found no significant differences in bone stiffness with depth [Jensen et al., 1988]. Though, they used donor material from below-knee amputations, which is likely weaker than cadaveric material due to lack of mechanical loading [Jensen et al., 1988].

1.4.2 Indentation Testing

Local elastic modulus and hardness properties can be identified with the characterisation of individual trabeculae and tissue-level components using depth-sensing techniques. Microhardness and nanoindentation can measure hardness and elastic modulus at 5-200 μm and 0.1-10 μm, respectively [Thurner, 2009]. Indentation techniques have been employed for more than twenty years to characterise various microstructural units (individual trabeculae, single osteons and lamellae) of trabecular bone [Lewis and Nyman, 2008, Zysset, 2009]. Microhardness testing (typically using a Vickers four-sided tip) is optimal for interstitial and osteonal sites, whilst nanoindentation (typically using a Berkovich diamond tip) can provide testing of individual lamallae. Nanoindentation has become a popular technique for testing bone tissue on the submicron scale (matrix-level) since Oliver Pharr improved its accuracy to within 5% [Oliver and Pharr, 1992].

As with macromechanical testing, specimen preparation steps are known to affect reported modulus values, including specimen dehydration [Hengsberger et al., 2002, Rho et al., 2002, Hoffler et al., 2005], embedding [Evans et al., 1990] and storage [Mittra et al., 2006]. Similarly, testing conditions are known to affect results, namely when bone is tested under dehydrated vs. wet conditions [Bushby et al., 2004, Hoffler et al., 2005, Dall'Ara et al., 2007, Guidoni et al., 2010, Wolfram et al., 2010]. The drying process has been found to increase trabecular modulus by approximately 24% [Townsend et al., 1975]. Parameters such as loading rate (200-800 μN/s) and indentation depth (200-500 μm) are not thought to significantly influence results, though thicker trabeculae lamellae can reduce the measured modulus [Hengsberger et al., 2002, Donnelly et al., 2006].

Few studies exist that have utilised nanoindentation to characterise tissue properties in the non-diseased knee or ankle (Table 1.4). Most commonly featured were macroscopic indentation techniques those that measure across multiple trabeculae[3]. Of the few relevant studies available, there was high variation to experimental methods, specimen diameter and testing conditions. Most studies did not hydrate the specimens, for example. One study reported combined elastic modulus values, which included early-stage OA and healthy bone from the proximal tibia [Johnston et al., 2011]. Similarly, another study [Hvid et al., 1985] did not report whether the specimen showing severe degeneration with suspected rheumatoid arthritis was included in the dataset. Moreover, most of the literature does not report mean values of stiffness or elastic modulus, which would make comparisons to other studies difficult. One study reported mean puncture force values (N) in the ankle by region, reporting higher puncture strength of bone anteriorly (medial and central) in the talus compared to posterior regions [Ulrich et al., 2017]. This highlights the potential local variation to bone stiffness that should be considered when comparing bone quality. Other studies report an overall lower mechanical properties of subchondral bone with depth, which provides more useful clinically-relevant information that may aid understanding failure mechanisms of joint replacement devices [Hvid et al., 1983, Aitken et al., 1985, Jensen et al., 1988, Harada et al., 1988, Vijayakumar and Quenneville, 2016].

---

[3] This includes osteopenetration which was developed in order to measure bone mechanical properties during total knee arthroplasty [Sneppen et al., 1982].

Overall, it is evident that very few recent studies exist to evaluate the tissue mechanical properties of non-diseased subchondral trabecular bone in the ankle.

STUDY	BONE	N	TEST (CONDITIONS)	COHORT (F/M) MEAN AGE (RANGE)	OBSERVATIONS
[Turner et al., 1999]	**DISTAL FEMUR**	30	Nanondentation (Berkovich, dry)	1 (0/1) 65 (-/-)	$\bar{E} = 18.14 \pm 1.7$ GPa
[Johnston et al., 2011]	**PROXIMAL TIBIA**	16	Indentation (3.5 mm ⌀, wet)	13 (0/10) 73.2 (51-88)	$\bar{E}_{\text{combined}}$ (incl. OA areas) = 452 ± 275 MPa
[Aitken et al., 1985]	**DISTAL TIBIA**	-	Indentation (4 mm ⌀)	15 (-/-) -(—)	E_{max}=427 MPa; E=300-450 MPa
[Jensen et al., 1988]	**DISTAL TIBIA**	-	Osteopenetration (2.5 mm ⌀)	8 (2/6) 45 (17-66)	No significant change in penetration stiffness from distal to proximal levels
[Hvid et al., 1985]	**DISTAL TIBIA & TALUS**	-	Osteopenetration (2.5 mm ⌀)	(Ankles) 10 (-/-) -(—)	Talus 12.7 MPa stronger than tibia
[Ulrich et al., 2017]	**DISTAL TIBIA & TALUS**	-	Indentation	(Ankles) 12 (3/9) 49.1 (36-56)	Max puncture force (talus) = 215 ±91 N (MA, C)

Table 1.4: Summary of key studies characterising indentation properties of healthy, human subchondral trabecular bone in the knee and ankle. N = number of specimens, MA= Medial Anterior, C= Centre.

1.4.3 Indirect Assessment using Numerical Models

The last twenty-five years have seen the development of high resolution computer tomography (CT). This advancement in technology has provided the ability to image volumes of bone in high detail. Numerical methods, such as finite element (FE) analyses can be used with high resolution images of bone to establish mechanical properties *in silico*. The main advantages of FE analyses are in their capability to repeatedly test single bone specimens in multiple scenarios, such as variations in direction and load [Müller and van Lenthe, 2006] without extensive experimental preparation and damage-related boundary artefacts.

FE models have been used extensively when analysing bone biomechanical behaviour. For example, predicting microdamage in trabecular bone [Goff et al., 2015]; trabecular failure modes [Niebur et al., 2000] and the impact of architecture on biomechanical behaviour [Jaasma et al., 2002, Morgan et al., 2004, Parr et al., 2013, Wang et al., 2015]. However, such models require validation from well-defined experimental investigations and appropriate sensitivity testing of input variables and the error it produces on the model outcomes [Mengoni et al., 2016]. This provides some assurance that the model agrees with the experimental test, though it is difficult to fully replicate the *in vitro* environment *in silico* [Chevalier et al., 2007].

The FE method can also be used to predict the apparent level mechanical properties of bone using two different types of model: trabecular-level, micro-FE (μFE) and homogenised or continuum FE models (hFE). Predictions of apparent-level properties can be based on sub-regions of tested specimens [Niebur et al., 2000, Bayraktar et al., 2004], but are prone to errors resulting from intra-specimen variations of morphology and size-dependent errors from mechanical testing [Chevalier et al., 2007, Bayraktar et al., 2004].

Generally trabecular cylinders (5-8 mm ⌀) or cubes (4-5 mm length) are modelled when FE is used to derive mechanical properties. Global thresholding techniques are used to segment the trabeculae from the background of CT image data and how accurately this is achieved has a profound impact on the bone volume fraction and trabecular structure represented by the model. Global thresholding methods in particular are known to thicken trabeculae with high grayscale due to the partial volume effect, whereby the boundary between soft tissue and bone is blurred during the imaging process [Hangartner, 2007]. The partial volume effect therefore causes slight errors in the measured bone density depending on the proportion of values included in the averaging process.

Bone is an anisotropic, heterogeneous material and so simulations should closely mimic the behaviour of these properties within a computational environment.

Orthotropic material properties can be derived computationally [Zysset, 2003, Pahr and Zysset, 2009], but typically lack *in vitro* validation. For analysis of small deformations, bone is widely modelled as linear elastic, though some studies have shown signs of non-linear elasticity at small strains [Harrison et al., 2008, Carretta et al., 2013]. This simplifies the problem and allows for faster computational solutions, but conversely, highlights the importance for investigation of viscoelasticity and damage accumulation.

Modelling bone non-linearity has been found to improve predictions of yield strength compared to linear ones [Bayraktar et al., 2004]. Accounting for non-linear geometric behaviour is required when modelling large strains, due to buckling and bending of trabeculae, but can be computationally costly. Prediction of yielding and damage requires inclusion of post-elastic behaviour, which many studies have explored [Pankaj, 2013, Mengoni et al., 2012, Kosmopoulos and Keller, 2008]. Bone tissue has a complex microstructure and composition, and hence inclusion of viscoelasticity, post-yield behaviour and investigation of damage can improve predictions of failure modes for numerous applications, such as injury or joint replacements.

1.4.3.a Continuum Finite Element Models

Continuum (hFE) models typically represent trabecular bone as an isotropic, inhomogeneous material by approximating complex microstructural features to a macrostructural, continuous relationship [Mengoni et al., 2016, Poelert et al., 2013]. hFE models have element sizes larger than individual trabeculae, so individual trabeculae cannot be resolved [Zapata-Cornelio et al., 2017, Mengoni et al., 2016]. If continuum properties vary between 20-30% over three to five trabeculae, the use of a hFE model may result in some minor errors [Harrigan et al., 1988]. Though a major advantage of using such models includes the computational cost benefits, as an element covers a large area to include marrow and trabeculae resulting in fewer elements being required [Mengoni et al., 2016]. CT-based hFE models require the effective material properties of the tissue as characterised through experimental testing [Zapata-Cornelio et al., 2017]. Previous studies have mainly utilised specimen-specific hFE modelling for whole bone simulation [Pahr and Zysset, 2008, Verhulp et al., 2006, Marangalou et al., 2012, Robson Brown et al., 2014, Day et al., 2020], though it has also been successfully used on smaller portions of bone [Zapata-Cornelio et al., 2017].

1.4.3.b Micro-Finite Element Models

Voxel-based (micro-finite element or μFE) models of bone were first pioneered in 1995 by Rietbergen et al. [van Rietbergen et al., 1995]. This approach utilised high-resolution imaging, namely μCT, to build models of bone with a realistic geometry. This focus on the trabecular structure in the model therefore accounts not only for the amount of bone, but also for the anisotropic properties. Both are key components known to contribute to the majority of variations to mechanical properties at multiple hierarchical levels [Maquer et al., 2015]. Rietbergen then indirectly derived a range of effective tissue moduli in the proximal tibia using average apparent-level test data. Providing the FE analysis is linear elastic, the apparent modulus can be scaled to match experimental apparent modulus, with the resulting scaling factor equal to the effective bone tissue modulus. Such models can be used to circumvent experiments in which boundary conditions are difficult to replicate [Rincón-Kohli and Zysset, 2009]. Hence, μFE models become highly dependent on the trabecular tissue properties [Wolfram et al., 2010], and the use of nanoindentation measures of tissue modulus can significantly improve correlation between experiment and simulation [Chevalier et al., 2007]. Hence, most voxel-based models assume an experimentally-derived isotropic tissue modulus [Ulrich et al., 1998, Morgan et al., 2004], but they can also be used to back-calculate tissue properties by matching experimental apparent properties [Bayraktar et al., 2004, Chevalier et al., 2007, Day et al., 2001]. The latter however is at risk of potential experimental errors (Section 1.4) and errors associated with modelling assumptions.

μFE models have shown good agreement with mechanical tests in compression, tension and torsion [Chevalier et al., 2007, Wolfram et al., 2010]. Limitations of μFE include the considerable computing time and power requirements to solve the models, which is a key consideration in both academic and clinical environments. However, care must be taken when extrapolating apparent-level mechanical behaviour from sub-regions of larger tested specimens [Chevalier et al., 2007], as results may be prone to errors resulting from intra-specimen variations to morphology and mechanical testing errors [Bayraktar et al., 2004]. These models may therefore also assume that the smaller volume of tissue is representative of the whole volume, which may not be the case due to variations in composition and structure. Moreover, the inclusion of density and fabric (anisotropy) information in multiaxial tests performed using μFE models are reported to explain up to 95% of variations in elastic properties [van Rietbergen et al., 1995, Homminga et al., 2003, Zysset, 2003, Maquer et al., 2015]. This is evaluated using multi-linear regression of morphological properties, and the stiffness tensor derived from μFE models and a morphology-elasticity relationship. However, this may be altered with disease.

Voxel meshes consist of eight-node brick elements (hexahedral or hex), where bone tissue is converted to equally sized elements [van Rietbergen, 2001]. These produce sharp edges, misrepresenting boundaries, known as staircase artifact, and may result in a lack of refinement at regions where failure occurs [Engelke et al., 2016]. Conversely, smooth meshes are based on a marching tetrahedron algorithm, where bone voxels are converted into varying sizes of tetrahedral elements. This results in a smoother mesh, more representative of trabecular bone geometry, but with fewer degrees of freedom per element compared to a voxel-based mesh [van Rietbergen, 2001]. Mesh smoothing can reduce peak stresses in a model, but excessive smoothing can result in element distortion [Boyd and Müller, 2006].

μFE models are also sensitive to mesh size, as demonstrated by Van Rietbergen et al. who reported a 20% change in apparent stiffness when mesh size was changed from 20 to 100 μm for their μFE model of tibial trabecular bone [van Rietbergen et al., 1995]. Increasing voxel size, known as downsampling, can save on computational power and time. However, significant changes to voxel size can alter mechanical properties. E_{app} is negatively correlated with increasing voxel size for bone with thin trabeculae [Ulrich et al., 1998]. Ulrich et al. showed there is no significant difference between mass-compensated hexahedral and tetrahedral meshes for linear cases only [Ulrich et al., 1998]. Moreover, they showed that the different types of mesh are impacted by the size of voxel; tetrahedral elements perform better compared to hexahedral elements as the loss of trabecular connections were reduced [Ulrich et al., 1998]. Coarsening a 40 μm voxel size by a factor of two has been found to result in slightly larger values of tissue modulus [Verhulp et al., 2008b] and, in another study, coarsening a 36 μm voxel size by six times resulted in 60-80% lower apparent modulus [Topoliński et al., 2012]. Overall, to conserve trabecular connections in the model a high-resolution image or sufficiently small voxel size (one quarter trabecular thickness) is recommended [Niebur et al., 1999, Guldberg et al., 1998].

A significant source of error in the modelling of bone originates from the assumption of frictionless boundary conditions during a parallel plate compression, though this can be overcome with the use of rigid end-caps [Jacobs et al., 1999, Keaveny et al., 1997]. It should be noted that a frictionless boundary condition during experimental testing is unlikely to be achieved practically. This assumption has been report to result in a 15-30% error, but it can be assumed systematic in magnitude across all groups, so would not impact the overall trend in the data [Day et al., 2001].

1.5 Osteoarthritis of the Ankle

Osteoarthritis (OA) is a disease of the synovial joint most notably causing the symptomatic degradation of articular cartilage [Madry et al., 2012, McGonagle et al., 2010, Felson and Hodgson, 2014]. The most common form of OA in the ankle joint is secondary, caused by injury or trauma (post-traumatic osteoarthritis, PTOA) [Delco et al., 2017]. With improved understanding, OA is increasingly considered a disease of the whole joint, due to its impact on both cartilage and subchondral bone, but also to surrounding muscles, tendons and ligaments [Dieppe, 2011, Egloff et al., 2012].

1.5.1 Epidemiology

Osteoarthritis as a whole affects 15% of the worlds' population, predominantly affecting the elderly [Egloff et al., 2012]. An increase in cases is expected due to rising rates of patient obesity and extended life expectancy [Agha and Agha, 2017, Organisation, 2018]. In 2013, it was reported that 7% of men and women (an estimated 1.77 million people) over the age of 45 years were seeking some form of treatment for foot and ankle OA in the UK [Arthritis Research UK, 2013]. Globally, ankle OA is thought to affect over 1% of the adult population [Glazebrook et al., 2008] and around 70% of cases are thought to be post-traumatic [Saltzman et al., 2005]. Hence, an increasingly younger population are seeking treatment for ankle OA compared to other joints, due to its association with sport-related injuries [Nakamura et al., 2016, Valderrabano et al., 2009, Saltzman et al., 2005, Maffulli et al., 2011, Anderson et al., 2011, Arthritis Research UK, 2013]. This challenges the preconception that OA is just a disease for the elderly. Consequently, there are significant socio-economic implications associated with diagnosis of OA, as patients are left in pain and become increasingly inactive [Glyn-Jones et al., 2015, Furman et al., 2006].

1.5.2 Etiology

The mechanisms by which OA develops are widely disputed [Madry et al., 2012], but are likely multifactorial. Cartilage, ligament, meniscal, subchondral bone and synovial-derived secondary OA mechanisms have been explored [McGonagle et al., 2010] and show a significant pathomechanical component to disease progression. PTOA involves an initial sprain or (micro-)trauma to the joint, causing a fracture to evolve [Delco et al., 2017]. The majority of ankle PTOA is believed to involve the medial tibial plafond impacting the medial talar dome [Kimizuka et al., 1980] (Fig 1.6). The resulting increase in abnormal stresses in that area of the joint ultimately results in the formation of osteochondral lesions (OCL) on the medial side of the talar dome (OLT) [Raikin et al., 2007, McGonagle et al., 2010, Castañeda et al., 2012, Furman et al., 2006]. The large majority (around 95%) of severe ankle sprains are thought to result in OCL formation; over half of OCLs will develop into OA years after the initial trauma [Delco et al., 2017].

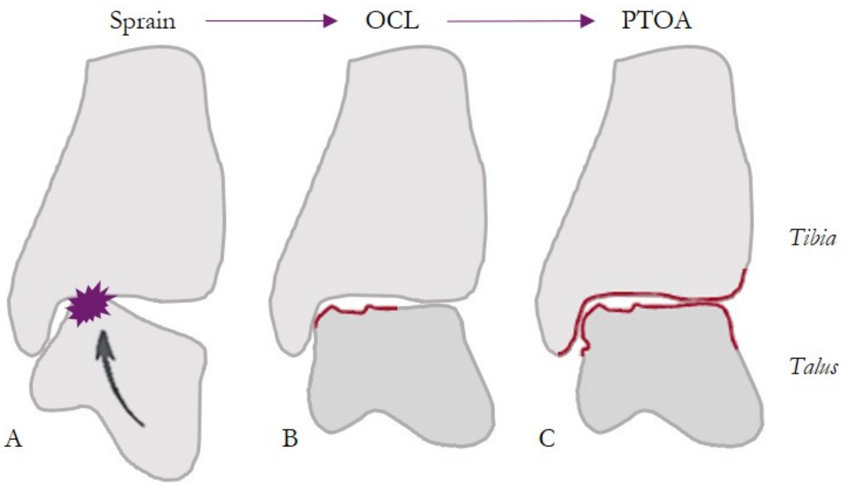

Figure 1.6: Mechanism of PTOA originating from initial ankle sprain (A) causing the formation of an osteochondral lesion on the talus (B) that results in degradation of cartilage and bone at points of contact leading to further degradation and eventually, osteoarthritis (C). *Adapted from [Delco et al., 2017].*

Patients often suffer from muscle weakness with OA, with over 35% loss of muscle strength in dorsiflexion and plantar flexion [Valderrabano et al., 2006, Palmieri-Smith et al., 2010]. Gait studies have shown that with arthritis patients have a slower walking speed, reduced motion and increased cadence [Leardini et al., 2014, Stauffer et al., 1977]. Presentation of OA in the ankle is different to that observed in the knee. Studies by Meachim et al. found full-thickness defects in 44% of knee joints compared to only 2% of ankles (21-92 years of age) [Meachim and Emery, 1974, Meachim, 1975]. In the fifty cadavers Muehleman et al. studied, knee joints were more often affected by full-thickness defects than the ankle joint, but found that in both joints (36 to 94 years), the medial side was predominantly affected [Muehleman et al., 1995, Muehleman et al., 1997]. One study of the ankle showed severe cartilage degeneration in 7 out of 30 cadavers (30 to 93 years of age), with evidence of degeneration in 98% of the 82 joints from both sexes (25 men and 16 women) [Tsukahara, 1990]. Clinically however, symptomatic OA with radiographic changes are thought to occur over nine times more in the knee compared to ankle [Wilson et al., 1990, Cushnaghan and Dieppe, 1991].

1.5.3 Diagnosis

With the presentation of symptomatic OA, diagnosis is achieved using plain x-ray radiographs, with the caveat that this often means that the OA is likely advanced enough to be irreversible [Glyn-Jones et al., 2015], as subchondral bone pathology precedes radiographically-observable changes. Radiographic mid-late stage OA presents itself as a narrowing of the joint space, observable osteophyte formation and subchondral cysts and sclerosis (Fig. 1.7). If necessary, Magnetic Resonance (MR) Imaging can be used to further investigate the impact on cartilage and surrounding soft-tissue. Whilst a Computed Tomography (CT) scan provides more information on the bone quality, it is less likely to be used due to increased radiation risks to the patient. CT can be performed at clinical resolution (high-resolution peripheral quantitative CT, HR-pQCT) to minimise radiation dosage, but the trabecular detail of the bone becomes difficult to resolve.

Numerous systems exist for grading OA joints, including the Kellgren and Lawrence scale [Kellgren and Lawrence, 1957] for radiographic evaluation based on bony spur (osteophyte) formation, and popular standardised histological gradings systems, such as the International Cartilage Repair Society (ICRS) and Osteoarthritis Research Society International (OARSI) histopathology assessment systems [Pritzker et al., 2006] (Table 1.5). These systems have been compared and critiqued extensively [Waldstein et al., 2016]. The grading of OA is susceptible to human error, though minimised through the use of double-blind scoring, and may lead to discrepancies amongst studies [Hintermann and Ruiz, 2014].

1.5.4 Osteoarthritis: A Disease of Cartilage or Bone?

The degeneration of subchondral bone during OA is often overlooked, due to the more observable changes to cartilage [Matsui et al., 1997, Dequeker et al., 1997]. Yet, a synergistic relationship exists between cartilage and subchondral bone. Radin and Rose [Radin et al., 1972, Radin and Rose, 1986] first proposed the involvement of subchondral bone in the development and progression of OA. They suggested a cascade of events in the early stages of the disease involving trabecular microfracture [Burr, 2004, Burr and Radin, 2003], resulting from high loads, which initiates bone remodelling and consequential stiffening of the bone plate. This leads to increased shear stresses in the cartilage. They observed higher trabecular stiffness [Pugh et al., 1974] and lower energy absorption [Radin et al., 1970] in the age-matched knee specimens they analysed, and found lower bone viscoelastic properties that could no longer provide shock-absorbing capabilities to the joint. Conversely, some believe bone stiffness changes could result from normal bone remodelling resulting in bone volume and mineral density

Table 1.5: Kellgren and Lawrence (K&L), International Cartilage Repair Society (ICRS) and Osteoarthritis Research Society International (OARSI) OA grading systems.

GRADE	K&L	ICRS	OARSI
0	No radiographic features of OA are present	Normal	Surface & cartilage intact
1	Small number of osteophytes	Superficial lesions; soft indentation and/or superficial fissures & cracks	Uneven but instact surface, possible features: superficial fibrillation, cell death and proliferation
2	Definite osteophyte presence, joint space unimpaired	Lesions extending down to <50% of cartilage depth	Surface discontinuity
3	Narrowing of joint space	Cartilage defects extending down > 50% of cartilage depth; down to calcified layer and to, but not through, bone	Vertical fissures
4	Joint space greatly impaired, subchondral bone sclerosis	Complete loss of cartilage thickness	Erosion
5	-	-	Denudation

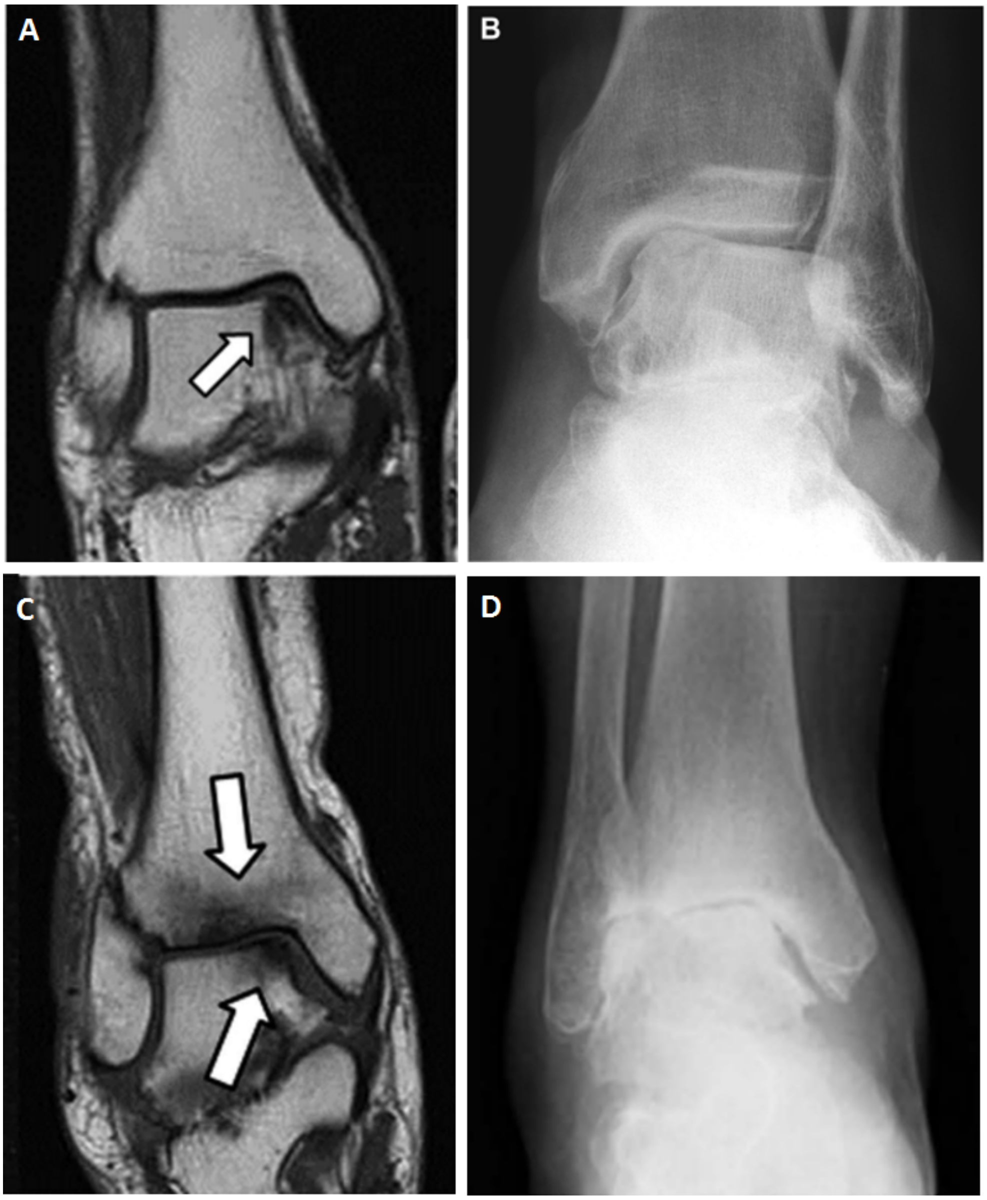

Figure 1.7: Mortise view MR and plain radiograph images KL Grade I: A) bony alterations observed in talus T1W MR [Nakamura et al., 2016], B) lateral talar ostephyte formation in plain radiograph [Kraus et al., 2015] and Grade IV: C) T1W MR showing bone signal changes in distal tibia and talus [Nakamura et al., 2016], D) narrowing of joint space shown in plain radiograph [Nakamura et al., 2016] *Images from [Nakamura et al., 2016] obtained under CC-BY license. Images from [Kraus et al., 2015] obtained with permission © 2015 Osteoarthritis Research Society International.*

changes [Martel-Pelletier, 1999], or endochondral ossification, in which new bone is formed by replacing the cartilage [Oegema et al., 1997, Burr, 2004, Goldring, 2009, Cox et al., 2013].

The subchondral bone plate (SBP) at the epiphysis is thinner than that present on the main portion of a long bone, and hence there is a higher influence of the underlying subchondral trabecular bone at the joint [McGonagle et al., 2010]. The close integration of bone to the cartilage may imply a direct and complex influence on OA progression [Radin et al., 1972]. For example, the direction of trabeculae can impact the mechanical loading and consequential mechanical effects on the whole joint, including the cartilage [Kamibayashi et al., 1995b]. Moreover, subchondral trabecular bone being vascular, impacts the regenerative properties of cartilage. A degenerated, thinner cartilage is subjected to more shear stress and consequently this may cause further degradation [Madry et al., 2012]. As OA progresses the effects on the subchondral bone become significant that this becomes a source of pain for the patient, as subchondral bone is innervated.

McKinley et al. used digital image correlation to show that large changes in strain are observed with small cartilage defects in the tibial plafond [McKinley and Bay, 2001]. These small defects accentuate load through the trabecular bone. Once cartilage degrades down to the bone, bone becomes more sclerotic and a higher population of osteophytes (bony spurs) are observed. In the ankle, it is thought that osteophytes are more prevelant in the distal tibia than the talus [Kuettner and Cole, 2005]. Radiographically, flattening of the bone (attrition), bone marrow lesions and a narrowing of the joint space are observed (Fig.1.7) [Wiewiorski et al., 2016, Glyn-Jones et al., 2015, Li et al., 2013, Johnston et al., 2016, Castañeda et al., 2012, Sharma et al., 2013, Neogi, 2012]. It is therefore important to remove test specimens from the upper layers of subchondral bone, immediately underlying the SBP, as bone closest to the joint surface (<5 mm) is the most relevant to OA [Harada et al., 1988] and therefore has the greatest potential to affect overlying cartilage negatively [Brown et al., 1984].

1.5.4.a Influence of OA on Bone Microarchitecture

It is well known that with OA there is significantly greater trabecular thickness (Tb.Th) and bone volume fraction (BV/TV) in knee subchondral bone due to increased remodelling [Kamibayashi et al., 1995b, Bobinac et al., 2003, Finnilä et al., 2017, Chen et al., 2018, Gatenholm et al., 2019]. The trabeculae are thought to reorientate more normal to the articular surface in the presence of OA, particularly in the upper levels of bone [Kamibayashi et al., 1995a]. On the contrary, Patel et al. found that, in the first 6 mm of subchondral bone in the medial proximal tibia, BV/TV and Tb.Th are lower with late-stage OA [Patel et al., 2003]. SMI was larger, indicating more rod-like trabeculae in OA specimens, though the study was underpowered with only three severely OA specimens out of a total eleven cadaveric knees. However, SMI is now considered an absolete measure of trabecular morphology (see Section 1.2.2). Studies in the knee joint have shown more plate-like trabeculae present with early [Ding et al., 2003] and late-stage OA [Finnilä et al., 2017], but also utilise SMI.

More recent studies have utilised individual-trabecular segmentation (ITS) methods to evaluate changes to rod-plate combinations more accurately. For 8 mm cuboidal volumes of trabecular bone in the knee joint, Chen et al. found an overall loss of rod-like trabeculae and plate thickening in advanced OA specimens underneath both intact and damaged articular cartilage (Fig. 1.8) [Chen et al., 2018]. In the hip joint, studies have showed larger numbers of both rod- and plate-like trabeculae with OA using ITS [Chu et al., 2020, He et al., 2020]. This demonstrates how plate and rod combinations are sensitive to joint geometry and in turn, the biomechanical environment, that alters with OA.

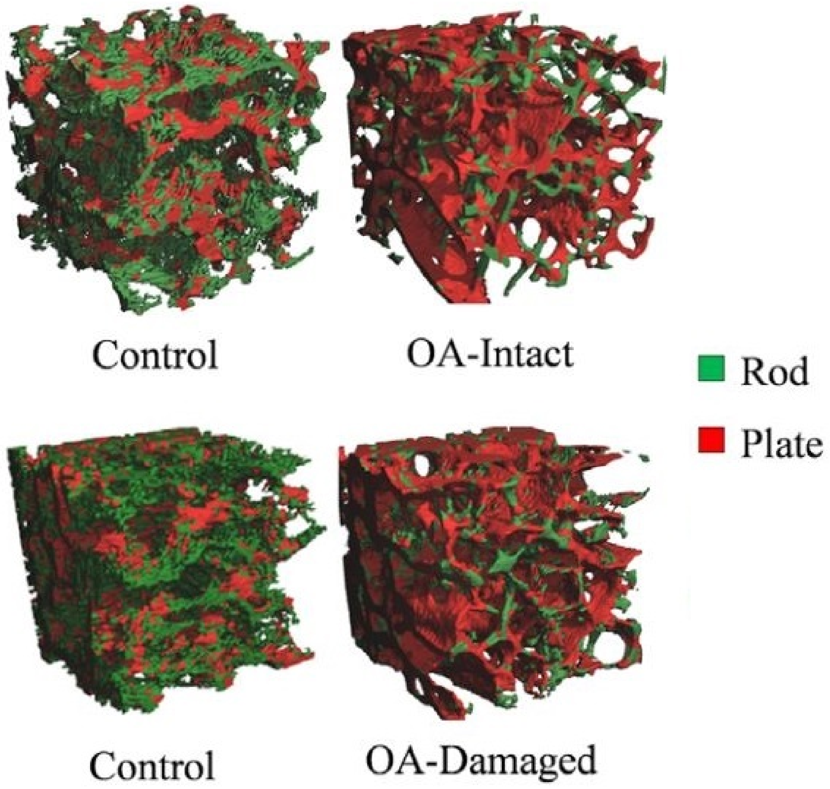

Figure 1.8: Exemplary 8 mm cuboidal volumes of knee subchondral trabecular bone beneath both intact and damaged cartilage, segmented into trabecular plates (red) and rods green) using ITS. *Image adapted from [Chen et al., 2018] with permission from John Wiley and Sons, © 2017 American Society for Bone and Mineral Research.*

Few studies have characterised microarchitecture changes to subchondral bone in the ankle. Nakasa et al. reported larger subchondral bone plate (SBP) thickness in the talar dome (1.04 ± 0.13 mm) - particularly in the medial and posterior regions - with associated subchondral bone sclerosis compared to non-OA ankle bone (0.79 ± 0.03 mm) for the few samples they had studied (N=11) [Nakasa et al., 2014]. This was compared to their observed thinning of the SBP with a lower BV/TV in their early-stage OA samples. Muehlemann et al. studied thirty-nine bilateral pairs of human tali to find that bone density does not positively correlate with cartilage degeneration, but lowers instead [Muehleman et al., 2002]. This may be due to the use of larger regions of interest i.e. total cross-sections of the tali that may not pick up on more local, subchondral density changes. More recently a study evaluating Hounsfield Unit (HU)-based density between OA and non-diseased ankle bones showed no significant differences in talar bone density in 1 mm intervals from the SBP [Harnroongroj et al., 2019]. However, there was significant changes to bone density between 6-10 mm above the tibial plafond. In both groups, bone density reduced away from the articular surface of both the talus and distal tibia.

1.5.4.b Influence of OA on Bone Biomechanics

The effects of OA on the subchondral bone in the foot and ankle is poorly studied compared to other joints [Barr et al., 2015]. However, some comparisons can be made to other lower limb joints - namely the knee joint. Extrapolating findings from the ankle to the knee is cautioned, but such limited ankle research permits some comparisons to be made [Treppo et al., 2000, Delco et al., 2017]. Due to similar joint geometry, bone quality changes with osteoarthritis in the ankle may be akin to those observed in the knee [Bobinac et al., 2003, Chappard et al., 2006, Buckland-Wright et al., 2000]. However, the ankle joint is exposed to higher loads per mm^2 compared to the hip and knee, and histologically, ankle cartilage has a higher proteoglycan density, higher compressive stiffness and lower matrix degradation compared to other joints [Kuettner and Cole, 2005]. These properties cause higher stiffness and reduced permeability of the ankle cartilage compared to the knee. Lastly, ankle OA is more likely to be post-traumatic in nature, compared to the knee, meaning comparisons may be limited by the mechanisms by which OA develops.

1.5.4.c Apparent-Level

Table 1.7 summarises literature characterising changes to lower limb subchondral bone with osteoarthritis. Overall, there was a high variation in patient demographics, sample sizes and degenerative state (OA grade), but similar techniques (uniaxial compression testing or a form of indentation) were used to mechanically characterise bone quality changes.

Two studies did not have control groups, but instead compared to values reported in the literature [Wixson et al., 1989] or to early-stage specimens [Zysset et al., 1994]. Some studies showed reduced apparent mechanical properties with OA in the knee [Zysset et al., 1994, Ding et al., 2001]. Ding et al. had high variation of E in their control specimens that were compared to early-stage OA specimens, though the specimens were age and sex-matched. Zysset et al. studied early- to mid-stage OA specimens obtained from only six cadaveric knees [Zysset et al., 1994]. They studied 3 mm cuboidal specimens at the subchondral bone level and 6 mm specimens at a further three levels. The results indicated reduced mechanical stiffness of subchondral bone with the progression of OA. Whilst a large number of specimens were retrieved at multiple depths, there are limitations to the mechanical testing due to the geometry and small size of the subchondral bone specimens. The sharp edges of the cuboidal specimen can become stress-raisers and affect the biomechanical behaviour during compression. Wixson et al. tested a large number of cylindrical OA specimens obtained from knee arthroplasty patients (N=46 patients) and found a reduced elastic modulus compared to similar studies of ND knee bone specimens in the literature [Wixson et al., 1989]. However, the cores of bone were subjected to platen compression without the use of endcaps so may be subjected to end artifacts, and the results showed 68% variations to stiffness values.

Lereim et al. reported reduced hardness of OA specimens in the knee compared to controls [Lereim et al., 1974]. However, their OA donor group was much older compared to the age of the controls and the severity of OA was unclear. Similarly, Finlay et al. found a reduced stiffness from their indentation results in late-stage OA knee specimens, but suffered from approximately 68% variation in stiffness in each test region [Finlay et al., 1989]. Their study did also demonstrate regional variations (medial vs. lateral) to stiffness in the healthy tibias, albeit non-significant. Lastly, an indentation study by Johnston et al. lacked values of stiffness from purely OA or ND compartments, but instead focusing on localised regions to compare. However, they showed that the density measures in the first 2.5 mm of subchondral bone predicted the greatest variation to bone stiffness [Johnston et al., 2011].

		Cohort (F/M) Mean Age(Range)				
Study	**Bone(s)**	**ND**	**OA**	**Grading**	**Test** *Sample size, (∅, h)*	**Observations**
[Wixson et al., 1989]	**Proximal Tibia & Distal Femoral Condyles**	N/A	46 (29/17) 66.8(-,-)	Late Stage	Uniaxial Compression *107 (5,4.6-7.0)*	$\overline{E}_{\text{OA,late}} = 154 \pm 105$ MPa, $\sigma_{\text{max, OA, late}} = 5.9 \pm 3.6$ MPa
[Zysset et al., 1994]	**Proximal Tibia**	N/A	4 (3/1) 74 (61-91)	Ahlbäck I-III	Uniaxial Compression *78, (-,3)*	$k \downarrow$ 65% in OA_{III}; 16% in OA_{I}; E_{all} = 32-1116 MPa
[Ding et al., 2001]	**Proximal Tibia**	10 (0/7) 72(58-85)	10 (0/7) 73(63-81)	Mankin 0.5-4.9	Uniaxial Compression *120 (7.5,7.5)*	$\overline{E}_{\text{lateral control}}$, $\overline{E}_{\text{normal medial}}$ & $\overline{E}_{\text{OA,early}}$ = 293, 475 & 275 MPa
[Lereim et al., 1974]	**Proximal Tibia**	23 (0/0) -(20-90)	16 (0/0) -(62-91)	Unknown	Brinell hardness (5mm ∅) *OA: 21 (10,5), ND: 36 (10,5)*	$\overline{H}_{\text{ND}}$ & $\overline{H}_{\text{OA}} = 7.6 \pm 2.3$ & $3.9 \pm 2.5\ \text{kp/mm}^2$

[Finlay et al., 1989]	**Tibial Plateau**	15 (6/9) 45.5 (-,-)	28 (18/10) 67(-,-)	Late Stage	Indentation (4 mm ⌀) *-, (-,-)*	$\bar{k}_{\text{OA,late}}$ = 1083.17 N/mm, $\bar{k}_{\text{ND,young}}$ & $\bar{k}_{\text{ND,old}}$ = 1427.83 & 1084.33 N/mm
[Johnston et al., 2011]	**Proximal Tibia**	13 (0/10) 73.2(51-88)		ICRS 0-3	Indentation (3.5 mm ⌀) *OA: 23, ND:27*	$\bar{E}_{\text{pooled,early}}$ = 452 ± 275 MPa
[Day et al., 2001]	**Proximal Tibia**	10 (3/7) 73(58-85)	10 (3/7) 73(63-81)	Mankin 0.0 - 7.0	Uniaxial Compression *- (7.5,7.5)*	$\bar{E}_{\text{tiss, OA}}$ = 2- 9 GPa & $\bar{E}_{\text{tiss, ND}}$ = 3-20 GPa (↓ with OA)
[Zuo et al., 2016]	**Tibial Plateau**	20 (-/-) 57.1 ± 6.3		I-IV (Mankin <3 - >12)	Nanoindentation *10 (5,-)*	$\bar{E}_{\text{OA,early}}$ =13.90±2.75 GPa, $\bar{E}_{\text{OA,late}}$ =17.33±3.13 GPa
[Peters et al., 2018]	**Distal Femur & Proximal Tibia**	12 (4/8) 62.2(31-88)		ICRS 0-4	Nanoindentation *80 (-,-)*	$\bar{E}_{\text{OA,pooled}}$ = 11.12-15.33 GPa

Table 1.7: Multiscale mechanical characterisation of lower limb osteoarthritic subchondral trabecular bone. h = specimen height (mm), ND = non-diseased, H = hardness.)

1.5.4.d Tissue & Matrix-Level

Matrix hardness as measured through nanoindentation can be a good characteristic to evaluate bone quality changes and has been found to correlate with mineralisation, elasticity and fracture toughness [Dall'Ara et al., 2011]. Though there are conflicting opinions on the changes to osteoporotic bone at the tissue and matrix levels [Osterhoff et al., 2016], studies report little change to tissue hardness with osteoporosis (a disease resulting in skeletal deterioration and fragility) when measured using indentation [Zysset, 2009, Weaver, 1966], whereas the impact of osteoarthritis is thought to lower mechanical properties at this level [Lereim et al., 1974, Mansell and Bailey, 1998, Day et al., 2001, Day et al., 2004b].

Day et al. back-calculated tissue mechanical properties from apparent mechanical tests to find a reduced tissue modulus in medial pre-arthritic areas of bone compared to controls in the knee [Day et al., 2001]. Though they state the obvious limitations in these observations when replicating boundary conditions *in silico*, they assume this is of a similar magnitude in all groups. More recent nanoindentation studies report changes to tissue mechanical properties with the progression of OA in the knee joint [Zuo et al., 2016, Peters et al., 2018] (Table 1.7). Zuo et al. did not report the donor information and did not use non-diseased controls, but compared early to late-stage bone in both osteonal and lamellar sites. They found higher elastic properties and hardness in the late-stage OA specimens, which shows improved stiffness, but also brittleness of the bone with disease [Zuo et al., 2016]. Peters et al. reported higher tissue elastic modulus with both age and OA, but the OA samples were less severely osteoarthritic (no grade IV specimens) [Peters et al., 2018]. However, neither study reported the depth at which the indentations were made or whether specimen hydration was maintained during testing.

What remains unclear is the age of bone being tested - whether it is newly remodelled or not - and the impact of naturally occurring age-related changes- both of which can impact the trends observed in the results [Yamada et al., 2002, Burr and Gallant, 2012]. Mechanical changes at this scale are likely due to the changes in mineralisation [Grynpas et al., 1991] and also as a result of scale effects originating at lower length scales, namely the collagen matrix [Day et al., 2004b, Burr and Gallant, 2012]. Increased deposition of hypomineralised bone would result in a lower material density, which may lower the apparent stiffness of the bone, as demonstrated in multiple studies on hip OA [Li and Aspden, 1997b, Li and Aspden, 1997a, Day et al., 2001, Bailey et al., 2004, Day et al., 2004b]. Mathematical models by Cox et al. using mineralisation data showed local changes to subchondral bone mineralisation and BV/TV underneath severely degenerated cartilage, whilst depth-dependent increases to BV/TV were thought to be a mechanoregulated response to counteract increased bone strain resulting from lower mineralisation [Cox et al., 2012]. However, Zuo et al. reported the presence of highly crystallised calcium-phosphate phases in late-stage bone specimen, which indicated more stable crystals and reduced bone turnover, which resulted in stiffer bone [Zuo et al., 2016].

1.5.5 Treatment

Non-surgical interventions such as: weight loss, footwear interventions (gait modifications) and muscle strengthening, are used to inhibit OA progression by adjusting the pressures on the joint. In the later stages, these methods become ineffective and surgical interventions are explored [Egloff et al., 2012]. An osteotomy may be used as an early-mid stage treatment to correct malalignment through the removal of small portions of bone. This hinders the progression of OA by changing the wear patterns in the joint and introduce a more even spread of load across the articulating surfaces.

Late-stage surgical interventions include arthrodesis (joint fusion) and arthroplasty (total ankle replacement, TARs). Arthrodesis is currently the gold-standard treatment and involves the placement of surgical screws to align and fix the distal tibia and talus into a neutral position. This does inhibit the motion of the joint, but the severity of this hindrance is deemed less than fusion of other joints [Bhatia, 2014].

Ankle arthroplasty involves the implantation of a TAR device between the distal tibia and talus. Such devices increase the mobility of the joint and allow efficient, patient-specific solutions with minimally invasive surgery [Egloff et al., 2012, Bhatia, 2014]. However, many TAR devices have survival rates much lower than hip and knee replacements [Jackson and Singh, 2003, Egloff et al., 2012]. The significant removal of bone is could be a major factor in the higher failure rate of TARs, causing difficulties in achieving stable device fixation, resulting in stress-shielding, loosening, subsidence and increased fracture risk [Glazebrook et al., 2009, Hintermann et al., 2012, Currier et al., 2019]. The resection of tibial and talar bone in done to level the surfaces for implantation of the device [Egloff et al., 2012, Aitken et al., 1985]. These upper levels of bone removed are thought to be the strongest regions of both bones [Hvid et al., 1985]. The removal of the bone plate also weakens the bone and increases stress on the underlying subchondral bone. The volume of resected bone can reach highs of approximately 30% in the tibia and 22% in the talus [Goetz et al., 2016]. Though these values are dependent on the type of device implemented. One study found that by removing portions of the SBP, abnormal stresses appear on the underlying talar subchondral bone

[Calderale et al., 1983]. Their investigation of the effects of the resection of bone during ankle arthroplasty highlights the mechanical impacts of the surgery. The once uniformly distributed stresses in the joint become less uniform and an outwardly increasing stress and strain results in higher overall stresses in the bone.

Though the removal of bone is minimised wherever possible, it is inevitable that some bone will be sacrificed which will weaken the joint and make revision surgery more difficult due to lack of good quality bone stock. For many patients, bone regeneration will also be limited due to their age or as the result of previous surgical inventions. Hence during surgery, bone grafting may be inserted into the joint to help facilitate bone union, though the ideal TAR patient needs good bone stock [Hintermann and Ruiz, 2014]. Overall however, improvements to the understanding of joint biomechanics and implant design have seen more devices being implanted each year in the UK (Fig. 1.9). Devices such as the INBONE system for example, have a modular tibial stem component that can be lengthened to improve stability, improved alignment, and modular talar components with fixation pegs for when insufficient bone stock is present and thus mitigating subsidence [DeOrio, 2020].

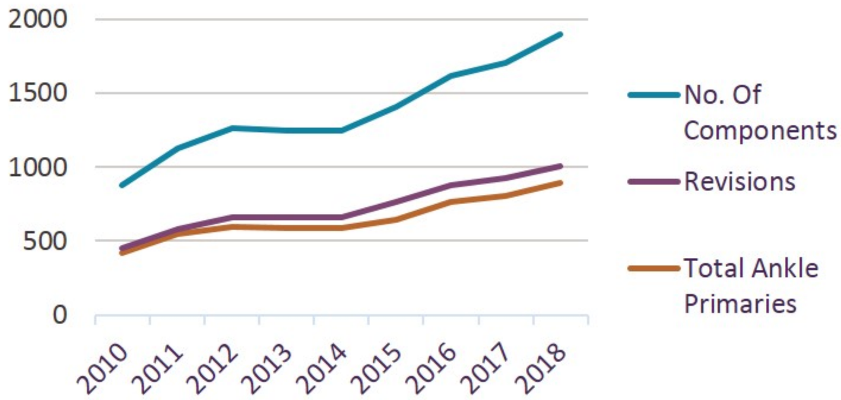

Figure 1.9: Total ankle arthroplasty clinical data from the National Joint Registry (UK) showing increased number of surgeries from 2010 to 2018.

Resurfacing devices are slowly being introduced as an alternative early-stage intervention. These specifically target localised arthritic zones of the talar dome and restore the surface whilst preserving tissue. Initial studies have shown promise in re-articulating larger arthritic talar dome defects in the ankle [Holton et al., 2013] without excessive pressure on the opposing articular cartilage [van Bergen et al., 2010]. However, identifying early-osteoarthritic areas of bone in the joint is difficult when clear clinical presentations of the disease are not observed. The mapping of bone quality in a joint would allow for the study of OA progression, identifying target treatment areas and aiding surgical planning by accurately identifying areas of OA bone before clinical presentation. Numerous regenerative therapies also exist to prevent the progression of early-OA, including arthrodiastasis or joint distraction, which can be used in patients with normal joint alignment to activate self-regeneration in the osteochondral tissue [El-Jawhari et al., 2018]. Targeting the mesenchymal stem cell population within bone is an increasingly popular means by which to delay OA progression and promote joint regeneration [Ilas et al., 2017].

1.5.6 Conclusions

Total ankle arthroplasty is an option for patients to regain ankle mobility that was otherwise lost due to osteoarthritis. However, loss of bone stock and low bone quality in the joint remains an issue for the success of these devices, potentially resulting in device failure and need for revision.

Little has been reported about the mechanical and morphological changes that occur in subchondral bone with osteoarthritis in the ankle joint. However, this knowledge could be invaluable to inform the design of better replacement devices, or enable patient-specific mapping of bone properties based solely on medical images to plan treatments or predict fracture risk.

CHAPTER 2

SUMMARY & RESEARCH OBJECTIVES

2.1 Summary

Literature on the characterisation of osteoarthritic ankle bone on different length scales is scarce, leaving a large gap for new investigations. The clinical motivations are clear: healthy subchondral bone is vital to the mechanical strength of the ankle joint, playing a huge part in the biomechanics of the ankle complex, and therefore destructive interventions should be avoided if possible. Bone quality mapping could provide clinicians with a useful pre-operative aid when planning early-stage interventions that target arthritic bone directly, and also to manage the biomechanical stability of the joint after multiple interventions. Osteoarthritic changes to trabecular morphology in the ankle should be investigated and a comparisons made to other studies. Microstructural effects of OA on ankle bone have rarely been reported, but changes to this level may impact the mechanical properties of the whole bone. Therefore, it is suggested that lower scale effects on bone quality are investigated to best decide the appropriate scale at which to characterise and model arthritic bone changes in the ankle. This includes the development of specimen-specific, imaged-based finite element (FE) models, which provides the capability to predict and map stiffness using CT images alone. This also allows further *in silico* characterisation of smaller volumes of osteoarthritic bone to indirectly evaluate the changes in apparent mechanical behaviour without the need for characterisation. Similarly, the direct characterisation of tissue mechanical properties can be achieved using nanoindentation and compared to those values estimated *in silico*.

2.2 Research Aims & Objectives

The investigation of multiscale biomechanical changes to ankle subchondral bone with osteoarthritis is crucial to improving treatment options for patients, and it is therefore important to answer the following research questions:

- Are there significant changes to bone tissue and apparent mechanical properties with osteoarthritis in the ankle?
- How do changes in trabecular structure alter mechanical properties with

the presence of osteoarthritis?

Hence, the aim of this research was to characterise subchondral trabecular bone in the osteoarthritic ankle using a combination of experimental and computational techniques.

The following objectives were used to achieve the research aims:

- **Objective 1**: To characterise the structural changes to ankle bone with osteoarthritis using both standard and individual trabeculae segmentation (ITS)-based morphological analyses.
- **Objective 2**: To develop an inverse FE methodology to estimate the apparent mechanical properties of osteoarthritic ankle bone compared to non-diseased controls.
- **Objective 3**: To perform nanoindentation to characterise matrix-level properties of osteoarthritic ankle bone to quantify changes to tissue mechanical properties compared to non-diseased controls.

2.3 Thesis Overview

The research workflow is summarised in Fig. 2.1.

Chapter 1 explored relevant background knowledge and prior work in the characterisation of subchondral trabecular bone. The focus was particularly on *in vitro* and *in silico* investigation of multiscale mechanical properties in the lower-limb, as well as the mechanical and structural changes to subchondral trabecular bone with osteoarthritis.

Chapter 3 details the general materials and methods used in this thesis. This chapter details the specimen preparation; imaging and image analysis; mechanical characterisation and statistical analyses used in this research.

Chapter 4 reports findings of extensive morphological analysis of osteoarthritic ankle subchondral trabecular bone.

The development of the inverse FE methodology using porcine tissue is reported in Chapter 5 & 6 and its translation to human tissue is explored in Chapter 7.

Chapter 8 details the mechanical characterisation of matrix-level changes in osteoarthritic subchondral trabecular bone using nanoindentation testing.

In Chapter 9 the key findings of this work is summarised and critically reviewed with recommendations for future work. Key scientific communications presented or published within the duration of this PhD (publications and conference abstracts) are presented in Appendix D.

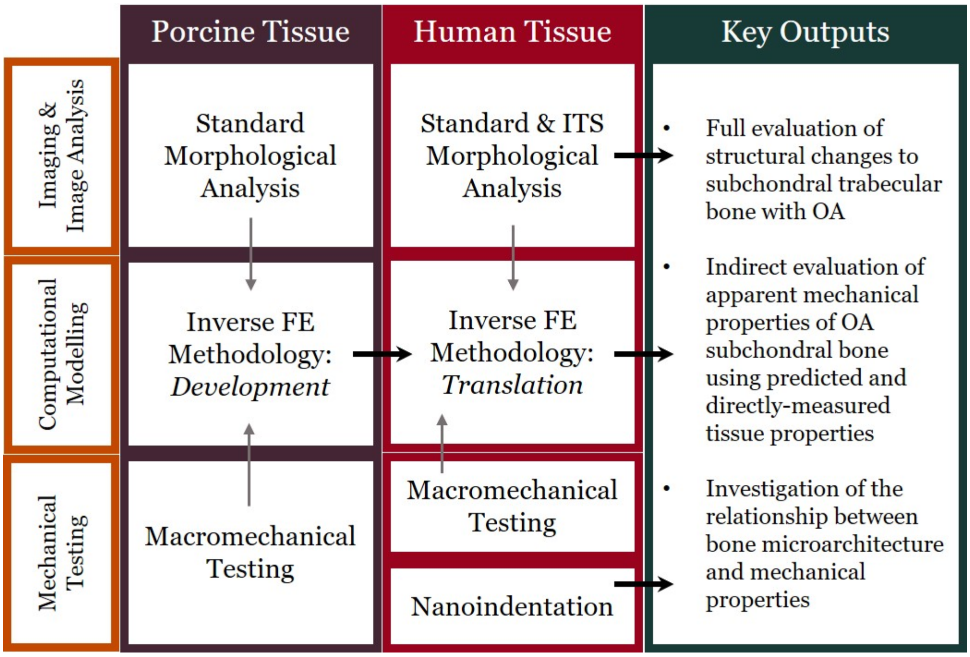

Figure 2.1: Project workflow summarising the techniques used on each type of tissue and the key outputs of the thesis.

Human cadaveric dissections were performed with consultant foot & ankle surgeons, Dr Ippokratis Pountos and Dr Nazzar Tellisi (Chapel Allerton Hospital). Osteoarthritic specimens were retrieved from ankle surgeries conducted by consultant foot & ankle surgeons, Dr Mark Farndon and Dr David Lavalette (Harrogate & District NHS Foundation Trust).

The author consulted with Dr Nagitha Wijayathunga (University of Leeds) on the development of the medical imaging protocols for both porcine and human tissue (HR-pQCT and μCT). Dr Wijayathunga also assisted with the extraction of bone cores from the cadaveric ankle bones.

The author collaborated with Dr Uwe Wolfram at the Institute of Mechanical, Process & Energy Engineering (IMPEE), Heriot-Watt University, Edinburgh. The author designed the study with Dr Wolfram and prepared non-diseased samples at IMPEE. However, due to travel constraints associated with the COVID-19 pandemic, the preparation of the osteoarthritic samples and the nanoindentation testing was completed by Mr Samuel McPhee under the supervision of Dr Uwe Wolfram.

Macro-mechanical testing, medical imaging, image analysis and finite element analyses were performed solely by the author.

CHAPTER 3

GENERAL MATERIALS & METHODS

This chapter details the materials and developed methodologies used in later chapters. In brief, a methodology involving a combination of mechanical, imaging and computational analyses was used to characterise the structural and mechanical properties of porcine subchondral trabecular bone and human ankle bone in both non-diseased and osteoarthritic states. The resources used in the following chapters are listed in Appendix A.

3.1 Specimen Preparation

3.1.1 Porcine Tissue

Eight fresh-frozen tali were isolated from juvenile porcine ankles (Fig. 3.1) (mean weight= 79.8 kg (range 61.2 - 95.2 kg), Appendix B). Porcine tissue was chosen for its geometric similarity to human tali, low cost and high availability from the local agri-food industry so it does not require ethical review. Fifteen cylindrical specimens (6 mm $\varnothing$) were extracted from the talar dome surface (on average two specimens per tali) using a tubular chisel and hammer (Fig. 3.1).

The cartilage and subchondral bone plate were removed using a scalpel to leave subchondral trabecular bone specimens of average height 8.63 ± 1.29 mm (6.0 - 9.9 mm range). The ends of each cylinder were then sanded to a flat-surface and rinsed in phosphate-buffered solution (PBS). Specimen height was measured using a thickness gauge. Custom Delrin endcaps were fixed to each end of the specimens by using a thin layer of polymethyl-methacrylate cement (PMMA) and clamping within a bench vice. This left an average gauge length of 6.23 ± 1.29 mm.

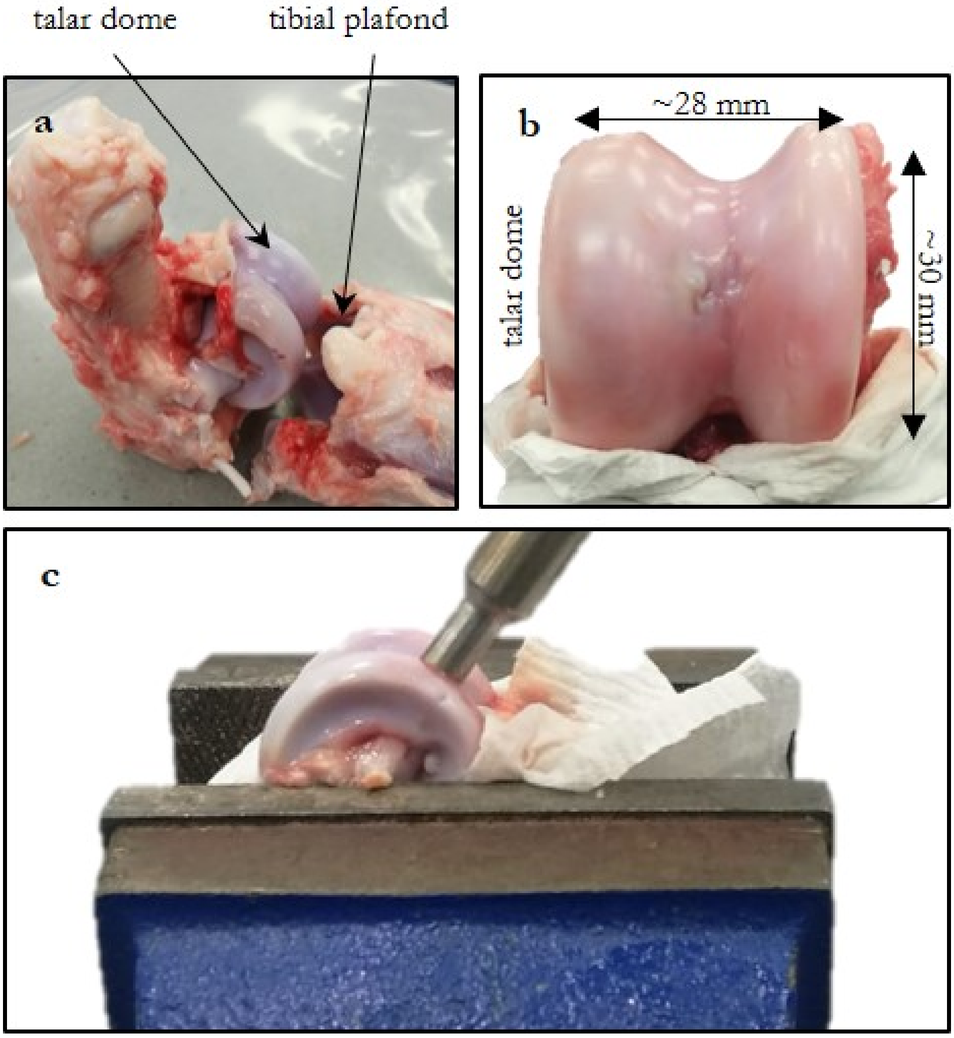

Figure 3.1: Porcine specimen preparation. Isolation of the talus from porcine trotter (a,b). Removal of bone cores from the talar dome (c).

3.1.2 Osteoarthritic Human Tissue

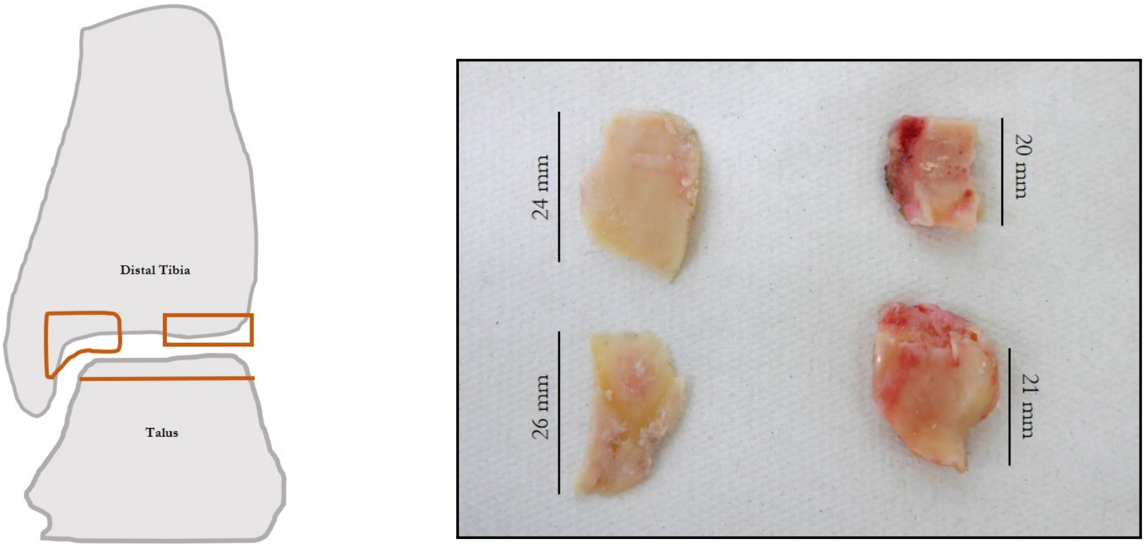

(i) Locations of exemplary OA samples where specimens were retrieved.

(ii) Talus (left) and tibial (right) specimens.

Figure 3.2: Exemplary set of late-stage osteoarthritic ankle bone samples obtained from patient undergoing total ankle arthroplasty.

Osteoarthritic bone specimens were retrieved from various locations in the talocural joint of patients undergoing total ankle arthroplasty at Harrogate & District NHS Foundation Trust (Fig. 3.2i). Ethical approval for sample collection was granted by NHS Yorkshire and Humberside National Research Ethics Committee (REC 07/Q1205/27). Specimens were classed as Stage IV (Kellgren-Lawrence scale). A total of five talar and six distal tibial specimens were collected from three patients (3 males; 58, 65 and 68 years; Appendix C, Section C.2.2 & Table C.1).

3.1.3 Non-Diseased Human Tissue

Three human, non-diseased cadaveric feet (three males; 43, 50 and 57 years of age) were sourced (*MedCure USA*, Appendix C, Table C.1) and stored at -80°C until dissection. Ethical approval was granted by the University of Leeds MEEC research ethics committee (MEEC 18-027). Exclusion criteria for the tissues included a reported prior lower limb trauma or surgery, or a history of diabetes.

Samples were thawed in the refrigerator for 48 hrs at 4°C prior to dissection. Pairs of distal tibiae and tali were dissected from each foot and cleaned from surrounding soft tissue by foot and ankle specialist consultant orthopaedic surgeons (Fig. 3.3). Each bone (Appendix C, Section C.2.1) was wrapped in PBS-paper soaked and frozen at -80°C until specimen removal.

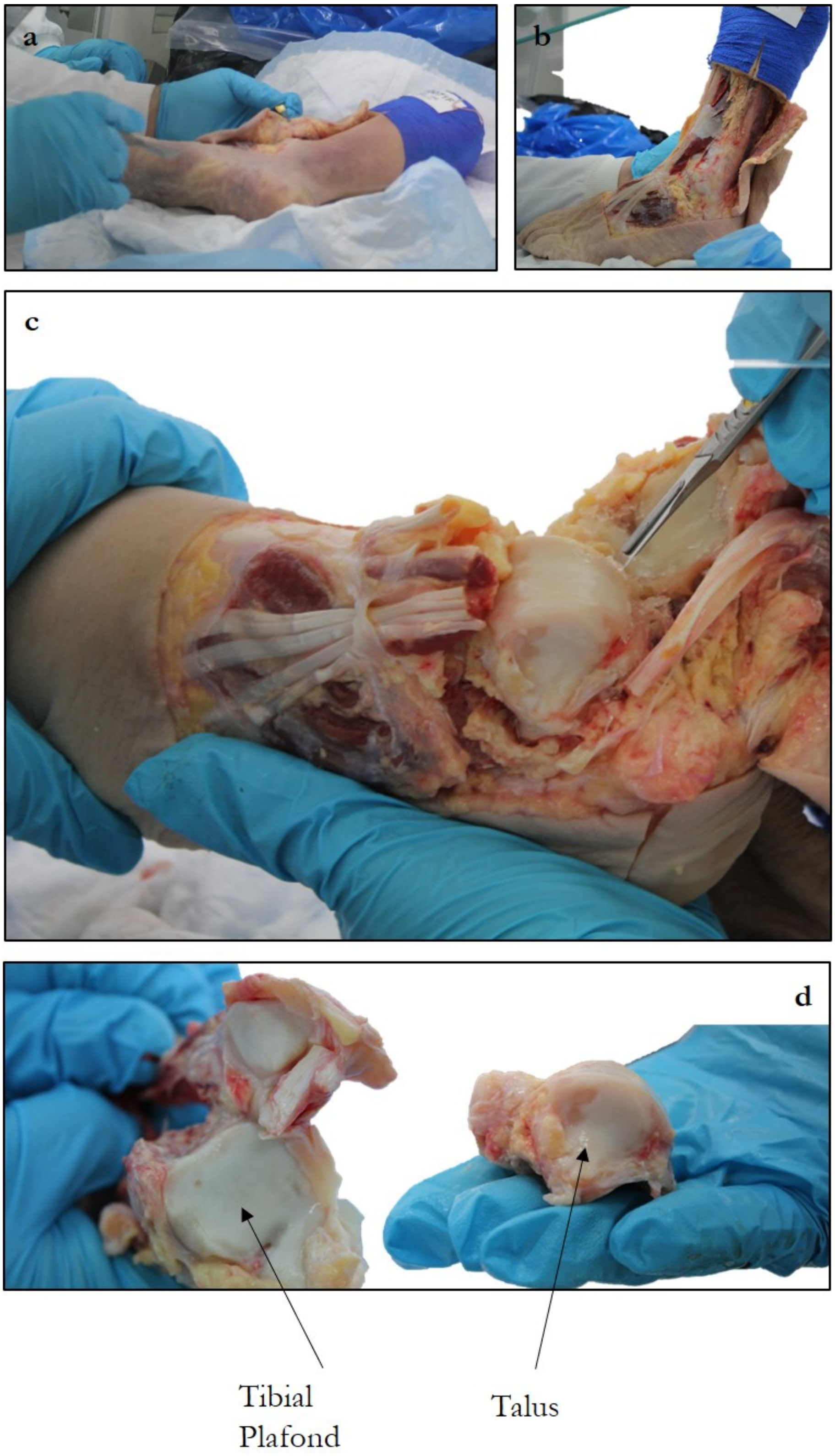

Figure 3.3: Initial dissection involved peeling back the skin of the foot (a) and gently breaking away layers of tissue to expose the joint (b,c). The talus and distal tibia were removed of their surrounding tissue and stored as seperate specimens (d).

3.1.3.a Specimens for compression testing

Each bone was fully thawed in a refrigerator at 4°C for 24 hours before specimen removal. Cylindrical osteochondral cores were removed from the articulating surfaces of each distal tibia and tali (Fig. 3.4, N=21 total: twelve talar and ten tibial) using a tubular chisel (6.5 mm ⌀, *Smith and Nephew mosaicplasty kit*). Each bone was secured into custom rigs (Fig. 3.4i and Fig. 3.4ii). Specimens were removed from the centre of four regions of the distal tibia: MP, LP, MA, LA and six regions of the talus: MA, MC, MP, LA, LC, LP (Fig. 3.5).

(i) Core extraction **(ii)** Custom rig **(iii)** Core preparation

Figure 3.4: Cores of bone were removed from the ankle bones using hammer and chisel and various rigs to secure the bones (3.4i and 3.4ii). The bone cores were each trimmed, sanded and cleaned of debris ready for testing (3.4iii).

The cartilage and subchondral bone plate were removed using a scalpel to leave subchondral trabecular cores (mean height = 8.54 ± 1.05 mm). The ends of each cylinder were sanded to a flat-surface and rinsed with PBS to remove debris. Each specimen was then exposed to ultrasound at 35 kHz for five minutes in an ultrasonic bath to further remove debris (Fig. 3.4iii). Custom Delrin endcaps were fixed to each end of the specimens using a thin layer of PMMA leaving an average gauge length of 7.34 ± 1.05 mm. Specimens were stored at 4°C in PBS for no more than 24 hours until testing.

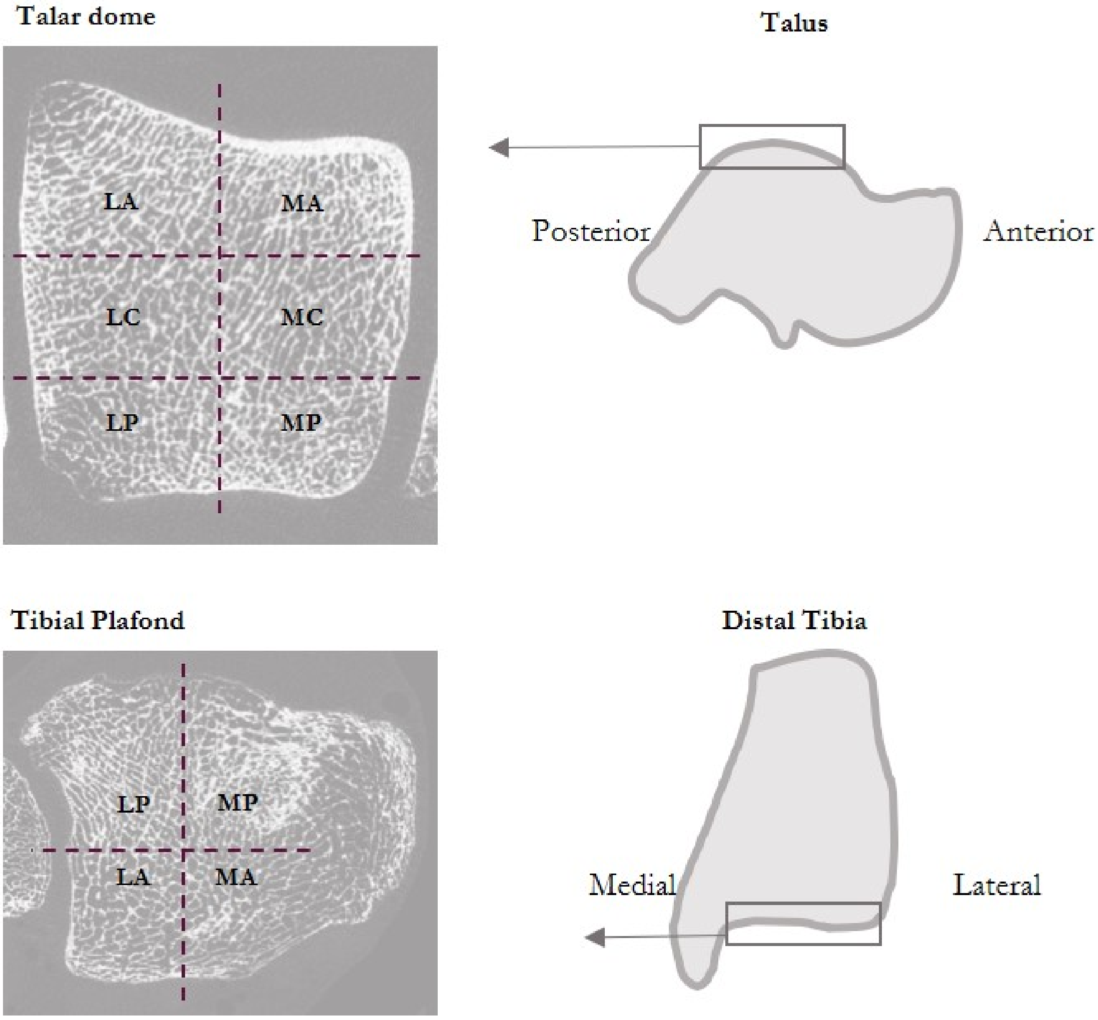

Figure 3.5: Anatomical regions (**C**entre, **M**edial, **L**ateral, **A**nterior or **P**osterior) on the tibial plafond and talar dome.

3.1.3.b Specimens for nanoindentation testing

For each of the three ND ankles, the bone remaining following the removal of bone core extraction was further dissected along the central saggital plane to remove two 5 mm-thick bone slices using a high-precision diamond-blade band saw (*Exakt, Norderstedt, Germany*) under constant water irrigation. The slices were further sliced to form smaller specimens suitable for nanoindentation. Three specimens were created per tali section, and two per tibial section, approximately 20 mm length. The cartilage layer was then removed using a scalpel. A total of thirty specimens were available for testing.

The specimens were cleaned of their marrow under running water for two minutes followed by exposure to ultrasound for 5 min at 35 kHz in an ultrasonic bath. This was then repeated until the majority of the marrow was clear. Specimens were then dipped in acetone to further aid dehydration and then left to dry

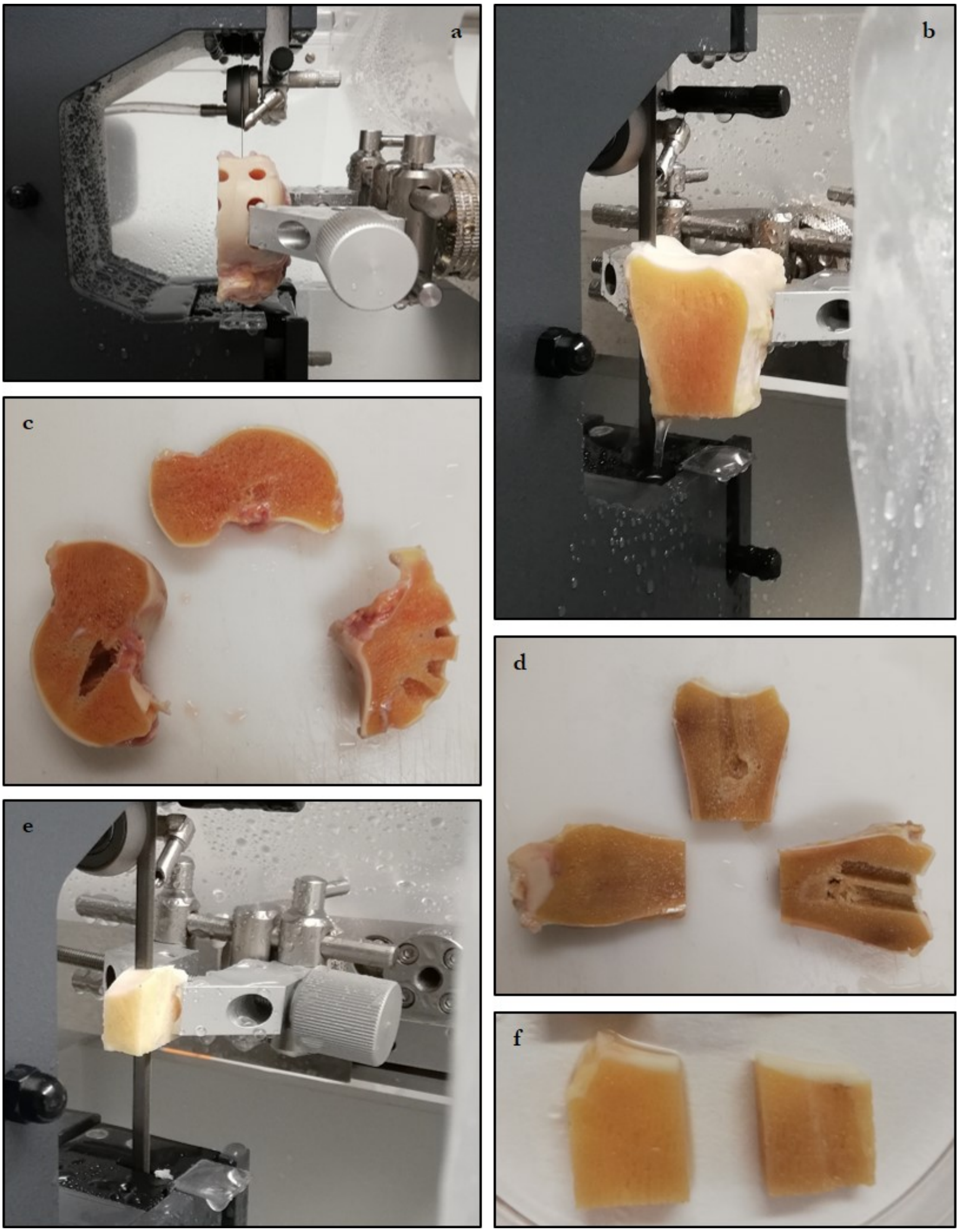

Figure 3.6: Preparation of specimens for nanoindentation. (a,b) Central saggital slices of talus and distal tibia were removed from each bone (c,d). Smaller sections were trimmed further (e) leaving the final slice samples (f).

at room temperature for at least 24 hours. A visual inspection was performed under a microscope (*Leica DFC7000T, Leica Microsystems, Wetzlar, Germany*) to check for remaining water, marrow or significant fractures before embedding.

Each specimen was embedded in cold-curing, clear resin (*Technovit 4006 SE-Heraeus, Germany*) with the longitudinal plane of the specimen exposed for nanoindentation. Specimens were glued to the bottom of the moulds using a thin layer of cyanoacrylate to ensure the specimens stayed flat during embedding. Specimens were subsequently cured under elevated pressure (2 bar for 30 mins) to remove air bubbles and to promote the infiltration of the resin into the pores of the bone.

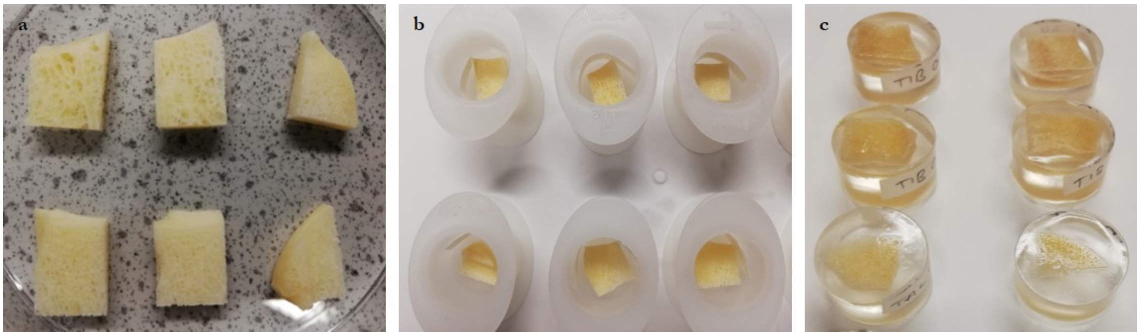

Figure 3.7: The embedding process. (a) Specimens were removed of marrow and placed within moulds accompanied by a specimen label marked with pencil on a small piece of paper (b). The moulds were filled with resin and cured under pressure to leave specimens ready for polishing (c).

Following curing, specimens were polished (*Struers LaboForce-Mi, Struers, Ballerup, Denmark*) using abrasive silicon carbide papers of decreasing particle size (P800, P1200, P2000, P4000) and finishing with 0.25μm polish with diamond suspension (*Hermes Abrasives, Hamburg, Germany*) to expose flat and parallel surfaces for indentation (Fig. 3.9). Specimens were exposed to ultrasound for 5 minutes between each stage of polishing. This was accompanied with a visual inspection of each specimen under a microscope to identify scratches (Fig. 3.8). This protocol was repeated for the OA specimens (N=6 tibial and N=5 talar). Due to the irregular geometry of the samples, sections were removed wherever feasible. A total of twelve tibial and sixteen talar samples were available for testing.

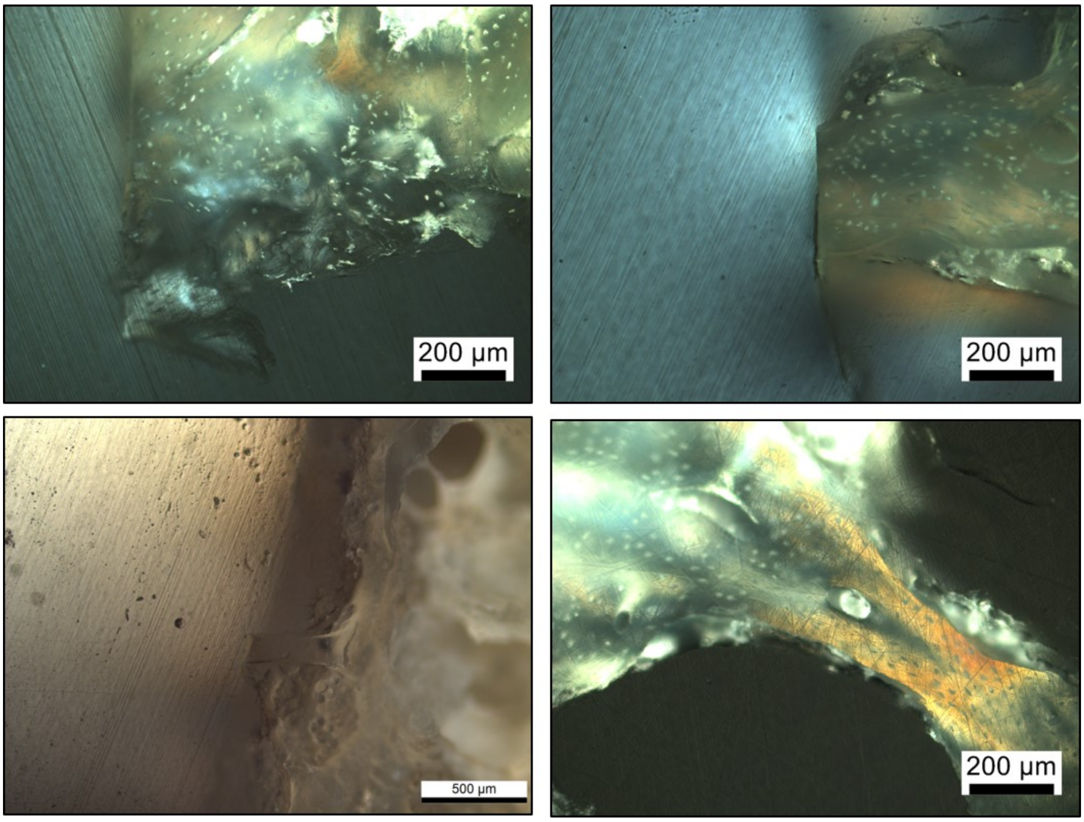

Figure 3.8: Exemplary pre-polished specimens for nanoindentation with scratches present on surface.

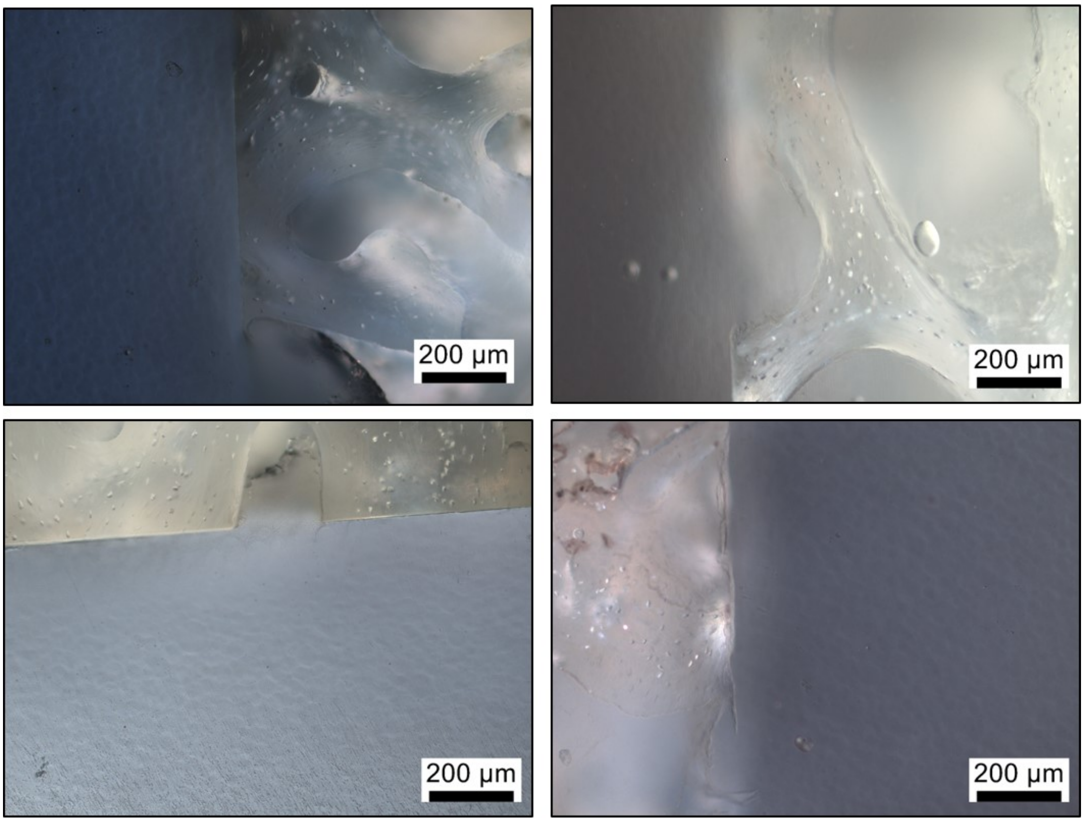

Figure 3.9: Final exemplary specimens showing fully polished surfaces ready for nanoindentation testing.

3.2 Imaging

3.2.1 μCT

Each osteoarthritic sample and all bone cores (porcine and non-diseased human) were scanned at an isotropic resolution of 16 μm (70kVP, 114 μA, 250ms integration time) in a μCT (*MicroCT100*). Specimens were scanned whilst submerged in PBS. Image data was extracted in proprietary scan format, ISQ, and converted using an in-house developed Matlab script (Appendix A) to a stack of normalised (0-255 grayscale, 8 bit) TIFF images. This process converts all negative HU values to 0 and the maximum theoretical HU value of the scanner to a value of 255.

3.2.2 HR-pQCT

Prior to dissection, each cadaveric foot was imaged at an isotropic resolution of 82 μm using HR-pQCT (*XtremeCT, ScanCo Medical, Switzerland*) to check for signs of joint deterioration to ensure samples had no undiagnosed damage present. Bones from the eldest donor, sample RM57, had visual striations on the articular cartilage (Appendix C, Fig. C.3). Further analysis of the CT images however, showed no obvious deterioration of the underlying bone and it was deemed as early signs of wear but not indicative of early osteoarthritis. Following a conversion of the ISQ to TIFF format as previously described, the image stacks were imported into ImageJ and a visual confirmation of the health of the ankle joint was performed.

3.3 Summary: Human Specimen Preparation

The following tables summarise the final number of specimens retrieved from ND cadaveric feet and OA tissue for testing.

ND DONOR	HR-PQCT	BONE	BONE CORES	μCT	NANO. SPECIMENS
LM43	✓	Talus	2	✓	6
		Distal Tibia	3	✓	4
RM50	✓	Talus	3	✓	6
		Distal Tibia	3	✓	4
RM57	✓	Talus	6	✓	5
		Distal Tibia	4	✓	4
	TOTAL		21		29

Table 3.1: Summary of ND specimens prepared for studies.

OA DONOR	ANKLE BONE	SAMPLES	μCT	NANO. SPECIMENS
RM58	Talus	2	✓	6
	Distal Tibia	1	✓	0
RM65	Talus	1	✓	4
	Distal Tibia	3	✓	8
LM68	Talus	2	✓	6
	Distal Tibia	2	✓	4
TOTAL		11		28

Table 3.2: Summary of OA specimens prepared for studies.

3.4 Image Analysis

3.4.1 Thresholding

The delineation of trabecular bone to the surrounding marrow or space is crucial to accurately capturing bone geometry to measure morphological properties (such as BV/TV) or in the construction of trabecular level, μFE, models. One means of performing image segmentation is to use automatic thresholding techniques, which convert image grayscale values into binary values, thus creating a binarised image clearly depicting bone trabeculae only. Various histogram-based global thresholding methods for binary segmentation data exist and are available within ImageJ. In this work Otsu's global thresholding technique [Otsu, 1979, Parkinson et al., 2008] was utilised to segment bone, such that trabeculae were in the foreground (gray value of 255).

BV/TV values were verified by using three exemplary specimens. Binarised image stacks were saved as a single MetaImage (.mha) file using the 3D IO plug-in for ImageJ. A Python script using the SimpleITK (SITK) image analysis package was then used to calculate BV/TV based on counting individual bone and marrow voxels. This value was compared to the output of BoneJ's "volume fraction" function and was identical to 3 decimal places (Appendix B, Table B.2).

3.4.2 Morphological Analysis

3.4.2.a Standard morphological analysis

Standard morphological properties were characterised using BoneJ [Doube et al., 2010] (Plugin for NIH ImageJ, Appendix A). The following standard indices were evaluated using BoneJ: bone volume fraction (BV/TV); degree of anisotropy (DA, where 0 is completely isotropic and 1 is fully anisotropic); connectivity density (Conn.D, mm^{-3}); trabecular thickness (Tb.Th, mm) and for cuboidal (4 mm) specimens located at the proximal end of the specimen, EF (ellipsoid factor) [Doube, 2015, Salmon et al., 2015]. EF was too computationally costly to run on the full bone cylinders. Hence, the measure was solely applied to the 4 mm cuboids using the parameters outlined in Table 3.3. On average, 85-90% of the volume was filled with ellipsoids. The mean EF value was obtained from the stack histogram of the EF image.

Table 3.3: Ellipsoid Factor parameter values used in BoneJ (ImageJ)

VARIABLE	VALUE
Sampling Incremement	0.005
Vectors	200
Skeleton Points	1
Contact Sensitivity	1
Maximum Iterations	100
Maximum Drift	1

Additionally, Structure Model Index (SMI) was characterised in human specimens to allow comparison of results to the literature of other human lower-limb joints.

3.4.2.b Individual Trabecular Segmentation (ITS)-based morphological analysis

In addition to the standard morphological measures, 3D Individual Trabecular Segmentation was used to obtain more detailed morphological indices (Chapter 1.2.2, Table 1.1) to further characterise microstructural changes to rod and plate geometry in ankle bone with OA [Liu et al., 2009]. In brief, each binarised 4 mm cuboidal volume (stack of .tiff images) was converted into a single .RAW file format in ImageJ and loaded into the ITS software (Appendix A).

3.5 Mechanical Testing

3.5.1 Uniaxial Compression

Apparent mechanical properties were evaluated using unconfined, uniaxial compression testing (*500N load cell, ± 0.5% accuracy of reading, Instron 3365*). Testing was performed under physiological conditions by immersing specimens in temperature-controlled PBS at 37°C within a BioBath (*Biopuls, Instron*, Fig 3.10).

Figure 3.10: Specimen setup within Instron 3365 whilst immersed within a temperature-controlled Biobath.

A pre-load of 0.3 N was applied for ten minutes to allow bedding-in of the specimen and allow the specimen stresses to relax under a baseline load. The specimens were then pre-conditioned at 0.006% s^{-1} up to 0.006 mm/mm for thirty cycles to promote bedding-in, allow material relaxation by reaching a steady viscoelastic state and near-zero strain (Fig. 3.11i) before being loaded at a quasi-static rate of 0.01% s^{-1} to failure. Mechanical tests were not repeated for each specimen, and hence there was potential for variation of measured stiffness. Repeating the testing would be achievable provided the sample was not tested past its yield point, where it would begin to plastically deform. This point may differ slightly between each sample and therefore setting a specified limit to stop testing is difficult to apply across all samples. Maximum *in vitro* stiffness, k_{exp}, was derived from the largest slope of the linear-elastic region of the force - (crosshead) displacement (Fig. 3.11ii) data using a custom-written Matlab script. This script was used to first crop the data to the elastic region (removing pre-conditioning cycles) and calculate the (maximum) gradient using a moving average to avoid noise in the data.

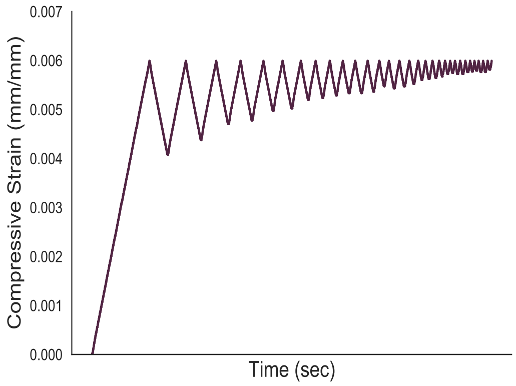

(i) Impact of pre-conditioning cycles on compressive strain of specimens over time.

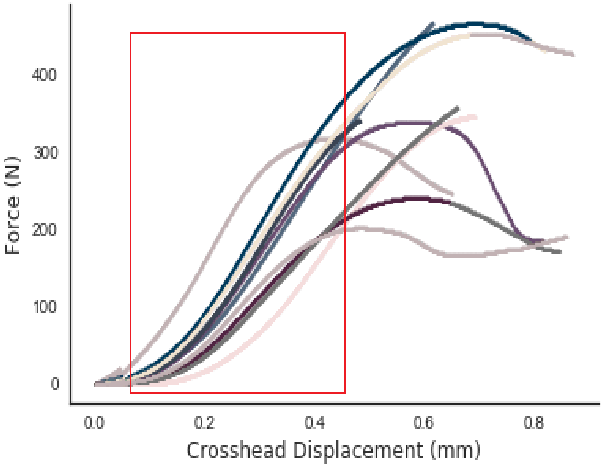

(ii) Approximate elastic region of force-displacement curves.

Figure 3.11: (3.11i) shows diminishing creep (primary stage) reaching a steady state of viscoelasticity and hence, material relaxation, preceding testing. (3.11ii) collates force-displacement data of all porcine specimens showing the approximate elastic region from which stiffness was calculated.

3.5.2 Nanoindentation

This work was conducted at Heriot-Watt University in collaboration with Dr Uwe Wolfram. As stated in Section 2.3, the author this thesis defined the experiment design and prepared the non-diseased samples, but the nanoindentation testing and OA specimen preparation was conducted by Mr Samuel McPhee. Prior to indentation, specimens were rehydrated for 1.5 hours in HBSS (*Hank's Balanced Salt Solution, Sigma Aldrich*). Specimens were kept moist during testing using a custom-made wet cell containing a drop of HBSS. Probe and compliance calibration was conducted in accordance with the manufacturer protocol (*Triboindenter 900, Hysitron, Minneapolis, USA*).

Specimens were mounted to a custom wet cell that was secured to the machine bed to reduce axial compliance. This accommodated a 1.5 mm layer of HBSS to ensure specimens maintained hydration during testing. Probe drift rate was calculated prior to each indent by applying a pre-load of 100 nN for 40 s and fitting a first order polynomial to the load-displacement data points for the final 20 s. Each indentation consisted of a trapezoidal load-controlled function to a maximum load of 80 mN such that the achieved depth resulted in tip contact across several lamellae. Load was applied at a rate of 120 mN/min, following by a 30 second dwell and an unloading rate of 480 mN/min. The unloading portion of the force-displacement curve was used to calculate the tissue modulus ($E_{tiss,nano}$) [Oliver and Pharr, 1992]. A total of twenty-five indentations per specimen were obtained in areas of transverse lamellae progressively from the subchondral bone plate to identify tissue property depth-dependence in subchondral trabecular bone. Specimen tissue modulus was calculated ($\overline{E}_{tiss,nano}$, where ν_{tiss} = 0.3) using Equation 3.1.

$$E_{tiss,nano} = \frac{E_i E_r (1 - \nu_{tiss}^2)}{E_i - E_r (1 - \nu_i^2)} \tag{3.1}$$

where E_i and ν_i are the indenter modulus (1141 GPa) and Poisson's ratio (0.07) [Rho et al., 1997] and E_r is the reduced elastic modulus, which represents the combined modulus of the indenter and material, calculated using Equation 3.2.

$$E_r = \frac{S\sqrt{\pi}}{2\beta\sqrt{A_c}} \tag{3.2}$$

where β is the geometry correction factor (β = 1.034 for Berkovich indenter [Rho et al., 1997]); A_c is the projected tip contact area, calculated by:

$$A_c = 24.5 h_c^2 \tag{3.3}$$

where,

$$h_c = h_t - \epsilon\beta\frac{P_t}{S} \tag{3.4}$$

Here, h_t and P_t are the displacement and load at initial unloading, respectively. The constant, ϵ, is calculated by $\epsilon = [2(\pi - 2)]/\pi = 0.72$. However, 0.75 is commonly used as it is shown to account for non-uniformities in the material response as load is reduced. The slope (stiffness of contact), S, is defined as the derivative of the fitted polynomial to the initial unloading curve of the load (P) - displacement (h) data at the maximum displacement point, h_{max} using Equation 3.5.

$$S = \left.\frac{dP}{dh}\right|_{h=h_{max}} \tag{3.5}$$

Specimen-specific average elastic moduli were obtained by averaging all indentations for each bone ($\overline{E}_{tiss,nano,tal}$ or $\overline{E}_{tiss,nano,tib}$).

3.6 Statistical Analyses

All statistical tests were computed in R (*RStudio 1.1.463*).

The mean (AVG) and standard deviation (± SD) for each microarchitectural, computational and mechanical property was calculated and reported for all specimens. The Coefficient of Variance (CoV, %) was calculated as SD/AVG.

Correlation was measured using the Square of the Pearson Product-Moment Correlation Coefficient, r^2. r values were reported where the strength and direction of a linear relationship was of interest. Agreement was quantified using Concordance Correlation Coefficient (CCC) values [Lawrence and Lin, 1989] (Equation 3.6), where ρ is the Pearson correlation coefficient between the two variables; μ_x and μ_y are the means for the two variables and σ_x^2 and σ_y^2 are the corresponding variances. CCC values ranged from 0 (no agreement) to +1 (perfect agreement) or -1 (perfect, negative agreement).

$$CCC = \frac{2\rho\sigma_x\sigma_y}{\sigma_x^2 + \sigma_y^2 + (\mu_x - \mu_y)^2} \tag{3.6}$$

Agreement between two (stiffness) variables was visually represented using Bland-Altman analyses [Bland and Altman, 1999] with 95% limits of agreement on the verified assumption that the differences to stiffness are normally distributed. Normality of data was tested using a Shapiro-Wilk Test [Shapiro and Wilk, 1965].

Root Mean Square Error (RMSE) was calculated using Equation 3.7, to quantify the fit of the model using the observed (y_i) and predicted ($\hat{y}$) values. This is reported as a percentage (%).

$$RMSE = \sqrt{\sum \left(\frac{y_i - \hat{y}}{y_i} \right)^2} * 100 \tag{3.7}$$

Independent samples t-test's were used to test for differences between two groups (osteoarthritic vs. non-diseased) with Tukey's test or Bonferroni correction to adjust for multiple comparisons ($\alpha = 0.05$). Equality of variances was established using an f-test.

Chapter 4

Characterising Structural Changes to Subchondral Bone with OA

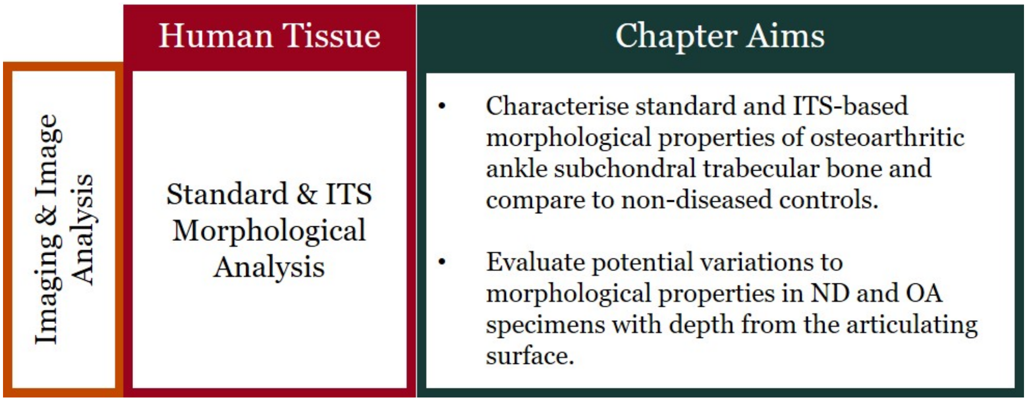

Imaging & Image Analysis

Human Tissue

Standard & ITS Morphological Analysis

Chapter Aims

- Characterise standard and ITS-based morphological properties of osteoarthritic ankle subchondral trabecular bone and compare to non-diseased controls.
- Evaluate potential variations to morphological properties in ND and OA specimens with depth from the articulating surface.

This chapter quantifies structural changes to human ankle subchondral bone with osteoarthritis. Microarchitecture is a key pillar of bone quality, but significant changes are known to occur with osteoarthritis, though few studies have characterised these changes in the ankle. Characterising alterations to trabecular architecture and morphology will aid in understanding how the bone remodels in the presence of osteoarthritis and its impact on biomechanical properties. Morphological properties are thought to vary with depth from the articulating surface and so this was also investigated in this study. This is important when exploring the potential sacrifice of joint strength resulting from bone resections during ankle replacement surgery.

4.1 Introduction

Microarchitecture is a determinant aspect of bone mechanical properties and is essential to the evaluation and prediction of apparent bone stiffness. Trabecular bone is composed of different types of trabeculae: rods and plates. These are known to influence apparent mechanical properties [Stauber et al., 2006, Liu et al., 2006, Du et al., 2019]. Whilst standard morphological analysis provides an overall analysis of apparent morphological changes, detailed microstructural analysis of rod and plate properties can be achieved with the use of dedicated software, such as individual trabecula segmentation (ITS) [Liu et al., 2009].

Higher subchondral bone apparent stiffness has been reported in advanced OA [Stauber et al., 2006, Wang et al., 2015, Chen et al., 2018]. This is known to correlate with alterations to the microstructure that occur as a result of accelerated, irregular bone remodelling [Burr and Gallant, 2012]. It is well known that higher bone density and trabecular thickness are also present in OA bone [Ding, 2010, Burr and Gallant, 2012, Finnilä et al., 2017, Chen et al., 2018, Gatenholm et al., 2019], but also the combination and properties of the trabecular types (rod and plate) also alter [Ding, 2010, Finnilä et al., 2017, Chen et al., 2018, He et al., 2020].

Such changes are under-reported in the ankle joint, but fully characterising these alterations will improve our understanding of the correlations between microarchitecture and apparent mechanical properties, which can be invaluable for predicting fracture risk or developing novel implant designs [Stauber et al., 2006, Wang et al., 2015, Chen et al., 2018].

4.1.1 Study Aims

The aim of this study was to characterise changes to ankle subchondral bone microarchitecture with osteoarthritis. The following objectives were defined:

- Characterise standard and ITS-based morphological properties of osteoarthritic ankle subchondral bone and compare to non-diseased controls.
- Evaluate variations to morphological properties in ND and OA specimens with depth from the articulating surface.

4.2 Materials and Methods

Non-diseased (ND) ankle bones (distal tibia and talus pairs) were dissected from human cadaveric feet (N=3). Subchondral bone cores were removed from the tibial plafond (N=10) and talar dome (N=12), and trimmed to just below the SBP (as described in Chapter 3, Section 3.1.3).

Late-stage osteoarthritic (OA) specimens were sourced from patients undergoing total ankle arthroplasty (distal tibia: N=6, talus: N=5; Section 3.1.2). Most of the talar OA specimens lacked sufficient bone volume to be analysed (Appendix C.2.2), leaving only five distal tibia specimens and one talar specimen for use in this study. As the talar OA group was severely underpowered it was omitted from the comparison between OA and ND groups (nonetheless the values obtained were still reported in the raw data). Hence, this study solely focused on the specimens from the distal tibia for microarchitectural comparisons to ND control tissue.

4.2.1 Imaging

Both the OA specimens and ND bone cores were scanned using μCT at an isotropic resolution of 0.016 mm (as described in Section 3.2.1). Each stack of images was trimmed to just below the subchondral bone plate. For the ND specimens, a cuboidal volume of trabecular bone was extracted (4 mm edge length) from the centre of the proximal end of the cylinder (Fig. 4.1). Similarly, cuboidal volumes were extracted from each OA specimen image stacks. A total of five OA volumes and ten ND volumes were available for analysis.

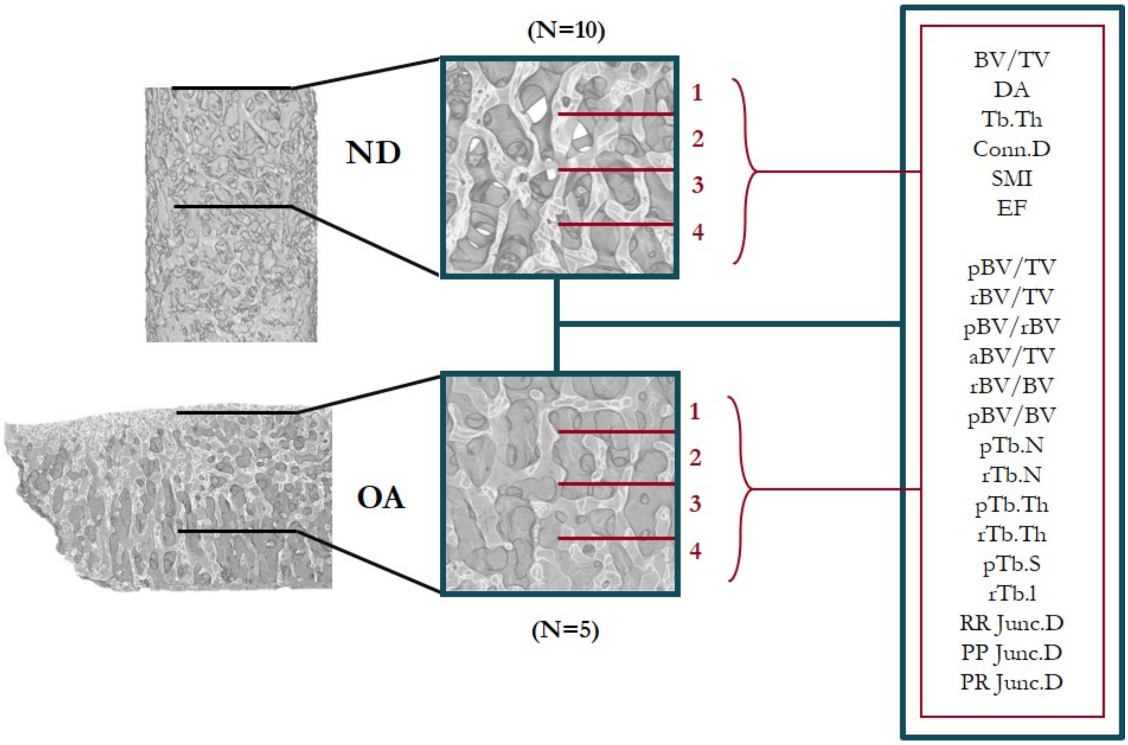

Figure 4.1: Study workflow showing the extraction of cuboidal volumes of interest from exemplary OA and ND μCT image volumes for full morphological analyses as whole cuboids and in regular 1 mm intervals with increasing distance from the SBP.

4.2.2 Morphological Analysis

All image stacks were binarised using Otsu thresholding. Standard morphological properties (BV/TV, DA, Tb.Th, Conn.D, SMI and EF) were evaluated using BoneJ (as defined in Section 3.4). Standard measures of trabecular morphology, SMI and EF, do not indicate specific changes to individual plate or rod trabecular properties, and so to evaluate these changes in higher detail, dedicated 3D ITS software was used to evaluate numerous ITS-based morphological properties (defined in Section 3.4).

4.2.3 Variations to Morphological Properties with Depth

To establish variations to morphological properties with depth from the tibial plafond, each OA and ND cuboidal volume was trimmed at regular 1 mm intervals from the top surface (Fig. 4.1) and labelled as follows:

- Level 1 = 0-1 mm
- Level 2 = 1-2 mm
- Level 3 = 2-3 mm
- Level 4 = 3-4 mm

Full morphological analyses (standard and ITS) were performed on each volume at each depth level.

4.2.4 Statistical Analysis

The mean (AVG) and standard deviation (SD) for each morphological property was calculated for all specimens grouped by state (ND or OA). Independent samples t-test with Bonferroni correction ($\alpha = 0.05$) was used to compare significant differences between OA and ND morphological properties.

4.3 Results

All raw data are presented in Appendix C: Table C.4 (standard morphological results); Table C.5 (ITS-based morphological results) and Tables C.6 & C.7 (depth-dependent morphological variations - standard and ITS).

4.3.1 Standard Morphological Results

Significantly higher BV/TV ($p<0.01$) and Tb.Th ($p<0.001$) were observed in OA samples (Table 4.1), as well as significantly lower DA ($p<0.05$). Significantly higher mean EF value ($p<0.05$) showed a larger number of rod-like trabeculae present in OA specimens (Fig. 4.2). Comparatively, a lower SMI was observed indicating a higher presence of plate-like trabeculae in OA specimens, though this was non-significant (p>0.05, Fig. 4.3).

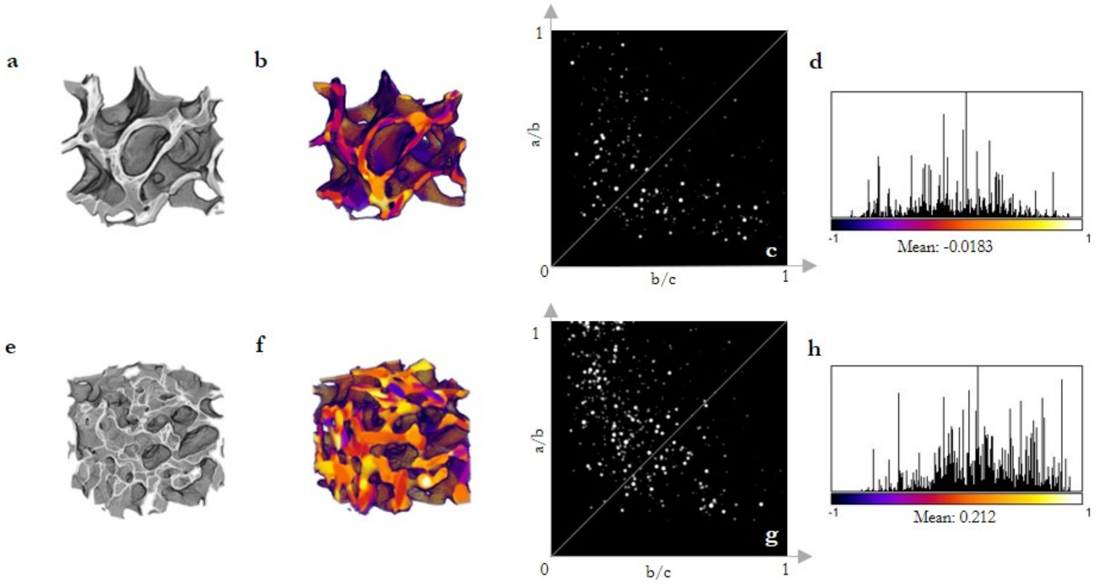

Figure 4.2: A comparison between ND (**a**) and OA **e**) exemplary specimen subvolumes (2 mm). EF results show EF >0 (yellow-orange, **f**) or more rod-like trabeculae in the OA specimens. In comparison, ND specimens show EF <0 (purple-blue, **b**) indicating more plate-like trabeculae. Finn peak plots (**c,g**) show volume-weighted axis ratios of the fitted ellipsoids with a shift of distribution towards the bottom-right of the plot for plate-dominated geometry (**c**) and top-left for rod-dominated geometry (**g**). Histograms and summary statistics (**d,h**) further demonstrate the shift in values towards either +1 (**h**; rod-dominated geometry) or -1 (**d**; plate-dominated geometry). See 1.2.2.b)

	OA		**ND**		
	AVG	±SD	AVG	±SD	**p value**
BV/TV	0.464	0.100	0.334	0.058	0.0066 **
DA	0.572	0.078	0.714	0.110	0.0238 *
Tb.Th (mm)	0.315	0.045	0.228	0.023	0.0002 ***
Conn.D (mm^{-3})	4.581	0.951	4.387	1.945	ns
EF	0.071	0.034	0.003	0.045	0.0101 *
SMI	0.237	0.933	0.949	0.423	ns
pBV/TV (%)	42.293	9.237	31.597	5.310	0.0127 *
rBV/TV (%)	3.985	1.156	1.793	0.600	0.0003 ***
pBV/rBV	11.032	2.573	18.587	3.762	0.0015 **
aBV/TV	0.256	0.053	0.230	0.028	ns
pBV/BV	0.913	0.022	0.947	0.010	0.0009 ***
rBV/BV	0.087	0.022	0.053	0.010	0.0009 ***
pTb.N (1/mm)	3.361	0.222	3.078	0.308	ns
rTb.N (1/mm)	2.424	0.214	1.928	0.209	0.0009 ***
pTb.Th (mm)	0.148	0.002	0.139	0.006	0.0102 *
rTb.Th (mm)	0.090	0.003	0.090	0.002	ns
pTb.S (mm^2)	0.075	0.003	0.079	0.012	ns
rTb.l (mm)	0.355	0.029	0.318	0.014	0.0047 **
RR Junc.D (1/mm^3)	1.816	0.904	1.277	0.480	ns
PR Junc.D (1/mm^3)	30.497	7.752	17.541	5.393	0.0022 **
PP Junc.D (1/mm^3)	30.316	6.607	22.703	7.124	ns

Table 4.1: Mean (AVG) and standard deviation (± SD) values of the standard and ITS-based morphological properties from OA and ND distal tibia specimens. Statistically significant differences between both groups were calculated using an independent samples t-test with Bonferroni correction. Levels of significance are indicated using: * ($p<0.05$), ** ($p<0.01$), *** ($p<0.001$) and ns ($p>0.05$)

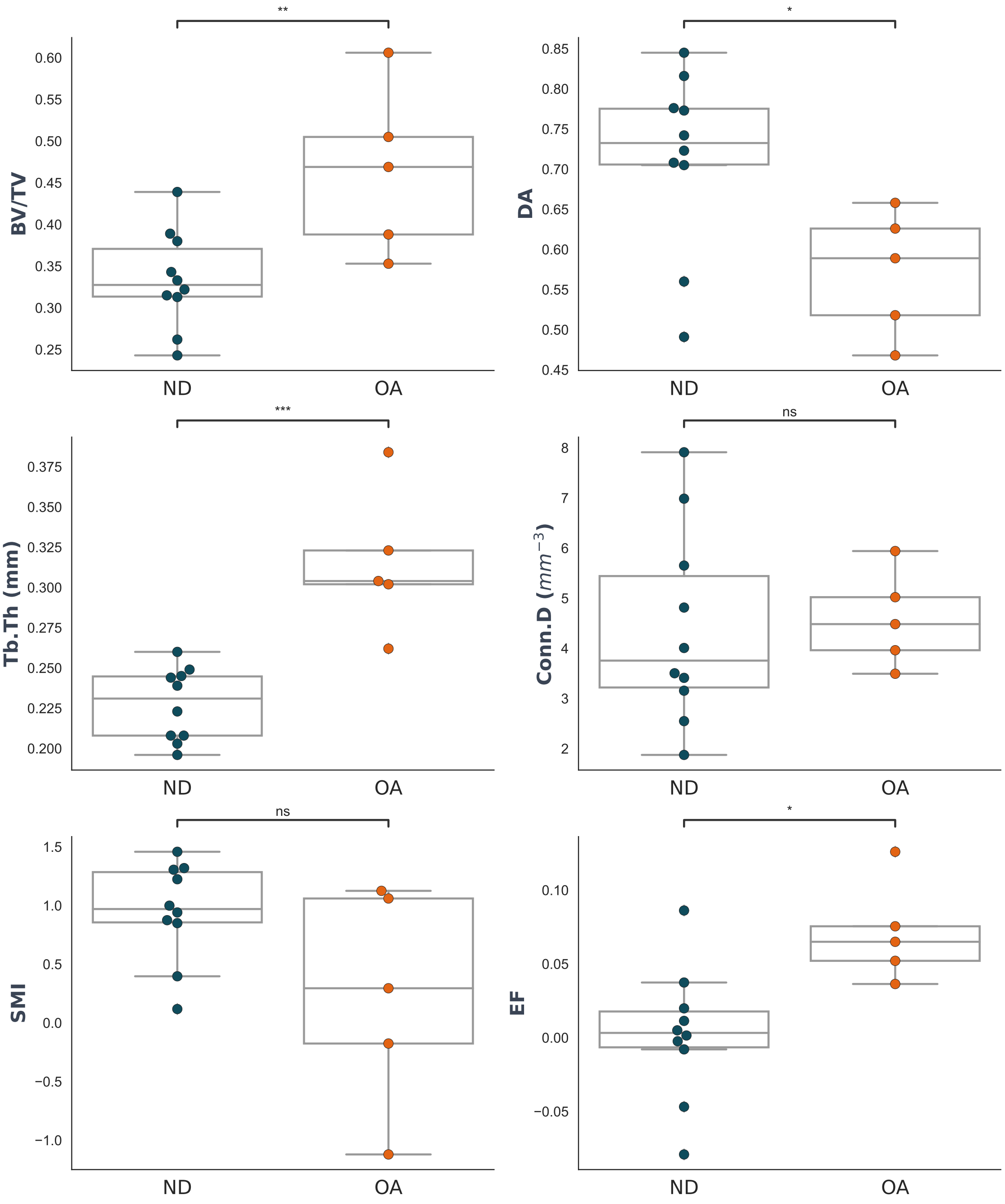

Figure 4.3: Distribution of standard morphological values for OA vs. ND groups of distal tibial specimens. The box plots represent the median and interquartile range of values for N=5 OA specimens and N=10 ND specimens. Significance levels are indicated using: * p<0.05, ** p<0.01, *** p<0.001, ns = non-significance.

4.3.2 ITS-based Morphological Results

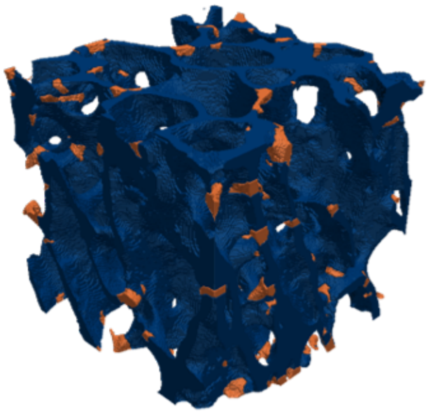

(i) ND specimen

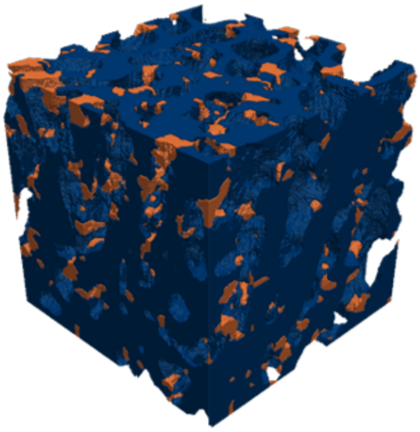

(ii) OA specimen

Figure 4.4: 3D rendered volumes of exemplary OA and ND specimens indicating plate-like trabeculae (blue) and rod-like trabeculae (orange).

The ITS-based morphological results showed significantly higher rod fractions, rBV/TV ($p<0.001$) and rBV/BV ($p<0.001$) in the OA group compared to controls. This is countered with lower plate fractions, pBV/BV ($p<0.001$), but higher plate thickness, pTb.Th ($p<0.05$,) was observed in the OA group with an overall larger pBV/rBV ($p>0.01$) (Fig. 4.5). Whilst standard morphological analysis showed significantly lower DA in OA samples, ($p<0.05$), aBV/TV was not significantly different between the two groups. Similarly, standard morphological analysis showed higher Tb.Th with OA ($p<0.001$), but the ITS results show higher pTb.Th only ($p<0.05$) and not rTb.Th. Higher rTb.N ($p<0.001$) correlated with the higher mean EF value, indicating a larger presence of rod-like trabeculae in the OA group. These rod-like trabeculae also appear to elongate with OA (rTb.l; $p<0.01$).

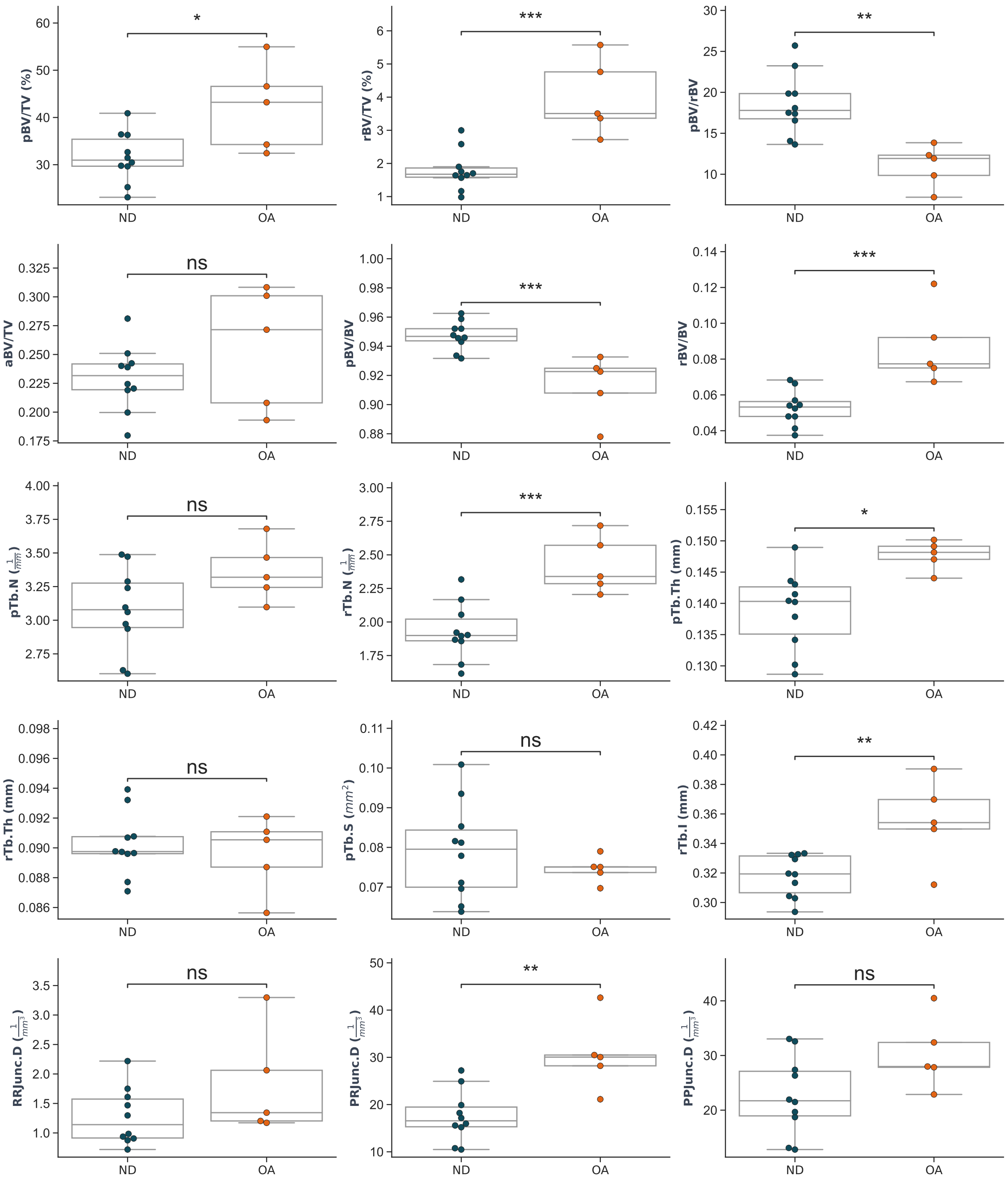

Figure 4.5: Distribution of ITS-based morphological values for OA vs. ND groups for specimens from the distal tibia. The box plots represent the median and interquartile range of values for OA specimens (N=5) and ND specimens (N=10). Levels of significance indicated using: * $p<0.05$, ** $p<0.01$, *** $p<0.001$, ns= no significance.

4.3.3 Variation with Depth

Standard morphological analysis of each depth-level showed significant differences solely in BV/TV between Level 1 and 4 ($p<0.05$) in ND tibial specimens (Fig. 4.6). Though for both OA and ND groups, there was a clear decreasing trend in BV/TV and increasing trend in SMI with increasing depth (Fig. 4.7). For each level, there was high negative correlation between BV/TV and SMI (-0.985,-0.994,-0.981 and -0.918 for Level 1, 2, 3 and 4, respectively).

Figure 4.6: Comparison of AVG (bars) ± SD (error bars) BV/TV, with increasing depth from the SBP for tibial specimens from OA (purple) and ND (green). Levels of significance indicated using: * $p<0.05$, ** $p<0.01$, *** $p<0.001$.

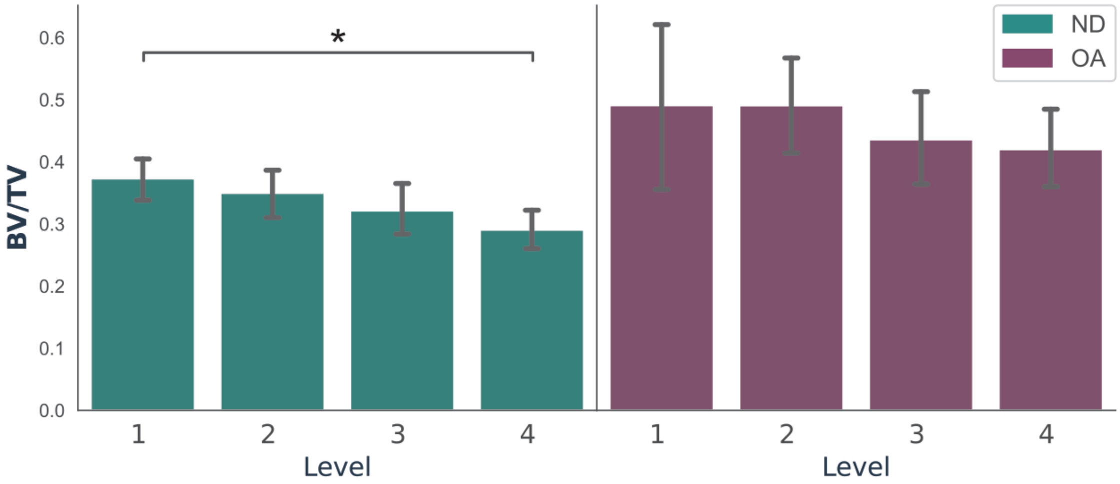

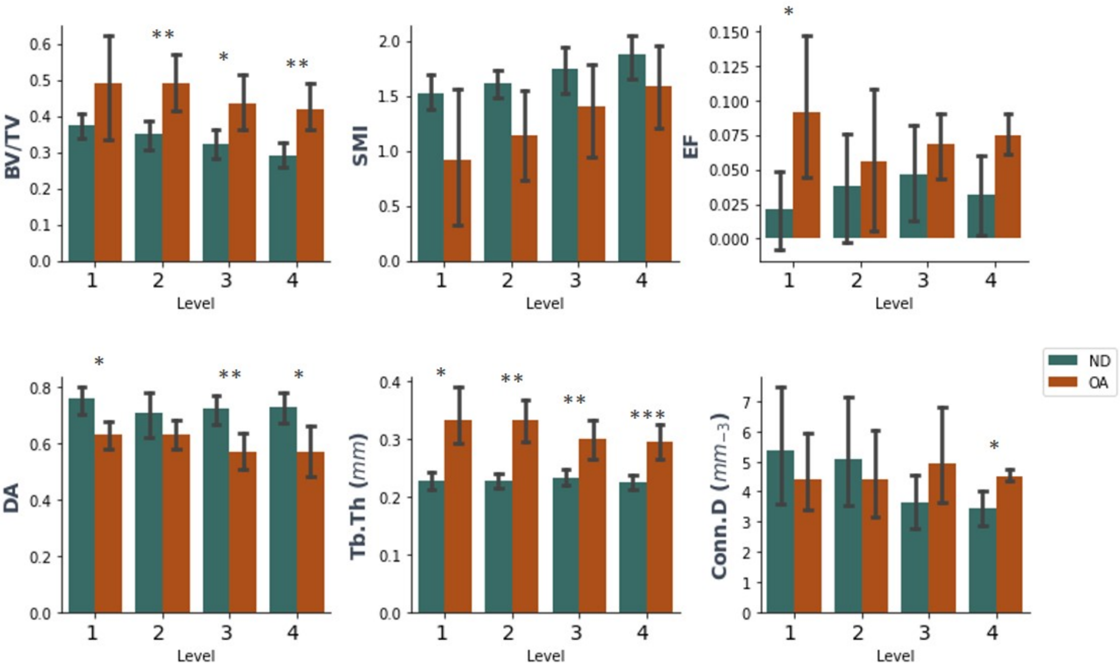

Figure 4.7: Comparison of standard morphological properties for OA and ND specimens at each depth level.The bar plots represent the mean (bars) and ± SD (error bars) of values for OA specimens (N=5) and ND specimens (N=10). Levels of significance indicated using: * p<0.05, ** p<0.01, *** p<0.001, ns= no significance.

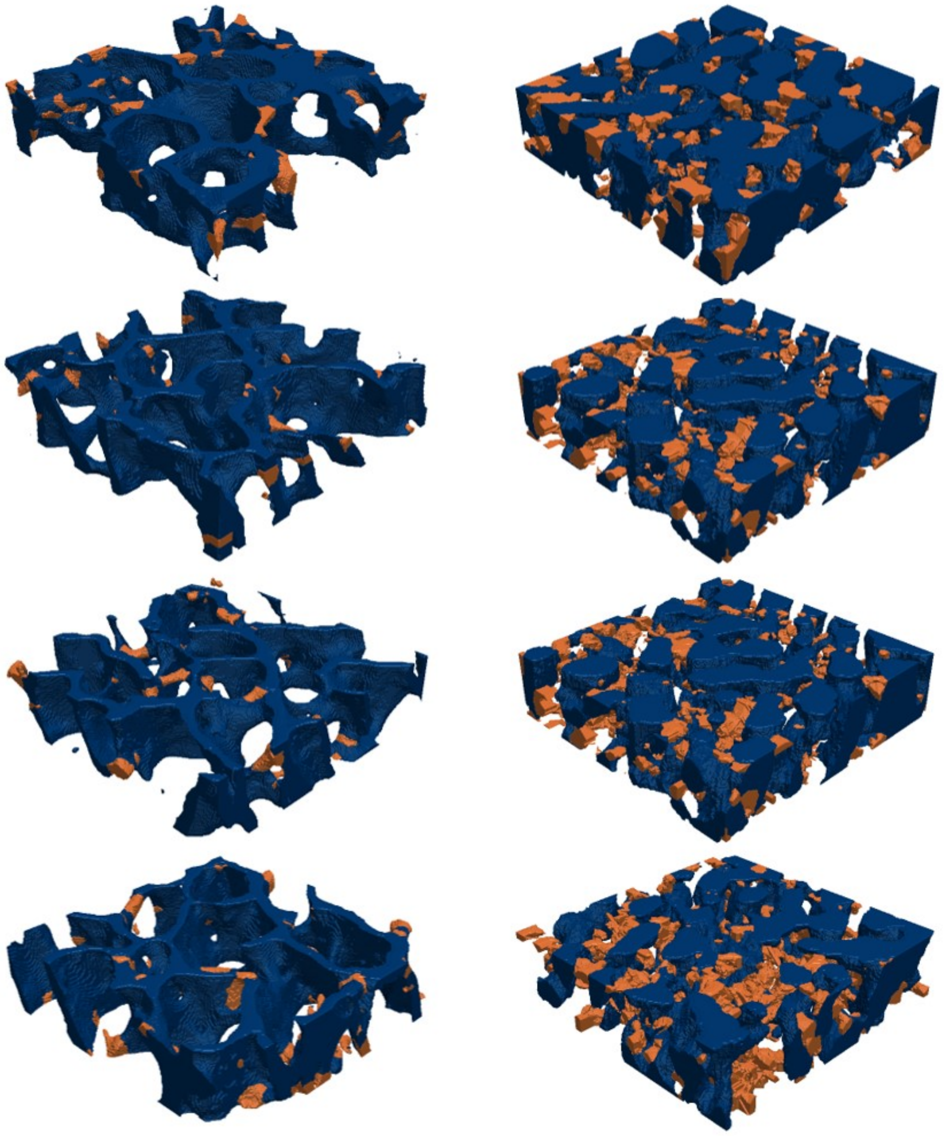

Figure 4.8: Visualisation of variation to rod-like (orange) and plate-like (navy) trabeculae with increasing depth (top to bottom) in exemplary ND (left) and OA (right) specimen.

The ITS-based morphological analysis highlights more detailed trends compared to the standard morphological analysis (Fig. 4.8). Generally there was a downward trend in pBV/TV with depth in both the ND and OA groups, which lowers between Level 1 and 4 in the ND group ($p<0.05$) (Fig. 4.9). However, between the ND and OA groups there was significantly higher pBV/TV on Levels 2 ($p<0.01$), 3 ($p<0.05$) and 4 ($p<0.05$) (Fig. 4.10). Additionally, there was significantly higher number of plates, pTb.N on Level 4 ($p<0.05$) in the OA group. rBV/TV values appear to increase at all levels with OA ($p<0.05$ on Level 2, $p<0.01$ on Level 3 and $p<0.05$ on Level 4), but with no significant differences between each level. Similarly, higher rod density (rTb.N) was found with OA in lower levels: 2 ($p<0.05$), 3 ($p<0.05$) and 4 ($p<0.001$).

Figure 4.9: Comparison of AVG (bars) ± SD (error bars) 3D ITS-based morphological properties with increasing depth from the SBP for tibial specimens from OA (purple) and ND (green). Levels of significance indicated using: * p<0.05, ** p<0.01, *** p<0.001.

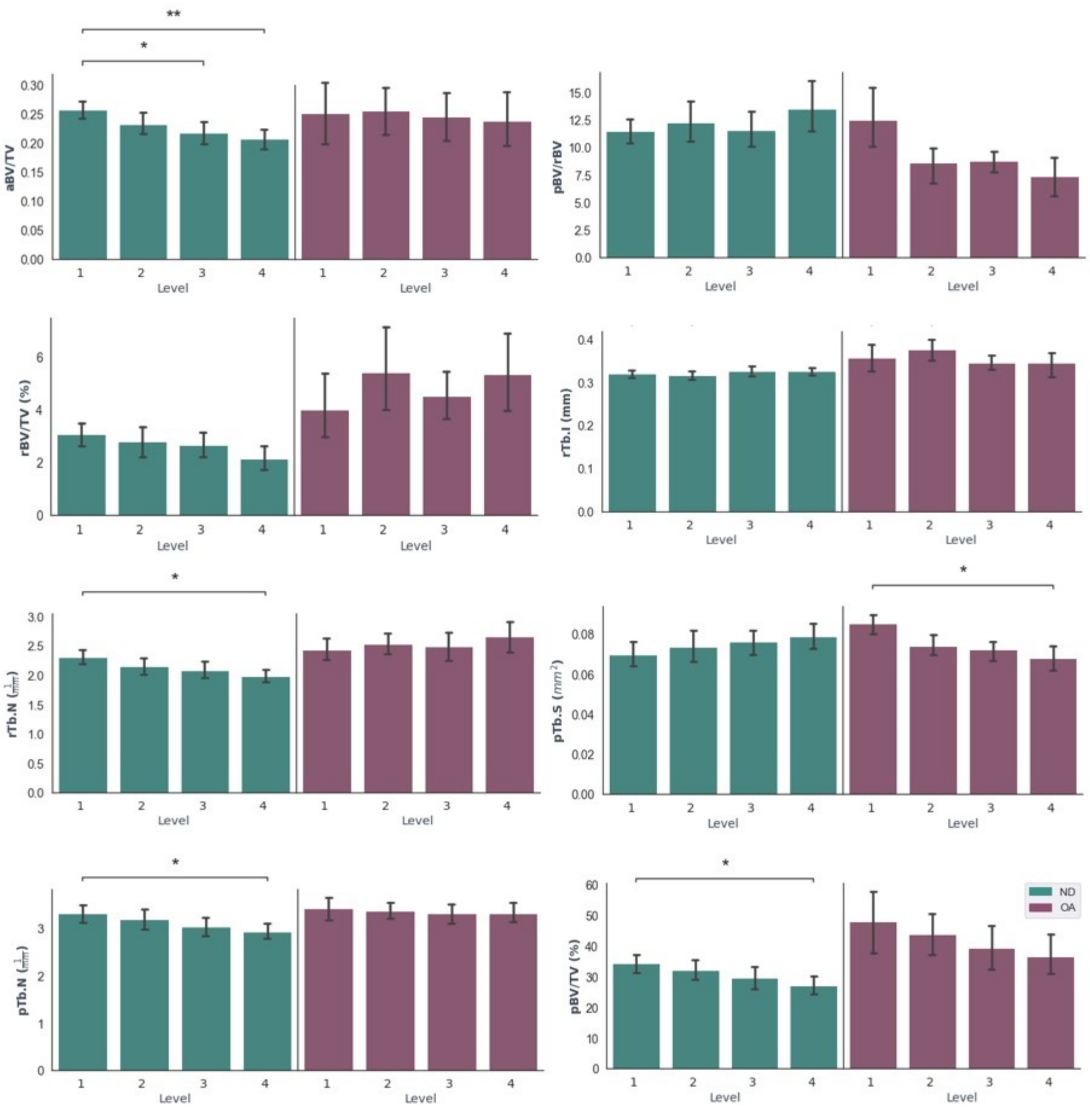

There was a significant difference in aBV/TV between Level 1 and 3 (p<0.01) and Level 1 to 4 (p<0.05) for ND specimens, indicating increasing trabecular alignment with increasing height (Fig. 4.9). With OA however, there is higher trabecular alignment in the lower levels resulting in a similar value of aBV/TV with depth.

Whilst both pTb.Th and rTb.Th were not sensitive to depth, the trends observed for pTb.S show a reversal in the OA group with significantly higher plate surface area towards the SBP (p<0.05) and a loss of plates in Level 4 (Fig. 4.10). Plate surface area, pTb.S, was much higher in Level 1 of OA samples compared to controls (p<0.01). Additionally, Level 2 of OA specimens featured elongated rod-like trabeculae (rTb.l) compared to controls (p<0.001).

Higher RR Junc.D, PR Junc.D and PP Junc.D were observed in Level 1 compared to Level 4 for ND specimens ($p<0.05$). However, in the OA group, RR Junc.D was higher with depth, and both PR Junc.D and PP Junc.D were of similar value across all levels. However, when comparing between groups, PR Junc.D was significantly higher in the OA specimens compared to ND specimens in lower levels (Fig. 4.10).

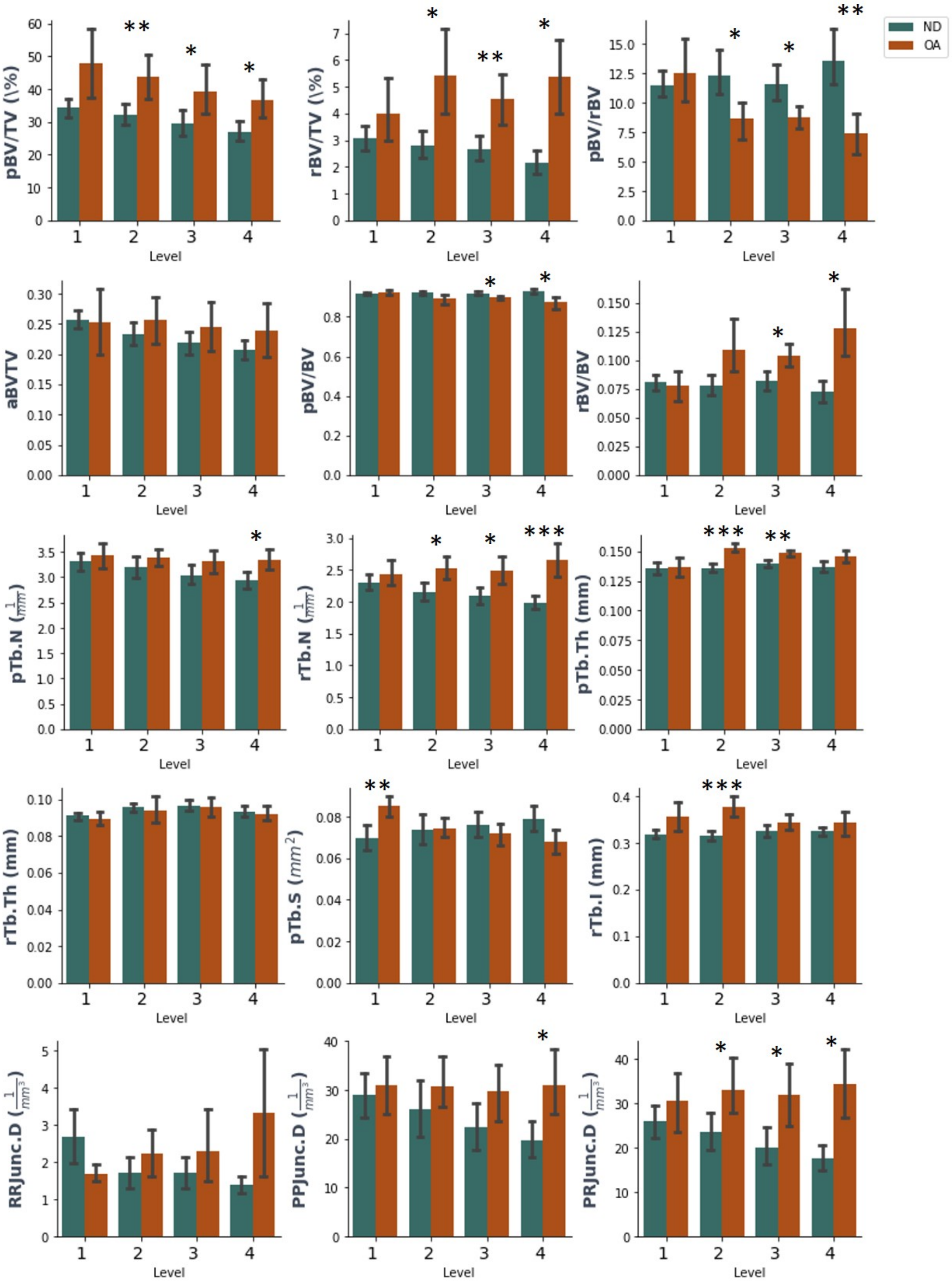

Figure 4.10: The bar plots represent the mean (bar) and ± SD (error bars) of values for OA specimens (N=5) and ND specimens (N=10). Levels of significance indicated using: * $p<0.05$, ** $p<0.01$, *** $p<0.001$, ns= no significance.

4.4 Discussion

This study evaluated changes to ankle subchondral bone microarchitecture with osteoarthritis using standard and ITS-based characterisation. In doing so, this provides an insight to the bone remodelling that occurs with the progression of OA in the ankle and its potential impact on bone quality. Furthermore, an analysis of morphological properties with increasing depth from the SBP was performed to identify properties sensitivity to depth. Due to lack of viable OA talar samples, specimens from the distal tibia were used for comparison.

In this study, significant increases to BV/TV ($p<0.01$) and Tb.Th ($p<0.001$) were observed in the OA group compared to controls. This observation agrees with other studies that describe higher bone density and trabecular thickness with OA progression in the knee [Kamibayashi et al., 1995b, Bobinac et al., 2003, Cox et al., 2013, Finnilä et al., 2017, Chen et al., 2018, Gatenholm et al., 2019] and the hip [Fazzalari and Parkinson, 1997, Li and Aspden, 1997a]. It is thought that this occurs as a result of accelerated bone remodelling, resulting in higher apparent bone density to counteract increased loads occurring due to the deterioration of articular cartilage [Burr and Gallant, 2012]. It was expected that BV/TV would be significantly higher in OA specimens than ND with depth from the SBP, as observed in the OA knee [Dequeker et al., 1995, Beuf et al., 2002, Patel et al., 2003]. However, the results here show BV/TV increasing with OA at each level, but was no longer significantly different with increased distance in the OA group (Fig. 4.6). Similar ankle studies evaluating change in morphological properties with depth have also observed no significant changes in bone density when analysing μCT images of ND and OA subchondral trabecular bone [Jones et al., 2020]. However, histological analyses showed significantly higher bone density ($p<0.01$) in the first 1 mm and between 1-3 mm of late-stage OA tibial bone compared to mild-OA specimens.

Trabecular orientation is known to be an important factor in determining mechanical stiffness [Goulet et al., 1994, Matsuura et al., 2008]. The results in this work show significant lower DA for OA specimens ($p<0.05$). Studies evaluating mild OA in the knee have observed similar reductions to DA and Conn.D, though non-significant [Ding et al., 2003]. This suggests that the trabeculae are remodelling to become more isotropic, which may be directed towards the joint surface in response to altered loads. This was observed in one study characterising late-stage OA in the proximal tibia [Kamibayashi et al., 1995a]. Higher trabecular bone volume fraction to the longitudinal axis, aBV/TV, in OA samples reinforces this idea, but was found to be non-significant (Fig. 4.5). Similarly, no significant alterations in aBV/TV are observed with depth in the OA group, but significantly higher aBV/TV was observed in the upper levels of ND specimens. The limited sample size of this work may limit the significance observed in these results; a larger dataset could help to identify specific levels of interest where remodelling activity is most pronounced.

A higher mean EF value was observed in the OA group compared to controls ($p<0.05$), indicating increased presence of rod-like trabeculae in OA bone (Table 4.1, Fig. 4.4ii). Contrastingly, there was a non-significant reduction in SMI value, indicating a more plate-like trabeculae in the OA group. However, SMI does not account for concave surfaces - as featured heavily in trabecular bone- and hence there is a shift towards the use of alternative measures, such as the EF [Doube, 2015, Salmon et al., 2015]. Though doing so limits the comparisons available to studies that have utilised SMI. Previous studies have observed more plate-like trabeculae present in both early [Ding et al., 2003] and late-stage [Chen et al., 2018] OA bone. The results of this study however, show higher plate and rod volume fractions (pBV/TV, $p<0.05$ & rBV/TV, $p<0.001$), with higher rBV/BV and lower pBV/BV in the OA groups compared to controls (both $p<0.001$). Both pBV/TV and rBV/TV significantly lower with OA on Levels 2, 3 and 4, but the results show particularly high rBV/TV values for Levels 2 ($p<0.01$) and 4 ($p<0.001$), suggesting unusual remodelling activity at these depths.

An overall plate thickening (pTb.Th; $p<0.05$), higher rod density (rTb.N; $p<0.001$) and rod length (rTb.l; $p<0.01$) was observed in OA specimens. pTb.S was found to be depth-sensitive in the OA group; pTb.S was higher in Level 1 compared to Level 4 ($p<0.05$) and was significantly higher in OA bone in Level 1 (Fig. 4.9). Larger plate thickness and surface area (pTb.Th and pTb.S) suggest an overall thickening of plate-like trabeculae to potentially reinforce their load-bearing capacity [Chen et al., 2018], particularly in the upper levels nearest the SBP where cartilage loss could be increasing the loads experienced in the bone. The presence of more rod-like trabeculae however, may lead to lower mechanical stiffness [Ding et al., 2002a]. A similar study utilising the same 3D ITS software also found plate thickening, but also a loss of rod-like trabeculae in their OA knee samples [Chen et al., 2018]. However, this study was analysing much larger volumes (8 mm cuboidal volumes) from across the lateral and medial condyles. Results from one study using smaller cylindrical volumes (5.4 mm ⌀ and height) compared primary-OA bone to ND controls from the hip. They showed higher plate and rod Tb.N, but lower plate and rod Tb.Th, pTb.S and rTb.l [He et al., 2020]. It is therefore difficult to draw comparisons to other lower-limb joints, due to variations in sample size and geometry, but also due to the differences in joint biomechanics which may alter OA progression.

The results of this study suggest an overall trabecular "sclerosis". Near the surface, trabecular plates thicken and increase in number, whereas lower levels have more, longer rod-like trabeculae. Higher numbers of rod-like trabeculae is typically associated with advancing age [Ding and Hvid, 2000]. However, the donors and patients used in this study are relatively young. Altered joint biomechanics with late-stage OA may have resulted in an abnormal biomechanical environment, which can affect bone remodelling behaviour according to Wolff's Law [Teichtahl et al., 2015]. However, it is not clear whether this newly deposited bone is sufficient to withstand these loads is governed by changes in tissue-level mechanical properties and mineralisation. Apparent increases to bone density (BV/TV), despite radiographic sclerosis, is thought to result from rapid deposition of hypomineralised bone, which will affect tissue mechanical properties leading to alterations in apparent bone stiffness [Grynpas et al., 1991, Burr and Gallant, 2012]. Conversely, higher apparent density could be in response to reduced tissue mineralisation [Cox et al., 2012, Li and Aspden, 1997a].

The differences in sample size, location and even the type of OA present (ankle OA is predominantly post-traumatic, though this cannot be confirmed for the specimens used in this study) will affect the strength of the conclusions drawn from these results. As mentioned previously, it is also difficult to draw comparisons to the few lower-limb studies available in the literature, to begin to understand the impact of OA on ankle subchondral bone. Furthermore, unlike other lower-limb joints, it is challenging to source donor-matched or age-matched OA and ND ankle samples. Moreover, it was difficult to correspond the state of the cartilage in the OA samples (Appendix C, Section C.2.2), as the specimens were taken from multiple locations during the cutting processes used in the TAA surgery. Therefore the samples may not necessarily display fully degraded cartilage, as they may not have been removed from the primary loading zone. Hence, there is unavoidable regional variation in the OA sample group, which somewhat limits the comparisons to the ND control specimens, since they were retrieved from the main articulating region of the tibial plafond. Future studies could look to analyse cartilage thickness and correlate these to changes in trabecular bone morphology. Numerous software exist to characterise microarchitecture, and hence there are obvious limitations in comparisons made to other studies that utilise different software. Future studies could look to compare the results obtained from different analysis software, such as ScanCo's Image Processing Language (IPL).

To conclude, this study has demonstrated changes to subchondral trabecular bone in the ankle with late-stage OA, such as higher BV/TV and Tb.Th. Significant alterations to trabecular morphology were observed as a result of accelerated remodelling, where some properties were depth-dependent. In this way, the response of subchondral trabecular bone with the progression of osteoarthritis can be speculated and relationships to biomechanical properties inferred.

Chapter Summary

- Standard morphological analysis revealed OA bone was denser and contained thicker trabeculae compared to ND controls, as reported for other lower-limb joints.
- Mean EF value was higher with OA, indicating increased presence of rod-like trabeculae in OA bone. However, further ITS analysis showed significantly higher plate and rod density with OA.
- Trabeculae were more isotropic (lower DA) and better aligned to the joint surface in OA samples (higher aBV/TV)
- With OA, plate-like trabeculae were thicker and had larger surface area, particularly near the bone plate. Rod-like trabeculae were longer and had increased connectivity (rod-rod junctions).
- Trabecular density, orientation and plate/rod morphology are properties of significance when evaluating the effect of remodelling on bone stiffness with OA.
- The upper regions of subchondral bone, beneath the bone plate, are of particular interest, as depth-based analysis reveals trabeculae in this region appear to adapt the most to alterations in the biomechanical environment resulting from degenerated cartilage.

CHAPTER 5

DEVELOPMENT OF INVERSE FE METHODOLOGY

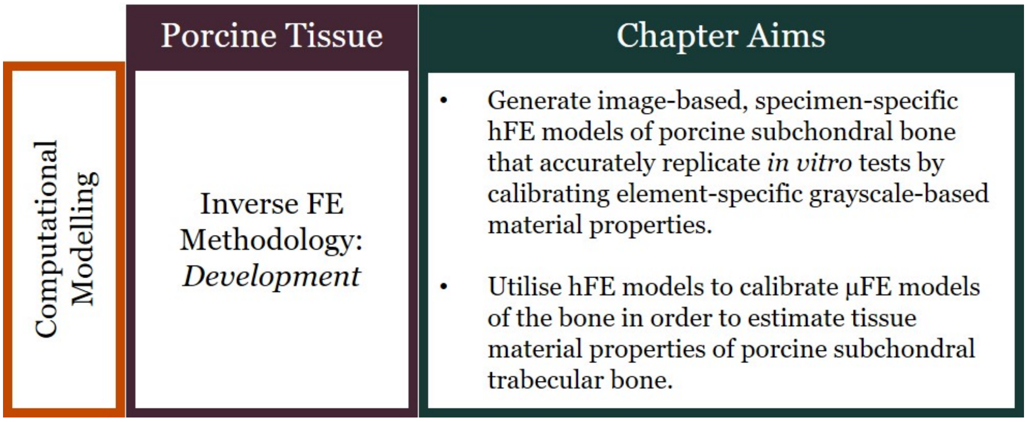

Computational Modelling

Porcine Tissue

Inverse FE Methodology: *Development*

Chapter Aims

- Generate image-based, specimen-specific hFE models of porcine subchondral bone that accurately replicate *in vitro* tests by calibrating element-specific grayscale-based material properties.
- Utilise hFE models to calibrate µFE models of the bone in order to estimate tissue material properties of porcine subchondral trabecular bone.

As discussed in Chapter 1 an inverse FE approach can be used to estimate tissue material properties of subchondral trabecular bone. This chapter explores the development of this using porcine ankle tissue. The success of this developed methodology was evaluated in Chapter 6 and further translated for use on human tissue in Chapter 7.

5.1 Introduction

Verification, validation and sensitivity testing are significant steps in the generation of reliable finite element (FE) models that best replicate the experiment *in silico* [Mengoni et al., 2016]. In particular, the influence of boundary conditions and mesh properties on the model output of interest (stiffness) should be explored and variables altered to balance computational cost and accuracy. The numerical accuracy, and hence "verification" aspect, of the FE models used throughout this thesis is met through the use of commercially-available software (Abaqus CAE).

5.1.1 Study Aims

- Develop image-based, specimen-specific hFE models of porcine subchondral bone with greyscale-based material properties.
- Utilise hFE models to develop calibrated μFE models of bone to estimate tissue material properties.
- Understand the sensitivity of both hFE and μFE models to key variables.

5.2 Specimen Preparation

The FE methodology was developed using porcine ankle subchondral bone specimens. Cylindrical trabecular bone cores (N=15, 6 mm ⌀) were extracted from fresh-frozen tali of juvenile porcine ankles (as detailed in Section 3.1.1). Specimens were trimmed to below the subchondral bone plate and rinsed using PBS. Each specimen was fixed into Delrin endcaps using a thin layer of PMMA cement. Mechanical stiffness was obtained using the protocol outlined in Section 3.5.1. Four specimens were excluded from the results due to displacement during mechanical testing. A further specimen was removed due to evidence of damage prior to testing. A total of ten specimens were available for analysis. Prior to mechanical testing, each bone core was imaged at an isotropic resolution of 0.016 mm using μCT (Section 3.2.1). The image data was converted from .ISQ file format to .TIFF and normalised to 0-255 grayscale (8 bit) to provide a more manageable number of material properties.

5.3 Resources

Supplementary information regarding the software and scripts used in the following section are listed in Appendix A. All models were generated using a custom-written Python script within Simpleware ScanIP software (*Synopsys*) to remove user variation and increase reproducibility. All hFE analyses were quasi-static and performed within Abaqus CAE (*Dassault Systemes*). The Opti4Abq toolbox [Mengoni et al., 2015] was developed by Dr Mengoni and used in the hFE model material property optimisation process. All μFE analyses were quasi-static and performed in Abaqus CAE using local high-performance computing facilities (*ARC3, High Performance Computing facilities, University of Leeds*). Geometric non-linearity was accounted for using the "NLGEOM" option within Abaqus.

5.4 Finite Element Methodology Development

Sensitivity tests were performed on a representative specimen to evaluate the sensitivity of outputs to different modelling properties and setup.

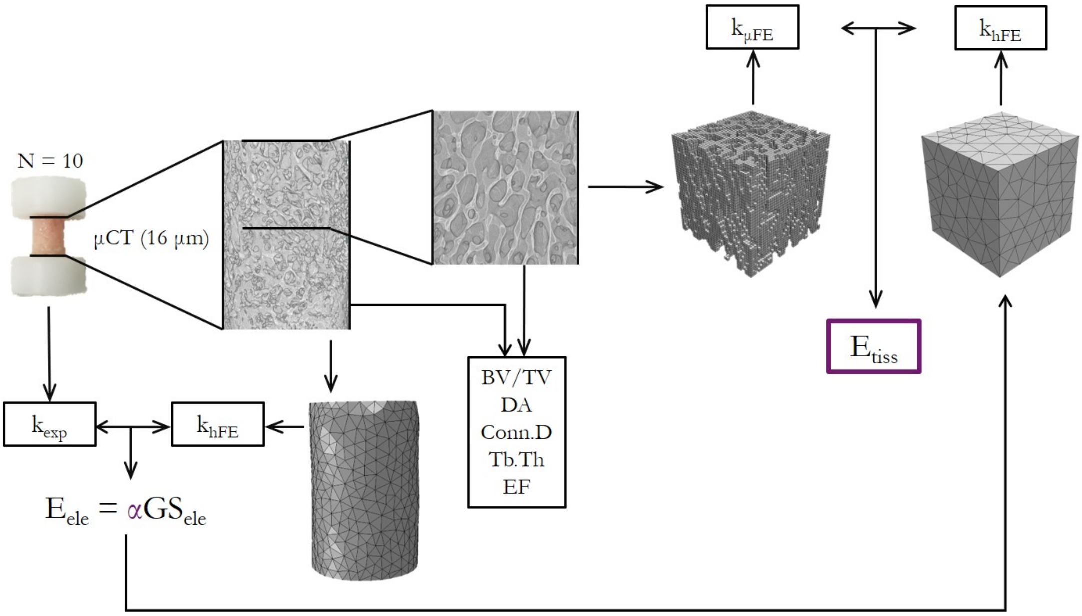

Figure 5.1: Inverse FE methodology to establish tissue mechanical properties from validated, continuum models with calibrated element-specific material properties based on element image grayscale.

A multiscale, computational approach was developed in order to characterise subchondral trabecular bone at the tissue level by means of back-calculating tissue properties from validated, continuum FE (hFE) models (Fig. 5.1).

Element-specific, grayscale-based material properties were chosen to capture bone heterogeneity through variation of bone density by mapping image data to material properties properties. A linear relationship can be used to map CT grayscale to material elasticity [Wijayathunga et al., 2008], provided the relationship is calibrated for the anatomical site, experimental conditions and image settings. In this way, a simple, calibrated linear relationship and a standardised modelling methodology can be used to develop models and test similar tissue in a controlled way.

Element-specific elastic modulus (E_{ele}) was defined dependent on the average element grayscale (GS_{ele}) using Equation 5.1:

$$E_{ele} = \alpha\ GS_{ele}(MPa) \tag{5.1}$$

The scaling factor, α, is determined by comparing computational and experimental data.

5.4.1 Sensitivity Analysis: hFE Mesh

A sensitivity test was performed to evaluate the effect of varying element size on output stiffness, as varying element size also varies the proportion of bone represented in each element and as such, the material properties of each element.

The μCT image stack of an exemplary specimen was downsampled to an isotropic resolution of 0.32 mm taking into account partial volume effects to avoid harsh boundaries/step changes in bone and marrow. The bone cylinder was segmented using thresholding and morphological operations. The mesh (tetrahedral elements) density was altered by varying the target edge length within ScanIP: 0.5, 0.75, 1.0, 1.5, 2.0, 2.5 and 3.0 mm. Element-specific, grayscale-based material properties were used without optimisation (*E*=*GS*). The model was imported into Abaqus CAE and subjected to uniaxial compression on the top cylinder face (u_x = 0, u_y= 0, u_z= -0.3 mm) with a fully constrained bottom surface.

5.4.1.a Results

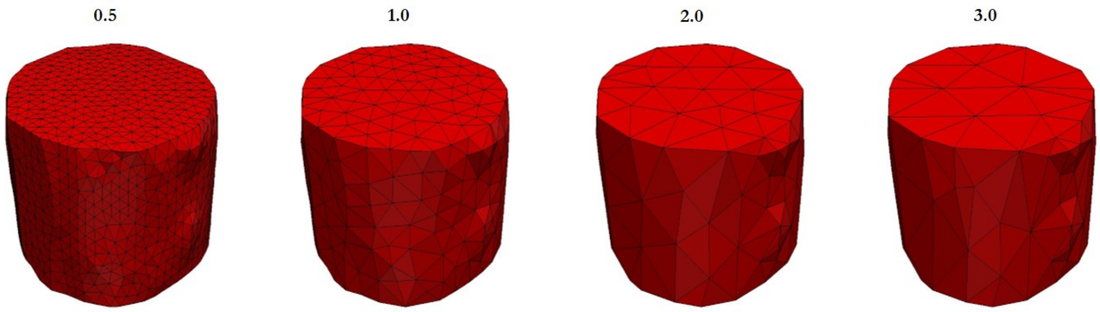

Figure 5.2: Visualisation of varying target mesh element number for target edge lengths: 0.5, 1.0, 2.0 and 3.0 mm.

A select few mesh volumes are shown in Fig. 5.2 and demonstrate the differences in element size and element number for the exemplary specimen. The results showed that lowering target edge length decreased apparent stiffness (Fig. 5.3).

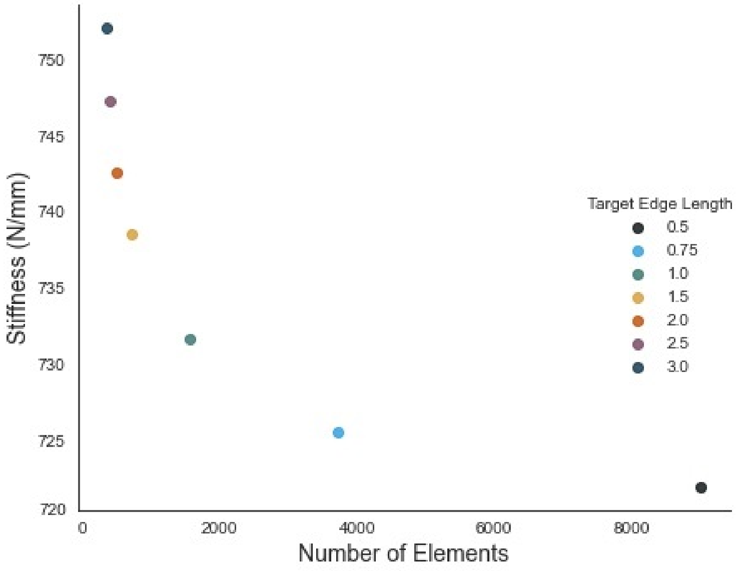

Figure 5.3: The effect of varying tetrahedral element edge length (mm) on hFE stiffness output.

5.4.1.b Discussion

A target size of 1 mm tetrahedral elements were selected, as these elements were sufficiently large to cover multiple trabeculae with minor impact on the value of stiffness compared to the next highest target edge length, and acceptable run times. An average of 2-3 trabeculae would be present per (1 mm) element. A downsampled resolution of 0.32mm (approximately 2x average Tb.Th) was used to avoid harsh boundaries between bone and marrow. However this downsampling of the scans prior to meshing likely sacrificed trabecular detail. Future studies could investigate the magnitude of the difference in results that this would cause. The ScanIP software presents a potential limitation to the mesh size accuracy, as the user can only input a desired minimum and maximum edge length. This may result in some unavoidable variation to element size, particularly at corners or edges.

Outcome: Target 1 mm edge length elements were used in the generation of hFE models.

5.4.2 Sensitivity Analysis: hFE Boundary Conditions

A computational model aims to fully replicate the conditions present *in vitro* by including all boundary conditions influencing the test specimen. However, different levels of complexity can be explored when setting up a model. The use of bone-only models may help create more idealised boundaries. Therefore for one specimen, the effects of varied boundary conditions were explored by developing two models: one including the bone and PMMA cement & Delrin endcaps (model a), and one with only the bone included (model b).

The image stack of a specimen was imported into ScanIP and downsampled to 0.32 mm with partial volume effects. For model "a", the endcaps, PMMA cement and bone were segmented as separate masks. All three materials were meshed using 1 mm tetrahedral elements. For both cases, the bone was assigned element-specific, grayscale-based bone material properties without optimisation (E=GS). Homogeneous material properties were set to 756 MPa (ν = 0.35) and 2.45 GPa (ν = 0.3) for the Delrin endcaps and the PMMA cement, respectively. Once imported into Abaqus CAE, tied constraints were used to connect the bone to the cement and the cement to the Delrin. Coupling constraints were used to tie the surface nodes of the endcaps to a central node at each end, onto which the uniaxial compression was applied (top: u_z=-0.3 mm, bottom: pinned).

The gauge length for the bone-only model (model "b") was defined as the length of bone between the endcaps. The full specimen was not modelled, as cement was found to ingress into the trabecular pores at each end of the bone. This altered the apparent bone density in the CT image of those areas. Hence, 1mm of bone was cropped at each end of the specimen before the model was generated. The model was setup the same as model "a", with the coupling constraints applied to the end surfaces of the bone.

5.4.2.a Results

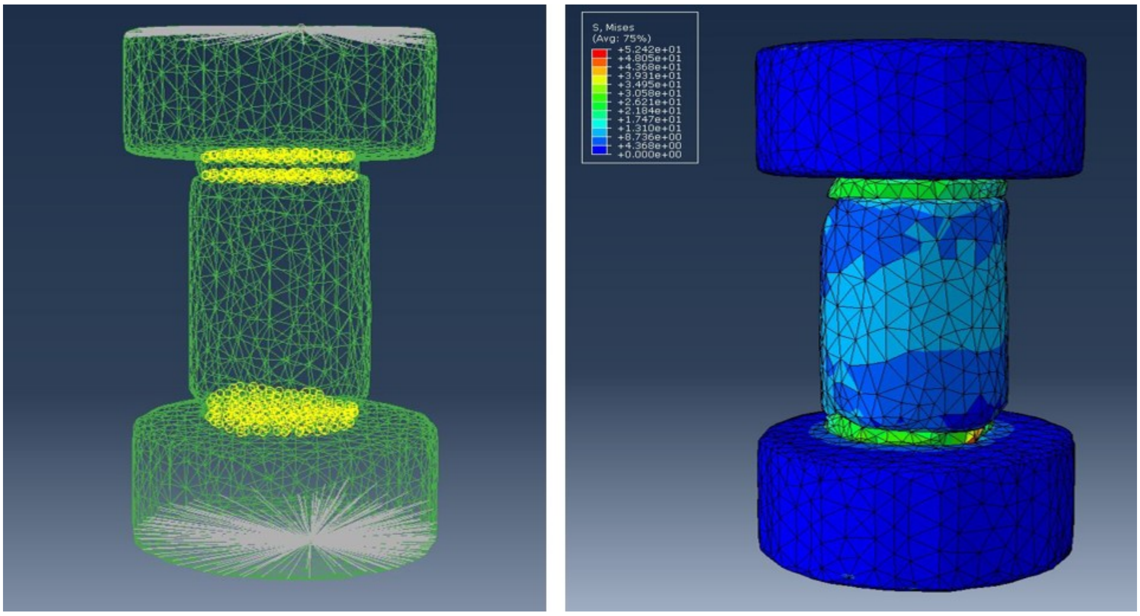

Figure 5.4: Bone-cement-Delrin exemplary volume depicting the model interactions (left) and results following compression (right).

The bone-cement-Delrin and gauge-length, bone-only models had stiffness values of 105.09 and 731.65 N/mm, respectively. The bone-cement-Delrin model (Fig. 5.4) resulted in high stress concentrations within the cement layer and subsequently, a very low stiffness output, which had not converged. The stiffness value was therefore calculated using the amount of displacement achieved.

5.4.2.b Discussion

Segmenting the cement accurately and in a reproducible manner was challenging, as it was not clearly visible on the scans, likely due to its small volume and similar opacity to bone. It was estimated that approximately 0.5 mm of cement was used to secure the bone into the Delrin endcaps (3.8 mm height). However, such a small volume of cement was difficult to mesh effectively, resulting in distorted elements that caused errors in the model which did not converge (Fig. 5.4).

Modelling the bone only was deemed more realistic and more reproducible. This model simplification has been found to produce minor errors in other studies [Bevill et al., 2009, Wolfram et al., 2010]. However, this was deemed more reproducible across all specimens.

Outcome: Simplified hFE models were generated using solely the gauge length of the bone core.

5.4.3 hFE Material Properties

Two methods are commonly employed to relate an elastic modulus (E) to image data (grayscale) [Mengoni et al., 2016]. A visual comparison of the two methodologies can be seen in Fig.5.5. The top row, the "grayscale (GS) method", shows the original μCT image data of an exemplary bone core imported into ScanIP (a); downsampled to an isotropic resolution of 0.1 mm (b). The bottom row depicts the "BV/TV methododology", where a pre-segmented binarised stack is imported to ScanIP (d) and downsampled, showing improved trabecular definition compared to the GS method.

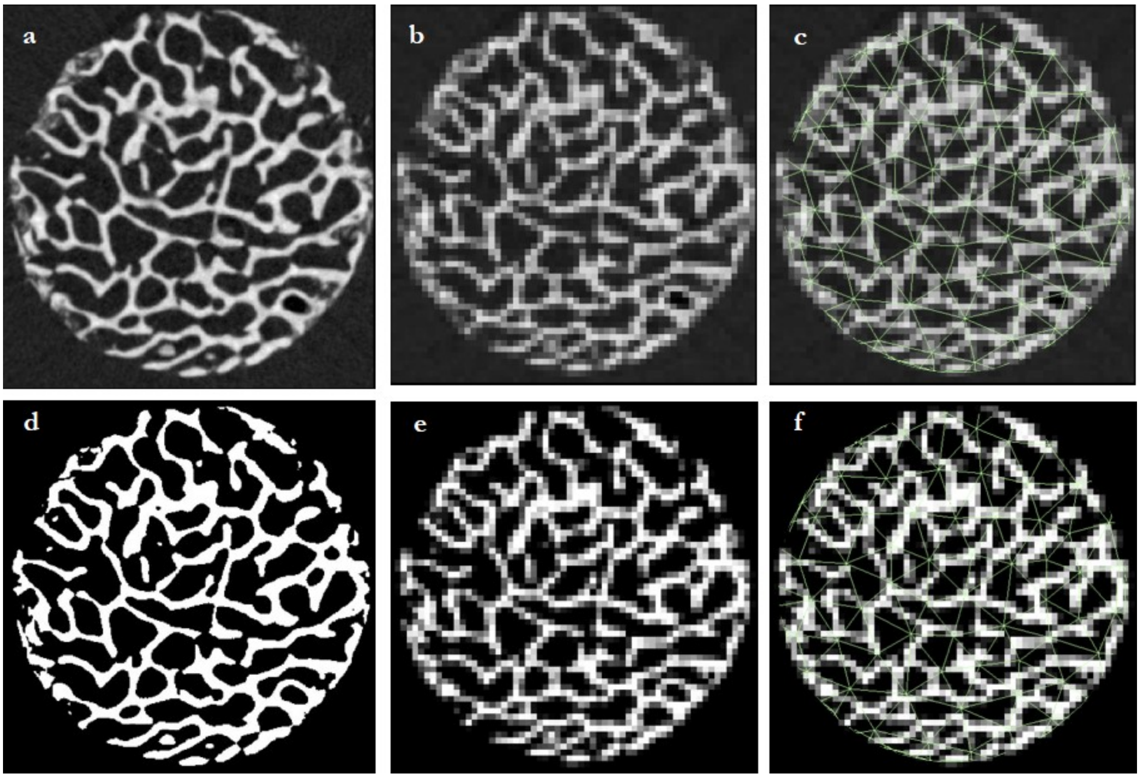

Figure 5.5: Comparison of the direct-grayscale (GS) method (*top row*, a-c) and the volume fraction (BV/TV) method (*bottom row*, d-f). The BV/TV method utilises pre-segmented image (d) to improve trabecular definition after downsampling, compared to the GS method (c) which uses the CT image stack directly. Both images are downsampled to 0.1 mm isotropic resolution in this example (b & e) from 0.016mm isotropic resolution (a & d). Images c & f add a mesh overlay to images b & e, showing the trabeculae covered by a 1mm target elements in ScanIP.

Image data was binarised within ImageJ using Otsu thresholding. Binarised (BV/TV) and grayscale image stacks were downsampled to an isotropic resolution of 0.32 mm taking into account partial volume effects within ScanIP. The bone cylinder was segmented using thresholding and morphological operations. The cylinder was meshed using target 1 mm edge tetrahedral elements, with element-specific, grayscale-based material properties without optimisation (E=GS). The model was imported into Abaqus CAE and subjected to uniaxial compression on the top cylinder face (u_x = 0, u_y= 0, u_z= -0.3 mm) with a full constrained bottom surface.

5.4.3.a Results

The agreement between computational and experimental value was slightly improved with the BV/TV method compared to the GS-based method (Fig. 5.6).

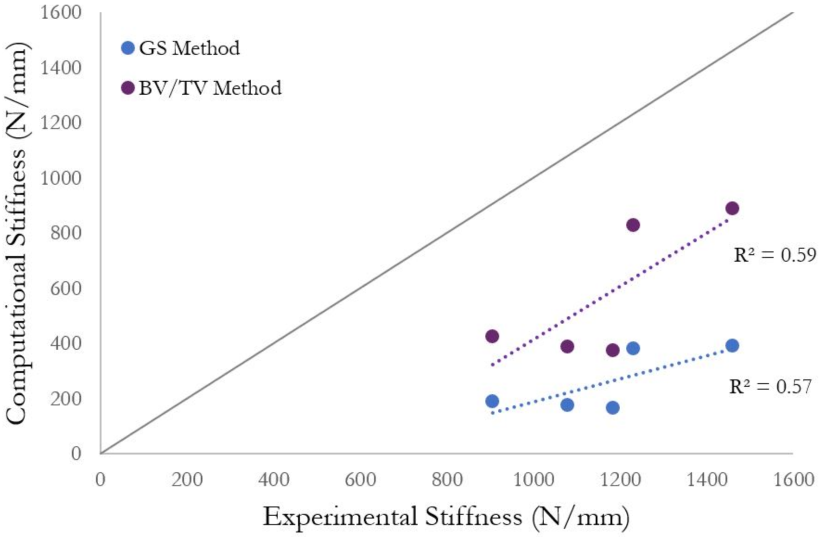

Figure 5.6: Five exemplary specimens comparing the "GS" and "BV/TV" methods by resulting agreement between experimental and computational stiffness values.

5.4.3.b Discussion

Upon closer inspection, the BV/TV method improves the definition of the trabeculae (Fig.5.5 c vs. f) and so this may indicate a more accurate replication of the experiment. In this case, each the voxel grayscale is proportional to the voxel BV/TV value. The use of the BV/TV method is favourable, as it allows the use of images from any μCT scanner providing that the same thresholding techniques are used to binarise the images. The BV/TV method had resulted in slightly lower errors between model and experiment for many studies [Day et al., 2020, Robson Brown et al., 2014, Wijayathunga et al., 2008, Tarsuslugil et al., 2013]. These studies predominantly focus on whole bone FE where the BV/TV methodology allows better representation of the cortical shell. However, the conclusions of sensitivity studies are difficult to translate, as relationships between E and GS are optimised for specific image settings, material properties and boundary conditions.

Outcome: the BV/TV methodology was implemented in subsequent hFE model generation.

5.4.4 Optimisation

To derive the linear proportionality constant, α, for this particular type of bone and with this given testing and imaging conditions [Zapata-Cornelio et al., 2017], a golden section search scalar optimisation process using Brent's method [Brent, 1971] was used. Specimens were randomly divided into two groups: calibration and validation. Optimisation of the root mean square (RMS) normalised difference between *in vitro* (k_{exp}) and *in silico* stiffness ($k_{hFE,cyl}$) values was performed on the calibration group using the Opti4Abq toolbox [Mengoni et al., 2015, Mengoni, 2015] using Brent's method implemented in SciPy (Python 2.7, *www.python.org*) (Fig. 5.7). Convergence was set at RMSE <10%.

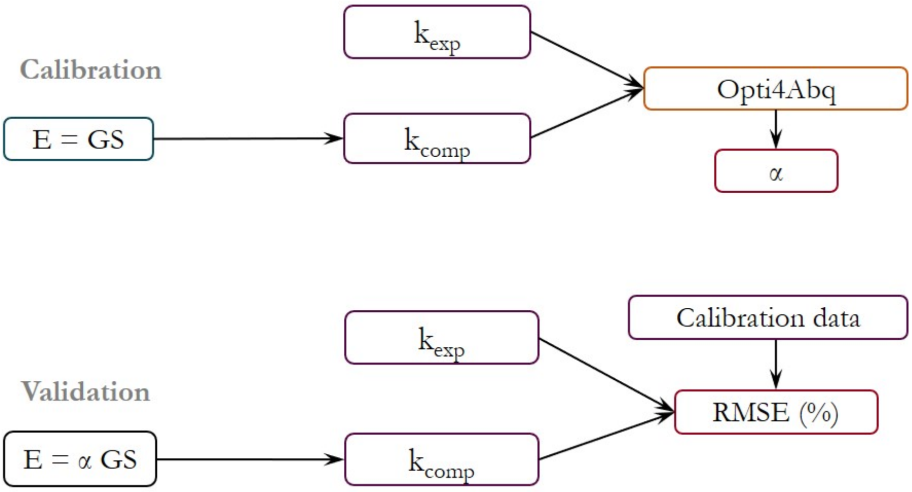

Figure 5.7: Optimisation methodology used to minimise the difference between k_{exp} and k_{comp} ($k_{hFE,cyl}$) for (N=5) calibration specimens to produce scaling factor, α, between element GS and E. This value is used to scale the material properties of (N=5) validation specimens. The success of each calibration and validation process is quantified using RMS error (RMSE, %).

5.4.5 Sensitivity Analysis: μFE Mesh

A sensitivity analysis was conducted in which the mesh resolution was altered from the native resolution (16 μm) to 32, 48, 64 and 100 μm isotropic resolutions. μFE voxel-based models were generated using 4 mm cuboids for the same specimen within ScanIP using the 1x1x1 FE grid algorithm, with material properties set as E=500 MPa and ν = 0.3. The output stiffness was measured by simulating a linear axial -0.1 mm displacement within Abaqus (ARC3; 8 cores 16 GB memory) with all other faces constrained.

5.4.5.a Results

The results are presented in Table 5.1. The 100 μm and 64 μm models were completed in under 1 min and 3 mins, respectively. The 48 μm models took 20 minutes to run, whereas the 32 μm models required larger memory (ARC3 high memory nodes; 64GB per core) and still only completed 66% of the step, i.e. the model did not converge.

Table 5.1: μFE mesh resolution sensitivity test results.

	100 μm	64 μm	48 μm	32 μm
$\bar{k}_{\mu FE}$ (N/mm)	698.165	552.433	488.594	-

5.4.5.b Discussion

Table 5.1 shows a convergence pattern, where model resolution changes were relatively large. There was a trend implying that the if the element size continued to be reduced, the change in stiffness would be very small. It was much more difficult to set up the 48 and 32 μm resolution models, due to difficulties selecting the surface node sets from which to apply the boundary conditions within Abaqus. These two model resolutions also resulted in more element distortion and the 32 μm models in particular were highly computationally expensive, requiring dedicated high memory nodes compared to the lower resolution models which used the standard HPC nodes. The results here oppose those observed in Niebur et al.'s study, which showed decreasing apparent modulus with decreasing resolution in two human and two bovine samples downsampled to similar intervals [Niebur et al., 1999]. However, it is hard to compare as pilot data for the optimisation of tissue modulus using the 100 μm models had the lowest errors and high agreement compared to lower resolutions (CCC=0.80). Though this is not the optimal resolution, it is the most practical for this work. However, by selecting the 100 μm case, a significant mesh-based error must be acknowledged. For the purposes of this work, a resolution of 100 μm was chosen for ease of setup and low computational cost, but the agreement with hFE models may be arbitrary.

Outcome: 100 μm mesh resolution was chosen for μFE models.

5.5 Model Generation: Summary

The final model generation methodology for hFE and μFE models based on the sensitivity tests described above are summarised in this section.

5.5.1 hFE Models

Specimen-specific, homogenised (continuum-level) finite element (hFE) models were setup by first downsampling the binarised image stacks to an isotropic resolution of 0.32 mm whilst taking into account partial volume effects (*Simpleware ScanIP*). The bone was segmented to capture the trabeculae and morphological operations used to remove internal voids and fully segment the volume. The segmented bone cylinder was then meshed with linear tetrahedral elements of approximate 1 mm length (average number of elements=2992). The bone was modelled as linear elastic with a Poisson's ratio, ν, of 0.3 and a grayscale-dependent elastic modulus. This was calibrated using the optimisation toolbox, Opti4Abq, as described earlier.

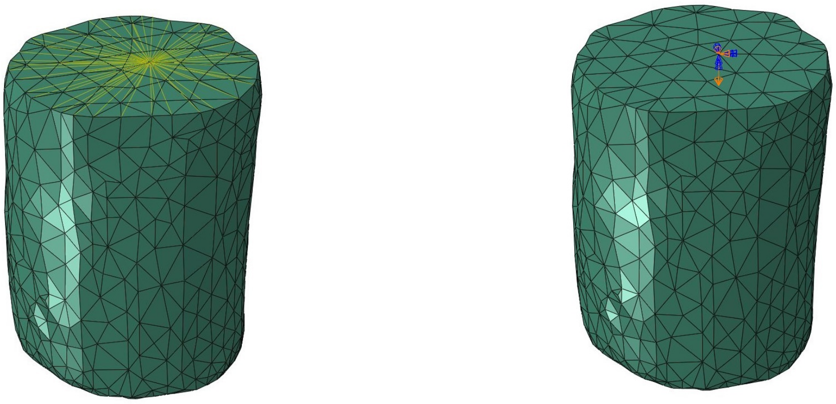

(i) Coupling constraint between master node and surface nodes. **(ii)** Displacement boundary condition applied to master node.

Figure 5.8: hFE model setup highlighting the coupling constraints (5.8i) from which displacements were applied (5.8ii).

Uniaxial compression was simulated *in silico* with simplified boundary conditions. Coupling constraints were used at each end of the bone to tie all surface nodes to a central node onto which the boundary conditions were applied (Fig. 5.8i). All degrees of freedom were constrained on the bottom surface and an axial displacement was applied to the top surface (Fig. 5.8ii) with all other degrees of freedom constrained (u_x = 0, u_y= 0, u_z= -0.3 mm). However, one limitation is that it was possible for the nodes towards both ends of the bone to expand due to Poisson's effect. This would not occur *in vitro* due to the use of cement and endcaps.

5.5.2 μFE Models

To compromise on computational cost, cubic volumes (4 mm length) were extracted from the centre of pre-segmented, binarised image stacks of each specimen. Trabecular-level (μFE) models were setup by first downsampling the image stack to an isotropic resolution of 0.1 mm with partial volume effects (*Simpleware ScanIP*). The bone was masked and each voxel was converted to a mix of tetrahedral and hexahedral elements (average number of elements = 35,965) using the FE grid algorithm set to 1 x 1 x 1 mm grid size within ScanIP.

Material properties were set to E = 1 MPa and ν = 0.3, as these would be calibrated against their corresponding cuboid hFE models (Fig. 5.9), which were built using the previously defined protocol (Section 5.5.1) with calibrated grayscale-based material properties.

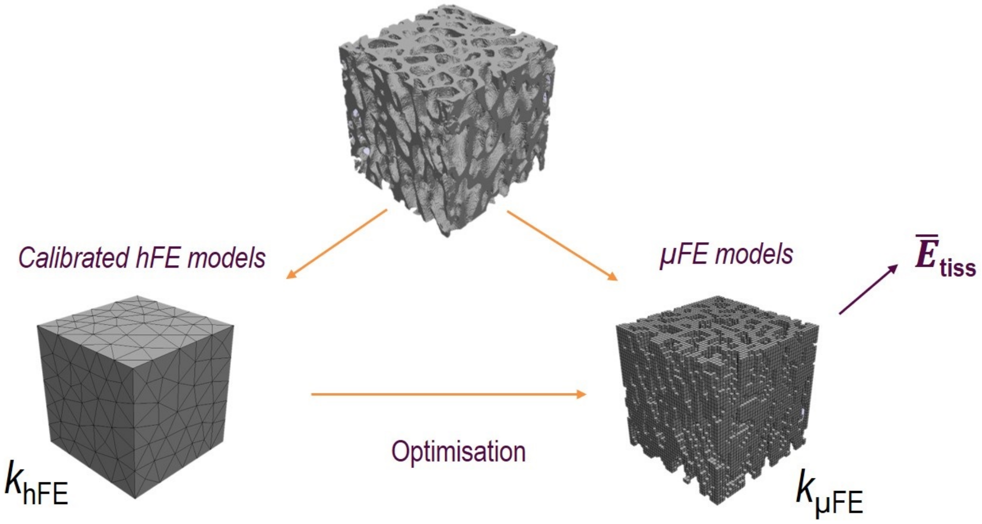

Figure 5.9: Methdology used to calibrated (tissue) material properties of μFE models using calibrated hFE models to within ± 1% by calculating an $\overline{E}_{tiss}$ using five calibration specimens.

The models were setup similarly to those previously described with an axial displacement applied to the top surface node. Five specimens were using to calibrate tissue elastic modulus through comparison of output stiffness to within ±1 % ($k_{hFE,cube}$). This yielded an average tissue modulus, $\overline{E}_{tiss}$, which was validated on a further five specimens. An average stiffness, $\overline{k}_{\mu FE}$, from all optimised models (E = $\overline{E}_{tiss}$) was established.

Chapter Summary

- Various sensitivity tests were conducted to optimise an inverse FE methodology for ankle subchondral bone, the results of which are reported in Chapter 6.

CHAPTER 6

ESTIMATING TISSUE-LEVEL PROPERTIES OF PORCINE TALAR SUBCHONDRAL BONE

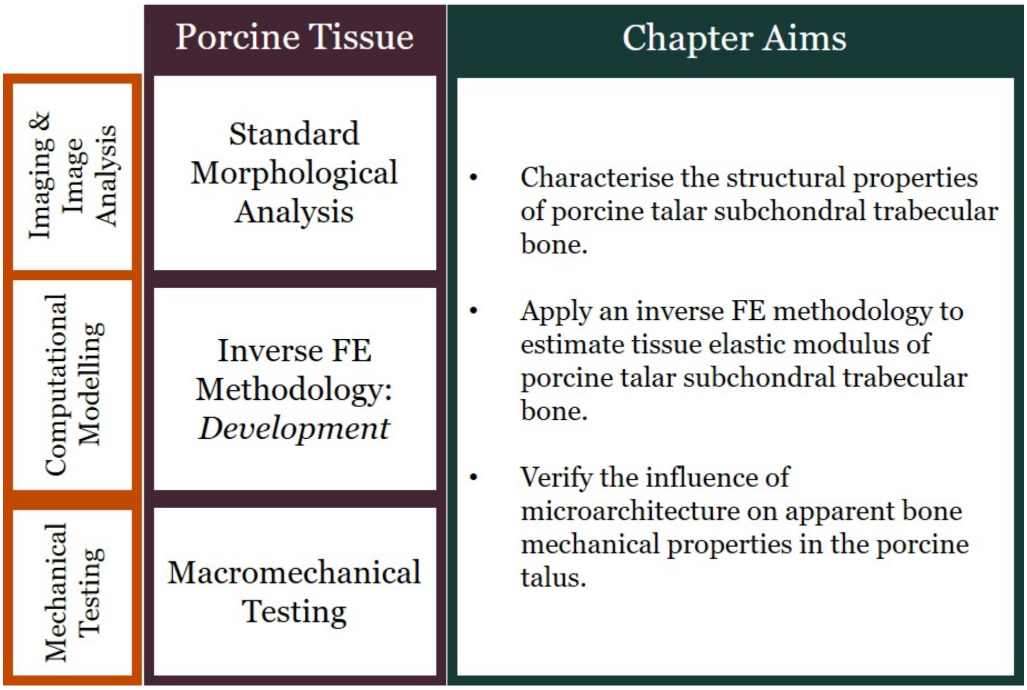

- Characterise the structural properties of porcine talar subchondral trabecular bone.
- Apply an inverse FE methodology to estimate tissue elastic modulus of porcine talar subchondral trabecular bone.
- Verify the influence of microarchitecture on apparent bone mechanical properties in the porcine talus.

This chapter reports the outcomes of the developed inverse FE methodology (Chapter 5) using subchondral bone cores retrieved from porcine tali. Porcine tissue is plentiful compared to human tissue and the porcine ankle is geometrically similar to humans making it ideal for this pilot study. The structural properties of the bone were also characterised and their impact on mechanical properties explored. This work has allowed for the translation of the methods to human tissue, reported in the following chapter. Parts of this chapter were published in [Koria et al., 2020].

6.1 Introduction

Computational models evaluating bone tissue mechanical properties can be used to circumvent somewhat difficult experiments that require measuring the mechanical properties of individual trabeculae. Using an inverse finite element (FE) approach it is possible to calibrate the stiffness of *in silico* models using macroscopic mechanical tests to indirectly estimate tissue properties [van Rietbergen et al., 1995, Bayraktar et al., 2004, Bevill et al., 2009, Marlène, 2020]. In doing so, this also allows for the development of a calibrated material model that relates image grayscale and stiffness, thus providing a means by which to map mechanical properties using medical image data alone. To date, the characterisation of tissue-level mechanical properties of subchondral bone in the ankle have not been investigated.

6.1.1 Study Aims

The aim of this study was to develop an inverse FE methodology to estimate tissue modulus of subchondral trabecular bone cores using image-based, specimen-specific FE models and macroscopic mechanical testing. The following study objectives were defined:

- Characterise the structural properties of porcine subchondral trabecular bone.
- Apply an inverse FE methodology to estimate tissue elastic modulus of porcine talar subchondral trabecular bone.
- Verify the influence of microarchitecture on apparent bone mechanical properties in the porcine talus.

6.2 Materials and Methods

Cylindrical trabecular bone cores (6 mm ⌀) were extracted from fresh-frozen tali of juvenile porcine ankles (as detailed in Chapter 3, Section 3.1.1). Specimens were trimmed to below the subchondral bone plate and rinsed using PBS. Each specimen was fixed into Delrin endcaps using a thin layer of PMMA cement. All specimens (N=15) were imaged using the protocol defined in Section 3.2.1.

6.2.1 Mechanical Testing

Uniaxial compression was used to characterise the stiffness of each specimen (Section 3.5.1). In brief, each specimen was pre-loaded with 0.3 N whilst submerged in PBS under physiological conditions within an Instron materials testing rig. After ten minutes, thirty pre-conditioning cycles were applied (0.006% s^{-1}), followed by a quasi-static load (0.01% s^{-1}) to failure. Stiffness, k_{exp}, was quantified using the slope of the force-(crosshead) displacement curve. Four specimens were excluded from results as they had displaced during mechanical testing. A further specimen was removed from the final dataset due to damage prior to testing. A total of ten specimens were available for analysis.

6.2.2 Inverse FE Methodology

A multiscale, computational approach was developed in order to characterise subchondral trabecular bone at the tissue level by means of back-calculating tissue properties from validated, continuum FE (hFE) models (Chapter 5).

In brief, μCT-based hFE models (N=10) were created for each specimen using the method outlined in Section 5.5.1. Each segmented bone cylinder was meshed with linear tetrahedral elements of approximate 1 mm edge-length (average number of elements = 2407). Grayscale-dependent material properties were calibrated using the Opti4Abq optimisation toolbox (Section 5.4). Specimens were randomly divided into two groups: calibration (N = 5) and validation (N = 5). Optimisation of the root mean square (RMS) normalised difference between in vitro (k_{exp}) and *in silico* stiffness values was performed on the calibration group with a convergence <10%. The models (N=5) were validated by scaling the material-properties using α and comparing the output stiffness ($k_{hFE,cyl}$) to k_{exp}. The experimental unconfined uniaxial compression was simulated in silico. All degrees of freedom were constrained on the bottom surface and an axial displacement of - 0.3 mm in compression was applied to the top surface with all other degrees of freedom constrained

μFE models were setup as per Section 5.5.2 for 4 mm cuboidal volumes (N=10) from the proximal end of the specimens (average number of elements = 35,965). hFE models of the same cuboids (N = 10) were formed according to the previously defined protocol using validated grayscale-based material properties. Five specimens were used to calibrate tissue elastic modulus through direct comparison of output stiffness to within ± 1% ($k_{hFE,cube}$). This yielded an average tissue modulus, E_{tiss}, which was validated on a further five specimens. An average stiffness, $k_{\mu FE}$, was established from all calibrated models (N = 10) using E_{tiss}. All FE analyses were quasi-static and performed in Abaqus using local high-performance computing facilities (ARC3).

6.2.3 Image Analysis

Image analysis was undertaken as described in Section 3.4. Each image stack was cropped to the gauge length height and binarised using Otsu thresholding (*ImageJ*). Standard morphological properties were obtained for each specimen

(BV/TV, DA, Conn.D and Tb.Th) using BoneJ, as well as EF for each cuboidal volume. The influence between each morphological property and mechanical properties were also explored in this study.

6.2.4 Statistical Analysis

The mean, standard deviation and coefficient of variance (CoV, %) for mechanical (experimental and computational) and morphological properties was calculated for all specimens. Correlation between: k_{exp} and $k_{hFE,cyl}$; $k_{\mu FE}$ and $k_{hFE,cube}$ and all stiffness values to morphological properties were measured using Square of the Pearson Product-Moment Correlation Coefficient (r^2). Agreement between k_{exp} and $k_{hFE,cyl}$, and $k_{\mu FE}$ and $k_{hFE,cube}$ were evaluated using Concordance Correlation Coefficient (CCC) values and Bland-Altman analyses.

6.3 Results

6.3.1 Experimental Results

Average stiffness *in vitro*, $\bar{k}_{exp}$, was 1140.67 ± 207 N/mm, as derived from the linear elastic portion of the force-displacement plot (Fig. 6.1).

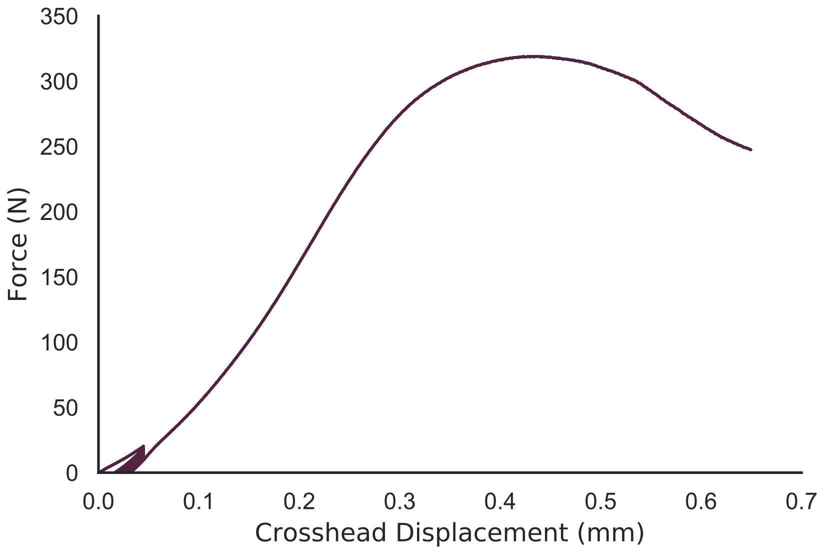

Figure 6.1: Exemplary plot of force-displacement for porcine talar subchondral trabecular bone specimen under uniaxial compression.

6.3.2 Microarchitecture results

For the full cylindrical models, morphological analyses showed that DA (CoV = 18%) and Conn.D (CoV = 24%) had the highest intra-specimen variations. Average values for BV/TV, DA, Tb.Th and Conn.D were: 0.37 ± 0.03, 0.59 ± 0.11, 0.16

± 0.02 mm and 6.79 ± 1.62 mm^{-3}, respectively.

For cuboidal specimens, high intra-specimen variations were observed to DA (CoV=16%) and Conn.D (CoV=22%). Average values for BV/TV, DA, Tb.Th, Conn.D and EF were 0.37 ± 0.05, 0.68 ± 0.11, 0.16 ± 0.019 mm, 16.81 ± 3.75 mm^{-3} and 0.009 ± 0.05, respectively. EF results indicate that the tissue is a mix of rod-like and plate-like trabeculae.

6.3.3 Apparent Level Model Calibration and Validation

A 69% correlation was found between *in silico* and *in vitro* stiffness values in cylinders (N=10, Fig. 6.2) and showed good agreement (CCC=0.66, Fig.6.3). The optimisation procedure terminated prior to the set convergence tolerance with a converged value of α rather than a converged RMSE; calibration and validation RMSE were 26% and 17%, respectively. Average apparent stiffness, $\overline{k}_{hFE,cyl}$, was 1066.42 ± 392 N/mm (CoV = 37%) (Fig. 6.4).

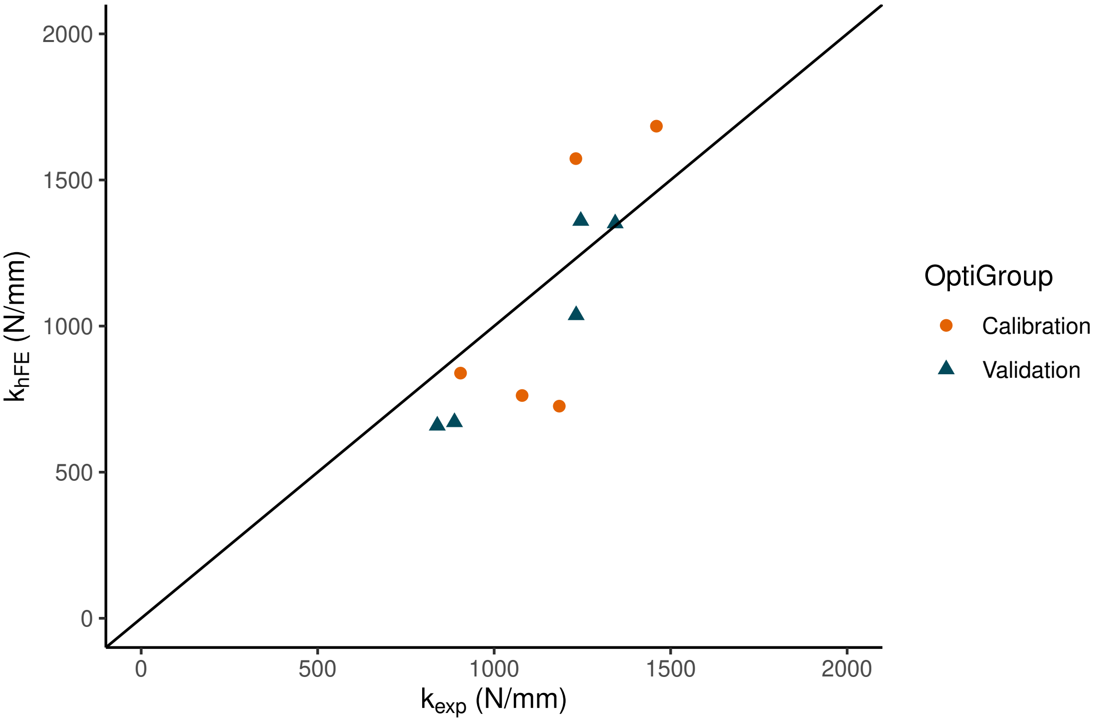

Figure 6.2: Correlation of experimental stiffness to computational (hFE) model stiffness (r^2=0.69). The straight line (x=y) indicates perfect correlation.

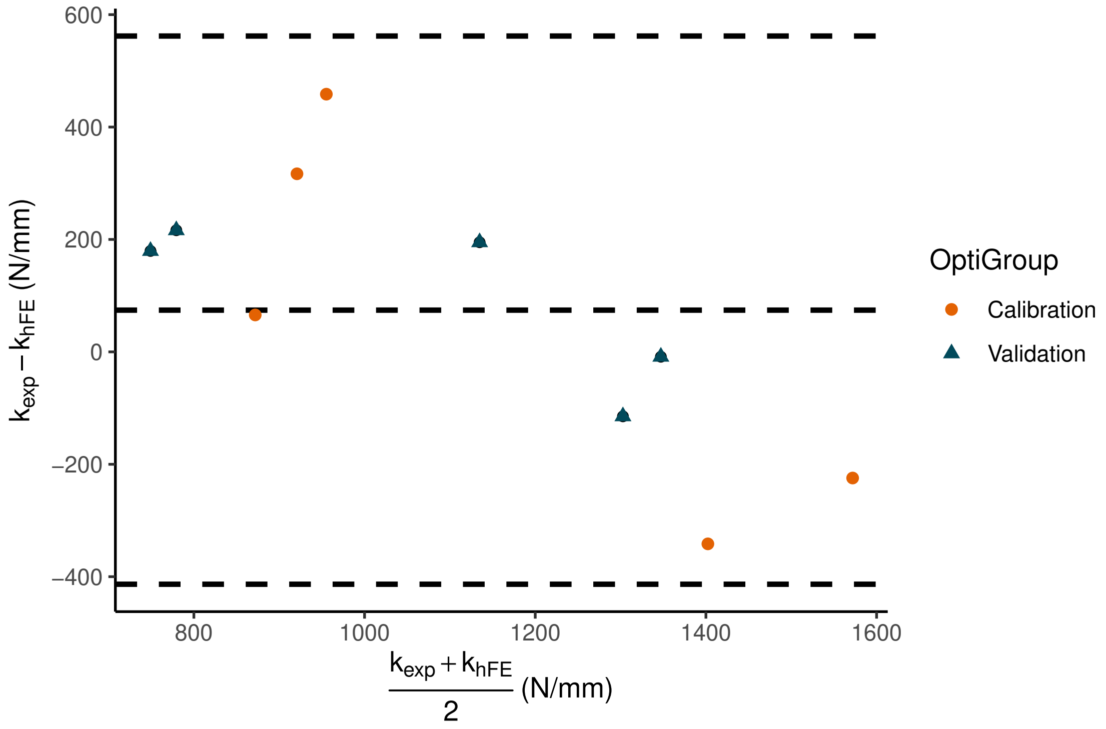

Figure 6.3: Bland-Altman plot showing agreement of experimental stiffness to computational (hFE) model stiffness (CCC=0.66).The dashed lines indicate the mean and ± 1.96 SD.

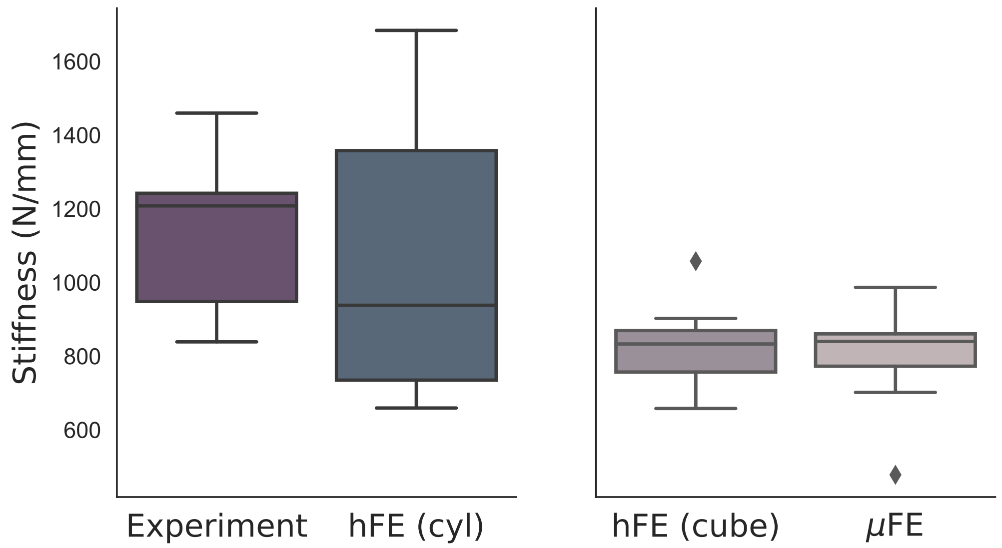

Figure 6.4: Experimental and computational stiffness values (N=10, N/mm) for porcine ankle subchondral bone. Boxplots indicate median and interquartile range of values. A ♦ indicates outliers (specifically, one k_{hFE} calibration specimen and one $k_{\mu FE}$ validation specimen, though not the same specimen).

6.3.4 Trabecular Level Model Calibration and Validation

Good correlation (r^2=0.69) was observed between the hFE and μFE stiffness values in cuboids (Fig. 6.5). The optimisation process for each of the calibration samples converged with an RMSE of 7%. Good agreement was observed for validation specimens (N=5, CCC = 0.75) and optimised specimens (N=10, CCC = 0.80). Fig. 6.6 highlights an outlier validation specimen which lies outside of the limits of agreement, which is reflected in the higher RMSE for the validation set (13%) compared to the calibration set (7%).

Average $\overline{E}_{tiss}$ (N=5) was 504.00 MPa ± 37.65 (CoV= 7%).

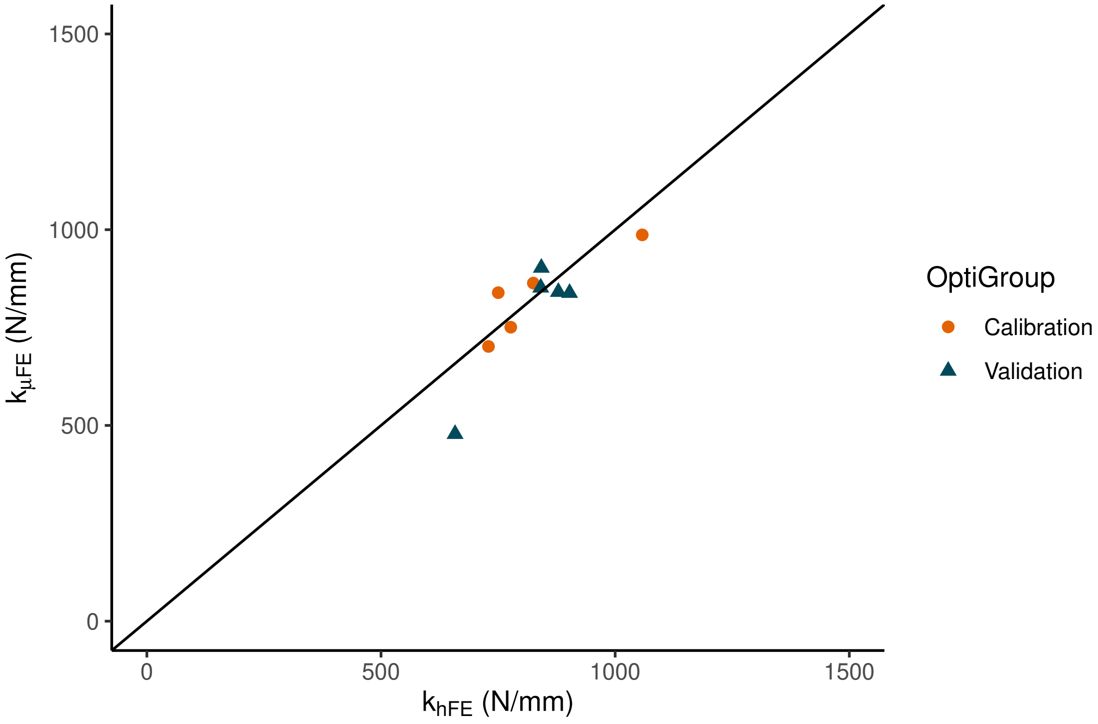

Figure 6.5: Correlation of continuum stiffness to trabecular level stiffness (r^2=0.69). The straight line (x=y) indicates perfect correlation.

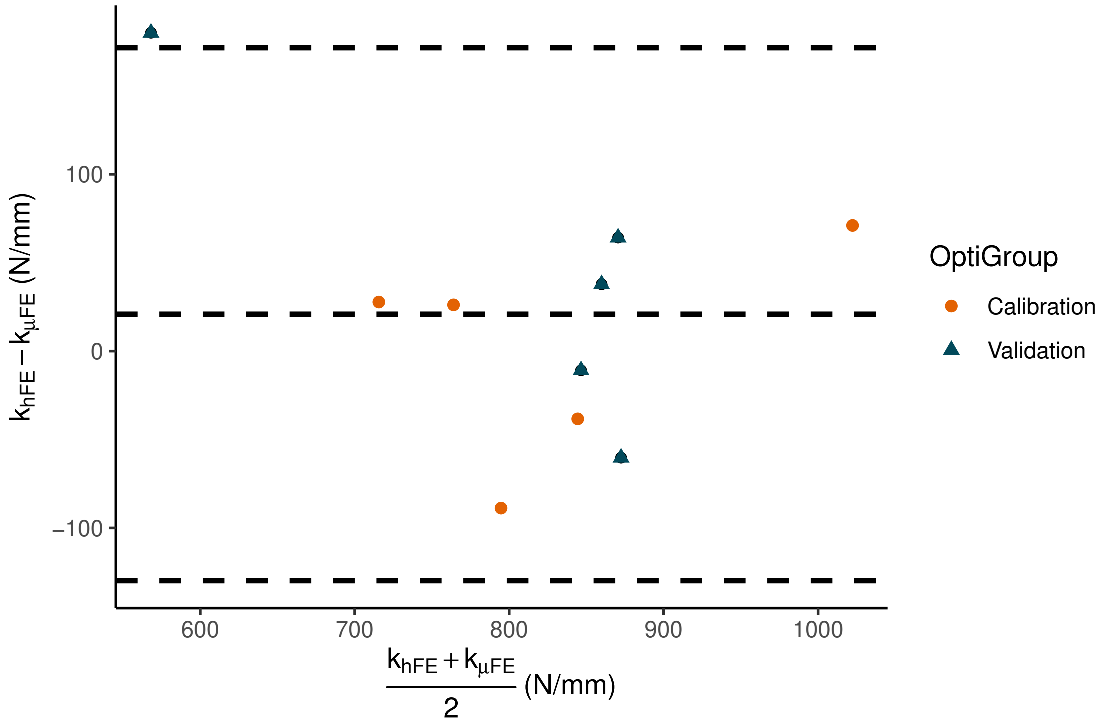

Figure 6.6: Bland-Altman plot showing agreement of continuum stiffness to trabecular-level stiffness (CCC=0.80). The dashed lines indicate the mean and ± 1.96 SD.

6.3.5 Correlations to Microarchitecture

The highest correlations to stiffness was between BV/TV and both k_{exp} ($r^2 = 0.48$) and $k_{\mu FE}$ ($r^2 = 0.67$) (Table 6.1). Correlations between k_{exp} and Conn.D (r = -0.34), and $k_{\mu FE}$ and EF (r = -0.62) were both negative.

At the apparent level, both BV/TV and DA account for around 85% of variations to *in silico* stiffness and 60% for *in vitro* stiffness (Fig. 6.7). At the trabecular level they account for 80% variations to μFE stiffness.

Table 6.1: Square of the Pearson Product-Moment Correlation Coefficient (r^2) of microarchitectural properties against apparent-level stiffness values. Colour scale (red to green) indicates increasing correlation.

	k_{exp}	k_{hFE}	$k_{\mu FE}$
BV/TV	0.48	0.21	0.67
DA	0.24	0.27	0.23
Conn.D	0.12	0.01	0.01
Tb.Th	0.20	0.01	0.07
EF	-	-	0.38

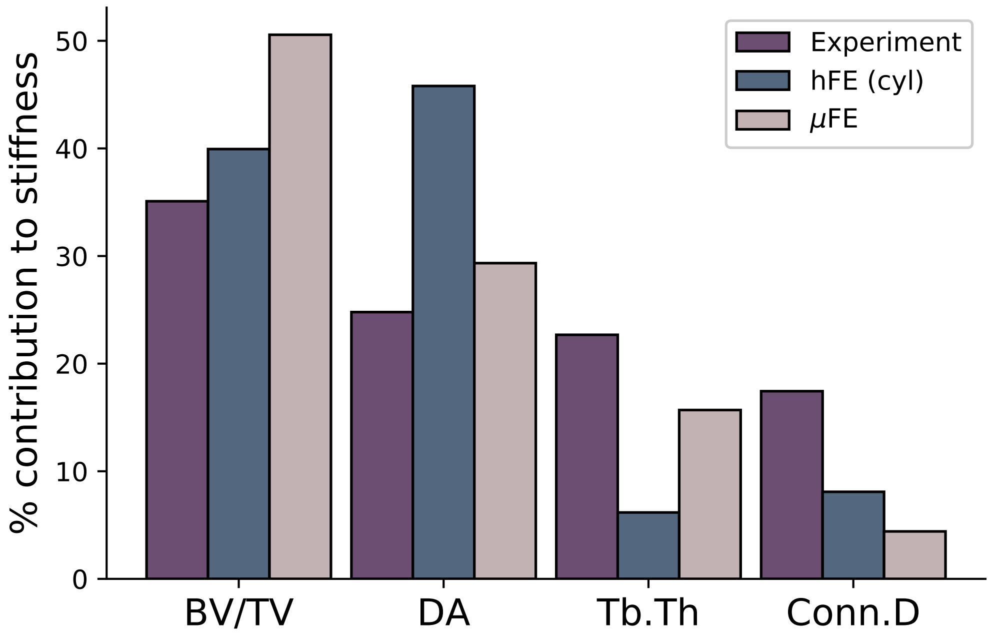

Figure 6.7: The percentage correlation of morphological properties on variations in experimental and computational stiffness values as calculated using the correlation coefficient value, r and represented by each bar. Experimental and hFE stiffness values were compared to morphological evaluation of full cylindrical specimens, whereas μFE stiffness was compared to morphological characterisation of cuboidal specimens.

6.4 Discussion

Specimen-specific models of porcine talar subchondral bone were developed by calibrating the apparent relationship between Young's modulus and image grayscale with good accuracy. Tissue-level properties were indirectly established by developing and calibrating trabecular-level models using equivalent calibrated continuum models with optimised grayscale-based material properties.

In this study, a low intra-specimen variation of around 7% was observed in tissue modulus. Large variations to tissue modulus can have significant effect on apparent-level mechanical properties, which make comparisons to the effective properties of diseased tissue more difficult, unless variations from microarchitecture are also accounted for. Though a tissue modulus CoV of under 20% is recommended [Jaasma et al., 2002] to avoid large errors in calculated apparent properties, some intra-donor variability is inevitable, but can translate to significant differences in effective biomechanical properties. It is therefore key that FE models describe the intra-specimen variability in microarchitecture, as well as variations to material properties in a specimen-specific manner, as demonstrated in this study. Quantifying tissue mechanical properties is essential for accurately predicting the macroscopic biomechanical behaviour of bone. However, calculating tissue properties from simulated apparent-level experiments may result in less-precise measures of tissue modulus [Bevill et al., 2009] compared to results obtained from specimen-specific micro-mechanical testing [Wolfram et al., 2010], and hence this method can only provide an estimate of tissue-level mechanical properties.

Relatively high intra-specimen variations to microarchitecture were observed in this study. Only BV/TV has been reported in other studies for porcine talar bone [den Dunnen et al., 2013], but is higher than reported in this work. Variations of the type of trabeculae present - combinations of rod- and plate-like trabeculae - are known to impact bone mechanical properties [Wang et al., 2015]. Ellipsoid Factor (EF) is an alternative measure to the structure model index (SMI) in measuring rod-to-plate ratios. It has been argued that SMI does not account for concave surfaces of bone and therefore does not fully represent the geometry of the tissue [Doube, 2015, Salmon et al., 2015]. Interestingly, EF was negatively correlated to $k_{\mu FE}$; increasing rod-like trabeculae potentially reduces apparent stiffness. However, it is hard to conclude this is indeed true for all ankle specimens with a limited sample size of ten specimens.

It is well known that the biomechanical behaviour of trabecular bone from multiple anatomical locations can be predominantly described by a combination of

BV/TV and DA [Matsuura et al., 2008, Maquer et al., 2015]. This was also observed in this study (Fig. 6.7) where over 65% variations to experimental, hFE and μFE stiffness values originated from BV/TV and DA. This highlights the importance of anisotropy when deriving relationships between apparent density and elastic modulus. DA had more of an impact on hFE stiffness (45%) than BV/TV (40%). This could be explained by the high variations in anisotropy of the specimens for this model (over 15%), but the small sample size limits the strength of such a conclusion. In this case, material anisotropy was not accounted for in the models, which may explain the sub-optimal correlation and agreement between the experimental and hFE (cyl) simulation stiffness values. However, the errors observed here are similar to that of previous work [Zapata-Cornelio et al., 2017], and the validation error was lower than the calibration error, hence even though sub-optimal agreement was found one can consider the method as valid.

The results in this work demonstrate the methodology to be valid for models to replicate apparent stiffness, however there is no indication of the validity of the strain field it produces. This study also further supports the validity of a linear relationship between image grayscale and apparent stiffness, as employed in other studies [Day et al., 2020, Zapata-Cornelio et al., 2017, Robson Brown et al., 2014, Wijayathunga et al., 2008]. Equally, this relationship is limited by its dependency on images acquired using the specific scanner and settings described in this study.

Trabecular-level model optimisation results showed a good agreement and high correlation between stiffness values. Compared to the hFE models, there was higher variation to apparent stiffness for the cylindrical models (37%) than for cuboidal models (13%). Selecting a smaller central region may have provided a more accurate representation of the tissue as this eliminates any lateral surface effects. The relatively similar values of microarchitecture measured from the cylinders and the cuboids shows that the cubes are representative of cylinders and hence building μFE models of the full cylinder was unnecessary.

A single specimen in the validation set used for μFE model calibration was found outside the limits of agreement in the Bland-Altman analysis. This specimen had the lowest stiffness values for both hFE and μFE models, as well as a relatively low BV/TV and DA values compared to other specimens. This may highlight a limitation of the methodology. The meshing algorithm may have difficulties in capturing sparser trabeculae, which can alter its simulated behaviour under load. This outlier may therefore affect overall trends to variations in stiffness and microarchitecture; the impact of this specimen is exacerbated by the limited sample size of the study.

Unlike the human talus, the porcine talar dome is more incongruent and features more convex trochlea which created difficulties in accurately extracting uniform, on-axis specimens. Efforts were made to retrieve specimens posteriorly on the talar dome in consideration for the likely loading pattern through the porcine ankle in the hope to retrieve cores that are orientated with the loading direction. It was difficult to extract more than two cores per joint on the talar dome in the posterior region, due to the impact of the hammer and progressive weakening of the bone, causing the talus to fracture. As a result, specimen height varied and most did not satisfy the suggested 2:1 height:diameter ratio for mechanical characterisation [Keaveny et al., 1993], but still satisfied the continuum assumption. This is not an issue as modulus values are not directly derived from experimental data, but are instead derived for exact replication in computational models. Of the fifteen specimens retrieved, four were excluded during testing due to malalignment with the testing platens. These four specimens were also the tallest specimens, which may suggest that a higher pre-load was required to secure these specimens in the testing rig.

Beyond variation in microarchitecture, variations to *in vitro* stiffness may have originated from varied bone marrow content and surface irregularities in the specimen, which translate to larger variations in density during thresholding. The bone marrow was not removed in this study, but would have negligible effects on mechanical properties at quasi-static strain rates [Carter and Hayes, 1977, Linde et al., 1991]. The removal of the marrow may have improved image quality, and in doing so, improve the contrast between bone and its surroundings. This extra step in the specimen preparation phase may also help to remove any residual debris from specimen extraction, which may impact on boundary conditions at the ends of the specimen. Improving thresholding would avoid any appreciable errors in BV/TV and predicting effective mechanical properties [Bevill et al., 2009].

This study demonstrated that non-diseased porcine talar subchondral trabecular bone has little intra-specimen variation to mechanical properties at the tissue level, and the estimated tissue modulus was higher than the apparent modulus found *in vitro*. The methods developed in this study can be applied to specimens of non-diseased human ankle bone to estimate tissue mechanical properties, which would then allow for the characterisation of the effective mechanical behaviour of osteoarthritic ankle tissue.

The outcomes of this section have shown the validity of this methodology in replicating experimental stiffness and providing tissue-level estimations of bone mechanical properties. The methodology therefore is suitable for application to human tissue, as reported in the following chapter.

Chapter Summary

- An image-based, specimen-specific inverse FE methodology was developed for ankle subchondral bone specimens which estimated tissue-level properties of porcine subchondral trabecular bone.
- Good agreement was observed for calibration and validation of hFE and μFE models.
- Low intra-specimen variation was observed, with the majority of variation originating from the microarchitecture (predominantly BV/TV and DA).
- The developed inverse FE methodology is deemed valid and suitable for translation to human ankle bone specimens.

CHAPTER 7

ESTIMATING APPARENT MECHANICAL PROPERTIES OF OA ANKLE SUBCHONDRAL BONE

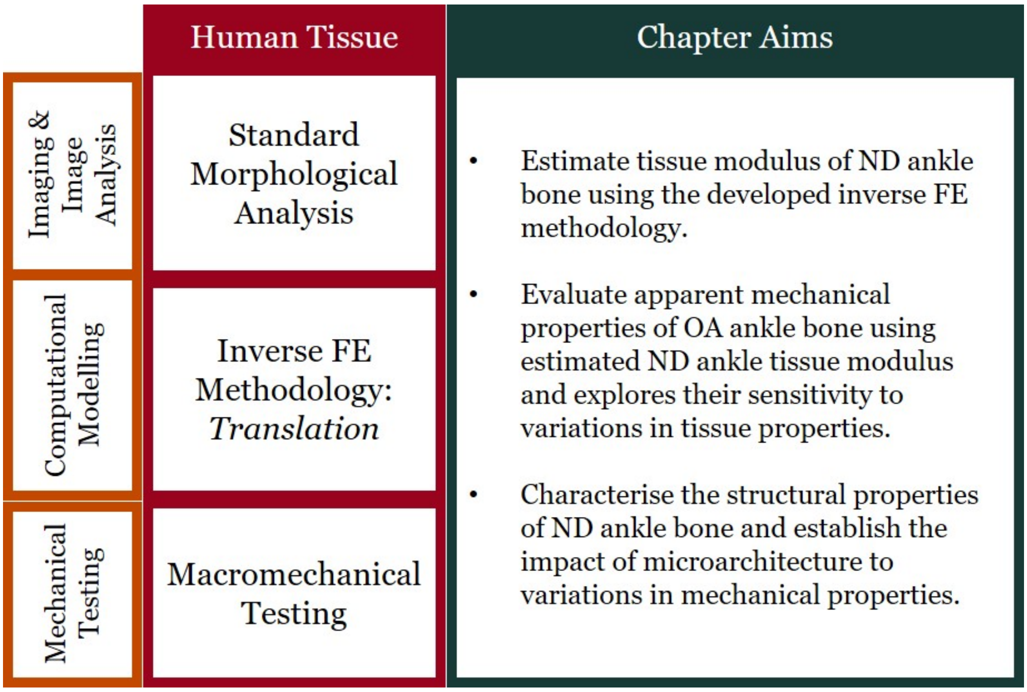

	Human Tissue	Chapter Aims
Imaging & Image Analysis	Standard Morphological Analysis	• Estimate tissue modulus of ND ankle bone using the developed inverse FE methodology. • Evaluate apparent mechanical properties of OA ankle bone using estimated ND ankle tissue modulus and explores their sensitivity to variations in tissue properties. • Characterise the structural properties of ND ankle bone and establish the impact of microarchitecture to variations in mechanical properties.
Computational Modelling	Inverse FE Methodology: *Translation*	
Mechanical Testing	Macromechanical Testing	

This chapter utilises the methods developed in Chapters 5 and 6 to estimate tissue-level mechanical properties of non-diseased (ND) ankle subchondral bone using image-based, specimen-specific FE models. Following this, the apparent mechanical properties of irregularly shaped osteoarthritic (OA) bone pieces can be estimated. This provided an opportunity to explore the changes to mechanical properties with OA and how microarchitectural alterations influence this (Chapter 4).

7.1 Introduction

A multiscale computational approach was previously developed to characterise porcine talar subchondral trabecular bone at the tissue level by means of back-calculating tissue properties from validated, hFE models (Chapters 5 and 6). The translation of this methodology (Fig. 7.1) allowed for the estimation of apparent mechanical properties of OA specimens, which are more difficult to test *in vitro* due to their small and irregular geometry. Tissue-level properties of ankle subchondral bone are currently unreported in the literature, but in other joints it is thought to increase in late-stage OA bone [Zuo et al., 2016, Peters et al., 2018]. *In silico* models allow for the sensitivity of the mechanical behaviour of OA ankle tissue to variations in tissue properties to be evaluated without direct characterisation. Based on the literature available in other joints, it was hypothesised that the apparent mechanical stiffness of ankle subchondral trabecular bone will increase with OA and be highly influenced by changes in bone density and trabecular structure due to accelerated bone remodelling [Kamibayashi et al., 1995a, Bobinac et al., 2003, Burr and Gallant, 2012, Finnilä et al., 2017, Chen et al., 2018].

7.1.1 Study Aims

The aim of this study were to characterise osteoarthritic changes to the mechanical properties of subchondral bone in the ankle and evaluate the influence of variations to tissue modulus and microarchitecture on apparent bone stiffness. The following objectives were defined:

- Estimate tissue modulus of ND tibial and talar subchondral bone using the previously developed inverse FE methodology.
- Evaluate apparent mechanical properties of OA ankle subchondral trabecular bone using the estimated ND tissue properties.
- Explore the sensitivity of OA ankle subchondral bone apparent stiffness to variations in tissue properties.
- Characterise the microstructural properties of ND ankle subchondral bone and establish the impact of microarchitecture to variations in mechanical properties.

7.2 Materials and Methods

Pairs of distal tibiae and tali were dissected from three human, non-diseased (ND) cadaveric feet as detailed in Section 3.1.3. Cylindrical bone cores (6.5 mm ⌀) were extracted from various regions across the tibial plafond (N=10) and the talar dome (N=11) (Section 3.1.3.a). Each specimen was trimmed to just below the subchondral bone plate and rinsed with PBS. Specimens were embedded into

Delrin endcaps using a thin layer of PMMA cement. Osteoarthritic ankle bone specimens were sourced from local patients undergoing total ankle arthroplasty (Section 3.1.2). All specimens were imaged (μCT; 16 μm) using the protocol described in Section 3.2.1. All ND specimens were subjected to mechanical characterisation as described previously (Section 3.5.1) but with an increased pre-load to 0.5 N to improve bedding-in of the specimens before testing. Experimental stiffness, k_{exp}, was measured for all ND specimens. Specimen height and anvil height (average $\pm$ SD) for tibial and talar specimens were 8.54 $\pm$ 1.05 and 7.34 $\pm$ 1.05 mm, respectively.

Image analysis of ND specimens was undertaken as described in Section 3.4. The full image stack of each specimen was binarised using Otsu thresholding in ImageJ. Standard morphological properties were measured for each specimen (BV/TV, DA, Conn.D and Tb.Th) using BoneJ. EF and ITS-based morphological evaluation was performed on ND cuboidal volumes (4 mm). The influence between each morphological property and mechanical properties were also explored in this study. Similarly, standard and ITS-based morphological values obtained for the tibial OA specimens in Chapter 4 were used to investigate the influence of microarchitecture on estimated apparent mechanical properties obtained in this study.

7.2.1 Inverse FE Methodology

The previously developed inverse FE methodology was translated for use on human tissue (Fig. 7.1). This workflow first estimated tissue modulus, E_{tiss}, for ND specimens from the distal tibia and talus. These values were then used on μFE models of OA volumes of bone (4 mm) to estimate apparent stiffness *in silico*.

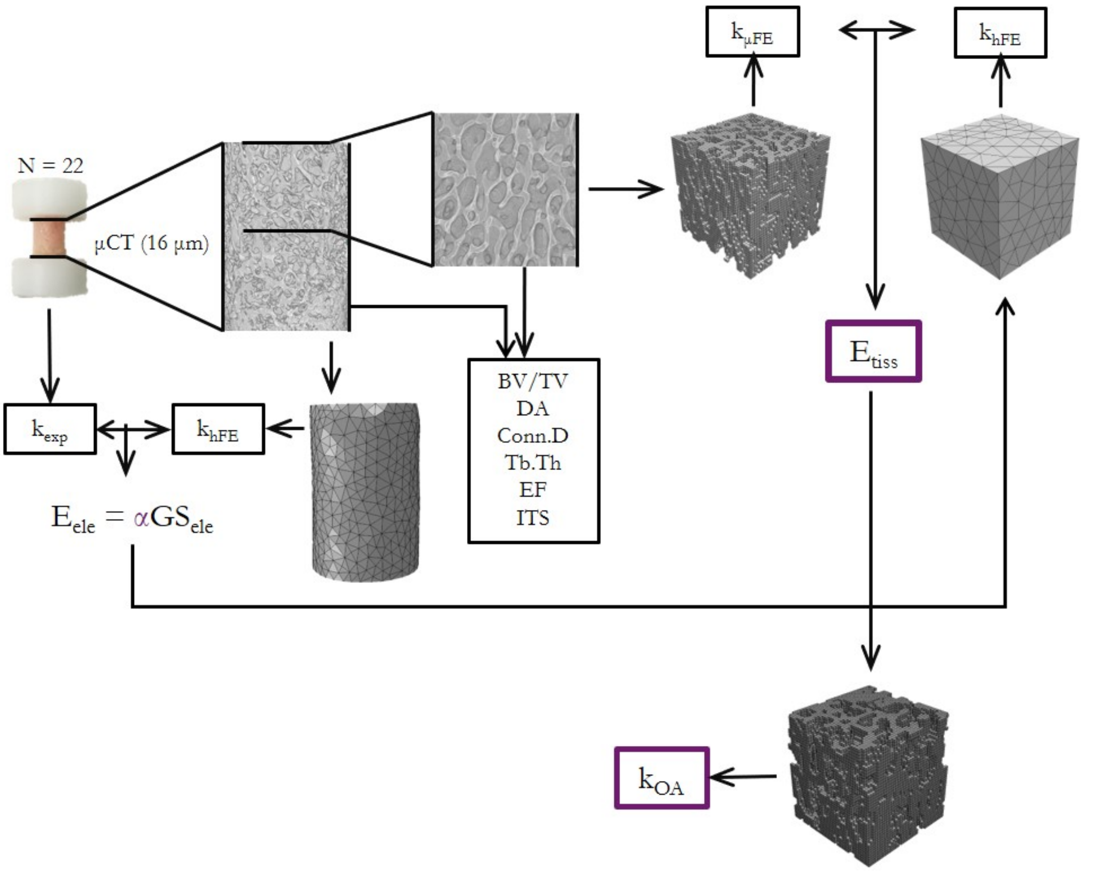

Figure 7.1: Translated inverse FE methodology to estimate tissue properties of ND ankle subchondral bone and in this way, characterise the apparent stiffness of OA bone specimens *in silico*.

The hFE models were setup as before, utilising the BV/TV methodology and downsampling to an isotropic resolution of 0.4 mm (2x average trabecular thickness, see 5.4.1). For the optimisation of grayscale material properties, the specimens were grouped by bone (distal tibia or talus) and split arbitrarily into even calibration and validation groups (N=5 tibial specimens per group and N=6 per talar specimens per group).

Previous sensitivity tests detailed the effects of hFE stiffness to boundary conditions (Section 5.4.2). In this study, it was found that using the gauge length of the specimens - as performed for porcine hFE model creation - was now detrimental to model output stiffness for human specimens (Table 7.1). This may be due to the extra cleaning step in the specimen preparation phase (Section 3.1.3.a), which resulted in more accurate segmentation of trabecular bone. Hence, the full stack of .tiff images were used to generate human hFE models.

Table 7.1: Sensitivity of hFE stiffness output for four exemplary specimens using the full image stack (FS) and the cropped image stack, or gauge length (GS), demonstrating improved agreement to specimen experimental stiffness prior to optimisation. All stiffness values in N/mm.

Experimental Stiffness	FS	GL
1517.60	1234.38	1013.78
834.92	932.99	672.52
1299.20	1158.82	1122.07
884.73	752.15	1928.78

ND μFE models were setup as previously described (Section 5.5.2). The same protocol was used to generate μFE models for OA specimens in order to estimate their apparent stiffness, k_{OA}. As with the ND specimens, a cuboidal volume (4 mm) of trabecular bone was extracted from the OA image stacks retrieved and processed from the μCT data (Section 3.2.1 and 3.4). μFE models were generated within ScanIP and setup within Abaqus using the same protocol as the ND tissue to simulate a -0.1 mm displacement on the top surface. The material properties of the OA μFE models were obtained using the appropriate (tibial or talar) average estimated ND tissue modulus value. A total of one talar and five tibial OA specimens were available for analysis. All FE analyses were quasi-static and performed in Abaqus (ARC3).

7.2.2 Sensitivity of OA Apparent Stiffness to Variations to Tissue Modulus

Sensitivity of ankle OA μFE models to variation in E_{tiss} was explored using tissue moduli obtained using nanoindentation on bone specimens from the knee [Zuo et al., 2016, Peters et al., 2018]. The percentage change in measured E_{tiss} with OA from the literature was applied to the estimated ND E_{tiss} tibial and talar values. These material properties were then applied to OA ankle μFE models to yield an apparent stiffness value for late-stage OA specimens. Limited data was available in the literature; Zuo et al. did not use non-diseased control specimens (OA0), hence early-stage OA (OA1) values (osteonal and lamellar) were used to measure the percentage increase in E_{tiss} (Table 7.2).

Table 7.2: E_{tiss} values from key studies in the knee joint [Zuo et al., 2016, Peters et al., 2018]. Percentage increases from zero/mild to mild/late-stage OA were used to scale the modulus values in the ankle to assess their sensitivity to the change in tissue modulus.

STUDY	RANGE	(GPa) $E_{tiss,knee}$	$\uparrow$ in E_{tiss} (%)	(GPa) $E_{tiss,tal}$	$E_{tiss,tib}$
Peters et al. 2018	OA0-OA4	12.56-15.20	21.02	3.73	3.61
Zuo et al. 2016	OA1-OA4	13.09-17.33	24.68	3.84	3.72
Zuo et al. 2016	OA1-OA4	13.46-16.00	18.87	3.67	3.54

Similarly, a 10% and 20% reduction in tissue modulus values were applied to establish the sensitivity of apparent stiffness in ankle OA bone to reductions in tissue properties. 10% and 20% reduced E_{tiss} were calculated using estimated ND tissue properties obtained from the inverse FE methodology.

7.2.3 Statistical Analysis

The mean (AVG), standard deviation (± SD) and coefficient of variance (CoV, %) for all mechanical (experimental and computational) and morphological properties were calculated for all specimens grouped by bone (*tib* and *tal*). Correlation between k_{exp} and $k_{hFE,cyl}$; $k_{\mu FE}$ and $k_{hFE,cube}$ and all stiffness values to morphological properties were measured using Square of the Pearson Product-Moment Correlation Coefficient (r^2). Agreement between k_{exp} and $k_{hFE,cyl}$, and $k_{\mu FE}$ and $k_{hFE,cube}$ was evaluated using Concordance Correlation Coefficient (CCC) values and Bland-Altman analyses. Independent samples t-test ($\alpha = 0.05$) was used to compare significant differences in stiffness values between OA (N=6) and ND (N=21) specimens and between distal tibia and talar specimens.

7.3 Results

The raw data are reported in Appendix C.

7.3.1 Non-Diseased (ND) Tissue

7.3.1.a Mechanical Testing

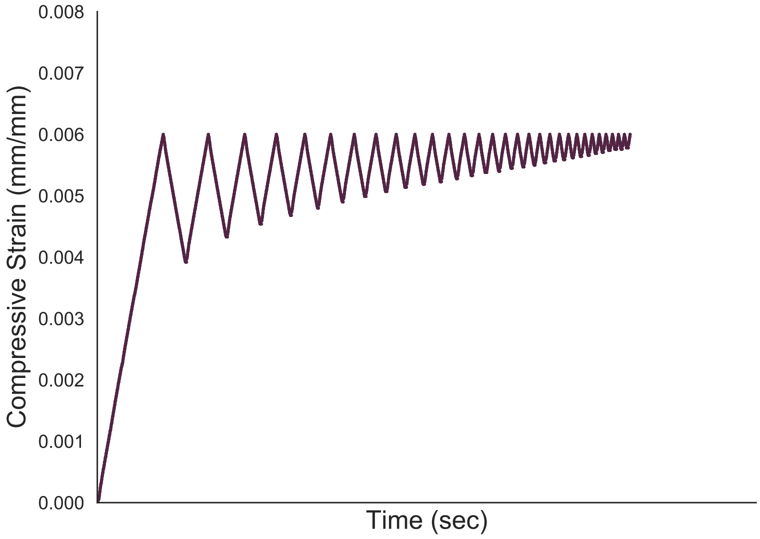

Figure 7.2: Diminishing creep (primary stage) reaching a steady state of viscoelasticity and hence, material relaxation, preceding testing of an exemplary ND ankle bone specimen.

The results in Fig. 7.2 confirm that the pre-conditioning protocol used on porcine specimens also allowed the ND specimens to reach a steady state of viscoelasticity prior to the quasi-static ramp to failure.

Average talar experimental stiffness, $\overline{k}_{exp,tal}$ was 1190.15 ± 175.11 N/mm (CoV = 14.71%). Average experimental stiffness in the distal tibia, $\overline{k}_{exp,tib}$, was 1135.11 ± 209.11 N/mm, but had higher variation in values compared to the talus (CoV = 18.42%). Similarly, average Young's modulus in the tibia and talus was 253.19 ± 74.30 MPa and 274.26 ±67.76 MPa, respectively (Fig. 7.3). No significant difference in stiffness values was observed between the two bones (p >0.05), but there was more localised variation to stiffness when comparing values from each donor (Fig. 7.4).

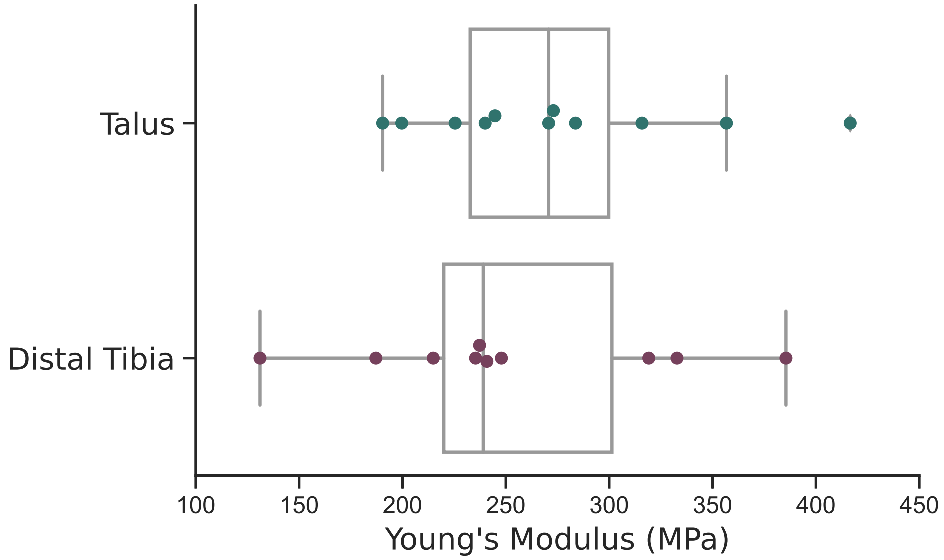

Figure 7.3: Comparison of Young's modulus values in the distal tibia and talus. Boxplots represent the median and interquartile range of values for N=10 tibial and N=11 talar samples.

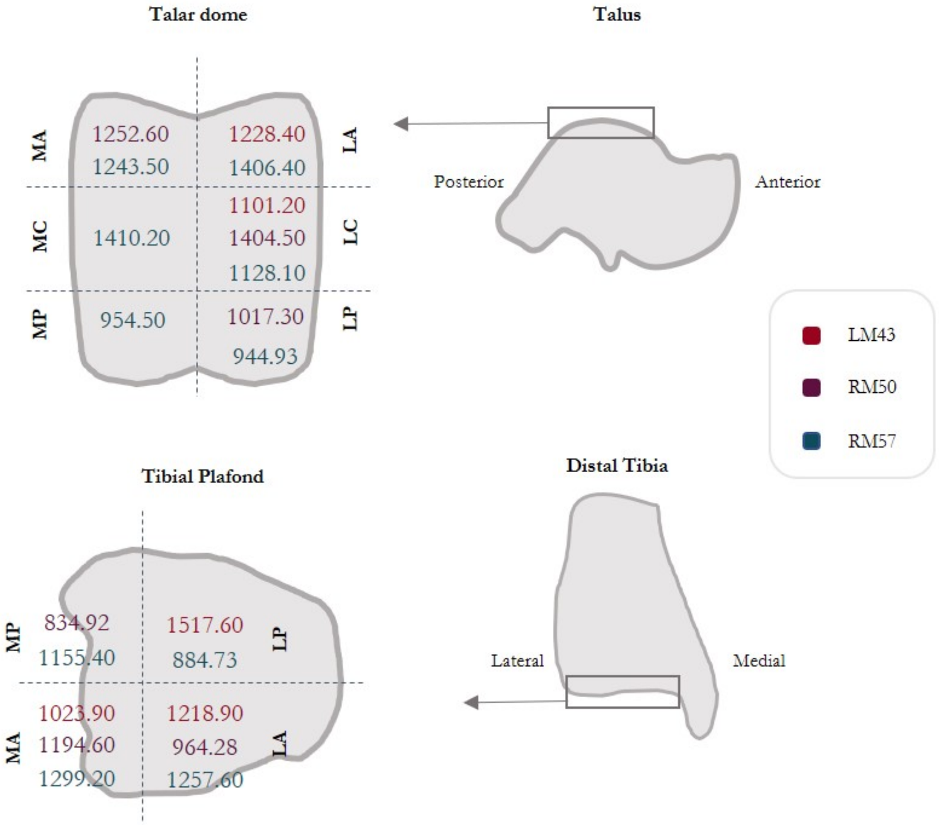

Figure 7.4: Regional variation in k_{exp} (N/mm). Each colour indicates donor origin (e.g. "LM45" = left-leg, male, 45 years of age).

7.3.1.b Apparent Level Model Calibration and Validation

For ND talar specimens, good agreement (CCC=0.67) and acceptable correlation (r^2=0.47) was found between *in silico* and *in vitro* stiffness values (N=11). Calibration and validation RMSE were 7.44% and 16.15%, respectively. Average apparent stiffness, $\bar{k}_{hFE,tal}$, was 1222.31 ± 188 N/mm (CoV = 15.4%).

For ND tibial specimens, good agreement (CCC=0.66) was also observed between *in silico* and *in vitro* stiffness values and showed acceptable correlation (r^2=0.49). The optimisation procedure terminated just prior to the set convergence tolerance (10%) with a converged value of α rather than a converged RMSE; calibration and validation RMSE were 11.33% and 13.67%, respectively. $\bar{k}_{hFE,tib}$ was 1089.83 ± 169 N/mm (CoV = 15%).

Overall, the results showed good agreement (CCC = 0.69, Fig. 7.5ii) and correlation (r^2 = 0.47, Fig. 7.5i) between experimental and computational stiffness values for all ankle specimens (N=21).

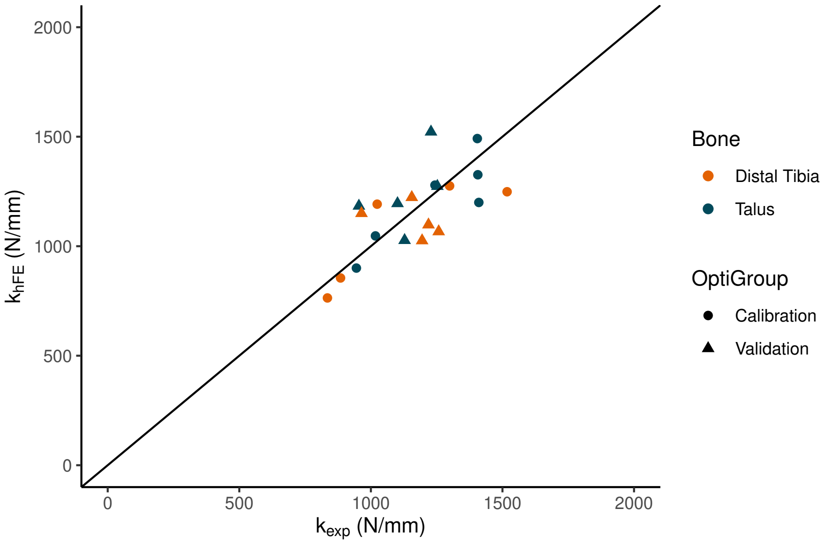

(i) Correlation of experimental stiffness to cylindrical continuum models (r^2=0.47).

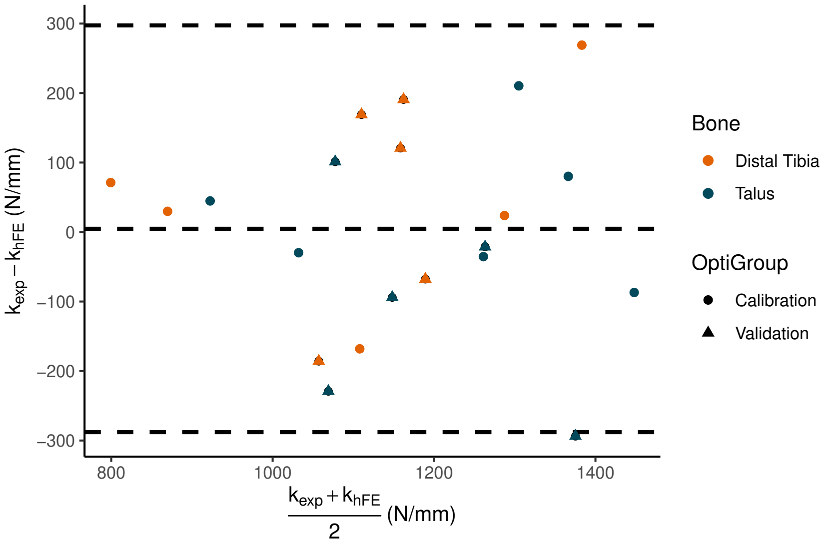

(ii) Bland-Altman plot showing agreement of experimental stiffness to cylindrical continuum models (CCC=0.69).

Figure 7.5: Correlation (7.5i) and agreement (Bland-Altman, 7.5ii) results for optimisation of hFE models. The straight line (x=y) in the correlation plot indicates perfect correlation. The dashed lines on the Bland-Altman plot indicate the mean and ± 1.96 SD.

7.3.1.c Trabecular Level Model Calibration and Validation

Good agreement, CCC=0.60 and CCC=0.81, was observed between the hFE and μFE stiffness values in talar and distal tibial cuboids, respectively. Calibration and validation RMSE (%) were 11.71% and 16%, and 8.09% and 12.39% in the talus and distal tibia, respectively. Combined there was good correlation (r^2 = 0.52, Fig. 7.6i) and agreement (CCC = 0.72, Fig. 7.6ii) between hFE and μFE models.

Average talar (N=6) and distal tibial (N=5) calibrated $\overline{E}_{tiss}$ were 3.08 ± 0.41 GPa

(CoV = 13.24%) and 2.98 ± 0.26 GPa (CoV = 8.60%), respectively.

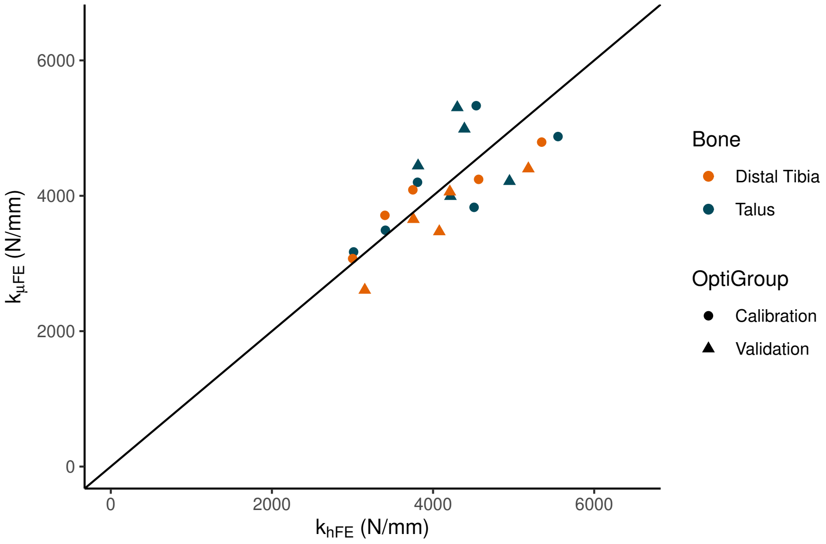

(i) Correlation of continuum stiffness to trabecular-level stiffness in cuboids (r^2=0.69).

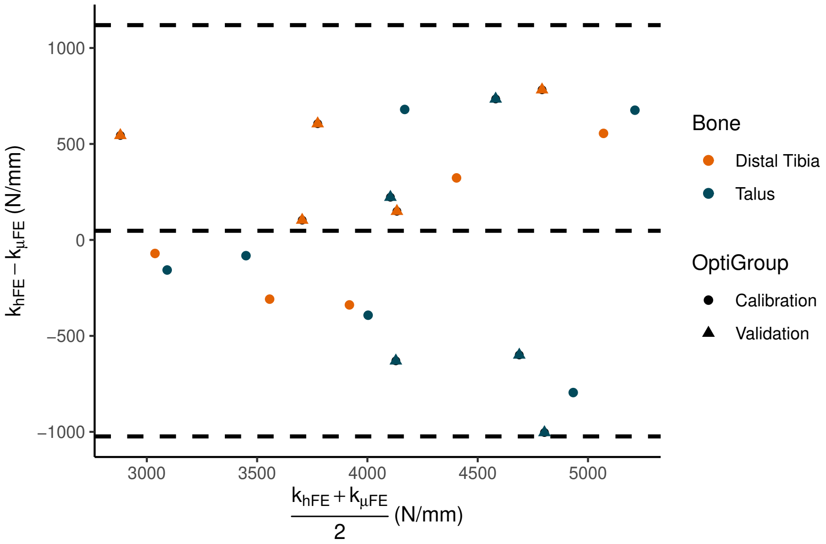

(ii) Bland-Altman plot showing agreement of continuum stiffness to trabecular stiffness in cuboids (CCC=0.80).

Figure 7.6: Correlation (7.6i) and agreement (Bland-Altman, 7.6ii) results for optimisation of μFE models. The straight line (x=y) in the correlation plot indicates perfect correlation. The dashed lines on the Bland-Altman plot indicate the mean and ± 1.96 SD.

7.3.1.d Correlations to Microarchitecture

Average values for each microarchitectural properties were calculated for both cylindrical (Table 7.3) and cuboidal volumes (Table 7.4) used in the FE methodology. The raw microarchitectural data is reported in Appendix C, Tables C.3.1 & C.3.3). No significant differences between structural properties in the talus and distal tibia were observed for both cylindrical or cuboidal volumes (p>0.05).

Table 7.3: Summary of microarchitectural data for cylindrical bone cores.

		BV/TV	**DA**	**Tb.Th (mm)**	**Conn.D (mm^{-3})**
Distal Tibia	AVG	0.35	0.58	0.21	6.43
	± SD	0.05	0.09	0.02	3.85
	CoV (%)	14.2	15.5	9.5	59.8
Talus	AVG	0.38	0.59	0.21	9.78
	± SD	0.04	0.12	0.02	3.85
	CoV (%)	10.5	20.3	9.5	39.3

Table 7.4: Summary of microarchitectural data for cuboidal bone volumes.

		BV/TV	**DA**	**Tb.Th (mm)**	**Conn.D (mm^{-3})**	**EF**
Distal Tibia	AVG	0.33	0.71	0.23	4.39	0.00
	± SD	0.06	0.11	0.02	1.94	0.04
	CoV (%)	17.5	15.4	9.9	44.3	-
Talus	AVG	0.37	0.64	0.23	6.41	0.01
	± SD	0.04	0.11	0.02	2.46	0.03
	CoV (%)	11.5	17.4	9.1	38.4	-

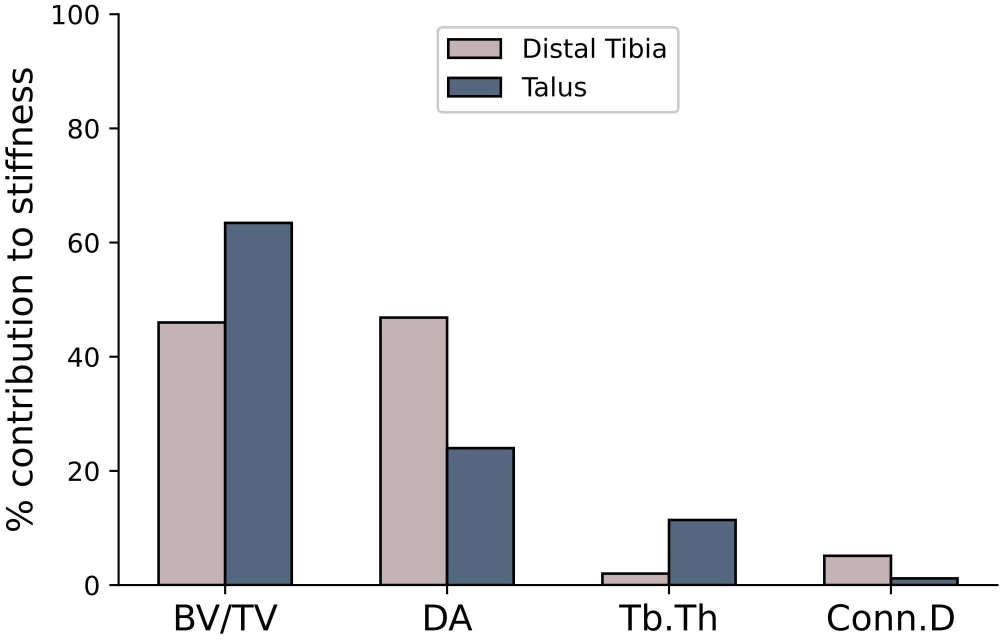

Figure 7.7: The relative contributions of standard morphological properties to variations in computational apparent stiffness (hFE), calculated using weighted values of r^2.

Weighted contributions were established by taking each r^2 value (correlation of morphological property and hFE stiffness) and dividing by the sum of the r^2 values for all properties (Fig. 7.7). Together, BV/TV and DA accounted for 92.86% and 87.43% of variations to apparent (hFE) stiffness in the distal tibia and talus, respectively. However, for μFE models most of the variations to stiffness originated from BV/TV (47.61% in the distal tibia, 33.98% in the talus) and EF (25.01% in the distal tibia, 27.18% in the talus). In comparison, BV/TV and DA accounted for 86.4% variations to experimental stiffness in the distal tibia. However in the talus, BV/TV, DA and Tb.Th had the highest weight influence on variations to experimental stiffness (40.04%, 28.98% and 27.86%, respectively).

The highest correlations to stiffness were observed between BV/TV, Tb.Th, EF and SMI with stiffness values obtained from trabecular level models (Table 7.5).

Table 7.5: Correlation (r and r^2) of microarchitectural properties against stiffness of cylindrical volumes (k_{exp} and k_{hFE}) and cuboidal volumes (k_{hFE} and $k_{\mu FE}$) in the distal tibia and talus. Colour scale (red to green) indicates increasing level of correlation.

Cylindrical		**Distal Tibia**		**Talus**	
		k_{exp}	k_{hFE}	k_{exp}	k_{hFE}
BV/TV	r	0.38	0.65	0.61	0.61
	r^2	0.14	0.42	0.37	0.38
DA	r	-0.29	-0.65	0.52	0.38
	r^2	0.08	0.42	0.27	0.14
Tb.Th	r	-0.03	0.14	0.51	0.26
	r^2	0.00	0.02	0.26	0.07
Conn.D	r	0.19	0.22	-0.17	0.08
	r^2	0.03	0.05	0.03	0.01
Cuboidal		**Distal Tibia**		**Talus**	
		k_{hFE}	$k_{\mu FE}$	k_{hFE}	$k_{\mu FE}$
BV/TV	r	0.90	0.90	0.92	0.75
	r^2	0.82	0.80	0.85	0.57
DA	r	0.04	-0.15	-0.10	0.64
	r^2	0.00	0.02	0.01	0.41
Tb.Th	r	0.66	0.54	0.66	0.22
	r^2	0.43	0.29	0.43	0.05
Conn.D	r	0.17	0.38	0.49	0.44
	r^2	0.03	0.14	0.24	0.19
EF	r	0.58	0.65	0.49	0.67
	r^2	0.34	0.42	0.24	0.45
SMI	r	-0.89	-0.79	-0.91	-0.59
	r^2	0.79	0.62	0.83	0.35

High correlation was observed between μFE stiffness and pBV/TV in the distal tibia (r=0.913) and talus (r=0.789) (Table 7.6). Similarly, aBV/TV had high correlation in both the distal tibia (r=0.977) and talus (r=0.968), respectively.

Table 7.6: Correlation of ND μFE stiffness to ITS-based morphological properties for distal tibia (as reported in Chapter 4) and talar specimens. Colour scale (red to green) indicates increasing level of correlation.

	Distal Tibia		**Talus**	
	r	r^2	r	r^2
pBV/TV	0.91	0.83	0.79	0.62
rBV/TV	0.63	0.40	0.34	0.12
pBV/rBV	-0.30	0.09	0.16	0.03
aBV/TV	0.98	0.95	0.97	0.94
pBV/BV	-0.35	0.12	0.06	0.00
rBV/BV	0.35	0.12	-0.06	0.00
pTb.N	0.77	0.59	0.69	0.47
rTb.N	0.69	0.48	0.36	0.13
pTb.Th	0.15	0.02	0.08	0.01
rTb.Th	-0.28	0.08	-0.38	0.14
pTb.S	-0.59	0.35	-0.26	0.07
rTb.l	0.21	0.04	0.25	0.06
RR Junc.D	0.51	0.26	0.16	0.03
PR Junc.D	0.69	0.47	0.45	0.20
PP Junc.D	0.72	0.52	0.62	0.38

7.3.2 Osteoarthritic (OA) Tissue

Talar apparent stiffness, $k_{OA,tal}$, (N=1) was 3602.31 N/mm, as derived from μFE modelling assuming an ND modulus. High variation in $\bar{k}_{OA,tib}$ was observed for OA distal tibia specimens (N=5, 9481.42 ± 3319.48 N/mm). Significant increase in apparent stiffness values between ND (N=10) and OA (N=5) tibial specimens ($p < 0.05$) was observed.

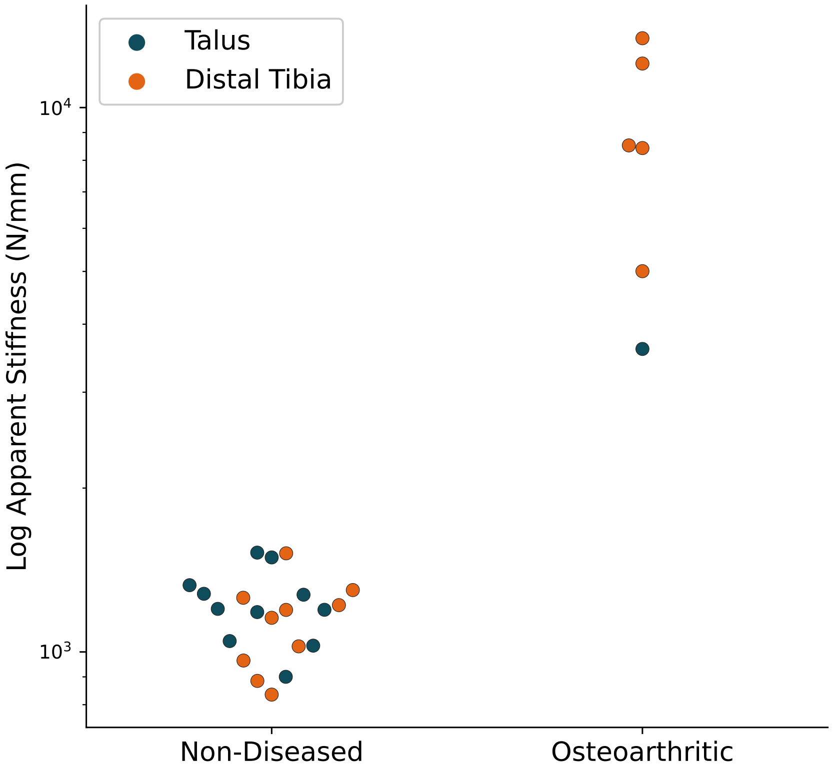

Figure 7.8: Swarm plot showing the significantly increased apparent stiffness (log values) of OA specimens compared to ND controls from the distal tibia and talus ($p<0.05$).

7.3.2.a Sensitivity of Apparent Stiffness to Variations in E_{tiss}

Sensitivity of OA apparent stiffness to increases in tissue properties was established using values from the literature (Section 7.2.2). Similarly, estimated ankle ND tissue properties (Section 7.3.1.c) were used to apply 10% and 20% reductions to tissue properties to the OA ankle bone models. This was 2.78 GPa and 2.47 GPa, and 2.68 GPa and 2.38 GPa, for talar and tibial specimens, respectively.

The apparent stiffness of OA μFE apparent stiffness with varied E_{tiss} showed an increase in apparent stiffness with increased E_{tiss} (Fig. 7.9). Specimens Tib 1, 2, 3 and 5 were more sensitive to change in E_{tiss} compared to the remaining OA specimens. For tibial specimens, both a 10% and 20% reduction in E_{tiss} still resulted in significantly higher apparent stiffness in OA specimens compared to controls (p<0.001).

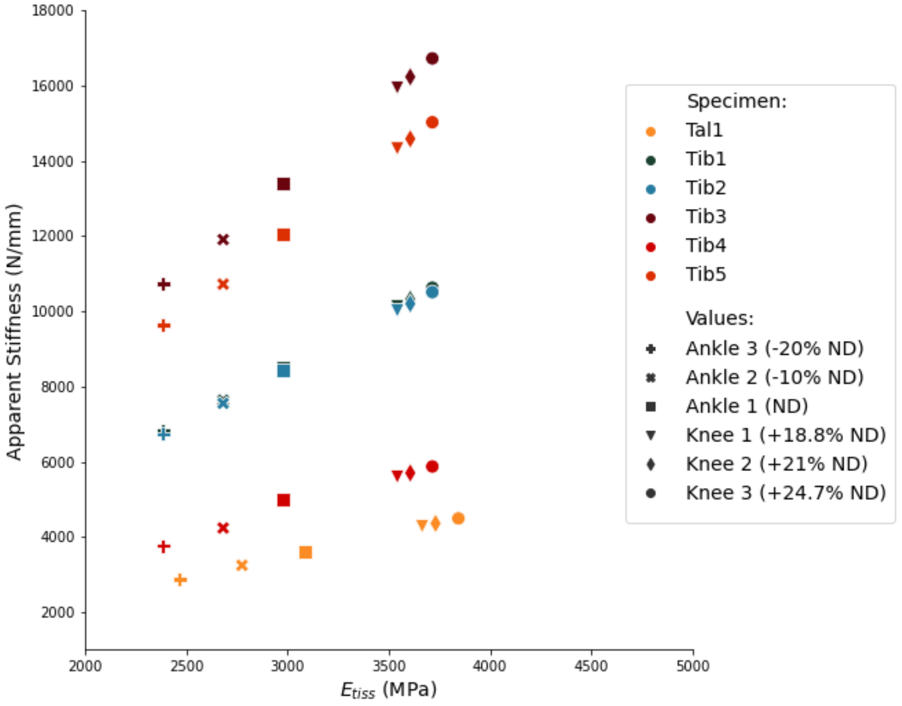

Figure 7.9: Estimated apparent stiffness values of ankle OA bone with varying tissue properties (E_{tiss}). Knee 1: +18.8% increase to estimated ND ankle E_{tiss} values [Zuo et al., 2016]; Knee 2: +21% increase to estimated ankle ND E_{tiss} values [Peters et al., 2018]; Knee 2: + 24.7% increase to estimated ankle ND E_{tiss} values [Zuo et al., 2016]; Ankle 1: estimated ND ankle E_{tiss} value; Ankle 2: -10% estimated ND ankle E_{tiss} values, and Ankle 3: -20% estimated ND ankle E_{tiss} values.

7.3.2.b Correlations to Microarchitecture

Using the morphological data reported in Chapter 4, correlations between microarchitecture and computationally-derived $k_{OA,tib}$ were evaluated (Table 7.7). High positive correlation was observed between $k_{OA,tib}$ and BV/TV (r=0.925); pBV/TV (r=0.86); aBV/TV (r=0.90); pTb.N (r=0.79) and PP Junc.D (r=0.75). Strong negative correlations were observed for SMI (r=-0.96), rTb.Th (r=-0.83) and RR Junc.D (r=-0.80).

Table 7.7: Correlation of morphological properties to $k_{OA,tib}$.

	r	r^2
BV/TV	0.93	0.86
DA	0.65	0.42
Tb.Th	0.56	0.31
Conn.D	0.07	0.00
EF	0.54	0.29
SMI	-0.96	0.93
pBV/TV	0.86	0.73
rBV/TV	0.19	0.04
pBV/rBV	0.51	0.26
aBV/TV	0.90	0.81
pBV/BV	0.58	0.33
rBV/BV	-0.58	0.33
pTb.N	0.79	0.63
rTb.N	0.22	0.05
pTb.Th	0.46	0.21
rTb.Th	-0.83	0.68
pTb.S	0.48	0.23
rTb.l	0.41	0.16
RR Junc.D	-0.80	0.64
PR Junc.D	0.56	0.32
PP Junc.D	0.75	0.56

7.4 Discussion

This study characterised the structural and mechanical properties of non-diseased human ankle bone tissue and utilised an inverse FE methodology to estimate tissue-level mechanical properties. In this way, an estimate of apparent-level mechanical properties of osteoarthritic tissue was established which allowed comparison to non-diseased controls, thus avoiding the need for technically challenging apparent mechanical characterisation of these specimens.

There were some issues with samples becoming slightly off-axis during testing causing short irregularities in the force-displacement data, as a couple of specimens moved within the endcaps before bedding-in sufficiently. These specimens were re-embedded within the endcaps until the issue was resolved, and the creep curve was satisfactory. Similarly to the porcine tissue, the specimen preparation was limited by the use of a scalpel to trim the ends of the bone and hence the surfaces would not be completely flat against the inside of the endcaps despite best efforts to sand the surfaces down. Therefore improvements to the specimen preparation of the bone cores would greatly improve the reliability of the mechanical testing.

The optimisation results for both ankle bones showed good correlation and agreement of both hFE and μFE model calibrations. As before, structural and material variation in the tissue samples is expected, hence the limited numbers of cadaveric donor tissue in this study cannot capture regional variations to morphology and its potential impact on stiffness. If trabecular morphology varies widely across the talar dome for example, it may mean that regional-specific material optimisations are required. This cannot be evaluated without a larger dataset.

The literature suggests that late-stage OA bone will have higher apparent stiffness than non-diseased bone, due to the higher bone density and trabecular thickness that compensates for reduced material properties [Chu et al., 2020, Chen et al., 2018, Li and Aspden, 1997a, Radin and Rose, 1986]. This is debated, as some report reduced apparent stiffness with OA [Burr, 2004], but these studies tend to characterise less severely arthritic bone [Day et al., 2001, Zysset et al., 1994, Ding et al., 1998]. For example, Zysset et al. found reduced elastic modulus with disease progression in human knees, with a strong dependency on bone level (taken in 3 and 6 mm intervals). Only one donor had moderate-late OA (grade III), and no severe (grade IV) bone samples were studied [Zysset et al., 1994]. In this study, ankle OA bone was found to have significantly higher apparent stiffness compared to ND bone (Fig. 7.8). However, this was based on the assumption that E_{tiss} is unaffected by the disease in the ankle. Studies utilising nanoindentation to directly evaluate changes to tissue mechanical properties have shown that E_{tiss}

is higher with OA [Zuo et al., 2016, Peters et al., 2018]. Hence, the sensitivity of ankle OA tissue to these values was characterised (Fig. 7.9). The study by Peters et al. lacked severe OA specimens, and therefore the values of Zuo et al. were considered to be more representative of late-stage OA values and therefore most appropriate to utilise, despite a lack of control samples. Even with a reduced tissue modulus, tibial specimens were still significantly stiffer than controls, which suggests that the change in microstructure is more significant than reduced tissue properties [Chen et al., 2018].

All specimens showed a linear relationship between E_{tiss} and apparent stiffness (Fig. 7.9), which was expected for a linear analysis [Bourne and van der Meulen, 2004, Chevalier et al., 2007]. Three specimens showed higher sensitivity to knee values of E_{tiss} (Tib 1, Tib 2, Tib 3 and Tib 5). These specimens were found to have higher density (BV/TV), reduced anisotropy (DA) and higher trabecular thickness (Tb.Th) compared to the other OA specimens (values reported in Chapter 4). Osteoarthritic bone quality has been shown to vary by region [Day et al., 2001, Jaasma et al., 2002]. Hence, as observed with the ND specimens, the mechanical properties of OA tissue is also highly influenced by variations to microarchitecture. Interestingly, one study demonstrated that a reduced tissue modulus can result in generally more stiffer bone with OA, and that alterations to microstructure, rather than mineralisation, plays more of a role in variations to apparent stiffness [Chen et al., 2018].

For ND specimens, variations to apparent stiffness were found to predominantly originate from BV/TV and DA (Fig. 7.7), as demonstrated in other studies [Maquer et al., 2015, Matsuura et al., 2008]. For the smaller volumes, BV/TV, Tb.Th, EF and SMI had higher impact on variations to apparent stiffness (Table 7.5). This reiterates the impact of trabecular thickness and trabecular morphology on bone mechanical properties. Moreover, the ITS-based morphological results showed high correlation of μFE stiffness to plate volume fraction (pBV/TV) and axial bone volume fraction (aBV/TV) in both bones (Table 7.6). These results show the dependency of apparent stiffness on the trabecular orientation and specifically, plate-like trabecular structures [Ding et al., 2003, Stauber et al., 2006, Wang et al., 2015, Chen et al., 2018]. Similarly, for OA tibial specimens, high correlation was observed between apparent stiffness and BV/TV, as expected [Burr and Gallant, 2012]. Moreover, plate fraction (pBV/TV), plate trabecular density (Tb.N) and the volume fraction of bone aligned with the joint surface (aBV/TV) also correlated well with OA apparent stiffness, which agrees with the results observed in similar studies [He et al., 2020, Chu et al., 2020]. However, strong negative correlation was observed between apparent stiffness and SMI (r=-0.96; increasing plate-like trabeculae may result in lower apparent stiffness). This is contrary to previous results, but may be due to the limitations of using SMI versus EF [Doube, 2015], which here showed positive correlation between stiffness and EF value (increasingly rod-like trabeculae results in higher stiffness). Overall, these results and the trends observed in Chapter 4, show that in ankle OA bone, increased presence of plate-like trabeculae and changes in trabecular orientation may be related to the observed apparent increase in mechanical stiffness.

This study was limited by the lack of age-matched samples available. Non-diseased ankle tissue typically originates from younger patients than those being referred for late-stage treatments (total ankle arthroplasty or arthrodesis), so this remains an unavoidable study limitation. Future studies should look to increase the study power to minimise the impact of variations to microarchitecture across the specimens, and aim to evaluate tissue modulus directly, which is suspected to alter with OA [Zysset et al., 1994, Day et al., 2001, Ding et al., 2003, Zuo et al., 2016, Peters et al., 2018].

This study demonstrated that the inverse FE methodology can be translated for use on human tissue, showing good agreement during model calibrations and validations. The use of ND tissue properties on OA specimens showed higher apparent stiffness in the OA specimens, with microarchitecture playing a key role in variations to stiffness for both ND and OA groups. However, direct measurement of tissue modulus is required in order to validate the conclusion that ankle subchondral bone becomes stiffer with OA.

Chapter Summary

- Image-based specimen-specific inverse FE methodology was successfully translated for use on human tissue, leading to an estimate tissue modulus for both distal tibia and talar subchondral bone.
- Good agreement was observed for calibration and validation of both hFE and μFE models.
- Microarchitecture played a significant role in variations to apparent stiffness - predominantly BV/TV and DA but also trabecular morphological properties (pBV/TV, aBV/TV, pTb.N, rTb.Th etc.).
- Increased apparent stiffness was observed in OA specimens when using ankle ND tissue modulus values and increased tissue properties obtained from the literature.
- Significant increases to apparent stiffness in tibial specimens was observed even with a reduced tissue modulus, suggesting a more significant contribution from altered microstructure than from tissue properties.
- Further investigation is required through direct measurement (nanoindentation) to verify an increased apparent stiffness is observed with OA, but the OA models in this study showed an increased apparent stiffness with increased tissue properties obtained from knee studies.

Chapter 8

Characterising Tissue-level Changes to OA Subchondral Bone using Nanoindentation

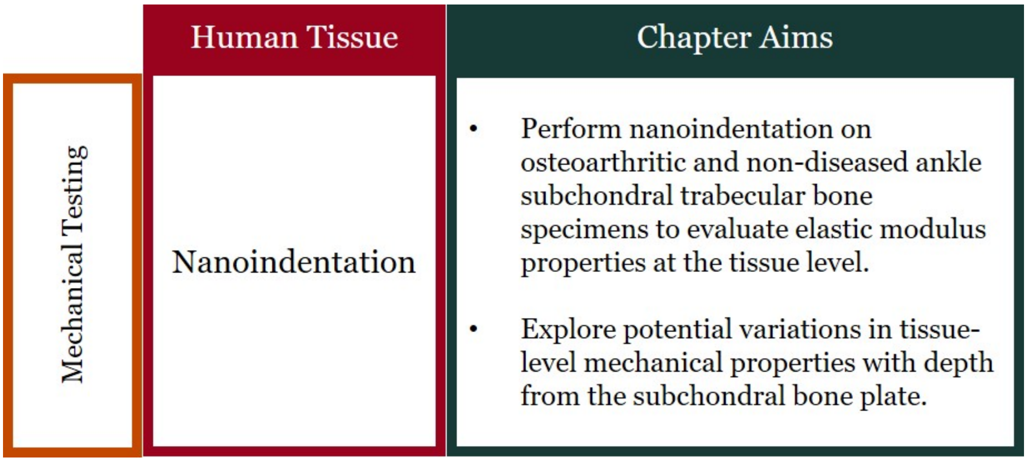

- Perform nanoindentation on osteoarthritic and non-diseased ankle subchondral trabecular bone specimens to evaluate elastic modulus properties at the tissue level.
- Explore potential variations in tissue-level mechanical properties with depth from the subchondral bone plate.

This chapter explores changes to matrix-level mechanical properties with OA using the depth sensing technique, nanoindentation. This technique is advantageous due to its ability to characterise small volumes of tissue, measuring stiffness of adjacent lamellae at 1μm resolution. This provides a precise means of characterising fragments of *ex vivo* osteoarthritic bone available from ankle surgeries where apparent level measurements are not possible due to the small and irregular shape of the samples. In this way, one can determine directional micromechanical properties and the observe changes, if any, with osteoarthritis. This study was conducted in collaboration with Dr Uwe Wolfram and Mr Samuel McPhee at Heriot-Watt University.

8.1 Introduction

Bone is a hierarchical material; its macroscopic behaviour is affected by the contributions of changes to mechanical, compositional and architectural properties at lower hierarchical levels. Depth-sensing indentation techniques with high spatial resolution, such as nanoindentation, can be used to directly measure the elastic properties of the bone matrix [Oliver and Pharr, 1992]. Other methods include acoustic microscopy (ultrasonic testing), but the waves can become heavily attenuated by trabecular spaces [Rho, 1996]. Similarly, micropillar compression tests could be performed, but challenges arise in sample preparation of individual trabeculae [Wu et al., 2018]. The results of nanoindentation studies, predominantly of bone from the hip and knee joints, can vary highly due to differences in sample preparation and indentation protocol [Wu et al., 2018, Zysset, 2009, Bushby et al., 2004]. However, nanoindentation provides a means of directly measuring lamellar or osteonal mechanical properties of trabecular bone, providing an insight into the changes with osteoarthritis at this level independent of macro- or micro-structure. Previous studies report increases to elastic modulus of subchondral trabecular bone in the late-stage osteoarthritic knee [Peters et al., 2018, Zuo et al., 2016]. One study of early-stage osteoarthritic bone in the proximal tibia back-calculated tissue mechanical properties in μFE models from macroscopic testing, and this found a 50% decrease in matrix modulus [Day et al., 2001]. However, such a method of establishing tissue properties can result in lower measures of tissue moduli compared to those measured directly [Chevalier et al., 2007]. To date, no studies have reported on the tissue properties of ankle subchondral bone with or without osteoarthritis.

8.1.1 Study Aims

This study aimed to characterise the micro-mechanical properties of ankle subchondral bone using nanoindentation to determine if there is a significant difference in tissue modulus when comparing non-diseased and osteoarthritic tissue. The following objectives were defined:

- Perform nanoindentation to evaluate the matrix-level properties of control (non-diseased cadaveric) and osteoarthritic (*ex vivo*) ankle subchondral trabecular bone specimens to evaluate changes to tissue modulus with osteoarthritis.
- Evaluate the sensitivity to tissue properties with depth in ankle subchondral bone.

8.2 Materials and Methods

Pairs of distal tibia and tali were dissected from three human, non-diseased (ND) cadaveric feet as outlined in Section 3.1.3. Specimens were extracted from leftover whole bone pieces following removal of cylindrical bone cores used in Chapter 7. Two 5 mm slices of trabecular bone were removed from three locations in the central sagittal plane of each talus and two locations in each distal tibia piece. A total of thirty specimens were cleaned of marrow using a waterpik and embedded into resin. OA samples (N=6 distal tibial and N=5 talar, Appendix C.2.2) from three patients were prepared in a similar fashion. A tibial sample from donor RM58 was unusable due to damage likely induced during resection. To account for this and to ensure a comparative number of indents were conducted for OA samples, two additional sections were taken from two tibial samples from RM65. A total of 12 tibial and 16 talar OA specimens were available for testing.

Total inclusion of resin into the trabecular pore spaces was not achieved by the positive pressure curing process for ND specimens. Therefore, indentations were chosen in transverse lamellae regions close to transecting axial orientated trabecular to mitigate bending of unsupported substructures (Fig. 8.1).

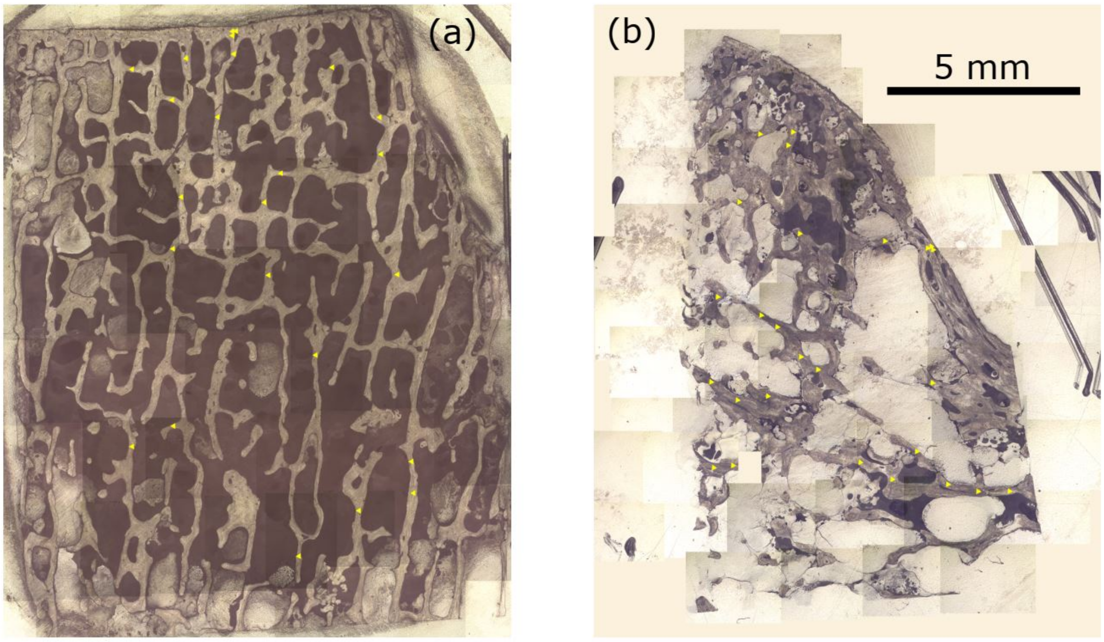

Figure 8.1: Stitched microscope images of RM50 2B (a) and LM43 2C talar specimens (b). (a) shows lack of resin infiltration into pore spaces during sample preparation. (b) shows a thin sectional cut where total inclusion was achieved. Yellow triangles indicate the indentation locations for the samples.

Fig 8.1 (a) shows the the inclusion of resin into the samples was most prevalent around the perimeter of the sample adjacent and opposite to the SBP. Inclusion was limited inward of the SBP such that any influence of structural compliance would be consistent across the length of the sample.

The protocol was amended to optimise the embedding process for OA specimens. Firstly, to prevent the specimens rising from the bottom of the moulds during curing, a small amount of PMMA was placed on the bottom of the mould and the top face of the specimen was dipped into PMMA to secure the face of the specimen to the bottom of the mould. The curing pressure was also reduced to 1 bar to further promote the infiltration of the resin into trabecular spaces, with fewer specimens (four) per batch. Specimens were examined under a microscope to evaluate the success of the adjusted methodology, which confirmed improved infiltration of resin into trabecular spaces (Fig. 8.2).

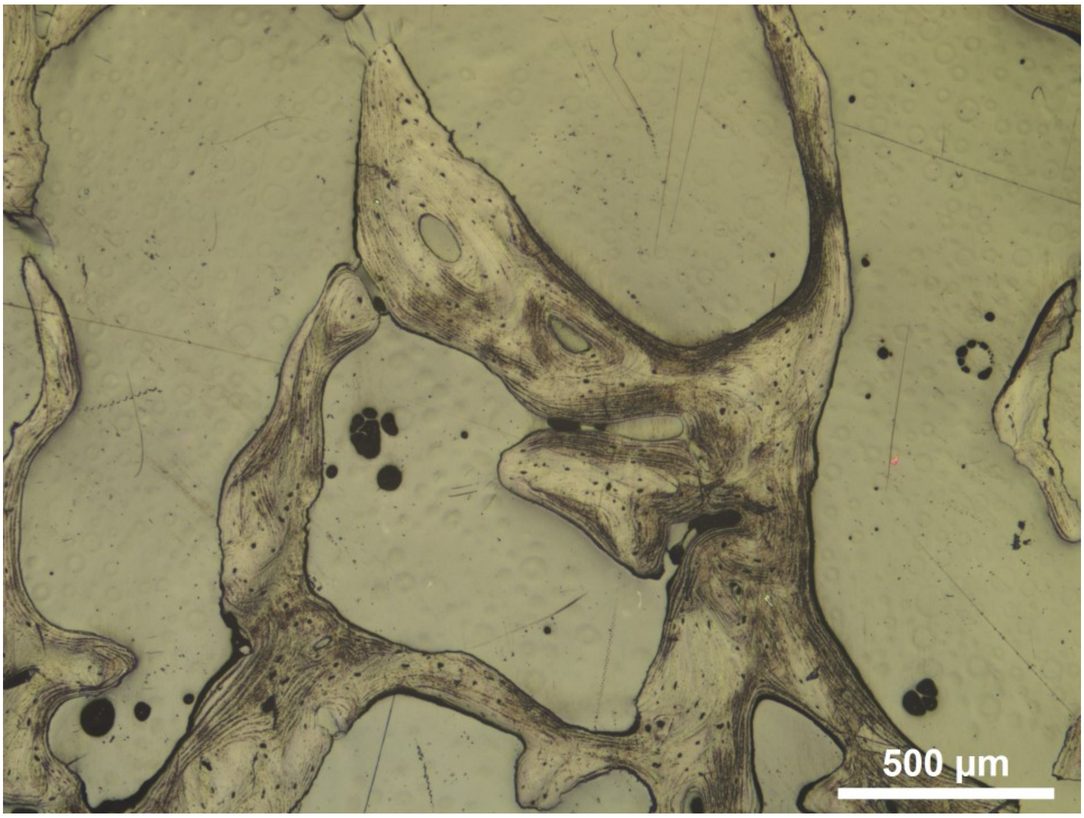

Figure 8.2: Microscope image of exemplary OA specimen showing improved infiltration of resin into the trabecular spaces.

Multiple polishing steps using progressively decreasing particle size were used to ensure the surfaces were smooth for nanoindentation testing (as described in Section 3.1.3.b). The micro-mechanical properties of each specimen were established using nanoindentation (as outlined in Section 3.5.2). Three initial indents per sample were conducted at the subchondral bone plate (SBP) region to establish a reference X-Y co-ordinate system. Tissue-modulus was taken from the unloading portion of the force-displacement curve and averaged over all distal tibia, $\overline{E}_{\text{tiss,tib}}$ and talar, $\overline{E}_{\text{tiss,tal}}$ specimens. Depth-dependence of E_{tiss} was established by grouping the data into intervals of 5 mm distance from the SBP. These were labelled as follows:

- Level 1 = 0.00 - 4.99 mm
- Level 2 = 5.00 - 9.99 mm
- Level 3 = 10.00 - 14.99 mm
- Level 4 = 15.00 + mm

For OA samples, the maximum achievable distance from the subchondral bone plate was limited by the sample originating from surgical procedures. For this reason, the distribution of indents was limited to 0-5 mm (Level 1) and 0-9 mm (Level 1 & 2) for talar and tibial samples, respectively.

8.2.1 Statistical Analysis

The mean (AVG), standard deviation (± SD) and coefficient of variance (CoV, %) for tissue elastic modulus, E_{tiss} were calculated. Independent samples t-test with Bonferroni correction ($\alpha = 0.05$) was used to compare significant differences in stiffness values between each bone, with disease and with depth from the SBP.

8.3 Results

The raw data are reported in Appendix C.

8.3.1 Non-Diseased Tissue

In total, 725 indentations were performed on 29 samples (one talar sample was omitted from the study due to lack of distinguishable SBP). Accounting for reference and inutile indentations (due to transducer noise and premature depth sensing) left a total of 627 indents for analysis (361/425 programmed tests for talar specimens and 266/300 programmed tests for tibial specimens). Mean, minimum and maximum specimen tissue modulus, E_{tiss}, are reported for grouped distal tibia and talar specimens (Table 8.1).

	E_{tiss} **(GPa)**		
	Min	Max	AVG ± SD
Distal Tibia	1.31	18.35	8.00 ± 3.02
Talus	1.66	16.42	8.09 ± 2.78

Table 8.1: Summary data for non-diseased distal tibia and talar samples. Minimum (min), maximum (max) and mean (AVG ± standard deviation, SD) values reported for tissue modulus, E_{tiss}.

There were no significant differences between average tibial and talar E_{tiss} values ($p>0.05$). Intra-donor variations in average E_{tiss} was evaluated (Fig. 8.3). Increased mean E_{tiss} was observed with age in talar specimens LM43 and RM50 (p<0.001).

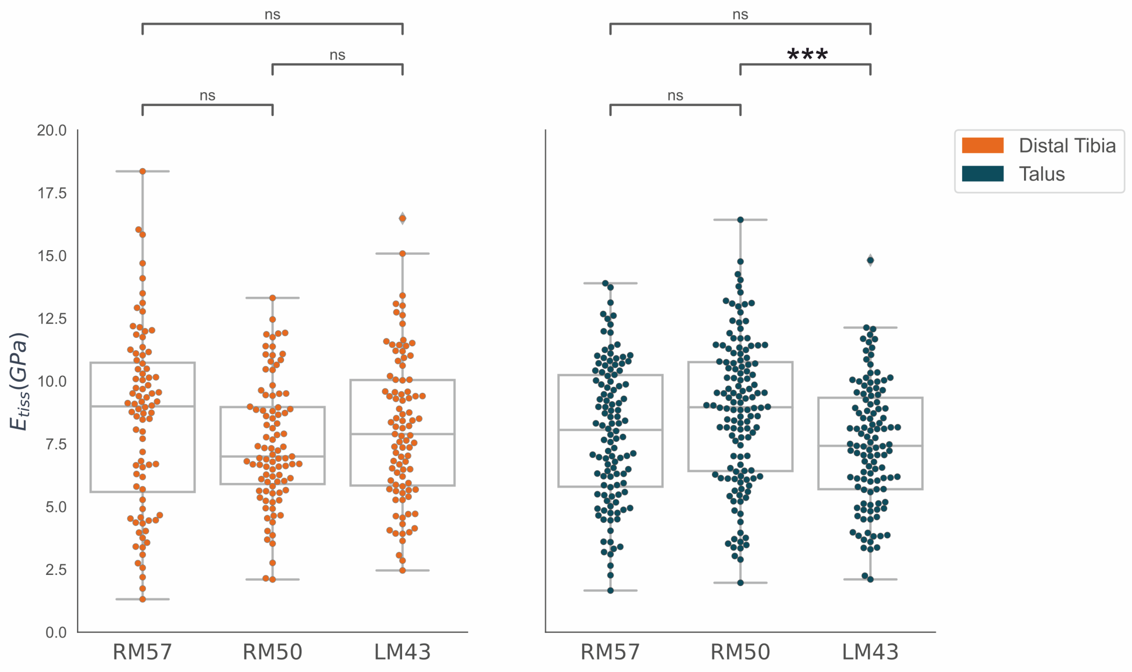

Figure 8.3: Intra-donor variation in E_{tiss} in the distal tibia and talus. Boxplots represent the median and interquartile range of values. Significance indicated using: * p<0.05, ** p<0.01, *** p<0.001, or ns (not significant).

8.3.1.a Tissue Properties with Depth

It was observed that there was a significant depth-dependence (p<0.05) of indentation properties (Fig. 8.4). The outliers were removed and in this way, the absence of resin inclusion mentioned previously is thought to have a negligible effect on the observed results. A decreasing trend in E_{tiss} was observed with depth from the SBP in both ankle bones. Level 4 of the talus and Level 3 of the tibia showed the highest variations in mean E_{tiss} (Table 8.2).

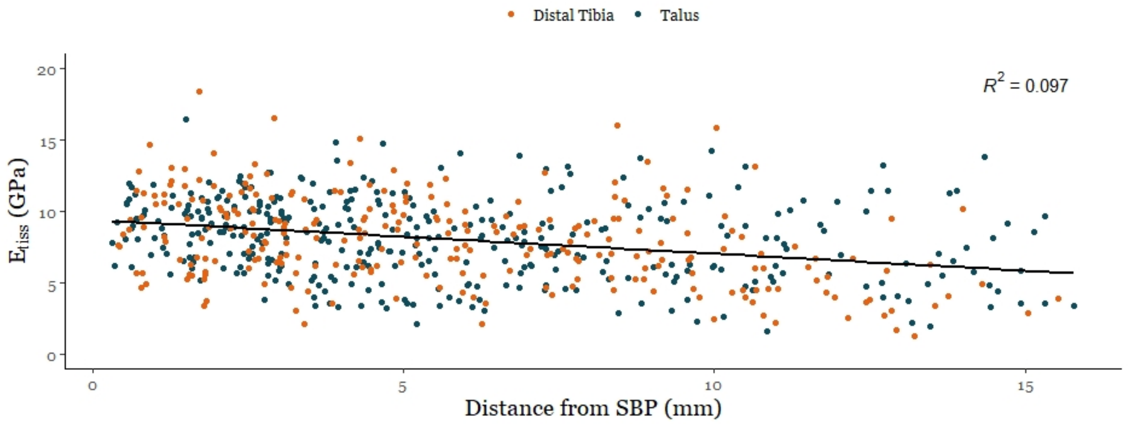

Figure 8.4: Influence of increasing depth from the SBP (mm) on tissue modulus, E_{tiss} (GPa) for distal tibia and talar specimens. Line depicts a linear regression between distance and elastic modulus (r^2=0.097).

Table 8.2: Summary data of depth-dependent tissue elastic properties in the ankle.

Level	Bone	N	Avg. E_{tiss} (GPa)	± SD	CoV (%)
1	Distal Tibia	133	8.84	2.87	32
	Talus	191	8.72	2.46	28
2	Distal Tibia	91	7.90	2.59	33
	Talus	111	7.56	2.88	38
3	Distal Tibia	40	5.65	2.96	52
	Talus	55	7.13	3.03	43
4	Distal Tibia	2	3.39	0.54	16
	Talus	4	6.30	2.83	45

In the distal tibia, there was significant decreases in mean E_{tiss} between all levels except 2 & 4, and 3 & 4 ($p>0.05$) (Fig.8.5i). In the talus however, significant differences were only observed between level 1 & 2 ($p<0.001$) and 1 & 3 ($p<0.001$) (Fig.8.5ii).

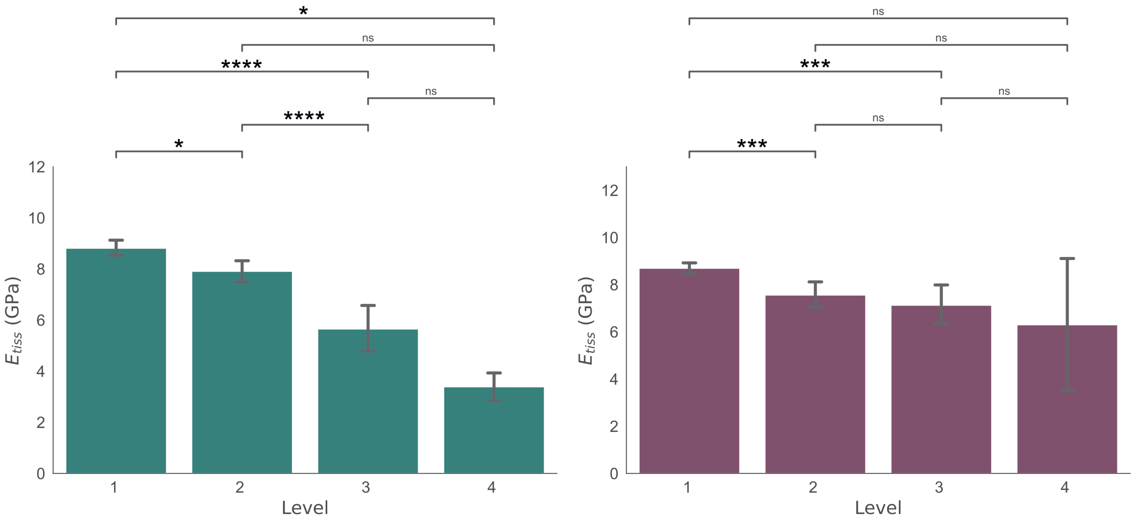

(i) Depth-dependence of E_{tiss} in the distal tibia.

(ii) Depth-dependence of E_{tiss} in the talus

Figure 8.5: Average E_{tiss} in 5 mm distance intervals from the SBP for specimens from the distal tibia (8.5i) and talus (8.5ii). Bar plots show AVG (bars) ± SD (error bars). Significance is indicated by: * p<0.05, ** p<0.01, *** p<0.001,**** p<0.0001, ns = not significant.

8.3.2 Osteoarthritic Tissue

A total of 553 indents were successful out of a total of 775 programmed indents. Failed indents resulted from premature depth sensing leading to large displacement registration prior to tissue contact. One talar sample (from donor LM68) was tested but omitted from the grouped data (Table 8.3), as a different load function was used. As mentioned previously, the OA samples had insufficient sample depth to allow a full comparison at all depth levels (Fig. 8.6). A total of N_{OA}=553 and N_{ND}=627 indents were available for comparison.

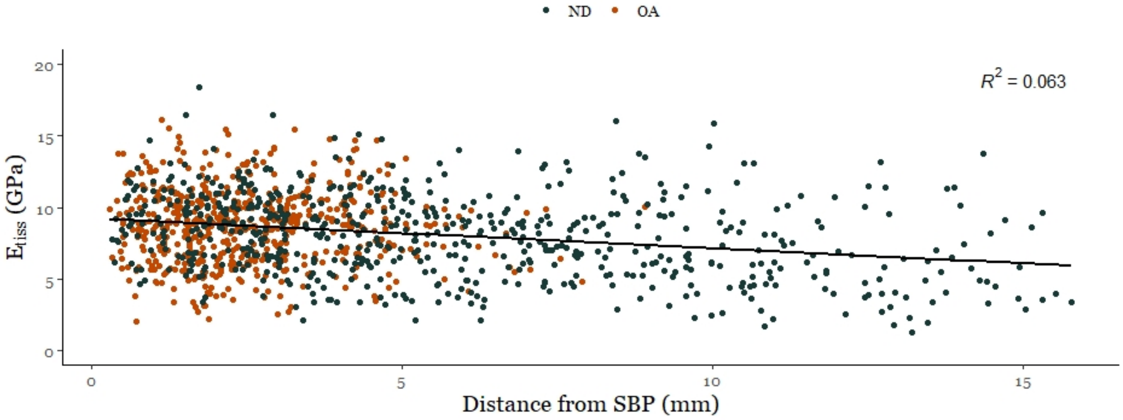

Figure 8.6: Influence of increasing depth from the SBP (mm) on tissue elastic modulus, E_{tiss} (GPa) for ankle OA and ND specimens. Line depicts a linear regression between distance and tissue modulus for all specimens (r^2=0.063).

The results show an increase in mean tissue modulus with osteoarthritis compared to controls ($p<0.0001$, Fig. 8.7). Significant increases were observed between average ND and OA E_{tiss} values in both tibial ($p<0.01$) and talar ($p<0.01$) subchondral bone.

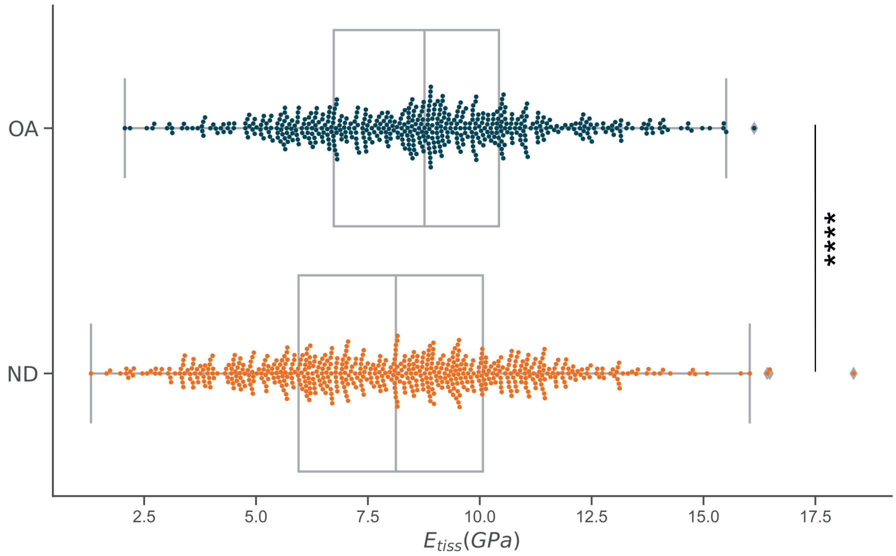

Figure 8.7: Comparison of OA and ND ankle bone E_{tiss} values. Boxplots represent the median and interquartile ranges of values. Significance is indicated by: * $p<0.05$, ** $p<0.01$, *** $p<0.001$,**** $p<0.0001$, ns = not significant.

	E_{tiss} **(GPa)**		
	Min	Max	AVG ± SD
Distal Tibia	2.07	15.51	8.97 ± 2.73
Talus	2.69	16.13	8.68 ± 2.54

Table 8.3: Summary data for distal tibia and talar osteoarthritic samples. Minimum (min), maximum (max) and mean (AVG ± standard deviation, SD) values reported for tissue modulus, E_{tiss}.

Unlike the ND control samples, there was no observed significant depth dependency in tissue modulus (Fig. 8.8). Evaluation of bone-specific data (Table 8.4) found no significant differences tissue modulus in Level 1 or 2 with OA in the distal tibia or in Level 1 of the talus ($p>0.05$). Mean E_{tiss} was found to decrease in Level 1 of OA specimens (tibial and talar) compared to the values reported for the equivalent ND specimens (Table 8.2).

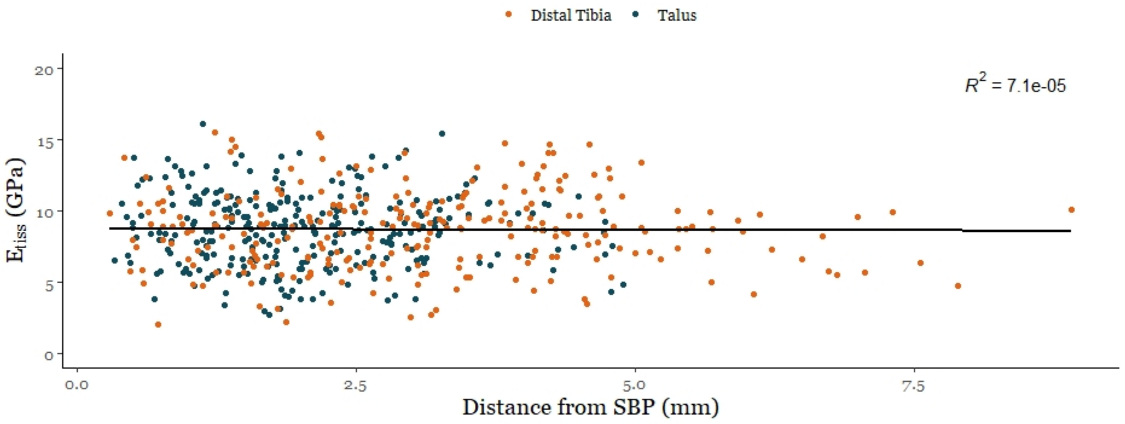

Figure 8.8: Influence of increasing depth from the SBP (mm) on tissue elastic modulus, E_{tiss} (GPa) for distal tibia and talar OA specimens. Line depicts a linear regression between distance and tissue modulus for all specimens (r^2 = 7.1e-05.)

Table 8.4: Summary data of tissue elastic properties in the osteoarthritic ankle at depth level 1 and 2.

Level	**Bone**	**N**	**Avg.** E_{tiss} (GPa)	± **SD**	**CoV (%)**
1	Distal Tibia	233	8.79	2.80	32
	Talus	290	8.68	2.54	29
2	Distal Tibia	30	7.93	2.00	25
	Talus	0	-	-	-

As observed with ND specimens (Fig. 8.3), an increasing trend in mean E_{tiss} was observed with donor age in the talus ($p<0.05$) and distal tibia ($p<0.01$) (Fig. 8.9).

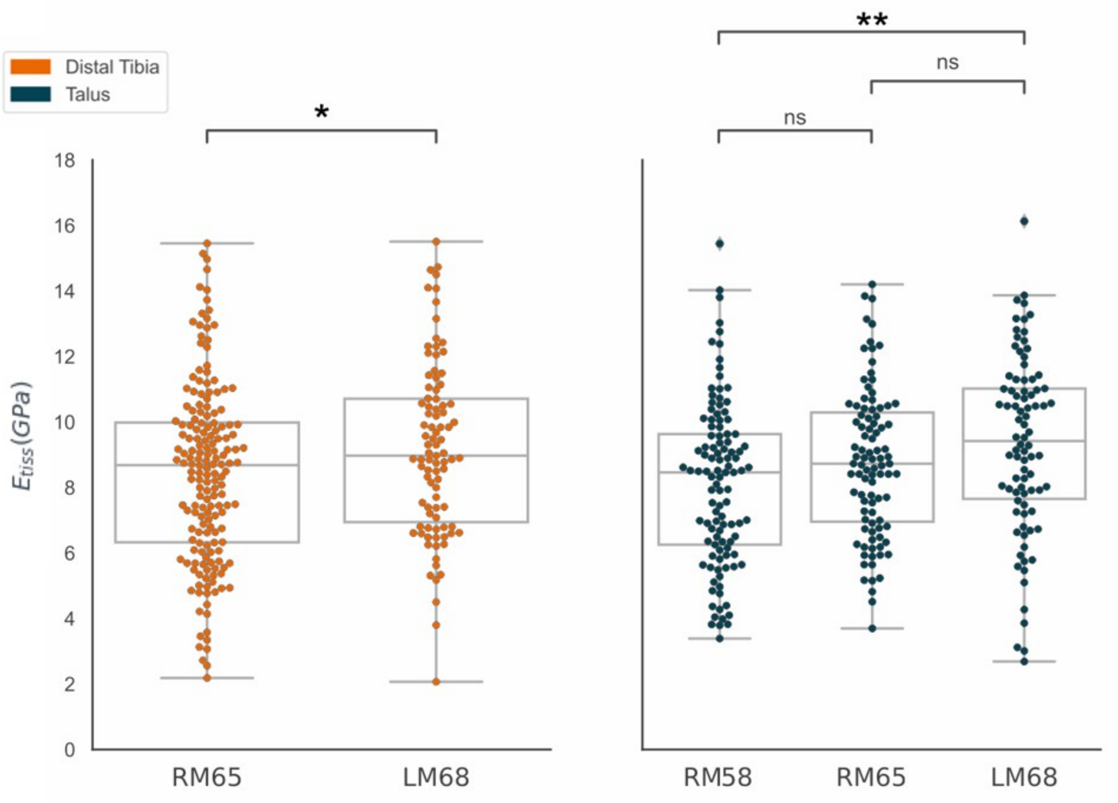

Figure 8.9: Intra-donor variation in E_{tiss} in the osteoarthritic ankle. Boxplots represent the median and interquartile ranges of values. Significance is indicated by: * $p<0.05$, ** $p<0.01$, *** $p<0.001$,**** $p<0.0001$, ns = not significant.

8.4 Discussion

This study aimed to characterise tissue-level properties of late-stage osteoarthritic ankle subchondral trabecular bone with comparison to non-diseased controls. Overall, the results show an apparent increase in tissue properties with OA in the ankle joint. Depth sensitivity was observed in ND tissue only, and non-significant small decreases in tissue properties were observed in Level 1 of OA tissue for both ankle bones.

This study found increased mean E_{tiss} values in grouped (tibial and talar combined) late-stage OA bone, but also when comparing each bone separately. This result aligns to other studies that have shown increased tissue properties with OA using nanoindentation [Peters et al., 2018, Zuo et al., 2016]. Peters et al. found increases to tissue properties in subchondral bone specimens with late-stage osteoarthritis, but not in trabecular bone [Peters et al., 2018]. They also reported a positive correlation between tissue modulus and age, as observed in this study. However, they did not specify the depth of bone that was used for testing or the depth at which they define subchondral and trabecular bone, which may explain their observed lack of correlation with OA in the trabecular dataset. Zuo et al. also found increased tissue properties in osteonal and lamellar regions with the progression of OA in the *ex vivo* knee specimens they tested [Zuo et al., 2016]. They also reported an increased crystallinity of the calcium-phosphate phase in grade IV bone, which may result in reduced bone remodelling and therefore the sclerotic, denser bone that leads to increased stiffness. However, in both literature studies the samples were tested dehydrated. Wet indentation is more physiologically relevant [Lewis and Nyman, 2008] and specimen dehydration will alter the measured modulus values resulting in higher stiffness [Bushby et al., 2004]. Therefore limiting comparisons of the results of this study to the literature.

Late-stage OA bone is known to have imbalanced remodelling, where bone resorption decreases without reduced rate of bone formation, resulting in subchondral "sclerosis". Despite increased bone density, late-stage OA subchondral bone is also known to be hypomineralised [Burr and Gallant, 2012, Li et al., 2013, Li and Aspden, 1997a] and studies in the hip [Tomanik et al., 2016, Li and Aspden, 1997a] and proximal tibia [Renault et al., 2020, Cox et al., 2012] have reported sensitivity of mineralisation with depth into the joint. It is reasonable to hypothesise that tissue material properties would also decrease as a result of decreased mineralisation [Day et al., 2004b, Li and Aspden, 1997b]. Chapter 4 showed that the first few levels of bone are more dense and plate-like with the progression of OA. Depth sensitivity of tissue modulus was only observed in ND specimens however, and although limited OA data was available at lower depth levels, slight decreases (non-significant) in tissue properties were found in the upper levels in both bones. It is thought that increases in bone density and reduced bone material stiffness could contribute to cartilage degradation [Karsdal et al., 2008], despite an increase in apparent stiffness. Hence, future work could investigate potential changes to mineralisation in ankle subchondral bone to verify the cause of the increased tissue material properties observed in this study.

Nevertheless, at the matrix level bone mineralisation has been found to have minor impact on the overall mechanical behaviour of bone [Gross et al., 2012]. Chapter 5 highlighted the sensitivity of apparent mechanical properties to changes in tissue modulus, where even a 20% reduction in tissue properties in OA tissue can results in significantly higher apparent stiffness compared to controls. Further μFE modelling of OA bone could be performed in future, using the tissue properties measured in this study, to verify that increased apparent stiffness is observed with OA. These studies have demonstrated that the observed increased apparent stiffness with OA originates more significantly from changes to microarchitecture, rather than tissue properties, but analysis of the correlation of tissue properties to variations in apparent stiffness is needed.

This study was limited by the low donor sample size, and the insufficient depth of the OA samples to allow for a full comparison to the ND tissue at each depth level. OA *ex vivo* tissue from surgery is limited in size due to the surgeon's need to minimise tissue resection, particularly from the talar dome, but also varies in its geometry. Hence, it became challenging to prepare consistent samples for embedding, as the samples were very fragile and irregular in size and shape. The differences in sample volume and available indentation points will affect the conclusions drawn by the results of E_{tiss} in OA samples compared to ND controls, limiting the comparison. Depth-specific analysis showed no significant differences in E_{tiss} in Level 1 of either bone, or Level 2 for the distal tibia. Hence, further work is needed to investigate the observations in this study across a larger dataset and at lower depth levels.

In summary, this study found apparent increases to tissue modulus in late-stage OA in the ankle. However, depth-specific analysis showed slight decreases to tissue modulus in the upper levels of both the distal tibia and talus with OA. Further work is needed to verify apparent mechanical changes using the values obtained in this study and explore the trends observed in this study with a larger sample size. Similarly, the evaluation mineralisation could help to understand the remodelling mechanisms taking place with the progression of OA in the ankle and its potential impact on bone quality.

Chapter Summary

- Grouped results revealed a significantly higher tissue elastic modulus with OA compared to controls ($p<0.0001$).
- Bone-specific evaluation showed higher E_{tiss} in the distal tibia ($p<0.01$) and talus ($p<0.01$) in OA specimens compared to controls.
- Depth-specific analysis showed slight reductions in tissue modulus with OA ($p>0.05$).
- Lower levels of ND ankle subchondral trabecular bone had lower material stiffness compared to bone near the joint surface, but insufficient data was available to verify this in the OA ankle.

CHAPTER 9

DISCUSSION

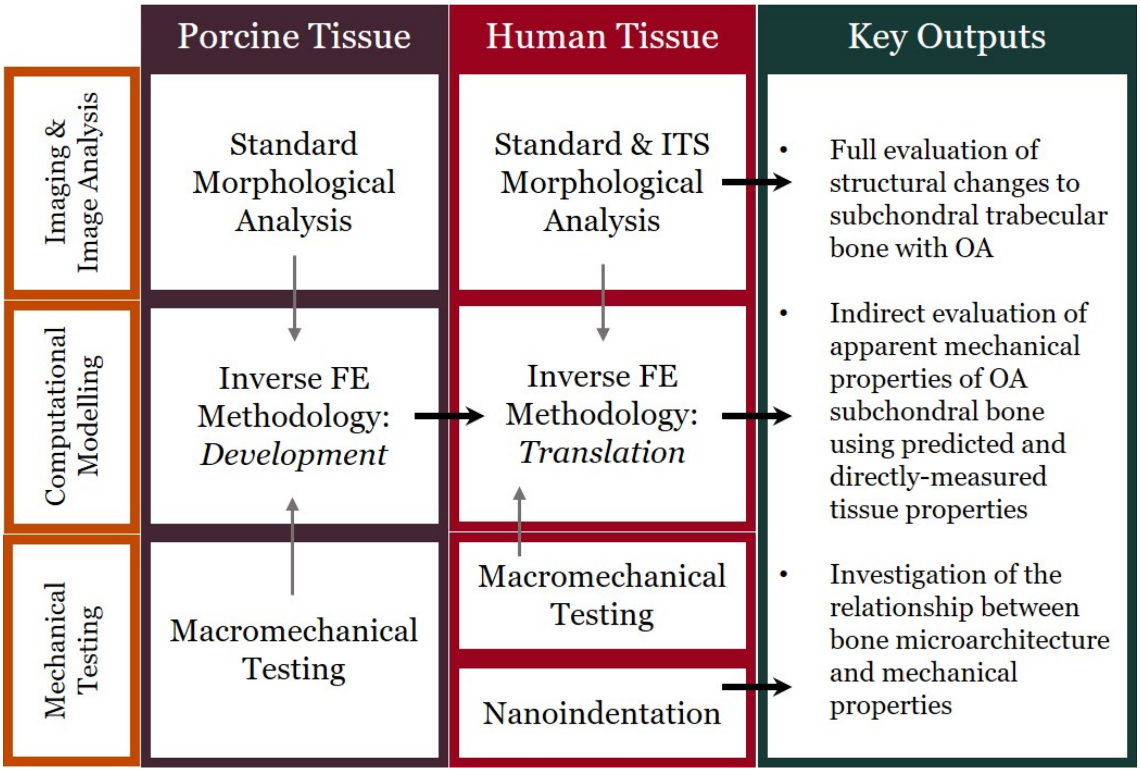

Figure 9.1: Research overview.

The overall aim of the studies compiled within this thesis was to characterise the structural and mechanical changes with osteoarthritis (OA) in ankle subchondral trabecular bone. This was achieved using standard and 3D individual trabecular segmentation (ITS) morphological analysis of OA specimens retrieved from total ankle arthroplasty surgeries compared to cadaveric, non-diseased (ND) controls (Chapter 4). An inverse finite element (FE) methodology was developed to indirectly obtain tissue mechanical properties of bone using porcine specimens (Chapters 5 & 6), and successfully translated for use on human ND specimens (Chapter 7). This provided an optimised linear relationship between element grayscale and elastic modulus specific to ankle bone, and an estimate of the tissue-level properties of ND human ankle bone with an insight into the relationship between ankle bone microarchitecture and stiffness. Furthermore, this also presented the opportunity to indirectly evaluate the apparent stiffness of OA bone, using μFE modelling, and explore the sensitivity to changes in tissue modulus. Nanoindentation directly characterised these micro-mechanical changes to allow a comparison of ND and OA ankle subchondral trabecular bone tissue properties (Chapter 8). The evaluation of the structural and mechanical alterations to subchondral trabecular bone provides the foundations from which we can begin to understand how osteoarthritis progresses in the ankle compared to other joints and how this affects bone quality. This information is critical to the development of novel ankle replacement devices, or other less-destructive interventions, such as resurfacing or osteochondral graft replacements.

9.1 Implications: New Insights to Bone Changes with OA in the Ankle

In the literature, osteoarthritic changes to subchondral bone in the ankle joint remain highly under-reported. However, this work has shown that significant structural and multiscale mechanical changes occur in the late-stage OA ankle. This work has verified key changes to subchondral bone with OA that are observed in other joints are also present in the ankle, including higher BV/TV, DA and apparent stiffness.

Morphological evaluation (Chapter 4) illustrated the significant architectural alterations that occur during the advancement of OA in ankle subchondral trabecular bone. Whilst the observed changes to standard morphological properties agreed with the literature [Chen et al., 2018, Chu et al., 2020, Burr, 2004], a comparison to the few studies available in the literature that characterise rod and plate combinations showed that ankle subchondral bone does not suffer trabecular rod loss as observed in the arthritic knee [Chen et al., 2018], or the numerous changes in the hip [He et al., 2020]. This may be due to differences in surface contact area between the joints, resulting in a differences to the stresses applied to the cartilage and therefore affecting the remodelling rate of the bone. Comparing to the knee, the ankle joint has much thinner cartilage [Treppo et al., 2000], and so as the cartilage deteriorates with OA, the stress applied to the underlying subchondral bone in the ankle is much higher with respect to that experienced in the knee. This may produce unique remodelling events that are specific to the ankle and are points of focus for future investigations into the potential mechanisms that cause and progress OA alterations in the ankle.

An inverse FE methodology was developed using porcine tissue (Chapter 6) and translated for use on ND human tissue (Chapter 5) in order to characterise OA bone *in silico*. The foundations of this modelling methodology originate from work on vertebral modelling [Day et al., 2020, Zapata-Cornelio et al., 2017, Wijayathunga et al., 2008], which demonstrated the viability of a simpler, linear relationship between element grayscale and elastic modulus for whole vertebrae, as well as individual bone cores. The results presented in Chapter 5 showed good agreement between experimental and computational stiffness, despite the higher variation of tissue morphological properties compared to the porcine tissue used for the developmental work (Chapter 6). Thus, these studies have demonstrated the successful translation of an existing modelling methodology to ankle subchondral bone. With improved specimen preparation and a larger dataset, the agreement is expected to improve. The development of calibrated, specimen-specific whole ankle bone models could then be developed and used to model the behaviour and characterise potential failure modes of a total ankle replacement in a patient-specific bone model generated solely using CT images. The initial steps towards this was achieved in the development of the ankle-specific grayscale-elastic modulus relationship, as part of the inverse-FE methodology.

The combination of FE modelling in Chapter 5 and morphological analysis in Chapter 4 confirmed that, on a macroscopic scale, ankle subchondral trabecular bone mechanical behaviour can be predicted using bone density (BV/TV) and trabecular orientation (DA), predominantly, as observed in numerous other joints [Maquer et al., 2015]. The addition of 3D ITS analysis highlighted the significance of certain trabecular properties, such as plate density and plate fractions, on variations to apparent stiffness. This type of analysis, in combination with mechanical data, is scarce in the literature for healthy or diseased bone.

Correlations to ND bone stiffness and ITS microarchitectural properties verified that plate fraction (pBV/TV) and the direction of the bone (aBV/TV) are the dominant properties in determining the mechanical stiffness of (tibial) bone in the ankle (Chapter 7) [Wang et al., 2015]. However, with osteoarthritis this is reduced slightly, as the ratio of rod to plates alters with imbalanced remodelling. For a total ankle replacement (TAR), good bone quality is essential to avoid instability. Whilst apparent bone stiffness was found to increase with OA, the higher density of rod-like trabeculae may increase the risk of TAR failure due to insufficient strength. This is of particular concern as the stronger plate-like trabeculae near the joint surface is removed during implantation, and that bone density reduces with depth (Chapter 4) [Harnroongroj et al., 2019]. Hence, the use of more conservative early-stage OA surgical treatments, such as the HemiCAP talar dome resurfacing implant, may help to minimise OA progression by replacing OA regions specifically. Such treatments can be targeted using patient-specific FE models that can map apparent bone stiffness changes based on CT grayscale.

The work presented in Chapter 5 highlighted that, even if there was reduced material properties, tibial OA specimens still presented with significantly higher apparent stiffness than non-diseased controls. This would suggest that altered microarchitecture plays a far more important role in variations to apparent stiffness than tissue properties. However, grouped nanoindentation results (Chapter 8) revealed higher tissue properties in OA bone. This trend is contrary to that observed in osteoporotic bone [Kim et al., 2014, Coats et al., 2003], but akin to that observed in the late-stage OA knee [Zuo et al., 2016, Peters et al., 2018]. More detailed evaluation of the morphological analysis and nanoindentation results showed depth-dependency of morphological & tissue properties, which is less frequently explored in other studies. Hence, this work highlights new properties that should be included in the derivation of ankle-specific predictive relationships, but also that this relationship alters with disease as a result of accelerated trabecular remodelling.

The results of this research may also help to improve our understanding of bone remodelling on cartilage degeneration with OA. This work could be a useful step towards understanding the mechanisms of OA progression in the ankle joint and alternative treatments involving stem cells [Jones et al., 2020]. Chapter 4 showed significantly altered trabeculae in the first level beneath the SBP; an increased presence of thicker, plate-like trabeculae was found in this level. The degradation of cartilage increases the mechanical forces onto the bone, reducing the lateral transmission of forces and increasing these instead in the radial direction down through the osteochondral unit. To accommodate this increase in load transmission, there is high bone turnover which results in higher apparent bone stiffness. Native mesenchymal stem cells (MSCs) have been found to be present in the OA ankle, causing subchondral bone plate thickening as a response to cartilage damage [Jones et al., 2020]. This corrective remodelling activity of bone-forming MSCs is therefore likely to explain the alterations in trabecular properties in the upper levels of subchondral trabecular bone.

The results of nanoindentation testing (Chapter 8) revealed a (non-significant) reduction in tissue properties within this level. The results of hypomineralisation, due to imbalanced remodelling, is well known to occur in other joints in late-stage OA [Burr and Gallant, 2012]. Hence, the observed reduced tissue properties could suggest that this thicker, plate-like bone is hypomineralised. Moreover, nanoindentation is affected by non-uniform mineralisation, which may vary the measured tissue elastic properties [Van der Linden et al., 2001]. The observed alteration of mechanical properties and microarchitecture at this level suggest a region of interest for further investigation; the distribution of mineralisation in OA ankle bone should be explored.

9.2 Challenges & Limitations

9.2.1 Tissue & Sample preparation

Cadaveric ankles were sourced to provide non-diseased (ND), control tissue for comparison to late-stage osteoarthritic tissue. Whilst every effort was made to source non-diseased ankle tissue there may be some history of ankle trauma that was unreported. Images for donor tissue "RM57" show some superficial striations in the articular cartilage, which suggest early signs of wear (Fig. C.3, Appendix C). However, each ankle was examined for bone cysts (CT) and severe cartilage damage prior to use in order to verify the tissue was not arthritic.

Generally, the extraction and trimming of the ND human bone specimens was easier than for the porcine specimens, possibly due to the slightly higher density of the juvenile porcine bone. Whilst porcine tissue can provide an affordable, ethical means of developing methods, it has its limitations. Namely, the human ankle is geometrically flatter and wider compared to porcine ankle bone. This meant that extracting bone cores was much easier from human cadaveric bone samples compared to porcine tissue. Similarly, the lack of good quality cores from the porcine tibial plafond meant that only talar specimens could be evaluated. As there is no clear definition of how deep the subchondral trabecular bone region is within the ankle, an approximate 6-8 mm depth was targeted to produce consistent FE results and avoid minor specimen errors due to depth-dependent properties. Improvements to the shaping of specimens could be achieved with the use of a diamond band saw to accurately remove the SBP and trim the cores to a specified height.

Late-stage osteoarthritic samples were sourced from patients undergoing total ankle arthroplasty (TAR). Whilst donor details of age and sex were collected, the type of OA could not be determined. For ankle OA, it is most likely that the osteoarthritis developed as a result of trauma [Liles et al., 2018, Lübbeke et al., 2012, Maffulli et al., 2011, Anderson et al., 2011, Furman et al., 2006]. The location from which the tibial OA specimens were extracted was not clear in most cases. TAR techniques typically involve resecting bone from the joint surfaces until it is sufficiently flat for an implant device to align correctly [Valderrabano et al., 2020]. For one set of samples, a diagram of the cuts was provided (Fig 3.2i), which showed that one of the tibial cuts was nearer the medial malleolus side, rather than the tibial plafond. This somewhat limits the comparisons that can be made to the ND specimens, which were removed from the tibial plafond, as the biomechanical environments and hence, the progression of OA, may differ between locations.

9.2.2 Experimental Methodologies

Uniaxial compression testing of porcine and ND human ankle bone specimens were performed to characterise apparent stiffness. This testing was repeatable for both porcine and human tissue. However, it proved challenging to keep the specimens within their endcaps and prevent them from laterally displacing during testing (despite the use of PMMA). The endcap design could therefore be improved, such as by fully embedding the ends of the specimens within PMMA only, similar to the approach used in [Wolfram et al., 2010]. Providing the specimen can be kept aligned well, this could increase the stability of the sample and minimise any displacement during testing.

Nanoindentation was performed on OA and ND specimens to allow the direct evaluation of tissue-level mechanical properties. However, the comparison of the nanoindentation results to other studies remains difficult, as specimen preparation and indentation protocols vary between studies [Wu et al., 2018] and therefore produce highly varied mechanical measurements [Mittra et al., 2006]. The embedding process was slightly amended for the OA group to improve the infiltration of resin into the trabecular pores, which was previously found to be sub-optimal during ND specimen preparation. This may have an impact on the findings of the study, as the resin provides support for the individual trabeculae during testing and ensures more consistency in the results [Bushby et al., 2004].

The evaluation of depth-dependency of tissue modulus was limited to the first level of the bone, due to insufficient depth of the OA specimens. The lack of available indents in the lower level of the talus, for example, explain the observed high variability of these results. Though correlations to age and tissue properties were established, correlations to sex were not possible due to the lack of female tissue donors. Other studies have shown that tissue properties are not sex-dependent [Hoffler et al., 2000, Dall'Ara et al., 2011]. However, further work is needed to verify that this is the case for bone in the ankle and the correlations with disease.

9.2.3 Finite Element Methodology

The optimisation of grayscale material properties was performed using an in-house developed optimisation toolbox (Opti4Abq) [Mengoni, 2015]. This allowed for the calibration of a linear relationship between element grayscale and elastic modulus via an optimised scaling factor (α) that is specific to the model properties and CT scanner settings. Good agreement (CCC) was achieved between predicted hFE apparent stiffness and experimental stiffness for porcine tissue, which improved when used for ND human tissue. The optimisation of material properties in this way was developed using vertebral bone models in the past

[Day et al., 2020, Marlène, 2020, Wijayathunga et al., 2008, Zapata-Cornelio et al., 2017]. The use of a linear relationship between bone density and elastic modulus is contrary to many studies that employ a power-law relationship. However, this work has verified that this methodology can be used on ankle tissue successfully. In future, a comparison between linear and power-law relationships could be compared to explore if this improves the agreement between experimental and predicted apparent stiffness in the ankle.

As reported in [Zapata-Cornelio et al., 2017], the optimisation is dependent on the scanner and the settings used. In this work, CT images were captured using μCT and therefore much higher than those achieved in clinic. Hence, this methodology will need to be translated for use on clinical-level images, typically captured by high-resolution peripheral quantitative computed tomography (HR-pQCT). This can be achieved through the use of imaging phantoms to establish comparable images from clinical CT (HR-pQCT) and μCT images by minimising the differences in scanner gray values [Zapata-Cornelio et al., 2017]. The addition of phantoms during the scanning of each specimen would cause a significant increase to scanning time, but could also be used to derive relationships between bone mineral density and elastic properties. This may also prove useful in future studies as a means to calibrate density [Knowles et al., 2016], which could improve thresholding and consequently, measured BV/TV.

The tissue modulus of tibial and talar ND bone measured in Chapter 8 are over twice (2.6-2.7x) those estimated using the inverse FE methodology from Chapter 5, which was used to evaluate apparent-level mechanical properties. It is not unexpected that the estimated values are lower than those directly measured, due to the high sensitivity of the finite element (FE) results on their input parameters, such as the selected global thresholding method and meshing technique. However, some studies have shown good agreement with predicted and directly-measured values [Rieger et al., 2018, Bayraktar et al., 2004, Niebur et al., 2000]. Limitations in the replication of the boundary conditions of the mechanical tests, [Chevalier et al., 2007], end artefacts and chosen global thresholding value have been shown to result in the underestimation of tissue modulus in ND specimens [Rieger et al., 2018].

Similar studies have shown less accurate predictions of apparent stiffness of bone when using an average tissue modulus [Wolfram et al., 2010, Verhulp et al., 2008a], which may be due to intra-specimen variations [Jaasma et al., 2002]. To evaluate the effect of OA on apparent tissue properties would then be challenging, as it is not possible to determine if the effects are due to mean tissue modulus and/or intra-specimen variation of modulus in the samples. Further work can be done to evaluate intra-specimen variations in directly-obtained tissue properties across a large set of ND and OA samples, so to inform the development of the material model of previous chapters that maps this heterogeneity based on CT greyscale in a specimen-specific manner [Harrison et al., 2008]. A larger non-diseased dataset would capture variations in mechanical properties and morphology that describe typical ND tissue. This would therefore form a better control group from which to compare changes with disease.

In this work, bone was assumed to be isotropic elastic. As variations to apparent stiffness appear to originate from microarchitecture and tissue properties, enhanced models could be made using material mapping procedures that directly assign element-specific morphological properties, such as anisotropy, and tissue material properties to produce enhance hFE models of ankle bone [Harrison et al., 2008, Pahr and Zysset, 2009, Matsuura et al., 2008]. This alternative means of assigning element-specific material properties may improve predictions of apparent stiffness.

9.3 Suggestions for Future Work

Cadaveric ankles are limited in number, expensive to source and are assumed to be healthy. Similarly, OA ankle tissue can be very difficult to source, as ankle arthritis is less common compared to knee or hip arthritis. Within the scope of this PhD research, it is acknowledged that compromises were made to scientific practice in terms of sample size and the age- and sex-matching of tissue. In this work, all tissue was obtained from male donors and the OA samples were sourced from older patients compared to control samples. Hence, the trends obtained in this work should be verified in future with a large sample set using tissue from both sexes and age-matched if possible. This would identify whether age-related bone thinning or the affects of bone changes due to menopause in women have influences on the trends observed in this work [Hernandez et al., 2003]. The use of age- and sex-matched tissue would control for these influences.

Experimental stiffness was found to somewhat vary by region in the ankle (Chapter 5). This is likely due to localised regional variation in microarchitecture to support the biomechanical environment of the joint [Nowakowski et al., 2013]. This was not explored in this work, but would be of particular interest if site-matched OA specimens were available for comparison. Regional mechanical and morphological data could also be correlated with gradings of articular cartilage to explore localised trends of OA progression in the ankle. This could be significant in identifying the need for a more localised calibrations of grayscale-modulus relationships are required, and helping to map stiffness changes in the bone in the earlier stages of ankle OA.

An ankle-specific calibrated relationship between image grayscale and mechanical properties, as explored in this thesis, would provide ankle surgeons with an invaluable surgical tool. However, the image analysis and FE modelling pipeline would need to be adapted for use on lower-resolution (HR-pQCT) images used in clinic. In this way, patient-specific models could be used to map regional stiffness values provided this relationship was calibrated for use on low-resolution images. The use of hFE models have been found to work effectively in enhanced vertebral models that incorporate morphological properties within the material definitions [Pahr and Zysset, 2009], but future work is required to determine the accuracy of these methods in ankle bone models.

The mineralisation of subchondral trabecular bone is known to change with OA [Nakasa et al., 2020] and thought to be just as important as porosity when characterising bone mechanical changes [Currey, 1984]. Hence future studies could characterise potential changes to mineralisation with OA to further understand matrix-level changes to subchondral bone with disease. This information will also help to understand the trends observed in the nanoindentation study, and explain the possible localised reduction in tissue properties with OA.

9.4 Conclusion

The aims and objectives for this research project were outlined in Chapter 2. In brief, this was to perform a multiscale characterisation of the mechanical and structural changes to subchondral trabecular bone in the osteoarthritic ankle. These objectives were met throughout Chapters 4 to 8.

In summary:

- In the late-stage OA ankle, subchondral trabecular bone thickens and increases in density (higher Tb.Th and BV/TV).
- The subchondral bone remodels to increase rod and plate-like trabeculae, with sensitivity to depth from the SBP.
- Plate-like trabeculae appear to thicken beneath the SBP (Level 1), and rod-like trabeculae increase in density and length.

- An image-based, specimen-specific inverse FE methodology was developed to estimate tissue-level properties of porcine subchondral trabecular bone
- hFE models were calibrated using element-specific, grayscale-dependent material properties.
- Low intra-specimen variation of tissue properties was observed, suggesting that the majority of variation to apparent stiffness originates from the microarchitecture (predominantly BV/TV and DA).

- The inverse FE methodology was successfully translated for use on human tissue, using optimised grayscale-based material properties, to estimate tissue properties of ND ankle bone.
- The sensitivity to changes in tissue modulus of OA bone models was explored; higher apparent stiffness was observed in OA specimens compared to controls, even with a 20% reduction of tissue modulus.
- Bone density, trabecular orientation and plate volume fraction were most positively correlated to apparent stiffness in ND and OA specimens, highlighting the influence of microarchitecture to apparent stiffness.

- Nanoindentation revealed an apparent increase in tissue material stiffness in grouped results of OA specimens compared to controls.
- ND tissue properties were depth-dependent, but this could not be verified for OA specimens due to insufficient data.
- In both ankle bones, Level 1 of subchondral trabecular bone exhibited a reduction (non-significant) in tissue properties, highlighting a region of interest for further characterisation work.

To conclude, the research compiled in this thesis and its conclusions have provided a vast amount data, most of which is otherwise unreported in the literature. However, a lot of new questions have arisen following this work and it remains to be seen how the impact of subchondral trabecular bone changes are linked to changes in the bone plate, articulating cartilage and stem cell behaviour. More work is therefore required to further explore the multiscale effects of OA and its impact on the biomechanical or biological capabilities of the ankle joint. Ultimately, this will aid in the development of more effective or tailored interventions that aim to delay the progression of OA in the ankle.

BIBLIOGRAPHY

[Agha and Agha, 2017] Agha, M. and Agha, R. (2017). The rising prevalence of obesity: part a: impact on public health. International journal of surgery. Oncology, 2(7):e17.

[Aitken et al., 1985] Aitken, G., Bourne, R., Finlay, J., Rorabeck, C., and Andreae, P. (1985). Indentation stiffness of the cancellous bone in the distal human tibia. Clinical orthopaedics and related research, 201:264–270.

[Anderson et al., 2011] Anderson, D. D., Marsh, J. L., and Brown, T. D. (2011). The pathomechanical etiology of post-traumatic osteoarthritis following intraarticular fractures. The Iowa orthopaedic journal, 31:1.

[Anderson et al., 1992] Anderson, M. J., Keyak, J., and Skinner, H. (1992). Compressive mechanical properties of human cancellous bone after gamma irradiation. JBJS, 74(5):747–752.

[Arthritis Research UK, 2013] Arthritis Research UK (2013). Osteoarthritis in general practice - Data and Perspectives - Arthritis Research UK. The Medical press, 222:253–258.

[Athavale et al., 2008] Athavale, S. A., Joshi, S. D., and Joshi, S. S. (2008). Internal architecture of the talus. Foot & ankle international, 29(1):82–86.

[Bailey et al., 2004] Bailey, A. J., Mansell, J. P., Sims, T. J., and Banse, X. (2004). Biochemical and mechanical properties of subchondral bone in osteoarthritis. Biorheology, 41(3-4):349–358.

[Barr et al., 2015] Barr, A. J., Campbell, T. M., Hopkinson, D., Kingsbury, S. R., Bowes, M. A., and Conaghan, P. G. (2015). A systematic review of the relationship between subchondral bone features, pain and structural pathology in peripheral joint osteoarthritis. Arthritis research & therapy, 17(1):228.

[Bayraktar et al., 2004] Bayraktar, H. H., Morgan, E. F., Niebur, G. L., Morris, G. E., Wong, E. K., and Keaveny, T. M. (2004). Comparison of the elastic and yield properties of human femoral trabecular and cortical bone tissue. Journal of biomechanics, 37(1):27–35.

[Beuf et al., 2002] Beuf, O., Ghosh, S., Newitt, D. C., Link, T. M., Steinbach, L., Ries, M., Lane, N., and Majumdar, S. (2002). Magnetic resonance imaging of normal and osteoarthritic trabecular bone structure in the human knee. Arthritis & Rheumatism, 46(2):385–393.

[Bevill et al., 2009] Bevill, G., Eswaran, S. K., Farahmand, F., and Keaveny, T. M. (2009). The influence of boundary conditions and loading mode on high-resolution finite element-computed trabecular tissue properties. Bone, 44(4):573–578.

[Bhatia, 2014] Bhatia, M. (2014). Ankle arthritis: Review and current concepts. Journal of Arthroscopy and Joint Surgery, 1(1):19–26.

[Bland and Altman, 1999] Bland, J. M. and Altman, D. G. (1999). Measuring agreement in method comparison studies. Statistical methods in medical research, 8(2):135–160.

[Bobinac et al., 2003] Bobinac, D., Spanjol, J., Zoricic, S., and Maric, I. (2003). Changes in articular cartilage and subchondral bone histomorphometry in osteoarthritic knee joints in humans. Bone, 32(3):284–290.

[Bourne and van der Meulen, 2004] Bourne, B. C. and van der Meulen, M. C. (2004). Finite element models predict cancellous apparent modulus when tissue modulus is scaled from specimen ct-attenuation. Journal of biomechanics, 37(5):613–621.

[Boyd and Müller, 2006] Boyd, S. K. and Müller, R. (2006). Smooth surface meshing for automated finite element model generation from 3d image data. Journal of biomechanics, 39(7):1287–1295.

[Brent, 1971] Brent, R. P. (1971). An algorithm with guaranteed convergence for finding a zero of a function. The Computer Journal, 14(4):422–425.

[Brockett and Chapman, 2016] Brockett, C. L. and Chapman, G. J. (2016). Biomechanics of the ankle. Orthopaedics and trauma, 30(3):232–238.

[Brown et al., 2006] Brown, T. D., Johnston, R. C., Saltzman, C. L., Marsh, J. L., and Buckwalter, J. A. (2006). Posttraumatic osteoarthritis: a first estimate of incidence, prevalence, and burden of disease. Journal of orthopaedic trauma, 20(10):739–744.

[Brown et al., 1984] Brown, T. D., Radin, E. L., Martin, R. B., and Burr, D. B. (1984). Finite element studies of some juxtarticular stress changes due to localized subchondral stiffening. Journal of biomechanics, 17(1):11–24.

[Buckland-Wright et al., 2000] Buckland-Wright, J., Lynch, J., and Dave, B. (2000). Early radiographic features in patients with anterior cruciate ligament rupture. Annals of the rheumatic diseases, 59(8):641–646.

[Burdett, 1982] Burdett, R. G. (1982). Forces predicted at the ankle during running. Medicine and Science in Sports and Exercise, 14(4):308–316.

[Burr, 2004] Burr, D. B. (2004). The importance of subchondral bone in the progression of osteoarthritis. Journal of Rheumatology-Supplements, 31(70):77–80.

[Burr and Gallant, 2012] Burr, D. B. and Gallant, M. A. (2012). Bone remodelling in osteoarthritis. Nature Reviews Rheumatology, 8(11):665.

[Burr et al., 1996] Burr, D. B., Milgrom, C., Fyhrie, D., Forwood, M., Nyska, M., Finestone, A., Hoshaw, S., Saiag, E., and Simkin, A. (1996). In vivo measurement of human tibial strains during vigorous activity. Bone, 18(5):405–410.

[Burr and Radin, 2003] Burr, D. B. and Radin, E. L. (2003). Microfractures and microcracks in subchondral bone: are they relevant to osteoarthrosis? Rheumatic Disease Clinics, 29(4):675–685.

[Bushby et al., 2004] Bushby, A., Ferguson, V., and Boyde, A. (2004). Nanoindentation of bone: Comparison of specimens tested in liquid and embedded in polymethylmethacrylate. Journal of Materials Research, 19(1):249–259.

[Calderale et al., 1983] Calderale, P., Garro, A., Barbiero, R., Fasolio, G., and Pipino, F. (1983). Biomechanical design of the total ankle prosthesis. Engineering in medicine, 12(2):69–80.

[Carretta et al., 2013] Carretta, R., Stüssi, E., Müller, R., and Lorenzetti, S. (2013). Within subject heterogeneity in tissue-level post-yield mechanical and material properties in human trabecular bone. Journal of the mechanical behavior of biomedical materials, 24:64–73.

[Carter and Hayes, 1977] Carter, D. R. and Hayes, W. C. (1977). The compressive behavior of bone as a two-phase porous structure. JBJS, 59(7):954–962.

[Castañeda et al., 2012] Castañeda, S., Roman-Blas, J. A., Largo, R., and Herrero-Beaumont, G. (2012). Subchondral bone as a key target for osteoarthritis treatment. Biochemical pharmacology, 83(3):315–323.

[Chappard et al., 2006] Chappard, C., Peyrin, F., Bonnassie, A., Lemineur, G., Brunet-Imbault, B., Lespessailles, E., and Benhamou, C.-L. (2006). Subchondral bone micro-architectural alterations in osteoarthritis: a synchrotron micro-computed tomography study. Osteoarthritis and cartilage, 14(3):215–223.

[Chen et al., 2018] Chen, Y., Hu, Y., Yu, Y. E., Zhang, X., Watts, T., Zhou, B., Wang, J., Wang, T., Zhao, W., Chiu, K. Y., et al. (2018). Subchondral trabecular rod loss and plate thickening in the development of osteoarthritis. Journal of Bone and Mineral Research, 33(2):316–327.

[Chevalier et al., 2007] Chevalier, Y., Pahr, D., Allmer, H., Charlebois, M., and Zysset, P. (2007). Validation of a voxel-based fe method for prediction of the uniaxial apparent modulus of human trabecular bone using macroscopic mechanical tests and nanoindentation. Journal of biomechanics, 40(15):3333–3340.

[Chu et al., 2020] Chu, L., He, Z., Qu, X., Liu, X., Zhang, W., Zhang, S., Han, X., Yan, M., Xu, Q., Zhang, S., et al. (2020). Different subchondral trabecular bone microstructure and biomechanical properties between developmental dysplasia of the hip and primary osteoarthritis. Journal of orthopaedic translation, 22:50–57.

[Ciarelli et al., 1991] Ciarelli, M., Goldstein, S., Kuhn, J., Cody, D., and Brown, M. (1991). Evaluation of orthogonal mechanical properties and density of human trabecular bone from the major metaphyseal regions with materials testing and computed tomography. Journal of Orthopaedic Research, 9(5):674–682.

[Coats et al., 2003] Coats, A. M., Zioupos, P., and Aspden, R. M. (2003). Material properties of subchondral bone from patients with osteoporosis or osteoarthritis by microindentation testing and electron probe microanalysis. Calcified Tissue International, 73(1):66–71.

[Commitee, 2019] Commitee, N. S. (2019). National joint registry for england, wales, northern ireland and the isle of man: 16th annual report, 2019. National Joint Registry Centre.

[Cowin, 1985] Cowin, S. C. (1985). The relationship between the elasticity tensor and the fabric tensor. Mechanics of Materials, 4(2):137–147.

[Cowin, 1986] Cowin, S. C. (1986). Fabric dependence of an anisotropic strength criterion. Mechanics of Materials, 5(3):251–260.

[Cowin and Yang, 1997] Cowin, S. C. and Yang, G. (1997). Averaging anisotropic elastic constant data. Journal of Elasticity, 46(2):151–180.

[Cox et al., 2012] Cox, L., van Donkelaar, C., van Rietbergen, B., Emans, P., and Ito, K. (2012). Decreased bone tissue mineralization can partly explain subchondral sclerosis observed in osteoarthritis. Bone, 50(5):1152–1161.

[Cox et al., 2013] Cox, L., Van Donkelaar, C., Van Rietbergen, B., Emans, P., and Ito, K. (2013). Alterations to the subchondral bone architecture during osteoarthritis: bone adaptation vs endochondral bone formation. Osteoarthritis and cartilage, 21(2):331–338.

[Currey, 1984] Currey, J. D. (1984). Effects of differences in mineralization on the mechanical properties of bone. Philosophical Transactions of the Royal Society of London. B, Biological Sciences, 304(1121):509–518.

[Currier et al., 2019] Currier, B. H., Hecht, P. J., Nunley, J. A., Mayor, M. B., Currier, J. H., and Van Citters, D. W. (2019). Analysis of failed ankle arthroplasty components. Foot & ankle international, 40(2):131–138.

[Cushnaghan and Dieppe, 1991] Cushnaghan, J. and Dieppe, P. (1991). Study of 500 patients with limb joint osteoarthritis. i. analysis by age, sex, and distribution of symptomatic joint sites. Annals of the rheumatic diseases, 50(1):8–13.

[Dall'Ara et al., 2007] Dall'Ara, E., Öhman, C., Baleani, M., and Viceconti, M. (2007). The effect of tissue condition and applied load on vickers hardness of human trabecular bone. Journal of biomechanics, 40(14):3267–3270.

[Dall'Ara et al., 2011] Dall'Ara, E., Öhman, C., Baleani, M., and Viceconti, M. (2011). Reduced tissue hardness of trabecular bone is associated with severe osteoarthritis. Journal of biomechanics, 44(8):1593–1598.

[Day et al., 2020] Day, G. A., Jones, A. C., and Wilcox, R. K. (2020). Optimizing computational methods of modeling vertebroplasty in experimentally augmented human lumbar vertebrae. JOR Spine, page e1077.

[Day et al., 2004a] Day, J., Ding, M., Bednarz, P., Van Der Linden, J., Mashiba, T., Hirano, T., Johnston, C., Burr, D., Hvid, I., Sumner, D., et al. (2004a). Bisphosphonate treatment affects trabecular bone apparent modulus through micro-architecture rather than matrix properties. Journal of Orthopaedic Research, 22(3):465–471.

[Day et al., 2001] Day, J., Ding, M., Van Der Linden, J., Hvid, I., Sumner, D., and Weinans, H. (2001). A decreased subchondral trabecular bone tissue elastic modulus is associated with pre-arthritic cartilage damage. Journal of orthopaedic research, 19(5):914–918.

[Day et al., 2004b] Day, J., Van Der Linden, J., Bank, R., Ding, M., Hvid, I., Sumner, D., and Weinans, H. (2004b). Adaptation of subchondral bone in osteoarthritis. Biorheology, 41(3-4):359–368.

[Delco et al., 2017] Delco, M. L., Kennedy, J. G., Bonassar, L. J., and Fortier, L. A. (2017). Post-traumatic osteoarthritis of the ankle: A distinct clinical entity requiring new research approaches. Journal of Orthopaedic Research, 35(3):440–453.

[den Dunnen et al., 2013] den Dunnen, S., Mulder, L., Kerkhoffs, G. M., Dankelman, J., and Tuijthof, G. J. (2013). Waterjet drilling in porcine bone: The effect of the nozzle diameter and bone architecture on the hole dimensions. Journal of the mechanical behavior of biomedical materials, 27:84–93.

[DeOrio, 2020] DeOrio, J. K. (2020). Inbone revision total ankle arthroplasty. Techniques in Foot & Ankle Surgery, 19(1):43–47.

[Dequeker et al., 1995] Dequeker, J., Mokassa, L., and Aerssens, J. (1995). Bone density and osteoarthritis. The Journal of rheumatology. Supplement, 43:98–100.

[Dequeker et al., 1997] Dequeker, J., Mokassa, L., Aerssens, J., and Boonen, S. (1997). Bone density and local growth factors in generalized osteoarthritis. Microscopy research and technique, 37(4):358–371.

[Dieppe, 2011] Dieppe, P. (2011). Developments in osteoarthritis.

[Ding, 2010] Ding, M. (2010). Microarchitectural adaptations in aging and osteoarthrotic subchondral bone issues. Acta Orthopaedica, 81(sup340):1–53.

[Ding et al., 1998] Ding, M., Dalstra, M., Linde, F., and Hvid, I. (1998). Mechanical properties of the normal human tibial cartilage-bone complex in relation to age. Clinical Biomechanics, 13(4):351–358.

[Ding et al., 2001] Ding, M., Danielsen, C. C., and Hvid, I. (2001). Bone density does not reflect mechanical properties in early-stage arthrosis. Acta Orthopaedica Scandinavica, 72(2):181–185.

[Ding and Hvid, 2000] Ding, M. and Hvid, I. (2000). Quantification of age-related changes in the structure model type and trabecular thickness of human tibial cancellous bone. Bone, 26(3):291–295.

[Ding et al., 2002a] Ding, M., Odgaard, A., Danielsen, C. C., and Hvid, I. (2002a). Mutual associations among microstructural, physical and mechanical properties of human cancellous bone. The Journal of bone and joint surgery. British volume, 84(6):900–907.

[Ding et al., 2003] Ding, M., Odgaard, A., Hvid, I., and Hvid, I. (2003). Changes in the three-dimensional microstructure of human tibial cancellous bone in early osteoarthritis. The Journal of bone and joint surgery. British volume, 85(6):906–912.

[Ding et al., 2002b] Ding, M., Odgaard, A., Linde, F., and Hvid, I. (2002b). Age-related variations in the microstructure of human tibial cancellous bone. Journal of Orthopaedic Research, 20(3):615–621.

[Donnelly et al., 2006] Donnelly, E., Baker, S. P., Boskey, A. L., and van der Meulen, M. C. (2006). Effects of surface roughness and maximum load on the mechanical properties of cancellous bone measured by nanoindentation. Journal of Biomedical Materials Research Part A: An Official Journal of The Society for Biomaterials, The Japanese Society for Biomaterials, and The Australian Society for Biomaterials and the Korean Society for Biomaterials, 77(2):426–435.

[Doube, 2015] Doube, M. (2015). The ellipsoid factor for quantification of rods, plates, and intermediate forms in 3d geometries. Frontiers in endocrinology, 6:15.

[Doube et al., 2010] Doube, M., Kłosowski, M. M., Arganda-Carreras, I., Cordelières, F. P., Dougherty, R. P., Jackson, J. S., Schmid, B., Hutchinson, J. R., and Shefelbine, S. J. (2010). Bonej: free and extensible bone image analysis in imagej. Bone, 47(6):1076–1079.

[Du et al., 2019] Du, J., Brooke-Wavell, K., Paggiosi, M. A., Hartley, C., Walsh, J. S., Silberschmidt, V. V., and Li, S. (2019). Characterising variability and regional correlations of microstructure and mechanical competence of human tibial trabecular bone: An in-vivo hr-pqct study. Bone, 121:139–148.

[Egloff et al., 2012] Egloff, C., Hügle, T., and Valderrabano, V. (2012). Biomechanics and pathomechanisms of osteoarthritis. Swiss Med Wkly, 142(0).

[El-Jawhari et al., 2018] El-Jawhari, J. J., Brockett, C. L., Ktistakis, I., Jones, E., and Giannoudis, P. V. (2018). The regenerative therapies of the ankle degeneration: a focus on multipotential mesenchymal stromal cells. Regenerative Medicine, 13(2):175–188.

[Engelke et al., 2016] Engelke, K., van Rietbergen, B., and Zysset, P. (2016). Fea to measure bone strength: a review. Clinical reviews in bone and mineral metabolism, 14(1):26–37.

[Evans et al., 1990] Evans, G., Behiri, J., Currey, J., and Bonfield, W. (1990). Microhardness and young's modulus in cortical bone exhibiting a wide range of mineral volume fractions, and in a bone analogue. Journal of Materials Science: Materials in Medicine, 1(1):38–43.

[Fazzalari and Parkinson, 1997] Fazzalari, N. and Parkinson, I. (1997). Fractal properties of subchondral cancellous bone in severe osteoarthritis of the hip. Journal of Bone and Mineral Research, 12(4):632–640.

[Felson and Hodgson, 2014] Felson, D. T. and Hodgson, R. (2014). Identifying and treating preclinical and early osteoarthritis. Rheumatic diseases clinics of North America, 40(4):699.

[Finlay et al., 1989] Finlay, J. B., Bourne, R. B., Kraemer, W. J., Moroz, T. K., and Rorabeck, C. H. (1989). Stiffness of bone underlying the tibial plateaus of osteoarthritic and normal knees. Clinical orthopaedics and related research, (247):193–201.

[Finnilä et al., 2017] Finnilä, M. A., Thevenot, J., Aho, O.-M., Tiitu, V., Rautiainen, J., Kauppinen, S., Nieminen, M. T., Pritzker, K., Valkealahti, M., Lehenkari, P., et al. (2017). Association between subchondral bone structure and osteoarthritis histopathological grade. Journal of Orthopaedic Research, 35(4):785–792.

[Furman et al., 2006] Furman, B. D., Olson, S. A., and Guilak, F. (2006). The development of posttraumatic arthritis after articular fracture. Journal of orthopaedic trauma, 20(10):719–725.

[Fyhrie, 2005] Fyhrie, D. P. (2005). Summary-measuring" bone quality". Journal of Musculoskeletal Neuronal Interactions, 5(4):318–320.

[Gatenholm et al., 2019] Gatenholm, B., Lindahl, C., Brittberg, M., and Stadelmann, V. A. (2019). Spatially matching morphometric assessment of cartilage and subchondral bone in osteoarthritic human knee joint with micro-computed tomography. Bone, 120:393–402.

[Glazebrook et al., 2008] Glazebrook, M., Daniels, T., Younger, A., Foote, C., Penner, M., Wing, K., Lau, J., Leighton, R., and Dunbar, M. (2008). Comparison of health-related quality of life between patients with end-stage ankle and hip arthrosis. JBJS, 90(3):499–505.

[Glazebrook et al., 2009] Glazebrook, M. A., Arsenault, K., and Dunbar, M. (2009). Evidence-based classification of complications in total ankle arthroplasty. Foot & ankle international, 30(10):945–949.

[Glyn-Jones et al., 2015] Glyn-Jones, S., Palmer, A., Agricola, R., Price, A., Vincent, T., Weinans, H., and Carr, A. (2015). Osteoarthritis. The Lancet, 386(9991):376–387.

[Goetz et al., 2016] Goetz, J. E., Rungprai, C., Tennant, J. N., Huber, E., Uribe, B., Femino, J., Phisitkul, P., and Amendola, A. (2016). Variable volumes of resected bone resulting from different total ankle arthroplasty systems. Foot & ankle international, 37(8):898–904.

[Goff et al., 2015] Goff, M., Lambers, F., Sorna, R., Keaveny, T., and Hernandez, C. (2015). Finite element models predict the location of microdamage in cancellous bone following uniaxial loading. Journal of biomechanics, 48(15):4142–4148.

[Goldberg et al., 2012] Goldberg, A. J., MacGregor, A., Dawson, J., Singh, D., Cullen, N., Sharp, R. J., and Cooke, P. H. (2012). The demand incidence of symptomatic ankle osteoarthritis presenting to foot & ankle surgeons in the united kingdom. The Foot, 22(3):163–166.

[Goldring, 2009] Goldring, S. R. (2009). Role of bone in osteoarthritis pathogenesis. Medical Clinics of North America, 93(1):25–35.

[Gomez, 2002] Gomez, S. (2002). Crisóstomo martinez, 1638-1694: the discoverer of trabecular bone. Endocrine, 17(1):3.

[Goulet et al., 1994] Goulet, R. W., Goldstein, S. A., Ciarelli, M. J., Kuhn, J. L., Brown, M., and Feldkamp, L. (1994). The relationship between the structural and orthogonal compressive properties of trabecular bone. Journal of biomechanics, 27(4):375379–377389.

[Gross et al., 2012] Gross, T., Pahr, D. H., Peyrin, F., and Zysset, P. K. (2012). Mineral heterogeneity has a minor influence on the apparent elastic properties of human cancellous bone: a srμct-based finite element study. Computer methods in biomechanics and biomedical engineering, 15(11):1137–1144.

[Grynpas et al., 1991] Grynpas, M., Alpert, B., Katz, I., Lieberman, I., and Pritzker, K. (1991). Subchondral bone in osteoarthritis. Calcified tissue international, 49(1):20–26.

[Guidoni et al., 2010] Guidoni, G., Swain, M., and Jäger, I. (2010). Nanoindentation of wet and dry compact bone: Influence of environment and indenter tip geometry on the indentation modulus. Philosophical magazine, 90(5):553–565.

[Guldberg et al., 1998] Guldberg, R., Hollister, S., and Charras, G. (1998). The accuracy of digital image-based finite element models.

[Halgrin et al., 2012] Halgrin, J., Chaari, F., and Markiewicz, É. (2012). On the effect of marrow in the mechanical behavior and crush response of trabecular bone. Journal of the mechanical behavior of biomedical materials, 5(1):231–237.

[Hangartner, 2007] Hangartner, T. N. (2007). Thresholding technique for accurate analysis of density and geometry in qct, pqct and muct images. Journal of Musculoskeletal and Neuronal Interactions, 7(1):9.

[Harada et al., 1988] Harada, Y., Wevers, H., and Cooke, T. (1988). Distribution of bone strength in the proximal tibia. The Journal of arthroplasty, 3(2):167–175.

[Harnroongroj et al., 2019] Harnroongroj, T., Volpert, L. G., Ellis, S. J., Sofka, C. M., Deland, J. T., and Demetracopoulos, C. A. (2019). Comparison of tibial and talar bone density in patients undergoing total ankle replacement vs non–ankle arthritis matched controls. Foot & Ankle International, 40(12):1408–1415.

[Harrigan and Mann, 1984] Harrigan, T. and Mann, R. (1984). Characterization of microstructural anisotropy in orthotropic materials using a second rank tensor. Journal of Materials Science, 19(3):761–767.

[Harrigan et al., 1988] Harrigan, T. P., Jasty, M., Mann, R. W., and Harris, W. H. (1988). Limitations of the continuum assumption in cancellous bone. Journal of biomechanics, 21(4):269–275.

[Harrison et al., 2008] Harrison, N. M., McDonnell, P. F., O'Mahoney, D. C., Kennedy, O. D., O'Brien, F. J., and McHugh, P. E. (2008). Heterogeneous linear elastic trabecular bone modelling using micro-ct attenuation data and experimentally measured heterogeneous tissue properties. Journal of biomechanics, 41(11):2589–2596.

[Hart et al., 2017] Hart, N. H., Nimphius, S., Rantalainen, T., Ireland, A., Siafarikas, A., and Newton, R. (2017). Mechanical basis of bone strength: influence of bone material, bone structure and muscle action. Journal of musculoskeletal & neuronal interactions, 17(3):114.

[He et al., 2020] He, Z., Chu, L., Liu, X., Han, X., Zhang, K., Yan, M., Li, X., and Yu, Z. (2020). Differences in subchondral trabecular bone microstructure and finite element analysis-based biomechanical properties between osteoporosis and osteoarthritis. Journal of Orthopaedic Translation.

[Helgason et al., 2008] Helgason, B., Perilli, E., Schileo, E., Taddei, F., Brynjólfsson, S., and Viceconti, M. (2008). Mathematical relationships between bone density and mechanical properties: a literature review. Clinical biomechanics, 23(2):135–146.

[Hengsberger et al., 2002] Hengsberger, S., Kulik, A., and Zysset, P. (2002). Nanoindentation discriminates the elastic properties of individual human bone lamellae under dry and physiological conditions. Bone, 30(1):178–184.

[Hernandez et al., 2003] Hernandez, C., Beaupre, G., and Carter, D. (2003). A theoretical analysis of the relative influences of peak bmd, age-related bone loss and menopause on the development of osteoporosis. Osteoporosis international, 14(10):843–847.

[Hernandez et al., 2001] Hernandez, C., Beaupre, G., Keller, T., and Carter, D. (2001). The influence of bone volume fraction and ash fraction on bone strength and modulus. Bone, 29(1):74–78.

[Hernandez and Keaveny, 2006] Hernandez, C. and Keaveny, T. (2006). A biomechanical perspective on bone quality. Bone, 39(6):1173–1181.

[Hernandez, 2016] Hernandez, C. J. (2016). Chapter 2: Cancellous bone. In Handbook of Biomaterial Properties, pages 15–21. Springer.

[Hildebrand and Rüegsegger, 1997] Hildebrand, T. and Rüegsegger, P. (1997). Quantification of bone microarchitecture with the structure model index. Computer Methods in Biomechanics and Bio Medical Engineering, 1(1):15–23.

[Hintermann et al., 2012] Hintermann, B., Knupp, M., Zwicky, L., and Barg, A. (2012). Total ankle replacement for treatment of end-stage osteoarthritis in elderly patients. Journal of aging research, 2012.

[Hintermann and Ruiz, 2014] Hintermann, B. and Ruiz, R. (2014). Ankle arthritis and the treatment with ankle replacement. Revista Médica Clínica Las Condes, 25(5):812–823.

[Hoffler et al., 2000] Hoffler, C., Moore, K., Kozloff, K., Zysset, P., and Goldstein, S. A. (2000). Age, gender, and bone lamellae elastic moduli. Journal of Orthopaedic Research, 18(3):432–437.

[Hoffler et al., 2005] Hoffler, C. E., Guo, X. E., Zysset, P. K., and Goldstein, S. A. (2005). An application of nanoindentation technique to measure bone tissue lamellae properties. Journal of biomechanical engineering, 127(7):1046–1053.

[Holton et al., 2013] Holton, C., Gudipati, S., and Budgen, A. (2013). Mid-term follow-up of talar dome resurfacing surgery using the hemicap device for osteochondral lesions: Review of 3 cases. Foot and Ankle Online Journal, 6(2).

[Homminga et al., 2003] Homminga, J., Mccreadie, B. R., Weinans, H., and Huiskes, R. (2003). The dependence of the elastic properties of osteoporotic cancellous bone on volume fraction and fabric. Journal of Biomechanics, 36(10):1461–1467.

[Horisberger et al., 2009] Horisberger, M., Valderrabano, V., and Hintermann, B. (2009). Posttraumatic ankle osteoarthritis after ankle-related fractures. Journal of orthopaedic trauma, 23(1):60–67.

[Huch et al., 1997] Huch, K., Kuettner, K. E., and Dieppe, P. (1997). Osteoarthritis in ankle and knee joints. In Seminars in arthritis and rheumatism, volume 26, pages 667–674. Elsevier.

[Hvid et al., 1983] Hvid, I., Christensen, P., Søndergaard, J., Christensen, P. B., and Larsen, C. G. (1983). Compressive strength of tibial cancellous bone: instron® and osteopenetrometer measurements in an autopsy material. Acta Orthopaedica Scandinavica, 54(6):819–825.

[Hvid and Jensen, 1984] Hvid, I. and Jensen, J. (1984). Cancellous bone strength at the proximal human tibia. Engineering in medicine, 13(1):21–25.

[Hvid et al., 1985] Hvid, I., Rasmussen, O., Jensen, N. C., and Nielsen, S. (1985). Trabecular bone strength profiles at the ankle joint. Clinical orthopaedics and related research, 199:306–312.

[Ilas et al., 2017] Ilas, D. C., Churchman, S. M., McGonagle, D., and Jones, E. (2017). Targeting subchondral bone mesenchymal stem cell activities for intrinsic joint repair in osteoarthritis. Future science OA, 3(4):FSO228.

[Jaasma et al., 2002] Jaasma, M. J., Bayraktar, H. H., Niebur, G. L., and Keaveny, T. M. (2002). Biomechanical effects of intraspecimen variations in tissue modulus for trabecular bone. Journal of biomechanics, 35(2):237–246.

[Jackson and Singh, 2003] Jackson, M. and Singh, D. (2003). Total ankle replacement. Current Orthopaedics, 17(4):292–298.

[Jacobs et al., 1999] Jacobs, C., Davis, B., Rieger, C., Francis, J., Saad, M., and Fyhrie, D. (1999). The impact of boundary conditions and mesh size on the accuracy of cancellous bone tissue modulus determination using large-scale finite-element modeling. Journal of Biomechanics, 32(11):1159–1164.

[Jastifer and Toledo-Pereyra, 2012] Jastifer, J. R. and Toledo-Pereyra, L. H. (2012). Leonardo da vinci's foot: historical evidence of concept. Journal of Investigative Surgery, 25(5):281–285.

[Jensen et al., 1988] Jensen, N. C., Hvid, I., and Krøner, K. (1988). Strength pattern of cancellous bone at the ankle joint. Engineering in medicine, 17(2):71–76.

[Johanson et al., 1993] Johanson, N. A., Charlson, M. E., Cutignola, L., Neves, M., DiCarlo, E. F., and Bullough, P. G. (1993). Femoral neck bone density: Direct measurement and histomorphometric validation. The Journal of Arthroplasty, 8(6):641 – 652.

[Johnston et al., 2016] Johnston, J. D., Burnett, W. D., and Kontulainen, S. A. (2016). Subchondral bone features and mechanical properties as biomarkers of osteoarthritis. Biomarkers in Bone Disease, pages 1–27.

[Johnston et al., 2011] Johnston, J. D., Kontulainen, S. A., Masri, B. A., and Wilson, D. R. (2011). Predicting subchondral bone stiffness using a depth-specific ct topographic mapping technique in normal and osteoarthritic proximal tibiae. Clinical Biomechanics, 26(10):1012–1018.

[Jones et al., 2020] Jones, W., El-Jawhari, J., Brockett, C., Koria, L., Ktistakis, I., and Jones, E. (2020). Multipotential stromal cells in the talus and distal tibia in ankle osteoarthritis–presence, potency and relationships to subchondral bone changes. Journal of Cellular and Molecular Medicine.

[Kakkar and Siddique, 2011] Kakkar, R. and Siddique, M. (2011). Stresses in the ankle joint and total ankle replacement design. Foot and Ankle Surgery, 17(2):58–63.

[Kamibayashi et al., 1995a] Kamibayashi, L., Wyss, U., Cooke, T., and Zee, B. (1995a). Changes in mean trabecular orientation in the medial condyle of the proximal tibia in osteoarthritis. Calcified tissue international, 57(1):69–73.

[Kamibayashi et al., 1995b] Kamibayashi, L., Wyss, U., Cooke, T., and Zee, B. (1995b). Trabecular microstructure in the medial condyle of the proximal tibia of patients with knee osteoarthritis. Bone, 17(1):27–35.

[Karsdal et al., 2008] Karsdal, M., Leeming, D., Dam, E., Henriksen, K., Alexandersen, P., Pastoureau, P., Altman, R., and Christiansen, C. (2008). Should subchondral bone turnover be targeted when treating osteoarthritis? Osteoarthritis and cartilage, 16(6):638–646.

[Keaveny et al., 1993] Keaveny, T. M., Borchers, R. E., Gibson, L. J., and Hayes, W. C. (1993). Trabecular bone modulus and strength can depend on specimen geometry. Journal of Biomechanics, 26(8):991997999–9951000.

[Keaveny et al., 2001] Keaveny, T. M., Morgan, E. F., Niebur, G. L., and Yeh, O. C. (2001). Biomechanics of trabecular bone. Annual review of biomedical engineering, 3(1):307–333.

[Keaveny et al., 2004] Keaveny, T. M., Morgan, E. F., and Yeh, O. C. (2004). Bone Mechanics. Standard Handbook of Biomedical Engineering and Design, pages 8.1–8.23.

[Keaveny et al., 1997] Keaveny, T. M., Pinilla, T. P., Crawford, R. P., Kopperdahl, D. L., and Lou, A. (1997). Systematic and random errors in compression testing of trabecular bone. Journal of Orthopaedic Research, 15(1):101–110.

[Kellgren and Lawrence, 1957] Kellgren, J. and Lawrence, J. (1957). Radiological assessment of osteo-arthrosis. Annals of the rheumatic diseases, 16(4):494.

[Keyak et al., 1994] Keyak, J., Lee, I., and Skinner, H. (1994). Correlations between orthogonal mechanical properties and density of trabecular bone: use of different densitometric measures. Journal of biomedical materials research, 28(11):1329–1336.

[Kim et al., 2014] Kim, G., Cole, J. H., Boskey, A. L., Baker, S. P., and van der Meulen, M. C. (2014). Reduced tissue-level stiffness and mineralization in osteoporotic cancellous bone. Calcified tissue international, 95(2):125–131.

[Kimizuka et al., 1980] Kimizuka, M., Kurosawa, H., and Fukubayashi, T. (1980). Load-bearing pattern of the ankle joint. Archives of orthopaedic and traumatic surgery, 96(1):45–49.

[Knowles et al., 2016] Knowles, N. K., Reeves, J. M., and Ferreira, L. M. (2016). Quantitative computed tomography (qct) derived bone mineral density (bmd) in finite element studies: a review of the literature. Journal of experimental orthopaedics, 3(1):36.

[Kopperdahl et al., 2002] Kopperdahl, D. L., Morgan, E. F., and Keaveny, T. M. (2002). Quantitative computed tomography estimates of the mechanical properties of human vertebral trabecular bone. Journal of orthopaedic research, 20(4):801–805.

[Koria et al., 2020] Koria, L., Mengoni, M., and Brockett, C. (2020). Estimating tissue-level properties of porcine talar subchondral bone. Journal of the Mechanical Behaviour of Biomedical Materials.

[Kosmopoulos and Keller, 2008] Kosmopoulos, V. and Keller, T. S. (2008). Predicting trabecular bone microdamage initiation and accumulation using a non-linear perfect damage model. Medical engineering & physics, 30(6):725–732.

[Kraus et al., 2015] Kraus, V. B., Kilfoil, T. M., Hash, T. W., McDaniel, G., Renner, J. B., Carrino, J. A., and Adams, S. (2015). Atlas of radiographic features of osteoarthritis of the ankle and hindfoot. Osteoarthritis and cartilage, 23(12):2059–2085.

[Kuettner and Cole, 2005] Kuettner, K. and Cole, A. (2005). Cartilage degeneration in different human joints. Osteoarthritis and cartilage, 13(2):93–103.

[Lawrence and Lin, 1989] Lawrence, I. and Lin, K. (1989). A concordance correlation coefficient to evaluate reproducibility. Biometrics, pages 255–268.

[Leardini et al., 2014] Leardini, A., O'Connor, J. J., and Giannini, S. (2014). Biomechanics of the natural, arthritic, and replaced human ankle joint. Journal of foot and ankle research, 7(1):1–16.

[Lereim et al., 1974] Lereim, P., Goldie, I., and Dahlberg, E. (1974). Hardness of the subchondral bone of the tibial condyles in the normal state and in osteoarthritis and rheumatoid arthritis. Acta Orthopaedica Scandinavica, 45(1-4):614–627.

[Lewis and Nyman, 2008] Lewis, G. and Nyman, J. S. (2008). The use of nanoindentation for characterizing the properties of mineralized hard tissues: State-of-the art review. Journal of Biomedical Materials Research Part B: Applied Biomaterials: An Official Journal of The Society for Biomaterials, The Japanese Society for Biomaterials, and The Australian Society for Biomaterials and the Korean Society for Biomaterials, 87(1):286–301.

[Li and Aspden, 1997a] Li, B. and Aspden, R. M. (1997a). Composition and mechanical properties of cancellous bone from the femoral head of patients with osteoporosis or osteoarthritis. Journal of Bone and Mineral Research, 12(4):641–651.

[Li and Aspden, 1997b] Li, B. and Aspden, R. M. (1997b). Mechanical and material properties of the subchondral bone plate from the femoral head of patients with osteoarthritis or osteoporosis. Annals of the Rheumatic Diseases, 56(4):247–254.

[Li et al., 2013] Li, G., Yin, J., Gao, J., Cheng, T. S., Pavlos, N. J., Zhang, C., and Zheng, M. H. (2013). Subchondral bone in osteoarthritis: insight into risk factors and microstructural changes. Arthritis research & therapy, 15(6):223.

[Liles et al., 2018] Liles, J. L., Steele, J. R., Chen, F., Nettles, D. L., and Adams Jr, S. B. (2018). Basic science behind the development of posttraumatic osteoarthritis of the ankle. Techniques in Foot & Ankle Surgery, 17(4):169–174.

[Linde and Hvid, 1987] Linde, F. and Hvid, I. (1987). Stiffness behaviour of trabecular bone specimens. Journal of biomechanics, 20(1):83–89.

[Linde et al., 1985] Linde, F., Hvid, I., and Jensen, N. C. (1985). Material properties of cancellous bone in repetitive axial loading. Engineering in medicine, 14(4):173–177.

[Linde et al., 1992] Linde, F., Hvid, I., and Madsen, F. (1992). The effect of specimen geometry on the mechanical behaviour of trabecular bone specimens. Journal of biomechanics, 25(4):359–368.

[Linde et al., 1991] Linde, F., Nørgaard, P., Hvid, I., Odgaard, A., and Søballe, K. (1991). Mechanical properties of trabecular bone. dependency on strain rate. Journal of Biomechanics, 24(9):803–809.

[Liu and Morgan, 2007] Liu, L. and Morgan, E. F. (2007). Accuracy and precision of digital volume correlation in quantifying displacements and strains in trabecular bone. Journal of biomechanics, 40(15):3516–3520.

[Liu et al., 2009] Liu, X. S., Bevill, G., Keaveny, T. M., Sajda, P., and Guo, X. E. (2009). Micromechanical analyses of vertebral trabecular bone based on individual trabeculae segmentation of plates and rods. Journal of biomechanics, 42(3):249–256.

[Liu et al., 2010] Liu, X. S., Cohen, A., Shane, E., Stein, E., Rogers, H., Kokolus, S. L., Yin, P. T., McMahon, D. J., Lappe, J. M., Recker, R. R., et al. (2010). Individual trabeculae segmentation (its)–based morphological analysis of high-resolution peripheral quantitative computed tomography images detects abnormal trabecular plate and rod microarchitecture in premenopausal women with idiopathic osteoporosis. Journal of bone and mineral research, 25(7):1496–1505.

[Liu et al., 2008] Liu, X. S., Sajda, P., Saha, P. K., Wehrli, F. W., Bevill, G., Keaveny, T. M., and Guo, X. E. (2008). Complete volumetric decomposition of individual trabecular plates and rods and its morphological correlations with anisotropic elastic moduli in human trabecular bone. Journal of Bone and Mineral Research, 23(2):223–235.

[Liu et al., 2006] Liu, X. S., Sajda, P., Saha, P. K., Wehrli, F. W., and Guo, X. E. (2006). Quantification of the roles of trabecular microarchitecture and trabecular type in determining the elastic modulus of human trabecular bone. Journal of Bone and Mineral Research, 21(10):1608–1617.

[Lübbeke et al., 2012] Lübbeke, A., Salvo, D., Stern, R., Hoffmeyer, P., Holzer, N., and Assal, M. (2012). Risk factors for post-traumatic osteoarthritis of the ankle: an eighteen year follow-up study. International orthopaedics, 36(7):1403–1410.

[Madry et al., 2012] Madry, H., Luyten, F. P., and Facchini, A. (2012). Biological aspects of early osteoarthritis. Knee Surgery, Sports Traumatology, Arthroscopy, 20(3):407–422.

[Madry et al., 2010] Madry, H., van Dijk, C. N., and Mueller-Gerbl, M. (2010). The basic science of the subchondral bone. Knee surgery, sports traumatology, arthroscopy, 18(4):419–433.

[Maffulli et al., 2011] Maffulli, N., Longo, U. G., Gougoulias, N., Caine, D., and Denaro, V. (2011). Sport injuries: a review of outcomes. British medical bulletin, 97(1):47–80.

[Mansell and Bailey, 1998] Mansell, J. P. and Bailey, A. J. (1998). Abnormal cancellous bone collagen metabolism in osteoarthritis. The Journal of clinical investigation, 101(8):1596–1603.

[Maquer et al., 2015] Maquer, G., Musy, S. N., Wandel, J., Gross, T., and Zysset, P. K. (2015). Bone volume fraction and fabric anisotropy are better determinants of trabecular bone stiffness than other morphological variables. Journal of bone and mineral research, 30(6):1000–1008.

[Marangalou et al., 2012] Marangalou, J. H., Ito, K., and van Rietbergen, B. (2012). A new approach to determine the accuracy of morphology–elasticity relationships in continuum fe analyses of human proximal femur. Journal of biomechanics, 45(16):2884–2892.

[Marlène, 2020] Marlène, M. (2020). Using inverse finite element analysis to identify spinal tissue behaviour in situ. Methods.

[Martel-Pelletier, 1999] Martel-Pelletier, J. (1999). Pathophysiology of osteoarthritis. Osteoarthritis and cartilage, 7(4):371–373.

[Matsui et al., 1997] Matsui, H., Shimizu, M., and Tsuji, H. (1997). Cartilage and subchondral bone interaction in osteoarthrosis of human knee joint: a histological and histomorphometric study. Microscopy research and technique, 37(4):333–342.

[Matsuura et al., 2008] Matsuura, M., Eckstein, F., Lochmüller, E.-M., and Zysset, P. K. (2008). The role of fabric in the quasi-static compressive mechanical properties of human trabecular bone from various anatomical locations. Biomechanics and Modeling in Mechanobiology, 7(1):27–42.

[McGonagle et al., 2010] McGonagle, D., Tan, A. L., Carey, J., and Benjamin, M. (2010). The anatomical basis for a novel classification of osteoarthritis and allied disorders. Journal of anatomy, 216(3):279–291.

[McKinley and Bay, 2001] McKinley, T. O. and Bay, B. K. (2001). Trabecular bone strain changes associated with cartilage defects in the proximal and distal tibia. Journal of Orthopaedic Research, 19(5):906–913.

[Meachim, 1975] Meachim, G. (1975). Cartilage fibrillation at the ankle joint in liverpool necropsies. Journal of anatomy, 119(Pt 3):601.

[Meachim and Emery, 1974] Meachim, G. and Emery, I. (1974). Quantitative aspects of patello-femoral cartilage fibrillation in liverpool necropsies. Annals of the rheumatic diseases, 33(1):39.

[Mengoni, 2015] Mengoni, M. (2015). opti4abq, a generic python code to run abaqus in an optimisation loop.

[Mengoni et al., 2015] Mengoni, M., Luxmoore, B., Jones, A., Wijayathunga, V., Broom, N., and Wilcox, R. (2015). Derivation of inter-lamellar behaviour of the intervertebral disc annulus. Journal of the Mechanical Behavior of Biomedical Materials, 48:164–172.

[Mengoni et al., 2016] Mengoni, M., Sikora, S., d'Otreppe, V., Wilcox, R. K., and Jones, A. C. (2016). In-silico models of trabecular bone: a sensitivity analysis perspective. In Uncertainty in Biology, pages 393–423. Springer.

[Mengoni et al., 2012] Mengoni, M., Voide, R., de Bien, C., Freichels, H., Jérôme, C., Léonard, A., Toye, D., Müller, R., van Lenthe, G. H., and Ponthot, J.-P. (2012). A non-linear homogeneous model for bone-like materials under compressive load. International journal for numerical methods in biomedical engineering, 28(2):273–287.

[Millington et al., 2007] Millington, S. A., Grabner, M., Wozelka, R., Anderson, D., Hurwitz, S., and Crandall, J. (2007). Quantification of ankle articular cartilage topography and thickness using a high resolution stereophotography system. Osteoarthritis and cartilage, 15(2):205–211.

[Milz and Putz, 1994] Milz, S. and Putz, R. (1994). Quantitative morphology of the subchondral plate of the tibial plateau. Journal of anatomy, 185(Pt 1):103.

[Mittra et al., 2006] Mittra, E., Akella, S., and Qin, Y.-X. (2006). The effects of embedding material, loading rate and magnitude, and penetration depth in nanoindentation of trabecular bone. Journal of Biomedical Materials Research Part A: An Official Journal of The Society for Biomaterials, The Japanese Society for Biomaterials, and The Australian Society for Biomaterials and the Korean Society for Biomaterials, 79(1):86–93.

[Morgan et al., 2003] Morgan, E. F., Bayraktar, H. H., and Keaveny, T. M. (2003). Trabecular bone modulus–density relationships depend on anatomic site. Journal of biomechanics, 36(7):897–904.

[Morgan et al., 2004] Morgan, E. F., Bayraktar, H. H., Yeh, O. C., Majumdar, S., Burghardt, A., and Keaveny, T. M. (2004). Contribution of inter-site variations in architecture to trabecular bone apparent yield strains. Journal of biomechanics, 37(9):1413–1420.

[Morgan and Keaveny, 2001] Morgan, E. F. and Keaveny, T. M. (2001). Dependence of yield strain of human trabecular bone on anatomic site. Journal of biomechanics, 34(5):569–577.

[Morgan et al., 2001] Morgan, E. F., Yeh, O. C., Chang, W. C., and Keaveny, T. M. (2001). Nonlinear behavior of trabecular bone at small strains. Journal of biomechanical engineering, 123(1):1–9.

[Muehleman et al., 1995] Muehleman, C., Bareither, D., Huch, K., COLE, A., and KUETTNER, K. (1995). Incidence of osteoarthritis in the joints of the lower-extremity. In FASEB JOURNAL, volume 9, pages A967–A967. FEDERATION AMER SOC EXP BIOL 9650 ROCKVILLE PIKE, BETHESDA, MD 20814-3998.

[Muehleman et al., 1997] Muehleman, C., Bareither, D., Huch, K., Cole, A. A., and Kuettner, K. E. (1997). Prevalence of degenerative morphological changes in the joints of the lower extremity. Osteoarthritis and cartilage, 5(1):23–37.

[Muehleman et al., 2002] Muehleman, C., Berzins, A., Koepp, H., Eger, W., Cole, A., Kuettner, K., and Sumner, D. (2002). Bone density of the human talus does not increase with the cartilage degeneration score. The Anatomical Record, 266(2):81–86.

[Müller and van Lenthe, 2006] Müller, R. and van Lenthe, G. H. (2006). Trabecular bone failure at the microstructural level. Current osteoporosis reports, 4(2):80–86.

[Nakamura et al., 2016] Nakamura, Y., Uchiyama, S., Kamimura, M., Komatsu, M., Ikegami, S., and Kato, H. (2016). Bone alterations are associated with ankle osteoarthritis joint pain. Scientific reports, 6.

[Nakasa et al., 2014] Nakasa, T., Adachi, N., Kato, T., and Ochi, M. (2014). Correlation between subchondral bone plate thickness and cartilage degeneration in osteoarthritis of the ankle. Foot & ankle international, 35(12):1341–1349.

[Nakasa et al., 2020] Nakasa, T., Ikuta, Y., Ota, Y., Kanemitsu, M., Sumii, J., Nekomoto, A., and Adachi, N. (2020). Bone mineralization changes in the subchondral bone of the medial gutter in chronic lateral ankle instability. Foot & Ankle International, page 1071100720938049.

[Nazemi et al., 2017] Nazemi, S. M., Amini, M., Kontulainen, S. A., Milner, J. S., Holdsworth, D. W., Masri, B. A., Wilson, D. R., and Johnston, J. D. (2017). Optimizing finite element predictions of local subchondral bone structural stiffness using neural network-derived density-modulus relationships for proximal tibial subchondral cortical and trabecular bone. Clinical Biomechanics, 41:1–8.

[Neogi, 2012] Neogi, T. (2012). Clinical significance of bone changes in osteoarthritis. In Arthritis research & therapy, volume 14, page A3. BioMed Central.

[Niebur et al., 1999] Niebur, G., Yuen, J., Hsia, A., and Keaveny, T. (1999). Convergence behavior of high-resolution finite element models of trabecular bone. Journal of biomechanical engineering, 121(6):629–635.

[Niebur et al., 2000] Niebur, G. L., Feldstein, M. J., Yuen, J. C., Chen, T. J., and Keaveny, T. M. (2000). High-resolution finite element models with tissue strength asymmetry accurately predict failure of trabecular bone. Journal of biomechanics, 33(12):1575–1583.

[Nowakowski et al., 2013] Nowakowski, A. M., Deyhle, H., Zander, S., Leumann, A., and Müller-Gerbl, M. (2013). Micro ct analysis of the subarticular bone structure in the area of the talar trochlea. Surgical and radiologic anatomy, 35(4):283–293.

[Oegema et al., 1997] Oegema, T. R., Carpenter, R. J., Hofmeister, F., and Thompson, R. C. (1997). The interaction of the zone of calcified cartilage and subchondral bone in osteoarthritis. Microscopy research and technique, 37(4):324–332.

[Öhman et al., 2007] Öhman, C., Baleani, M., Perilli, E., Dall'Ara, E., Tassani, S., Baruffaldi, F., and Viceconti, M. (2007). Mechanical testing of cancellous bone from the femoral head: experimental errors due to off-axis measurements. Journal of biomechanics, 40(11):2426–2433.

[Oliver and Pharr, 1992] Oliver, W. C. and Pharr, G. M. (1992). An improved technique for determining hardness and elastic modulus using load and displacement sensing indentation experiments. Journal of materials research, 7(6):1564–1583.

[Organisation, 2018] Organisation, W. H. (2018). Ageing and health. `https://www.who.int/news-room/fact-sheets/detail/ageing-and-health`.

[Osterhoff et al., 2016] Osterhoff, G., Morgan, E. F., Shefelbine, S. J., Karim, L., McNamara, L. M., and Augat, P. (2016). Bone mechanical properties and changes with osteoporosis. Injury, 47:S11–S20.

[Otsu, 1979] Otsu, N. (1979). A threshold selection method from gray-level histograms. IEEE transactions on systems, man, and cybernetics, 9(1):62–66.

[Pahr and Zysset, 2008] Pahr, D. H. and Zysset, P. K. (2008). Influence of boundary conditions on computed apparent elastic properties of cancellous bone. Biomechanics and modeling in mechanobiology, 7(6):463–476.

[Pahr and Zysset, 2009] Pahr, D. H. and Zysset, P. K. (2009). A comparison of enhanced continuum fe with micro fe models of human vertebral bodies. Journal of Biomechanics, 42(4):455–462.

[Pal and Routal, 1998] Pal, G. P. and Routal, R. V. (1998). Architecture of the cancellous bone of the human talus. The Anatomical Record: An Official Publication of the American Association of Anatomists, 252(2):185–193.

[Pal, 2014] Pal, S. (2014). Mechanical properties of biological materials. In Design of Artificial Human Joints & Organs, pages 23–40. Springer.

[Palmieri-Smith et al., 2010] Palmieri-Smith, R. M., Thomas, A. C., Karvonen-Gutierrez, C., and Sowers, M. F. (2010). Isometric quadriceps strength in women with mild, moderate, and severe knee osteoarthritis. American journal of physical medicine & rehabilitation/Association of Academic Physiatrists, 89(7):541.

[Pankaj, 2013] Pankaj, P. (2013). Patient-specific modelling of bone and bone-implant systems: the challenges. International journal for numerical methods in biomedical engineering, 29(2):233–249.

[Parfitt et al., 1987] Parfitt, A. M., Drezner, M. K., Glorieux, F. H., Kanis, J. A., Malluche, H., Meunier, P. J., Ott, S. M., and Recker, R. R. (1987). Bone histomorphometry: standardization of nomenclature, symbols, and units: report of the asbmr histomorphometry nomenclature committee. Journal of bone and mineral research, 2(6):595–610.

[Parkinson et al., 2008] Parkinson, I., Badiei, A., and Fazzalari, N. (2008). Variation in segmentation of bone from micro-ct imaging: implications for quantitative morphometric analysis. Australasian Physics & Engineering Sciences in Medicine, 31(2):160–164.

[Parr et al., 2013] Parr, W., Chamoli, U., Jones, A., Walsh, W., and Wroe, S. (2013). Finite element micro-modelling of a human ankle bone reveals the importance of the trabecular network to mechanical performance: new methods for the generation and comparison of 3d models. Journal of biomechanics, 46(1):200–205.

[Patel et al., 2003] Patel, V., Issever, A. S., Burghardt, A., Laib, A., Ries, M., and Majumdar, S. (2003). Microct evaluation of normal and osteoarthritic bone structure in human knee specimens. Journal of Orthopaedic Research, 21(1):6–13.

[Peters et al., 2018] Peters, A. E., Akhtar, R., Comerford, E. J., and Bates, K. T. (2018). The effect of ageing and osteoarthritis on the mechanical properties of cartilage and bone in the human knee joint. Scientific reports, 8(1):5931.

[Poelert et al., 2013] Poelert, S., Valstar, E., Weinans, H., and Zadpoor, A. A. (2013). Patient-specific finite element modeling of bones. Proceedings of the Institution of Mechanical Engineers, Part H: Journal of Engineering in Medicine, 227(4):464–478.

[Pritzker et al., 2006] Pritzker, K. P., Gay, S., Jimenez, S. A., Ostergaard, K., Pelletier, J.-P., Revell, P., Salter, D., and Van den Berg, W. (2006). Osteoarthritis cartilage histopathology: grading and staging. Osteoarthritis and cartilage, 14(1):13–29.

[Pugh et al., 1974] Pugh, J. W., Radin, E. L., and Rose, R. M. (1974). Quantitative studies of human subchondral cancellous bone: its relationship to the state of its overlying cartilage. JBJS, 56(2):313–321.

[Radin et al., 1972] Radin, E., Paul, I., and Rose, R. (1972). Role of mechanical factors in pathogenesis of primary osteoarthritis. The Lancet, 299(7749):519–522.

[Radin et al., 1970] Radin, E. L., Paul, I. L., and Tolkoff, M. J. (1970). Subchondral bone changes in patients with early degenerative joint disease. Arthritis & Rheumatology, 13(4):400–405.

[Radin and Rose, 1986] Radin, E. L. and Rose, R. M. (1986). Role of subchondral bone in the initiation and progression of cartilage damage. Clinical orthopaedics and related research, 213:34–40.

[Raikin et al., 2007] Raikin, S. M., Elias, I., Zoga, A. C., Morrison, W. B., Besser, M. P., and Schweitzer, M. E. (2007). Osteochondral lesions of the talus: localization and morphologic data from 424 patients using a novel anatomical grid scheme. Foot & ankle international, 28(2):154–161.

[Renault et al., 2020] Renault, J.-B., Carmona, M., Tzioupis, C., Ollivier, M., Argenson, J.-N., Parratte, S., and Chabrand, P. (2020). Tibial subchondral trabecular bone micromechanical and microarchitectural properties are affected by alignment and osteoarthritis stage. Scientific reports, 10(1):1–10.

[Rho, 1996] Rho, J.-Y. (1996). An ultrasonic method for measuring the elastic properties of human tibial cortical and cancellous bone. Ultrasonics, 34(8):777–783.

[Rho et al., 1995] Rho, J.-Y., Hobatho, M., and Ashman, R. (1995). Relations of mechanical properties to density and ct numbers in human bone. Medical engineering & physics, 17(5):347–355.

[Rho et al., 1998] Rho, J.-Y., Kuhn-Spearing, L., and Zioupos, P. (1998). Mechanical properties and the hierarchical structure of bone. Medical engineering & physics, 20(2):92–102.

[Rho et al., 1997] Rho, J.-Y., Tsui, T. Y., and Pharr, G. M. (1997). Elastic properties of human cortical and trabecular lamellar bone measured by nanoindentation. Biomaterials, 18(20):1325–1330.

[Rho et al., 2002] Rho, J. Y., Zioupos, P., Currey, J. D., and Pharr, G. M. (2002). Microstructural elasticity and regional heterogeneity in human femoral bone of various ages examined by nano-indentation. Journal of biomechanics, 35(2):189–198.

[Rieger et al., 2018] Rieger, R., Auregan, J.-C., and Hoc, T. (2018). Micro-finite-element method to assess elastic properties of trabecular bone at micro-and macroscopic level. Morphologie, 102(336):12–20.

[Rincón Kohli, 2003] Rincón Kohli, L. (2003). Identification of a multiaxial failure criterion for human trabecular bone. Technical report, EPFL.

[Rincón-Kohli and Zysset, 2009] Rincón-Kohli, L. and Zysset, P. K. (2009). Multi-axial mechanical properties of human trabecular bone. Biomechanics and modeling in mechanobiology, 8(3):195–208.

[Robson Brown et al., 2014] Robson Brown, K., Tarsuslugil, S., Wijayathunga, V., and Wilcox, R. (2014). Comparative finite-element analysis: a single computational modelling method can estimate the mechanical properties of porcine and human vertebrae. Journal of The Royal Society Interface, 11(95):20140186.

[Salmon et al., 2015] Salmon, P. L., Ohlsson, C., Shefelbine, S. J., and Doube, M. (2015). Structure model index does not measure rods and plates in trabecular bone. Frontiers in endocrinology, 6:162.

[Saltzman et al., 2005] Saltzman, C. L., Salamon, M. L., Blanchard, G. M., Huff, T., Hayes, A., Buckwalter, J. A., and Amendola, A. (2005). Epidemiology of ankle arthritis: report of a consecutive series of 639 patients from a tertiary orthopaedic center. The Iowa orthopaedic journal, 25:44.

[Schiff et al., 2007] Schiff, A., Li, J., Inoue, N., Masuda, K., Lidtke, R., and Muehleman, C. (2007). Trabecular angle of the human talus is associated with the level of cartilage degeneration. J Musculoskelet Neuronal Interact, 7(3):224–30.

[Shapiro and Wilk, 1965] Shapiro, S. S. and Wilk, M. B. (1965). An analysis of variance test for normality (complete samples). Biometrika, 52(3/4):591–611.

[Sharma et al., 2013] Sharma, A. R., Jagga, S., Lee, S.-S., and Nam, J.-S. (2013). Interplay between cartilage and subchondral bone contributing to pathogenesis of osteoarthritis. International journal of molecular sciences, 14(10):19805–19830.

[Sneppen et al., 1982] Sneppen, O., Christensen, P., Larsen, H., and Vang, P. (1982). Mechanical testing of trabecular bone in knee replacement. International orthopaedics, 5(4):251–256.

[Sophia Fox et al., 2009] Sophia Fox, A. J., Bedi, A., and Rodeo, S. A. (2009). The basic science of articular cartilage: structure, composition, and function. Sports health, 1(6):461–468.

[Stauber et al., 2006] Stauber, M., Rapillard, L., van Lenthe, G. H., Zysset, P., and Müller, R. (2006). Importance of individual rods and plates in the assessment of bone quality and their contribution to bone stiffness. Journal of Bone and Mineral Research, 21(4):586–595.

[Stauffer et al., 1977] Stauffer, R. N., Chao, E., and Brewster, R. C. (1977). Force and motion analysis of the normal, diseased, and prosthetic ankle joint. Clinical orthopaedics and related research, (127):189–196.

[Steiner et al., 2020] Steiner, L., Synek, A., and Pahr, D. H. (2020). Comparison of different microct-based morphology assessment tools using human trabecular bone. Bone reports, 12:100261.

[Tarsuslugil et al., 2013] Tarsuslugil, S. M., O'Hara, R. M., Dunne, N. J., Buchanan, F. J., Orr, J. F., Barton, D. C., and Wilcox, R. K. (2013). Development of calcium phosphate cement for the augmentation of traumatically fractured porcine specimens using vertebroplasty. Journal of biomechanics, 46(4):711–715.

[Teichtahl et al., 2015] Teichtahl, A. J., Wluka, A. E., Wijethilake, P., Wang, Y., Ghasem-Zadeh, A., and Cicuttini, F. M. (2015). Wolff's law in action: a mechanism for early knee osteoarthritis. Arthritis research & therapy, 17(1):207.

[Thurner, 2009] Thurner, P. J. (2009). Atomic force microscopy and indentation force measurement of bone. Wiley Interdisciplinary Reviews: Nanomedicine and Nanobiotechnology, 1(6):624–649.

[Tomanik et al., 2016] Tomanik, M., Nikodem, A., and Filipiak, J. (2016). Microhardness of human cancellous bone tissue in progressive hip osteoarthritis. journal of the mechanical behavior of biomedical materials, 64:86–93.

[Topoliński et al., 2012] Topoliński, T., Cichański, A., Mazurkiewicz, A., and Nowicki, K. (2012). The relationship between trabecular bone structure modeling methods and the elastic modulus as calculated by fem. The Scientific World Journal, 2012.

[Torres-del Pliego et al., 2013] Torres-del Pliego, E., Vilaplana, L., Güerri-Fernández, R., and Diez-Pérez, A. (2013). Measuring bone quality. Current rheumatology reports, 15(11):373.

[Townsend et al., 1975] Townsend, P. R., Rose, R. M., and Radin, E. L. (1975). Buckling studies of single human trabeculae. Journal of biomechanics, 8(3-4):199–201.

[Treppo et al., 2000] Treppo, S., Koepp, H., Quan, E. C., Cole, A. A., Kuettner, K. E., and Grodzinsky, A. J. (2000). Comparison of biomechanical and biochemical properties of cartilage from human knee and ankle pairs. Journal of Orthopaedic Research, 18(5):739–748.

[Tsukahara, 1990] Tsukahara, T. (1990). Degeneration of articular cartilage of the ankle in cadavers studied by gross and radiographic examinations. Nihon Seikeigeka Gakkai Zasshi, 64(12):1195–1201.

[Turner et al., 2001] Turner, C., Burr, D., and Cowin, S. (2001). Bone mechanics handbook. Experimental Techniques for Bone Mechanics, ed, 2.

[Turner et al., 1999] Turner, C. H., Rho, J., Takano, Y., Tsui, T. Y., and Pharr, G. M. (1999). The elastic properties of trabecular and cortical bone tissues are similar: results from two microscopic measurement techniques. Journal of biomechanics, 32(4):437–441.

[Ulrich et al., 1999] Ulrich, D., Van Rietbergen, B., Laib, A., and Ruegsegger, P. (1999). The ability of three-dimensional structural indices to reflect mechanical aspects of trabecular bone. Bone, 25(1):55–60.

[Ulrich et al., 1998] Ulrich, D., van Rietbergen, B., Weinans, H., and Rüegsegger, P. (1998). Finite element analysis of trabecular bone structure: a comparison of image-based meshing techniques. Journal of biomechanics, 31(12):1187–1192.

[Ulrich et al., 2017] Ulrich, S. D., Parks, B. G., Tsai, M. A., and Miller, S. D. (2017). Distribution of subchondral bone puncture strength in the talus and tibial plafond: A biomechanical study. Foot & Ankle Specialist, page 1938640017700975.

[Valderrabano et al., 2009] Valderrabano, V., Horisberger, M., Russell, I., Dougall, H., and Hintermann, B. (2009). Etiology of ankle osteoarthritis. Clinical Orthopaedics and Related Research, 467(7):1800–1806.

[Valderrabano et al., 2020] Valderrabano, V., Nunley, J. A., DeOrio, J. K., Easley, M. E., Alsayel, F., Herrera, M., and Wiewiorski, M. (2020). Surgical technique of the vantage total ankle arthroplasty. Techniques in Foot & Ankle Surgery, 19(1):3–9.

[Valderrabano et al., 2006] Valderrabano, V., Von Tscharner, V., Nigg, B. M., Hintermann, B., Goepfert, B., Fung, T. S., Frank, C. B., and Herzog, W. (2006). Lower leg muscle atrophy in ankle osteoarthritis. Journal of orthopaedic research, 24(12):2159–2169.

[van Bergen et al., 2010] van Bergen, C. J., Zengerink, M., Blankevoort, L., van Sterkenburg, M. N., van Oldenrijk, J., and van Dijk, C. N. (2010). Novel metallic implantation technique for osteochondral defects of the medial talar dome: a cadaver study. Acta orthopaedica, 81(4):495–502.

[Van der Linden et al., 2001] Van der Linden, J., Birkenhäger-Frenkel, D., Verhaar, J., and Weinans, H. (2001). Trabecular bone's mechanical properties are affected by its non-uniform mineral distribution. Journal of Biomechanics, 34(12):1573–1580.

[van Rietbergen, 2001] van Rietbergen, B. (2001). Micro-fe analyses of bone: state of the art. In Noninvasive assessment of trabecular bone architecture and the competence of bone, pages 21–30. Springer.

[van Rietbergen et al., 1995] van Rietbergen, B., Weinans, H., Huiskes, R., and Odgaard, A. (1995). A new method to determine trabecular bone elastic properties and loading using micromechanical finite-element models. Journal of biomechanics, 28(1):69–81.

[Verhulp et al., 2006] Verhulp, E., van Rietbergen, B., and Huiskes, R. (2006). Comparison of micro-level and continuum-level voxel models of the proximal femur. Journal of biomechanics, 39(16):2951–2957.

[Verhulp et al., 2008a] Verhulp, E., van Rietbergen, B., Müller, R., and Huiskes, R. (2008a). Indirect determination of trabecular bone effective tissue failure properties using micro-finite element simulations. Journal of biomechanics, 41(7):1479–1485.

[Verhulp et al., 2008b] Verhulp, E., Van Rietbergen, B., Müller, R., and Huiskes, R. (2008b). Micro-finite element simulation of trabecular-bone post-yield behaviour–effects of material model, element size and type. Computer methods in biomechanics and biomedical engineering, 11(4):389–395.

[Viguet-Carrin et al., 2006] Viguet-Carrin, S., Garnero, P., and Delmas, P. (2006). The role of collagen in bone strength. Osteoporosis international, 17(3):319–336.

[Vijayakumar and Quenneville, 2016] Vijayakumar, V. and Quenneville, C. E. (2016). Quantifying the regional variations in the mechanical properties of cancellous bone of the tibia using indentation testing and quantitative computed tomographic imaging. Proceedings of the Institution of Mechanical Engineers, Part H: Journal of Engineering in Medicine, 230(6):588–593.

[Waldstein et al., 2016] Waldstein, W., Perino, G., Gilbert, S. L., Maher, S. A., Windhager, R., and Boettner, F. (2016). Oarsi osteoarthritis cartilage histopathology assessment system: A biomechanical evaluation in the human knee. Journal of Orthopaedic Research, 34(1):135–140.

[Wang et al., 2015] Wang, J., Zhou, B., Liu, X. S., Fields, A. J., Sanyal, A., Shi, X., Adams, M., Keaveny, T. M., and Guo, X. E. (2015). Trabecular plates and rods determine elastic modulus and yield strength of human trabecular bone. Bone, 72:71–80.

[Weaver, 1966] Weaver, J. K. (1966). The microscopic hardness of bone. JBJS, 48(2):273–288.

[Whitehouse, 1974] Whitehouse, W. (1974). The quantitative morphology of anisotropic trabecular bone. Journal of microscopy, 101(2):153–168.

[Wiewiorski et al., 2016] Wiewiorski, M., Hoechel, S., Anderson, A. E., Nowakowski, A. M., DeOrio, J. K., Easley, M. E., Nunley, J. A., Valderrabano, V., and Barg, A. (2016). Computed tomographic evaluation of joint geometry in patients with end-stage ankle osteoarthritis. Foot & ankle international, 37(6):644–651.

[Wijayathunga et al., 2008] Wijayathunga, V., Jones, A., Oakland, R., Furtado, N., Hall, R., and Wilcox, R. (2008). Development of specimen-specific finite element models of human vertebrae for the analysis of vertebroplasty. Proceedings of the Institution of Mechanical Engineers, Part H: Journal of Engineering in Medicine, 222(2):221–228.

[Wilson et al., 1990] Wilson, M. G., MICHET Jr, C. J., ILSTRUP, D. M., and MELTON III, L. J. (1990). Idiopathic symptomatic osteoarthritis of the hip and knee: a population-based incidence study. In Mayo Clinic Proceedings, volume 65, pages 1214–1221. Elsevier.

[Wixson et al., 1989] Wixson, R. L., Elasky, N., and Lewis, J. (1989). Cancellous bone material properties in osteoarthritic and rheumatoid total knee patients. Journal of Orthopaedic Research, 7(6):885–892.

[Wolff, 1986] Wolff, J. (1986). The law of bone remodeling. berlin, heibelberg.

[Wolfram et al., 2012] Wolfram, U., Gross, T., Pahr, D. H., Schwiedrzik, J., Wilke, H.-J., and Zysset, P. K. (2012). Fabric-based tsai–wu yield criteria for vertebral trabecular bone in stress and strain space. Journal of the mechanical behavior of biomedical materials, 15:218–228.

[Wolfram et al., 2010] Wolfram, U., Wilke, H.-J., and Zysset, P. K. (2010). Valid μ finite element models of vertebral trabecular bone can be obtained using tissue properties measured with nanoindentation under wet conditions. Journal of biomechanics, 43(9):1731–1737.

[Wright and Hayes, 1976] Wright, T. and Hayes, W. (1976). Tensile testing of bone over a wide range of strain rates: effects of strain rate, microstructure and density. Medical and biological engineering, 14(6):671.

[Wu et al., 2018] Wu, D., Isaksson, P., Ferguson, S. J., and Persson, C. (2018). Young's modulus of trabecular bone at the tissue level: A review. Acta biomaterialia.

[Yamada et al., 2002] Yamada, K., Healey, R., Amiel, D., Lotz, M., and Coutts, R. (2002). Subchondral bone of the human knee joint in aging and osteoarthritis. Osteoarthritis and cartilage, 10(5):360–369.

[Zapata-Cornelio et al., 2017] Zapata-Cornelio, F. Y., Day, G. A., Coe, R. H., Sikora, S. N., Wijayathunga, V. N., Tarsuslugil, S. M., Mengoni, M., and Wilcox, R. K. (2017). Methodology to produce specimen-specific models of vertebrae: application to different species. Annals of biomedical engineering, 45(10):2451–2460.

[Zhao et al., 2018] Zhao, S., Arnold, M., Ma, S., Abel, R., Cobb, J., Hansen, U., and Boughton, O. (2018). Standardizing compression testing for measuring the stiffness of human bone. Bone & joint research, 7(8):524–538.

[Zuo et al., 2016] Zuo, Q., Lu, S., Du, Z., Friis, T., Yao, J., Crawford, R., Prasadam, I., and Xiao, Y. (2016). Characterization of nano-structural and nano-mechanical properties of osteoarthritic subchondral bone. BMC musculoskeletal disorders, 17(1):367.

[Zysset, 2009] Zysset, P. (2009). Indentation of bone tissue: a short review. Osteoporosis international, 20(6):1049–1055.

[Zysset and Curnier, 1995] Zysset, P. and Curnier, A. (1995). An alternative model for anisotropic elasticity based on fabric tensors. Mechanics of Materials, 21(4):243–250.

[Zysset and Rincón, 2006] Zysset, P. and Rincón, L. (2006). An alternative fabric-based yield and failure criterion for trabecular bone. In Mechanics of biological tissue, pages 457–470. Springer.

[Zysset et al., 1994] Zysset, P., Sonny, M., and Hayes, W. (1994). Morphology-mechanical property relations in trabecular bone of the osteoarthritic proximal tibia. The Journal of arthroplasty, 9(2):203–216.

[Zysset, 2003] Zysset, P. K. (2003). A review of morphology–elasticity relationships in human trabecular bone: theories and experiments. Journal of biomechanics, 36(10):1469–1485.

APPENDIX A

LIST OF RESOURCES

A.1 Sample Preparation

NAME	MANUFACTURER	DESCRIPTION
Polymethyl-methacralate (PMMA)	WHW Plastics, UK	Powder + liquid mix to create PMMA cement.
Thermo Scientific Oxoid Phosphate-buffered Saline (PBS) tablets	Fisher Scientific UK Ltd.	Saline tablets to be mixed into distilled water to create buffer solution for biological tissues.
Thickness Gauge (DD-50-V)	Hans Schmidt & Co GmbH	Height measurements of bone cores to a resolution of 0.01 mm.
Chisel (6.5 mm ⌀)	Smith & Nephew	Part of a clinical osteochondral grafting (mosaicplasty) kit.
Cold-cure resin (Technovit 4006 SE)	Heraeus Kulzer GmbH, Germany	Embedding resin for nanoindentation.
Diamond suspension	Hermes Abrasives, Hamburg, Germany	Polishing suspension fluid.

A.2 Scripts

NAME	VERSION	DESCRIPTION
ISQtoTiff	1.0	Image conversion from .ISQ to .tiff in MatLab
opti4Abq	2.0.3	An optimisation Toolbox in Python; Github:[Mengoni, 2015]

A.3 Equipment

A.3.1 iMBE, University of Leeds

NAME	MANUFACTURER	PURPOSE
μCT100	ScanCo Medical, Switzerland	μCT scanner
XtremeCT	ScanCo Medical, Switzerland	HR-pQCT scanner
Instron 3365	Instron, Massachusetts, United States	Mechanical testing
BioPuls Bath	Instron, Massachusetts, United States	Temperature-Controlled BioBath
Advanced Research Computing (ARC3)	University of Leeds HPC	High Performance Computing facility for FEA

A.3.2 IMPEE, Heriot-Watt University

NAME	MANUFACTURER	PURPOSE
Band saw	Exakt, Norderstedt, Germany	Diamond blade band saw
Microscope (DFC7000T)	Leica Microsystems, Wetzlar, Germany	Microscope
LaboForce-Mi	Struers, Ballerup, Denmark	Polishing equipment

A.4 Software

NAME	VERSION	DEVELOPER	DETAILS
Abaqus CAE	2.0/2017	Dassault Systemes	Finite Element Analysis software.
Matlab	R2017a	Mathworks	Used to run scripts for image file format conversion & mechanical data analysis.
ImageJ	1.52i	NIH, USA	Image analysis & manipulation.
BoneJ	1.4.2	Doube et al.	Bone image analysis plugin for ImageJ [Doube et al., 2010].
ITS	-	X.Edward Guo et al.	3D Individual Trabecula Segmentation (ITS) Morphological Analysis & Modelling Technique (MS.Visual C++) [Liu et al., 2009]. Purchased via. Columbia Technology Ventures.
Simpleware ScanIP	M-2017.06-SP1	Synopsys	Used for image segmentation & meshing.
RStudio	1.1.463	RStudio Inc.	Used for statistical analyses (R) and to create figures.
Anaconda	4.9.0	Anaconda Inc.	Used as platform to run Python (2.7 & 3.8) for optimisation toolbox and to create figures.

APPENDIX B

PORCINE TISSUE

B.1 Porcine Tissue Information

Table B.1: Weight of pigs (kg) from which porcine tissue was retrieved. Samples sourced from local abbatoir, Scotlean Ltd and Yorkshire FA, UK

SPECIMEN	WEIGHT (KG)
1	90.9
2	95.2
4	91.7
5	68.1
6	87.6
7	61.2
8	66.9
9	77

B.2 Verification of BV/TV

A 4 mm cube of bone was extracted from binarised images of three porcine bone image stacks that were selected at random. Table B.2 shows the BV/TV values obtained from BoneJ (ImageJ), compared to those obtained using a Python script based on SimpleITK (SITK) where bone and space/marrow voxel are counted individually. It is clear that the values obtained from both are identical to at 3 decimal places.

Table B.2: Verification of BV/TV values obtained using BoneJ and SimpleITK (SITK).

SPECIMEN	BONEJ	SITK
1	0.327	0.327044992
2	0.375	0.375039168
3	0.365	0.36492256

B.3 Raw Data

B.3.1 Continuum-level model calibration: specimen dataset

SPECIMEN	k_{exp} (N/mm)	k_{comp} (N/mm)	E (MPa)	σ_{max}	BV/TV	DA	Conn.D (mm^3)	Tb.Th (mm)
Cal_1	1459.712	1700.610	380.750	11.28	0.411	0.681	5.449	0.183
Val_1	1232.339	1009.610	270.684	16.56	0.401	0.642	4.685	0.18
Cal_2	1184.466	714.432	353.143	12.03	0.395	0.43	6.146	0.182
Val_2	1245.415	1369.440	216.542	12.13	0.389	0.658	8.231	0.137
Cal_3	1079.212	743.014	259.647	12.27	0.337	0.707	4.795	0.154
Val_3	838.915	614.240	252.231	8.54	0.365	0.388	8.258	0.156
Cal_4	904.720	810.512	221.353	12.71	0.336	0.658	6.876	0.13
Val_4	1342.873	1336.200	400.286	16.53	0.37	0.613	6.052	0.153
Cal_5	1231.508	1585.700	286.769	16.09	0.3588	0.588	9.429	0.15
Val_5	887.576	620.544	284.923	7.17	0.35	0.491	7.955	0.155

B.3.2 Trabecular-level model calibration: specimen dataset

SPECIMEN	k_{hFE} (N/mm)	$k_{\mu\mathrm{FE}}$ (N/mm)	BV/TV	DA	Tb.Th (mm)	Conn.D (mm^3)	EF
Cal_1	722.34	669.37	0.327	0.785	0.165	16.219	-0.01
Val_1	892.51	831.89	0.401	0.732	0.185	10.217	-0.07
Cal_2	1047.16	996.87	0.465	0.605	0.189	11.848	-0.0167
Val_2	832.33	845.34	0.375	0.717	0.136	20.947	0.0321
Cal_3	768.72	736.15	0.346	0.737	0.149	15.018	0.0405
Val_3	651.09	432.10	0.296	0.436	0.156	15.256	-0.0997
Cal_4	742.28	837.19	0.333	0.726	0.130	18.959	00.0398
Val_4	833.49	911.92	0.372	0.75	0.162	18.568	-0.0779
Cal_5	816.26	867.30	0.365	0.708	0.165	20.549	0.00668
Val_5	869.24	837.68	0.391	0.590	0.163	20.525	0.045

APPENDIX C

HUMAN TISSUE

C.1 Donor information

Table C.1: Human donors: non-diseased cadaveric feet (MedCure USA) and patient osteoarthritic bone samples (Harrogate & District NHS Foundation Trust, Harrogate, UK).

DONOR ID	CONDITION	SEX (M/F)	AGE (YEARS)	FOOT (L/R)	BMI
LM43	Non-Diseased	M	43	L	28.13
RM50	Non-Diseased	M	50	R	29.56
RM57	Non-Diseased	M	57	R	20.61
RM58	Osteoarthritic	M	58	R	-
RM65	Osteoarthritic	M	65	R	-
LM68	Osteoarthritic	M	68	L	-

C.2 Sample Images

C.2.1 Non-Diseased Tissue

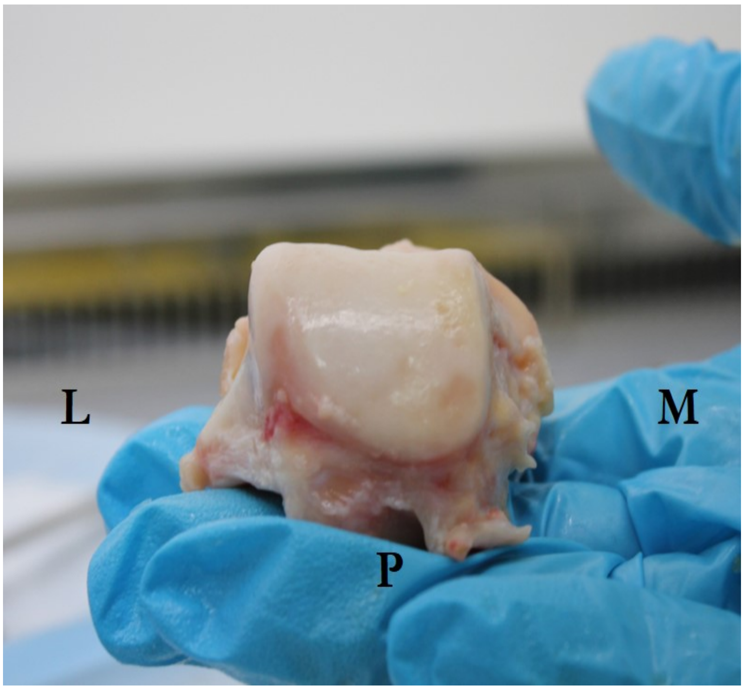

(i) Talus

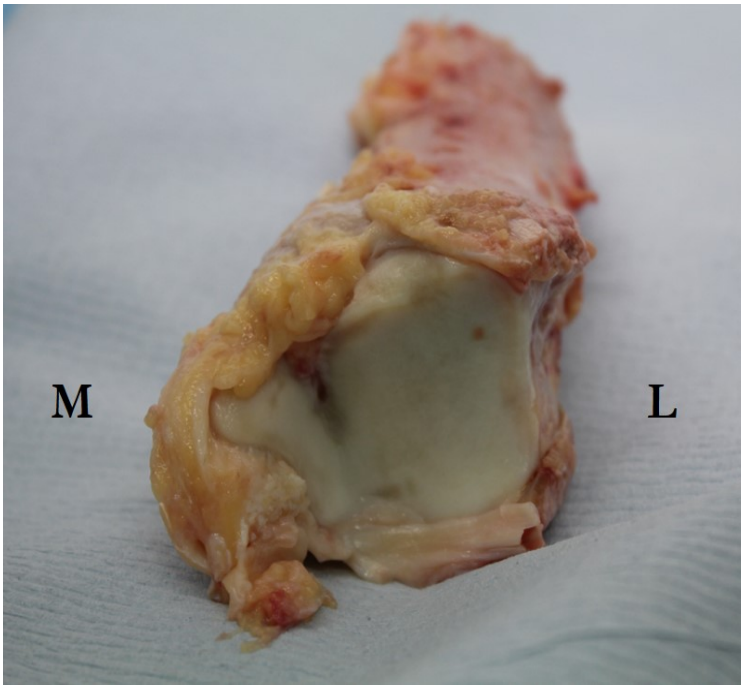

(ii) Distal tibia

Figure C.1: LM43 ankle

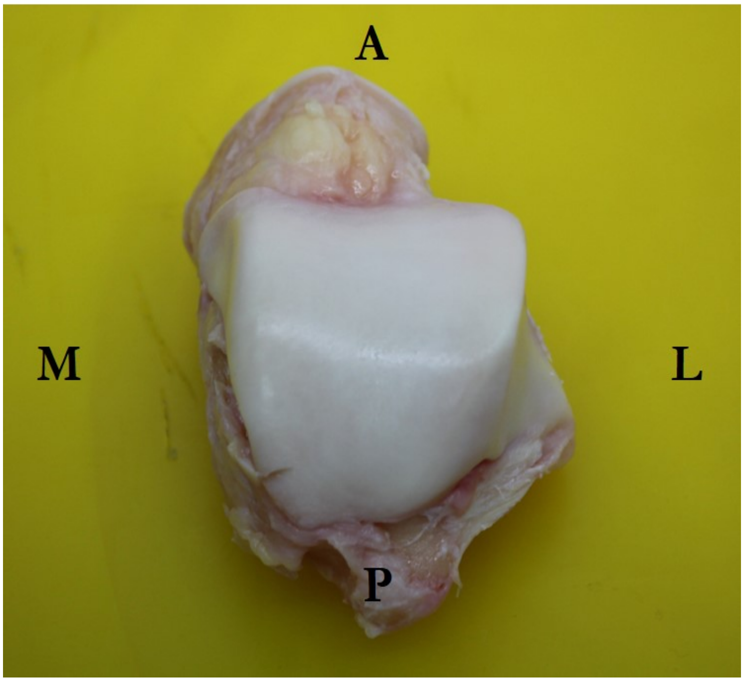

(i) Talus

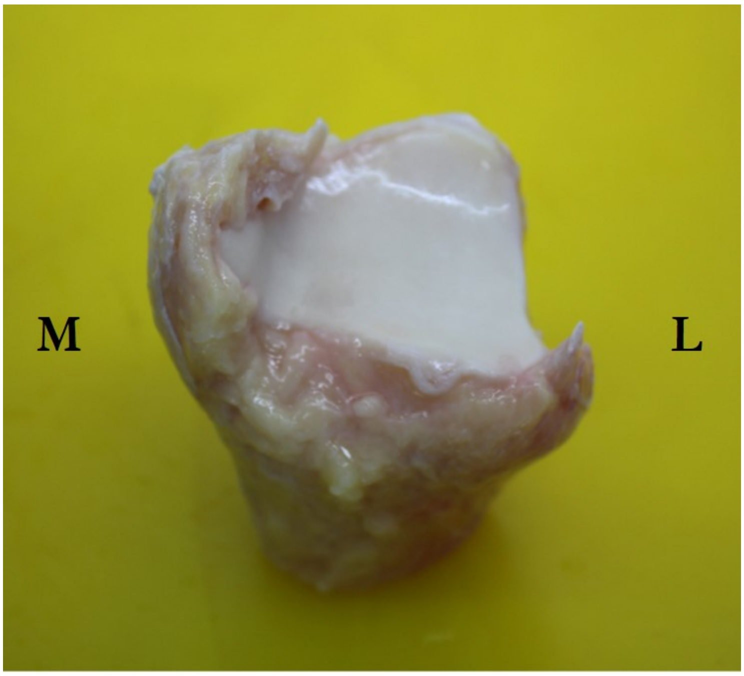

(ii) Distal tibia

Figure C.2: RM50 ankle

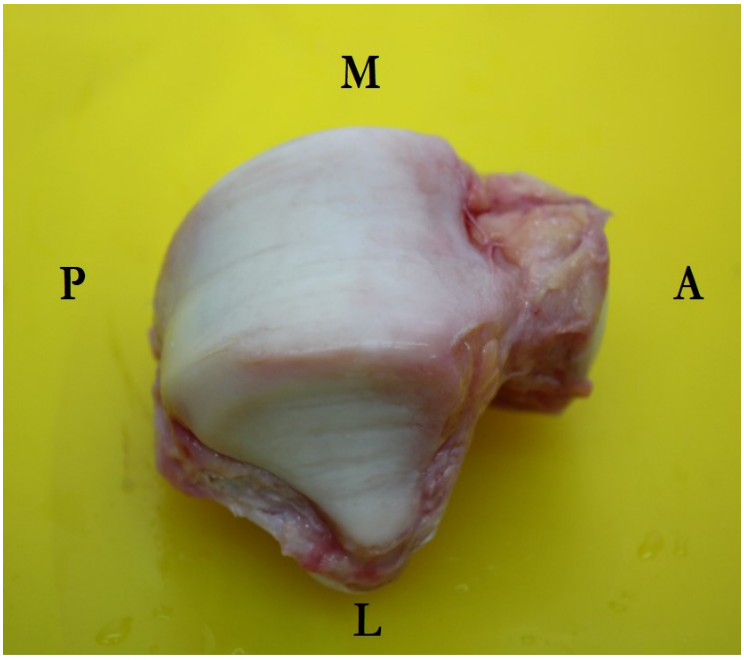

(i) Talus

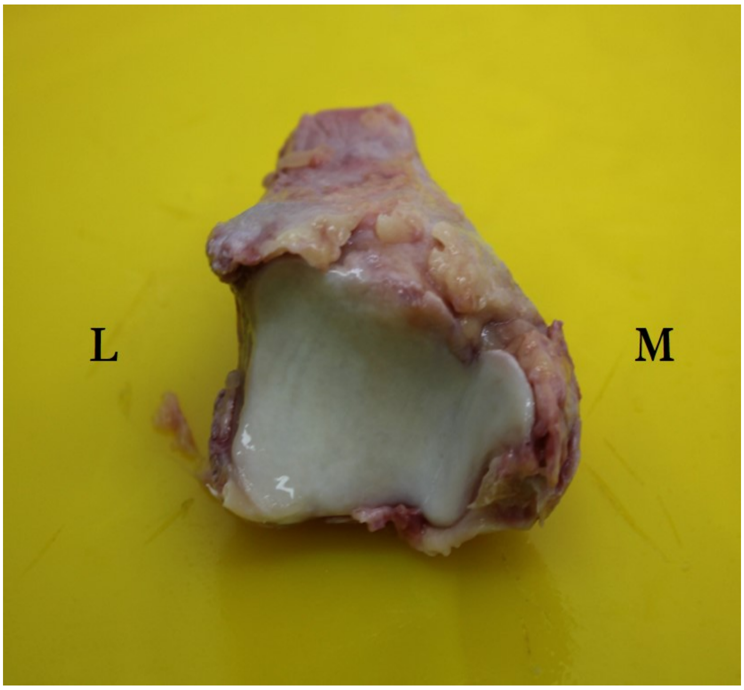

(ii) Distal tibia

Figure C.3: RM57 ankle

C.2.2 Osteoarthritic Tissue

Figure C.4: RM58 donor tissue showing superior (top) and angled views (bottom) with annotation of posterior (P) and anterior (blue lines) directions. LHS = talus (x2), RHS = distal tibia (x1).

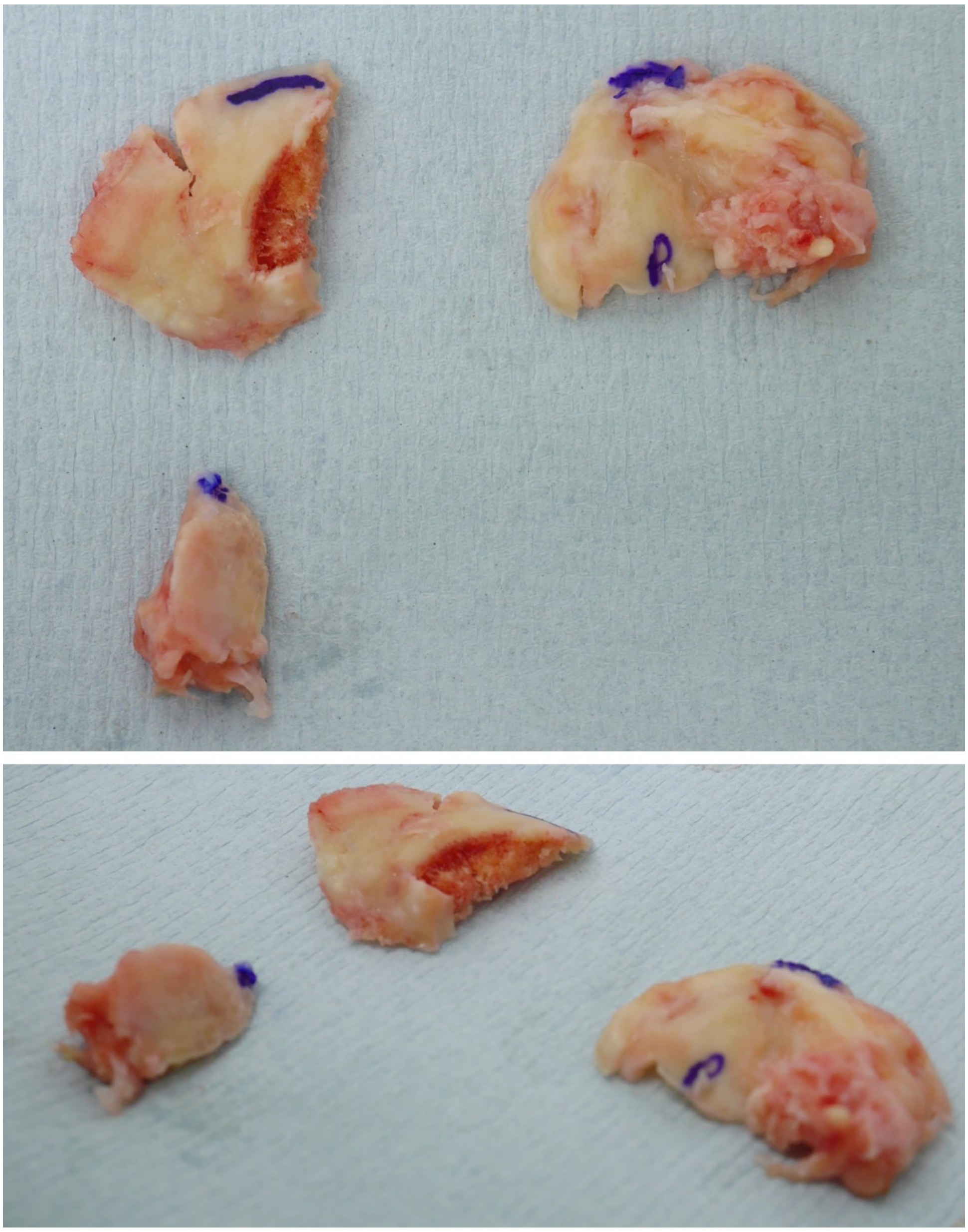

Figure C.5: RM65 donor tissue showing superior (top) and angled views (bottom) with annotation of anterior direction (blue line). LHS = talus (x1), RHS = distal tibia (x3).

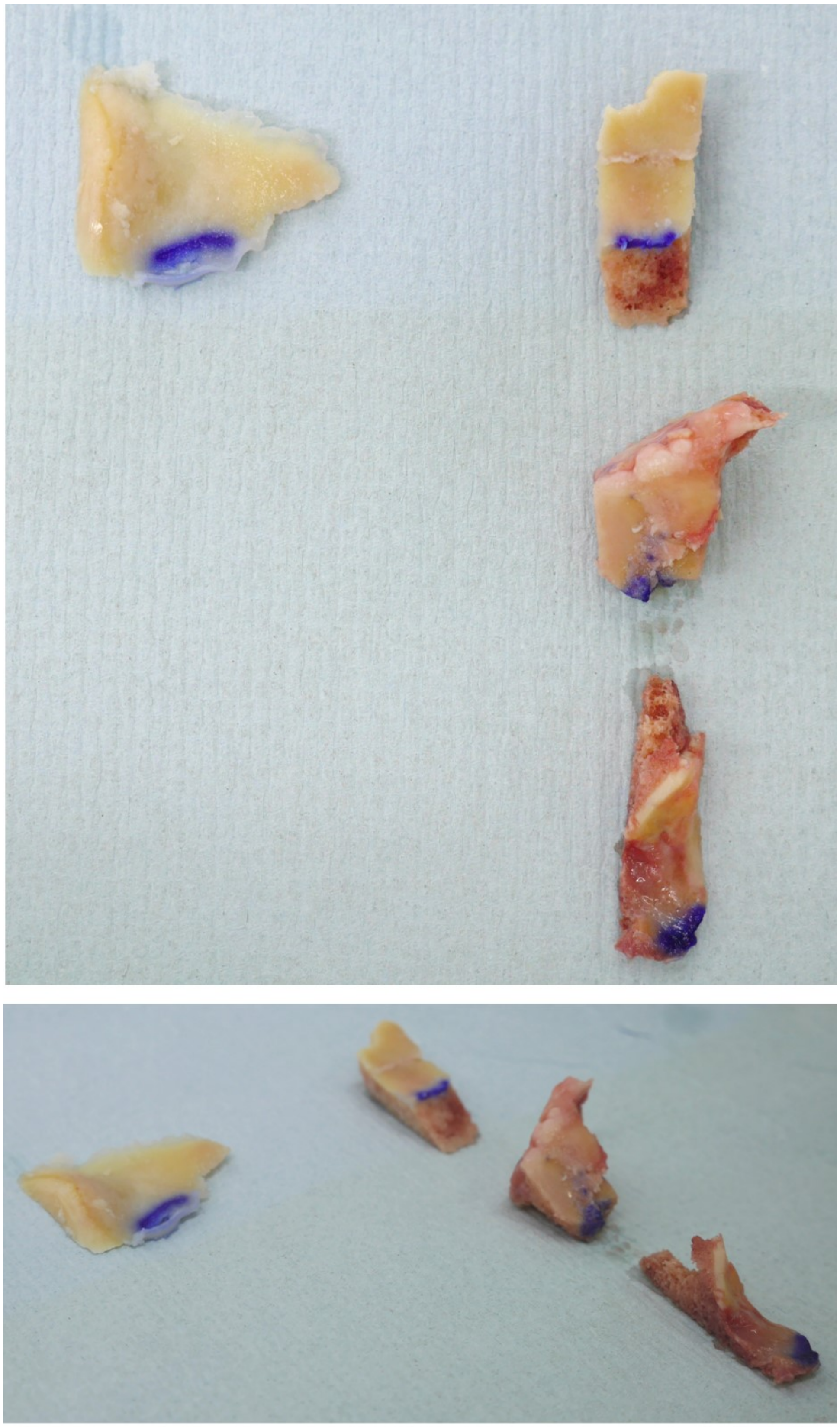

Figure C.6: LM68 donor tissue showing superior (top) and angled views (bottom). LHS = talus (x2), RHS = distal tibia (x2)

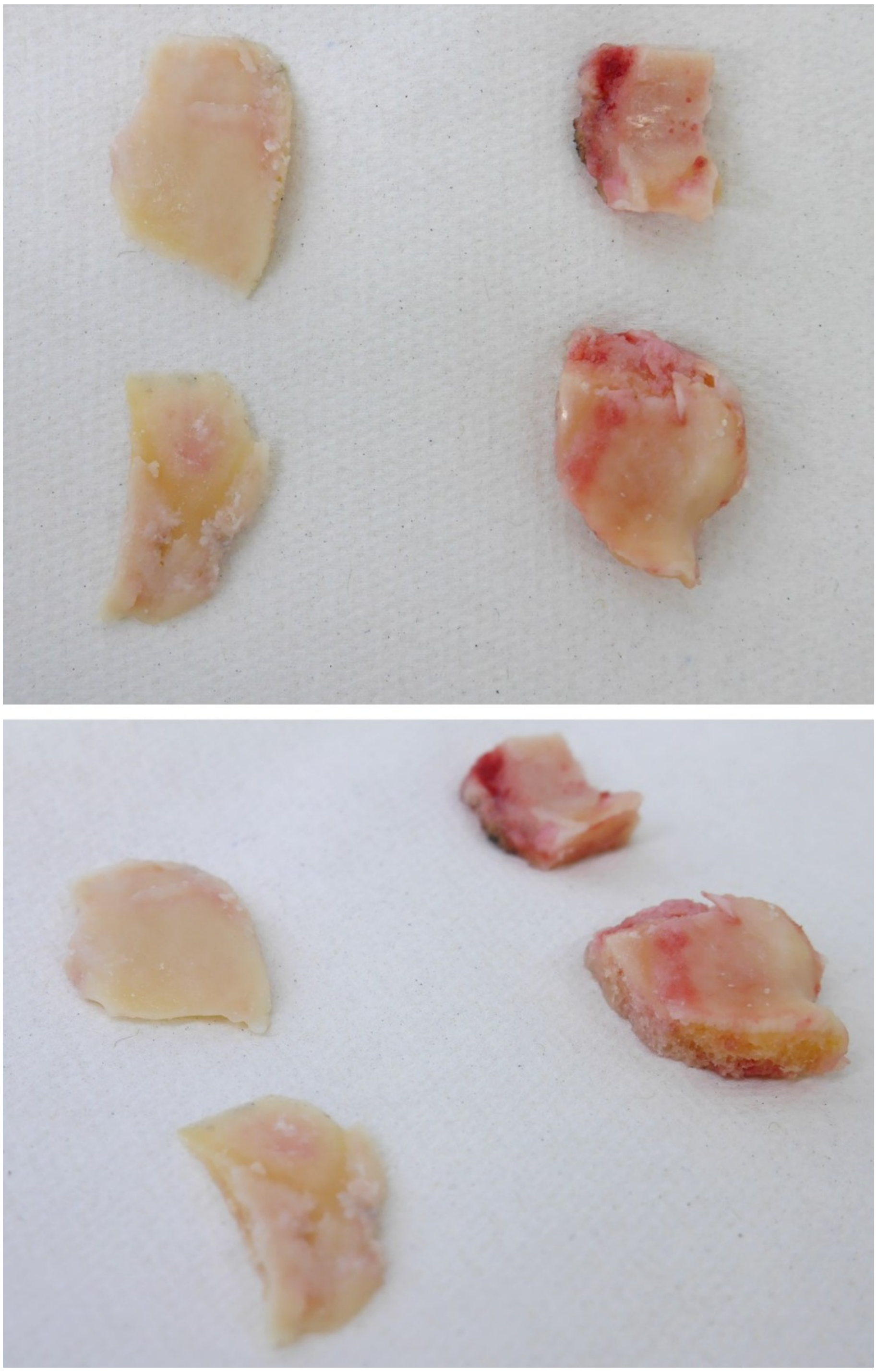

C.3 Raw Data

The following section provides the raw data from human tissue studies reported within this thesis.

C.3.1 Microarchitectural Properties: cylindrical volumes

BONE	BV/TV	DA	Tb.Th (mm)	Conn.D (mm^{-3})
Distal Tibia	0.379	0.539	0.187	8.431
Distal Tibia	0.354	0.602	0.191	12.312
Distal Tibia	0.369	0.471	0.198	7.672
Distal Tibia	0.27	0.687	0.194	4.379
Distal Tibia	0.263	0.597	0.19	4.06
Distal Tibia	0.321	0.558	0.2	2.298
Distal Tibia	0.375	0.569	0.233	2.791
Distal Tibia	0.431	0.45	0.235	12.691
Distal Tibia	0.366	0.753	0.231	6.976
Distal Tibia	0.343	0.542	0.228	2.723
Talus	0.431	0.74	0.197	15.071
Talus	0.403	0.667	0.189	14.889
Talus	0.333	0.546	0.189	15.035
Talus	0.391	0.407	0.219	11.755
Talus	0.353	0.68	0.214	4.888
Talus	0.367	0.365	0.22	7.154
Talus	0.432	0.724	0.237	6.768
Talus	0.375	0.669	0.215	6.303
Talus	0.319	0.526	0.199	6.935
Talus	0.403	0.532	0.237	8.39
Talus	0.409	0.634	0.216	10.367

Table C.2: Standard morphological data for non-diseased ankle specimens (cylindrical volumes; 6.5 mm ⌀) as measured using BoneJ.

C.3.2 Continuum-level and Trabecular-Level model calibration: specimen dataset

BONE	DONOR	GROUP	**hFE Model Calibration**		**μFE Model Calibration**	
			k_{exp} (N/mm)	k_{comp} (N/mm)	k_{hFE} (N/mm)	$k_{\mu FE}$ (N/mm)
Talus	RM57	Calibration	1406.40	1326.29	4535.36	5330.67
Talus	RM57	Calibration	944.93	900.17	3408.52	3490.66
Talus	RM57	Calibration	1243.50	1278.89	5550.72	4874.83
Talus	RM57	Calibration	1410.20	1199.80	4508.91	3829.18
Talus	RM50	Calibration	1017.30	1047.06	3013.77	3170.60
Talus	RM50	Calibration	1404.50	1491.51	3807.08	4199.34
Talus	RM57	Validation	954.50	1183.61	4215.56	3993.01
Talus	RM57	Validation	1128.10	1026.90	3813.97	4443.99
Talus	RM50	Validation	1252.60	1273.89	4948.60	4214.15
Talus	LM43	Validation	1228.40	1522.09	4300.81	5304.29
Talus	LM43	Validation	1101.20	1195.23	4388.73	4988.09
Distal Tibia	RM57	Calibration	1275.42	1299.20	3749.13	4087.76
Distal Tibia	RM57	Calibration	854.94	884.73	5347.93	4792.89
Distal Tibia	RM50	Calibration	763.75	834.92	3001.89	3072.44
Distal Tibia	LM43	Calibration	1248.65	1517.60	3402.47	3711.04
Distal Tibia	LM43	Calibration	1191.96	1023.90	4565.58	4242.45
Distal Tibia	RM57	Validation	1223.10	1155.40	5182.79	4400.36
Distal Tibia	RM57	Validation	1066.83	1257.60	4077.39	3471.65
Distal Tibia	RM50	Validation	1025.60	1194.60	3755.88	3652.65
Distal Tibia	RM50	Validation	1150.05	964.28	3152.32	2607.80
Distal Tibia	LM43	Validation	1098.03	1218.90	4208.40	4059.10

C.3.3 Microarchitectural Properties: cuboidal volumes

Table C.4: Standard morphological data for cuboidal volumes (4 mm) of OA and ND ankle bone specimens obtained using BoneJ.

BONE	GROUP	BV/TV	DA	Tb.Th (mm)	Conn.D (mm^{-3})	SMI	EF
Distal Tibia	ND	0.315	0.560	0.196	7.912	1.319	0.020
Distal Tibia	ND	0.333	0.742	0.203	6.986	1.224	0.005
Distal Tibia	ND	0.389	0.491	0.223	5.652	0.875	0.086
Distal Tibia	ND	0.313	0.708	0.244	3.412	0.999	-0.002
Distal Tibia	ND	0.262	0.776	0.208	1.875	1.305	-0.079
Distal Tibia	ND	0.243	0.773	0.208	2.549	1.458	-0.047
Distal Tibia	ND	0.343	0.723	0.245	4.008	0.850	0.011
Distal Tibia	ND	0.439	0.705	0.260	4.814	0.118	0.037
Distal Tibia	ND	0.380	0.845	0.249	3.156	0.397	-0.008
Distal Tibia	ND	0.322	0.816	0.239	3.504	0.941	0.001
Talus	ND	0.372	0.778	0.198	8.750	1.011	0.042
Talus	ND	0.390	0.716	0.204	10.365	0.947	0.020
Talus	ND	0.286	0.547	0.200	5.670	1.561	-0.034
Talus	ND	0.397	0.535	0.241	8.822	0.655	0.005
Talus	ND	0.339	0.701	0.226	3.912	1.318	-0.025
Talus	ND	0.377	0.487	0.236	5.305	0.765	0.017
Talus	ND	0.419	0.790	0.249	4.938	0.625	0.010
Talus	ND	0.381	0.777	0.238	3.852	0.888	0.012
Talus	ND	0.326	0.593	0.214	6.025	1.211	0.014
Talus	ND	0.438	0.540	0.260	9.303	0.359	0.037
Talus	ND	0.379	0.611	0.234	3.520	0.881	-0.030
Distal Tibia	OA	0.386	0.612	0.269	4.131	0.629	0.028
Distal Tibia	OA	0.444	0.598	0.304	3.137	0.127	0.017

Distal Tibia	OA	0.482	0.662	0.330	2.660	-0.561	0.013
Distal Tibia	OA	0.334	0.578	0.292	3.267	1.102	-0.008
Distal Tibia	OA	0.490	0.583	0.294	4.776	-0.364	0.108
Talus	OA	0.315	0.632	0.251	5.122	1.604	0.030

C.3.4 ITS morphological results

Table C.5: ITS-based morphological data for cuboidal volumes (4 mm) of osteoarthritic and non-diseased ankle bone (distal tibia "D.Tib" and talus "Tal").

		$\frac{BV}{TV}$ (%)		$\frac{pBV}{rBV}$	a $\frac{BV}{TV}$	$\frac{BV}{BV}$		Tb.N ($\frac{1}{mm^3}$)		Tb.Th (mm)		pTb.S	rTb.l	Junc.D ($\frac{1}{mm^3}$)		
BONE	GROUP	**p**	**r**			**p**	**r**	**p**	**r**	**p**	**r**	(mm^2)	(mm)	**RR**	**PR**	**PP**
Tal	OA	28.088	4.717	5.955	0.169	0.856	0.144	3.147	2.397	0.148	0.105	0.061	0.340	3.016	27.266	24.969
D.Tib	OA	46.584	3.364	13.848	0.301	0.933	0.067	3.466	2.339	0.149	0.089	0.075	0.350	1.203	30.047	32.391
D.Tib	OA	32.431	2.719	11.928	0.208	0.923	0.077	3.097	2.205	0.148	0.092	0.074	0.312	2.063	21.125	22.875
D.Tib	OA	43.217	3.506	12.327	0.272	0.925	0.075	3.320	2.285	0.150	0.091	0.079	0.370	1.172	28.203	27.984
D.Tib	OA	54.960	5.574	9.860	0.308	0.908	0.092	3.679	2.718	0.147	0.086	0.075	0.390	1.344	42.625	40.484
D.Tib	OA	34.272	4.762	7.197	0.193	0.878	0.122	3.244	2.571	0.144	0.091	0.070	0.354	3.297	30.484	27.844
D.Tib	ND	32.665	1.646	19.845	0.242	0.952	0.048	3.095	1.896	0.141	0.090	0.078	0.320	1.297	17.156	21.938
D.Tib	ND	40.890	2.998	13.639	0.251	0.932	0.068	3.473	2.317	0.140	0.087	0.070	0.329	2.219	27.219	32.578
D.Tib	ND	36.412	1.567	23.237	0.281	0.959	0.041	3.061	1.868	0.149	0.088	0.085	0.333	0.938	15.578	21.500
D.Tib	ND	30.473	1.753	17.383	0.224	0.946	0.054	2.972	1.903	0.143	0.090	0.081	0.333	1.469	15.969	19.672
D.Tib	ND	29.646	1.640	18.077	0.220	0.948	0.052	2.937	1.857	0.144	0.091	0.082	0.332	0.984	15.203	18.719
D.Tib	ND	25.241	0.982	25.704	0.200	0.963	0.037	2.628	1.616	0.138	0.090	0.101	0.303	0.719	10.484	12.797
D.Tib	ND	23.104	1.164	19.849	0.180	0.952	0.048	2.602	1.683	0.140	0.091	0.094	0.319	0.875	10.766	13.094
D.Tib	ND	29.781	1.701	17.508	0.219	0.946	0.054	3.288	1.921	0.129	0.093	0.065	0.304	0.906	18.219	27.375
D.Tib	ND	31.456	1.899	16.565	0.240	0.943	0.057	3.240	2.054	0.130	0.090	0.071	0.294	1.609	19.891	26.328
D.Tib	ND	36.303	2.582	14.060	0.239	0.934	0.066	3.488	2.167	0.134	0.094	0.064	0.313	1.750	24.922	33.031
Tal	ND	35.097	2.641	13.289	0.226	0.930	0.070	3.324	2.212	0.139	0.091	0.069	0.309	2.391	23.203	28.953

Tal	ND	39.168	2.715	14.427	0.283	0.935	0.065	3.322	2.211	0.143	0.090	0.075	0.323	1.875	24.516	28.750
Tal	ND	35.655	2.431	14.667	0.238	0.936	0.064	3.322	2.201	0.141	0.088	0.069	0.309	1.719	23.875	28.422
Tal	ND	30.617	2.023	15.134	0.214	0.938	0.062	3.141	1.987	0.135	0.094	0.073	0.309	1.766	17.766	23.234
Tal	ND	40.273	3.726	10.809	0.249	0.915	0.085	3.572	2.621	0.139	0.082	0.064	0.321	4.828	37.453	38.672
Tal	ND	35.232	2.718	12.962	0.229	0.928	0.072	3.349	2.271	0.141	0.090	0.066	0.311	1.859	26.422	29.984
Tal	ND	26.740	1.900	14.074	0.193	0.934	0.066	3.054	1.920	0.131	0.097	0.072	0.315	1.469	16.391	20.844
Tal	ND	36.754	2.947	12.472	0.227	0.926	0.074	3.415	2.383	0.141	0.086	0.066	0.309	4.313	29.047	32.406
Tal	ND	31.992	1.922	16.645	0.234	0.943	0.057	3.086	1.928	0.141	0.096	0.078	0.317	1.156	17.266	21.688
Tal	ND	35.418	1.813	19.536	0.289	0.951	0.049	3.409	1.990	0.131	0.089	0.068	0.315	1.313	20.203	29.656
Tal	ND	36.165	2.873	12.588	0.269	0.926	0.074	3.559	2.241	0.131	0.097	0.061	0.301	2.188	27.469	35.547

C.3.5 Morphological Variations with Depth

Table C.6: Standard morphological properties in OA and ND ankle bone with depth.

BONE	GROUP	LEVEL	BV/TV	DA	Tb.Th (mm)	Conn.D (mm^{-3})	SMI	EF
Talus	**OA**	**1**	0.295	0.667	0.249	7.458	2.254	0.148
		2	0.292	0.686	0.258	5.805	2.755	0.107
		3	0.349	0.569	0.280	6.247	2.082	0.058
		4	0.374	0.613	0.266	7.946	2.143	0.104
Distal Tibia	**OA**	**1**	0.373	0.588	0.288	4.119	1.637	0.136
		2	0.368	0.617	0.267	5.379	1.721	0.076
		3	0.327	0.613	0.248	4.340	1.874	0.096
		4	0.344	0.625	0.244	4.229	1.971	0.099
Distal Tibia	**OA**	**1**	0.600	0.696	0.344	4.174	0.481	0.039
		2	0.537	0.706	0.351	3.048	0.951	0.056
		3	0.390	0.641	0.301	4.213	1.793	0.077
		4	0.350	0.722	0.276	4.465	1.832	0.056

Distal Tibia	**OA**	**1**	0.669	0.586	0.436	2.914	0.160	0.048
		2	0.622	0.527	0.388	3.205	0.441	-0.018
		3	0.582	0.491	0.364	3.008	0.592	0.058
		4	0.554	0.513	0.349	4.449	0.782	0.065
Distal Tibia	**OA**	**1**	0.245	0.705	0.296	3.619	1.925	0.051
		2	0.408	0.689	0.336	3.240	1.623	0.009
		3	0.388	0.641	0.270	8.340	1.601	0.021
		4	0.412	0.425	0.313	4.883	1.986	0.067
Distal Tibia	**OA**	**1**	0.567	0.575	0.293	7.324	0.407	0.184
		2	0.518	0.631	0.312	7.200	0.937	0.158
		3	0.492	0.478	0.312	4.813	1.179	0.092
		4	0.440	0.555	0.295	4.528	1.346	0.087
Distal Tibia	**ND**	**1**	0.421	0.736	0.253	5.032	1.447	0.072
		2	0.345	0.727	0.233	5.146	1.606	0.018
		3	0.326	0.748	0.249	3.658	1.715	0.086
		4	0.281	0.801	0.244	2.166	1.865	0.030
Distal Tibia	**ND**	**1**	0.443	0.730	0.252	4.324	1.202	0.002
		2	0.439	0.749	0.259	6.200	1.234	0.111
		3	0.469	0.619	0.271	4.821	1.055	0.098
		4	0.403	0.549	0.259	4.001	1.189	0.053
Distal Tibia	**ND**	**1**	0.401	0.859	0.244	2.686	1.289	-0.048
		2	0.385	0.878	0.252	3.263	1.524	0.020
		3	0.389	0.777	0.261	3.348	1.343	0.055
		4	0.343	0.745	0.236	3.449	1.368	-0.015
Distal Tibia	**ND**	**1**	0.407	0.756	0.248	3.379	1.322	0.053
		2	0.324	0.731	0.237	4.449	1.893	0.008
		3	0.284	0.815	0.227	2.906	1.616	0.003
		4	0.273	0.735	0.243	3.292	2.056	0.003

Distal Tibia	**ND**	**1**	0.377	0.725	0.247	5.269	1.514	0.032
		2	0.324	0.774	0.240	3.596	1.638	0.005
		3	0.296	0.807	0.254	2.542	1.940	0.016
		4	0.253	0.827	0.234	2.473	1.890	0.020
Distal Tibia	**ND**	**1**	0.300	0.806	0.212	1.733	1.962	0.018
		2	0.272	0.805	0.206	2.271	1.916	-0.057
		3	0.245	0.813	0.211	1.271	1.864	-0.043
		4	0.232	0.809	0.203	2.441	1.950	-0.062
Distal Tibia	**ND**	**1**	0.283	0.820	0.220	2.126	1.836	-0.068
		2	0.233	0.805	0.197	2.271	1.866	-0.029
		3	0.227	0.758	0.207	2.403	2.217	-0.027
		4	0.228	0.692	0.207	3.386	2.080	0.037
Distal Tibia	**ND**	**1**	0.312	0.794	0.175	10.813	1.850	0.036
		2	0.388	0.505	0.203	13.098	1.439	0.084
		3	0.290	0.690	0.214	3.216	2.083	0.073
		4	0.268	0.752	0.196	4.024	2.139	0.085
Distal Tibia	**ND**	**1**	0.367	0.808	0.200	11.419	1.573	0.021
		2	0.358	0.676	0.209	5.588	1.646	0.075
		3	0.315	0.685	0.202	5.720	1.873	0.063
		4	0.293	0.790	0.201	5.182	2.213	0.052
Distal Tibia	**ND**	**1**	0.420	0.557	0.222	7.064	1.231	0.093
		2	0.429	0.427	0.228	4.844	1.403	0.145
		3	0.374	0.543	0.227	6.650	1.763	0.143
		4	0.331	0.598	0.217	3.835	1.961	0.119

Table C.7: ITS-based morphological properties in OA and ND ankle bone with depth.

			$\frac{BV}{TV}$ (%)		$\frac{pBV}{rBV}$	a$\frac{BV}{TV}$	$\frac{BV}{BV}$		Tb.N ($\frac{1}{mm^3}$)		Tb.Th (mm)		pTb.S	rTb.l	Junc.D ($\frac{1}{mm^3}$)		
BONE	GROUP	LEVEL	**p**	**r**			**p**	**r**	**p**	**r**	**p**	**r**	(mm^2)	(mm)	**RR**	**PR**	**PP**
Talus	**OA**	**1**	24.06	4.985	4.826	0.144	0.828	0.172	3.040	2.393	0.144	0.108	0.060	0.330	3.782	26.228	21.763
		2	24.078	5.094	4.727	0.145	0.825	0.175	2.999	2.523	0.147	0.102	0.061	0.329	4.402	25.112	21.453
		3	29.772	5.164	5.765	0.166	0.852	0.148	3.118	2.456	0.152	0.105	0.065	0.339	3.213	27.911	24.572
		4	29.856	7.598	3.929	0.182	0.797	0.203	3.365	2.758	0.143	0.108	0.055	0.343	5.418	39.504	31.187
Distal Tibia	**OA**	**1**	35.641	2.781	12.816	0.179	0.928	0.072	3.181	2.197	0.123	0.091	0.090	0.337	1.426	21.205	23.003
		2	33.506	3.401	9.852	0.222	0.908	0.092	3.211	2.326	0.149	0.093	0.068	0.332	2.108	27.840	26.538
		3	29.693	2.959	10.035	0.210	0.909	0.091	2.975	2.110	0.147	0.102	0.077	0.326	1.638	18.586	19.720
		4	29.616	4.799	6.171	0.202	0.861	0.139	3.222	2.804	0.140	0.088	0.063	0.289	5.922	30.683	27.281
Distal Tibia	**OA**	**1**	56.797	4.583	12.393	0.304	0.925	0.075	3.656	2.586	0.134	0.084	0.088	0.391	1.426	37.574	35.962
		2	48.822	4.639	10.524	0.304	0.913	0.087	3.362	2.460	0.155	0.091	0.084	0.380	1.302	31.932	29.080
		3	34.957	4.005	8.728	0.232	0.897	0.103	3.128	2.327	0.151	0.098	0.076	0.349	1.701	26.210	24.509
		4	31.629	3.339	9.473	0.222	0.905	0.096	3.010	2.169	0.154	0.101	0.075	0.347	1.512	22.366	21.547
Distal Tibia	**OA**	**1**	61.251	6.423	9.536	0.289	0.905	0.095	3.632	2.779	0.142	0.088	0.090	0.404	1.674	39.993	37.698
		2	55.374	5.93	9.338	0.300	0.903	0.097	3.743	2.867	0.148	0.084	0.071	0.374	2.976	45.759	41.977
		3	53.189	6.157	8.639	0.312	0.896	0.104	3.598	2.833	0.153	0.088	0.076	0.378	2.394	43.473	38.999
		4	49.173	6.531	7.529	0.312	0.883	0.117	3.688	2.841	0.145	0.088	0.068	0.377	1.575	44.733	42.654
Distal Tibia	**OA**	**1**	31.236	3.287	9.503	0.170	0.905	0.095	3.022	2.283	0.149	0.096	0.076	0.312	2.170	22.631	21.577
		2	36.554	4.273	8.555	0.189	0.895	0.105	3.162	2.345	0.153	0.095	0.075	0.383	1.612	25.484	24.864
		3	33.989	4.861	6.992	0.186	0.875	0.125	3.373	2.722	0.143	0.089	0.062	0.325	4.536	36.038	32.510
		4	33.307	7.913	4.209	0.175	0.808	0.192	3.468	3.024	0.137	0.092	0.058	0.343	5.733	44.985	36.101
Distal Tibia	**OA**	**1**	54.77	2.981	18.373	0.319	0.948	0.052	3.670	2.326	0.134	0.088	0.083	0.335	1.736	31.746	37.078
		2	44.77	8.785	5.096	0.267	0.836	0.164	3.413	2.626	0.159	0.107	0.073	0.413	3.162	33.606	31.498
		3	44.734	4.687	9.544	0.287	0.905	0.095	3.528	2.417	0.147	0.101	0.070	0.343	1.197	35.282	32.888
		4	39.949	4.183	9.550	0.282	0.905	0.095	3.264	2.442	0.150	0.090	0.077	0.368	1.827	28.919	27.281

Distal Tibia	**ND**	**1**	38.851	3.278	11.852	0.285	0.922	0.078	3.484	2.380	0.139	0.089	0.066	0.320	3.906	29.297	31.754
		2	31.914	2.677	11.922	0.242	0.923	0.077	3.192	2.124	0.136	0.095	0.072	0.328	1.701	22.807	25.328
		3	30.224	2.451	12.331	0.235	0.925	0.075	3.047	1.952	0.143	0.103	0.075	0.337	1.260	18.271	20.413
		4	27.934	1.17	23.875	0.224	0.960	0.040	2.699	1.715	0.152	0.087	0.097	0.325	0.819	12.979	14.302
Distal Tibia	**ND**	**1**	40.35	4.053	9.956	0.249	0.909	0.091	3.588	2.661	0.137	0.084	0.064	0.320	5.166	33.959	36.353
		2	40.045	4.041	9.910	0.236	0.908	0.092	3.535	2.395	0.137	0.094	0.066	0.348	1.638	31.565	34.022
		3	42.912	4.152	10.335	0.257	0.912	0.088	3.593	2.480	0.139	0.092	0.067	0.338	1.701	33.392	37.109
		4	37.127	3.203	11.591	0.221	0.921	0.079	3.417	2.288	0.138	0.092	0.068	0.338	1.449	26.777	30.872
Distal Tibia	**ND**	**1**	37.505	2.65	14.153	0.304	0.934	0.066	3.198	2.165	0.147	0.091	0.078	0.333	1.449	21.673	24.131
		2	36.056	2.531	14.246	0.309	0.934	0.066	3.128	2.142	0.146	0.093	0.081	0.324	1.197	21.232	23.248
		3	36.258	2.788	13.005	0.272	0.929	0.071	3.216	2.156	0.148	0.090	0.074	0.369	1.953	21.925	25.958
		4	32.291	2.401	13.449	0.264	0.931	0.069	3.074	2.061	0.145	0.096	0.078	0.321	2.016	18.649	22.240
Distal Tibia	**ND**	**1**	36.926	3.846	9.601	0.266	0.906	0.094	3.400	2.427	0.142	0.091	0.066	0.342	3.024	29.738	31.943
		2	30.255	2.311	13.092	0.223	0.929	0.071	3.054	2.119	0.140	0.089	0.076	0.323	1.890	20.665	20.854
		3	26.237	2.2	11.926	0.227	0.923	0.077	2.758	1.924	0.141	0.103	0.089	0.321	1.701	14.428	15.562
		4	24.99	2.364	10.571	0.205	0.914	0.086	2.839	2.061	0.141	0.091	0.077	0.347	1.701	17.515	17.956
Distal Tibia	**ND**	**1**	34.154	3.601	9.485	0.256	0.905	0.095	3.328	2.369	0.138	0.093	0.067	0.336	2.394	27.470	29.108
		2	29.542	2.847	10.377	0.233	0.912	0.088	3.107	2.090	0.139	0.101	0.071	0.321	1.071	22.240	22.555
		3	26.816	2.857	9.386	0.213	0.904	0.096	2.892	2.051	0.143	0.098	0.078	0.327	1.764	16.633	17.452
		4	23.633	1.679	14.076	0.196	0.934	0.066	2.652	1.790	0.139	0.098	0.091	0.334	1.008	11.971	13.861
Distal Tibia	**ND**	**1**	28.15	1.852	15.200	0.221	0.938	0.062	2.937	2.005	0.133	0.090	0.083	0.295	1.575	16.003	18.145
		2	26.009	1.258	20.675	0.220	0.954	0.046	2.670	1.707	0.137	0.097	0.100	0.293	0.882	13.294	14.932
		3	23.549	1.306	18.031	0.193	0.947	0.053	2.628	1.756	0.144	0.089	0.092	0.321	0.567	11.089	13.609
		4	21.504	1.759	12.225	0.178	0.924	0.076	2.670	1.796	0.131	0.099	0.086	0.333	1.386	13.546	12.979
Distal Tibia	**ND**	**1**	26.21	2.143	12.231	0.232	0.924	0.076	2.725	2.061	0.145	0.091	0.090	0.325	1.575	14.932	15.499
		2	21.692	1.752	12.381	0.180	0.925	0.075	2.631	1.835	0.135	0.101	0.088	0.301	1.008	13.294	12.916
		3	20.549	2.26	9.092	0.171	0.901	0.099	2.616	1.946	0.137	0.103	0.084	0.309	2.142	14.176	12.916
		4	21.246	1.512	14.052	0.156	0.934	0.066	2.725	1.912	0.133	0.088	0.079	0.301	1.575	14.239	15.121

Distal Tibia	**ND**	**1**	28.809	2.407	11.969	0.233	0.923	0.077	3.408	2.142	0.119	0.096	0.061	0.303	1.197	23.942	30.305
		2	35.235	3.662	9.622	0.217	0.906	0.094	3.702	2.456	0.125	0.095	0.056	0.298	2.961	33.959	40.197
		3	26.775	2.191	12.220	0.180	0.924	0.076	3.024	1.935	0.135	0.097	0.072	0.340	0.882	16.885	21.232
		4	25.169	1.683	14.955	0.209	0.937	0.063	2.925	1.924	0.132	0.091	0.076	0.316	0.882	15.814	18.523
Distal Tibia	**ND**	**1**	33.575	3.198	10.499	0.274	0.913	0.087	3.504	2.413	0.126	0.090	0.062	0.303	3.402	30.431	34.778
		2	32.955	2.85	11.563	0.233	0.920	0.080	3.299	2.304	0.134	0.091	0.069	0.302	2.142	23.311	28.478
		3	28.896	2.729	10.588	0.232	0.914	0.086	3.150	2.226	0.131	0.095	0.071	0.293	1.890	21.925	24.257
		4	27.159	2.197	12.362	0.220	0.925	0.075	3.135	2.124	0.127	0.090	0.070	0.308	1.449	21.484	23.059
Distal Tibia	**ND**	**1**	38.343	3.699	10.366	0.252	0.912	0.088	3.677	2.431	0.130	0.095	0.059	0.317	3.024	31.628	38.180
		2	38.887	4.108	9.466	0.237	0.904	0.096	3.686	2.402	0.131	0.100	0.059	0.324	2.583	33.518	39.378
		3	33.619	3.834	8.769	0.201	0.898	0.102	3.503	2.445	0.132	0.095	0.059	0.309	3.150	30.557	34.337
		4	29.684	3.473	8.547	0.203	0.895	0.105	3.264	2.204	0.132	0.102	0.065	0.330	1.701	23.627	27.848

C.3.6 Nanoindentation

Table C.8: Mean tissue modulus (E_{tiss}) and reduced modulus (E_r) for ND specimens. Units: GPa

Bone	Donor	ID	E_{tiss}	$\pm$ **SD**	E_r	$\pm$ **SD**
Distal Tibia	RM57	1A	7.93	2.85	8.64	3.09
Distal Tibia	RM57	1B	9.08	3.68	9.88	3.98
Distal Tibia	RM57	2A	7.68	4.62	8.36	5.00
Distal Tibia	RM57	2B	9.44	2.93	10.27	3.16
Distal Tibia	RM50	1A	7.92	2.15	8.64	2.33
Distal Tibia	RM50	1B	7.77	2.87	8.46	3.10
Distal Tibia	RM50	2A	6.65	2.58	7.26	2.80
Distal Tibia	RM50	2B	7.71	2.08	8.41	2.25
Distal Tibia	LM43	1A	8.66	2.31	9.43	2.49
Distal Tibia	LM43	1B	8.62	2.59	9.39	2.80
Distal Tibia	LM43	2A	7.28	4.04	7.92	4.37
Distal Tibia	LM43	2B	7.57	2.60	8.25	2.81
Talus	RM57	1A	8.12	2.98	8.85	3.22
Talus	RM57	1B	7.35	3.08	8.01	3.33
Talus	RM57	1C	9.34	2.02	10.17	2.19
Talus	RM57	2A	6.26	2.54	6.83	2.76
Talus	RM57	2B	8.38	2.42	9.13	2.62
Talus	RM50	1A	10.55	3.55	11.46	3.83
Talus	RM50	1B	9.66	2.50	10.51	2.70
Talus	RM50	1C	7.80	2.05	8.51	2.22
Talus	RM50	2A	9.00	2.12	9.81	2.30
Talus	RM50	2B	8.54	2.87	9.30	3.10
Talus	RM50	2C	6.66	2.93	7.27	3.18
Talus	LM43	1A	7.73	1.72	8.42	1.86
Talus	LM43	1B	7.00	2.57	7.64	2.79
Talus	LM43	1C	7.16	2.39	7.81	2.59
Talus	LM43	2A	7.30	2.31	7.96	2.50
Talus	LM43	2B	6.76	2.28	7.38	2.47
Talus	LM43	2C	8.86	2.73	9.65	2.95

Table C.9: Mean tissue modulus (E_{tiss}) and reduced modulus (E_r) for OA specimens. Units: GPa

BONE	DONOR	ID	E_{tiss}	± SD	E_r	± SD
Distal Tibia	RM65	1A	9.35	2.73	10.17	2.95
Distal Tibia	RM65	1B	8.40	2.09	9.15	2.26
Distal Tibia	RM65	1C	8.74	2.60	9.52	2.81
Distal Tibia	RM65	1D	8.09	2.89	8.81	3.12
Distal Tibia	RM65	3A	8.46	2.45	9.22	2.65
Distal Tibia	RM65	3B	6.74	2.57	7.35	2.78
Distal Tibia	RM65	3C	8.39	3.10	9.14	3.35
Distal Tibia	RM65	3D	10.05	2.82	10.94	3.04
Distal Tibia	LM68	1A	10.57	2.38	11.50	2.57
Distal Tibia	LM68	1B	9.66	2.67	10.51	2.88
Distal Tibia	LM68	1C	8.89	2.38	9.68	2.57
Distal Tibia	LM68	1D	7.67	2.46	8.37	2.67
Talus	RM65	1B	8.96	2.06	9.76	2.22
Talus	RM65	1C	9.32	2.19	10.15	2.36
Talus	RM65	1D	7.75	2.51	8.45	2.71
Talus	RM58	1A	8.44	2.26	9.20	2.44
Talus	RM58	1B	7.94	2.76	8.66	2.98
Talus	RM58	1C	6.81	1.84	7.43	2.00
Talus	RM58	1D	7.17	1.93	7.82	2.09
Talus	RM58	2B	6.98	2.22	7.62	2.40
Talus	RM58	2C	10.48	1.90	11.40	2.05
Talus	LM68	1A	8.72	2.65	9.49	2.87
Talus	LM68	1B	8.88	2.73	9.66	2.95
Talus	LM68	1C	7.37	2.63	8.03	2.85
Talus	LM68	2B	9.59	2.17	10.44	2.35
Talus	LM68	2C	11.20	2.15	12.18	2.32

APPENDIX D

SCIENTIFIC COMMUNICATIONS

D.1 Publications

Koria, L, Mengoni, M and Brockett, C (2020) “Estimating tissue-level properties of porcine talar subchondral bone”; Journal of the Mechanical Behaviour of Biomedical Materials; DOI: 10.1016/j.jmbbm.2020.103931

Jones, WG, El-Jawhari, J, Brockett, C, **Koria, L**, Ktistakis, I, Jones, E (2020) “Multipotential Stromal Cells in the Talus and Distal Tibia in Ankle Osteoarthritis – Presence, Potency and Relationships to Subchondral Bone Changes”; Journal of Cellular and Molecular Medicine.

D.2 Conferences

AUTHORS	CONFERENCE	LOCATION	DATE
L. Koria, M.Farndon, D.Lavalette, E.Jones, M.Mengoni, C.Brockett	British Orthopaedic Research Society	Virtual	Sept 2020
L.Koria, M.Farndon, D.Lavalette, E.Jones, M.Mengoni, C.Brockett	European Society of Biomechanics	(Cancelled)	July 2020
L.Koria, M.Mengoni, C.Brockett	British Orthopaedic Research Society	Cardiff, UK	Sept 2019
L.Koria, M.Mengoni, C. Brockett	Computer Methods in Biomechanics and Biomedical Engineering	New York, USA	August 2019
L.Koria, M.Mengoni, C. Brockett	European Society of Biomechanics	Vienna, Austria	July 2019
L.Koria, M.Mengoni, C. Brockett	Bath Biomechanics Symposium	Bath, UK	Sept 2018
L.Koria, M.Mengoni, C. Brockett	British Orthopaedic Research Society	Leeds, UK	Sept 2018
L.Koria, M.Mengoni, C. Brockett	IKC & Regener8	Leeds, UK	June 2018
L.Koria, M.Casper-Taylor, M.Mengoni, C. Brockett	MeDe Innovation	Sheffield, UK	Jan 2018